UNIVERSIDADE D
COIMBRA

Ana Gabriela Teixeira Martins

TAILORING BIOMATERIALS FOR VERTEBRAL BODY REPAIR

SYNTHESIS, CHARACTERIZATION AND APPLICATION

VOLUME 1

Tese no âmbito do doutoramento em Engenharia Química, supervisionada pela Professora Doutora Maria Helena Mendes Gil e pela Professora Doutora Maria Margarida Lopes Figueiredo e submetida ao Departamento de Engenharia Química da Faculdade de Ciências e Tecnologia da Universidade de Coimbra

Agosto de 2019

UNIVERSIDADE D
COIMBRA

Ana Gabriela Teixeira Martins

TAILORING BIOMATERIALS FOR VERTEBRAL BODY REPAIR
SYNTHESIS, CHARACTERIZATION AND APPLICATION

VOLUME 1

Tese no âmbito do doutoramento em Engenharia Química, supervisionada pela Professora Doutora Maria Helena Mendes Gil e pela Professora Doutora Maria Margarida Lopes Figueiredo e submetida ao Departamento de Engenharia Química da Faculdade de Ciências e Tecnologia da Universidade de Coimbra

Agosto de 2019

Ao meu Pai

À minha Mãe

À minha Irmã

Ao Amor daminha vida

João Tavares Ferreira

Resumo

As lesões da coluna, nomeadamente as fraturas por compressão em vértebras osteoporóticas, incentivaram o desenvolvimento de técnicas cirúrgicas sofisticadas, acompanhadas por progressos importantes em biomateriais para reparação óssea. Presentemente, a cifoplastia constitui um dos métodos mais avançados no tratamento e reparação de vértebras fraturadas. Trata-se de uma técnica minimamente invasiva que consiste na injeção percutânea de um cimento ósseo no corpo vertebral colapsado, após a sua altura ter sido restaurada por meio de um balão insuflado no seu interior. Após ser injetado, o cimento ósseo solidifica, conferindo assim maior resistência à vértebra reparada. Tipicamente, os cimentos ósseos utilizados são materiais poliméricos como o poli(metilmetacrilato) (PMMA), ou outras composições baseadas em acrilatos, cujo mecanismo de ação consiste numa reação de polimerização que permite a obtenção de uma pasta injetável e endurecível *in situ*, num curto período de tempo. A preparação do cimento ósseo envolve a mistura dos reagentes momentos antes da sua injeção e a sua aplicação é monitorizada através de técnicas radiológicas. Genericamente, este tipo de cimentos ósseos é considerado eficaz e seguro para aplicação em cifoplastia. Porém, permanecem diversos fatores de risco e limitações que, embora tenham a vindo a ser minimizados ao longo do tempo, justificam a investigação de novos biomateriais para esta técnica cirúrgica.

O presente trabalho centrou-se na pesquisa por um novo biomaterial para aplicação em cifoplastia, com o objectivo de obter uma alternativa viável e propriedades materiais superiores às dos cimentos ósseos comercialmente disponíveis, sobretudo baseados em PMMA. Pretendeu-se desenvolver um sistema injetável que, após solidificação nas condições fisiológicas do interior de uma vértebra, originasse um material compósito com composição e algumas propriedades semelhantes às do tecido ósseo. Como ponto de partida, pretendeu-se que a fase inorgânica do compósito incluísse componentes minerais baseados em hidroxiapatite natural, obtida a partir de osso, e um agente de contraste radiológico, tendo sido selecionado sulfato de Bário. Na fase orgânica do compósito, pretendeu-se utilizar poli (álcool vinílico), um polímero sintético hidrossolúvel, como constituinte principal de um sistema polimérico adequado à solidificação *in situ*. Este polímero permitiu obter suspensões homogéneas dos minerais selecionados; no entanto a escolha de reagentes reticulantes constitui um grande desafio.

Esta investigação envolveu o teste de múltiplos reagentes, originais ou manipulados, e o estudo de combinações que não tinham sido antecipadas no início dos trabalhos. Estes testes exigiram uma multiplicidade de técnicas experimentais que

culminaram numa formulação capaz de satisfazer os requisitos químicos, físicos e mecânicos previamente definidos. Obteve-se um pré-compósito baseado numa suspensão de minerais em solução aquosa de poli (álcool vinílico) modificado com uma carbodiimida, à qual se adicionou colagénio hidrolisado em meio alcalino e ainda persulfato de potássio. Para solidificar esta mistura e obter um material compósito, recorreu-se a 2-hidroxietilmetacrilato. Os ensaios *in vitro* mostraram que os compósitos obtidos eram biocompatíveis com osteoblastos humanos e a sua ação hemolítica não era significativa.

Adicionalmente, desenvolveram-se microcápsulas biodegradáveis com composição e estrutura específicos, com o objetivo de funcionarem como dispositivos de libertação de fármacos, ou de outras substâncias, contribuindo simultaneamente para a criação de porosidade adequada no compósito. As microcápsulas foram utilizadas para libertarem o agente reticulante na suspensão do pré-compósito.

Realizou-se um ensaio *in vivo* com modelo animal e confirmou-se que o contraste radiológico do compósito era adequado. A análise histológica mostrou que o compósito implantado era biocompatível e possuía propriedades osteocondutoras e osteoindutivas.

Este projeto conduziu à obtenção de biomateriais com propriedades moduladas à estrutura e à função, bem como à sua aplicação clínica em cifoplastia. Após adicionar o agente reticulante à suspensão de pré-compósito, a mistura permanece injetável e pronta a aplicar. A solidificação gradual *in situ*, no defeito ósseo, é acompanhada pela absorção dos fluidos circundantes, levando a um aumento de volume do compósito. Consequentemente, o defeito ósseo fica com melhor preenchimento e maior contacto interfacial com o tecido ósseo. A porosidade do biomaterial com microcápsulas adicionadas pode contribuir para a regeneração óssea.

Palavras-chave – Enxertos ósseos, cifoplastia; biomateriais, *in situ*, hidroxiapatite.

Abstract

Spine fractures, particularly those derived from osteoporotic vertebral compression fractures (VCFs), led to the development of sophisticated surgical techniques and concomitant progress on biomaterials for bone repair. At present days, kyphoplasty constitutes one of the most advanced methods to treat and repair fractured vertebrae. This is a minimally invasive surgical technique that consists in the percutaneous injection of a bone cement inside the collapsed vertebral body, after restoration of its height with an inflatable balloon tamp. After being injected, the bone cement becomes solid, thus increasing the mechanical strength of the repaired vertebra. Typically, the bone cements used in kyphoplasty are based in poly (methyl methacrylate) (PMMA), or other acrylate-based compositions, which mechanism of action consists of a polymerization reaction that enables the production of an injectable and *in situ* solidifying paste, in a short period of time. The preparation of the bone cement involves mixing the reagents just before its injection and the application is monitored through radiologic or fluoroscopic techniques. Generally, this type of bone cements is taken as efficient and safe to apply in kyphoplasty. However, there remain several risk factors and limitations that, despite they have been progressively minimized, justify the research for new biomaterials for this surgical technique.

The present work is focused in the search for a new biomaterial for kyphoplasty, having the objective of obtaining a viable alternative and material properties superior to those of the commercially available bone cements, mostly based in PMMA. The main purpose was to develop an injectable system that, after solidification at the physiological conditions of the interior of a vertebra, would originate a composite material possessing a composition and some properties similar to those of bone tissue. As starting point, the objective was that the inorganic phase of the composite would include mineral components based in natural, bone-derived hydroxyapatite, as well as a radiocontrast agent, being selected Barium sulphate. The organic phase of the composite was meant to include poly (vinyl alcohol), a synthetic water-soluble polymer, as the main constituent of a polymeric system adequate to solidify *in situ*. This polymer enabled to have homogeneous suspensions of the minerals, but the search for crosslinking reagents was a serious challenge.

This investigation involved the test of multiple reagents, as-received and manipulated, and the study of unpredicted combinations at preliminary stages of this work. These tests required multiple experimental techniques that culminated in a formulation able to comply the chemical, physical and mechanical requirements previously defined.

They resulted in a pre-composite based in a suspension of minerals in an aqueous solution of poly (vinyl alcohol) modified with a carbodiimide, to which collagen hydrolysed in alkaline medium and potassium persulfate were added. Then, 2-hydroxyethylmethacrylate was used to solidify this suspension and obtain a composite. The tests in vitro showed that the composites were biocompatible and that their hemolytic action was meaningless.

Furthermore, this work developed biodegradable microcapsules with specific composition and structure, with the purpose of acting as delivery devices of drugs, or other substances, and simultaneously contribute to create adequate porosity in the composite. The microcapsules were used to release the crosslinking agent in the pre-composite suspension.

A test *in vivo* with animal model confirmed that the radiologic contrast of the composite was appropriate. The histological analysis showed that the implanted composite was biocompatible and had osteocondutive, as well as osteoindutive properties.

This project achieved the synthesis of biomaterials with tailored properties regarding material structure and function, adequate for its clinical application in kyphopasty. After the addition of the crosslinker to the pre-composite suspension, the mixture remains injectable to allow its injection. As the gradual solidification in the bone defect occurs, *in situ*, the composite swells through the absorption of surrounding liquids, increasing its volume. Consequentially, the filling of the bone defect is increased, with enhanced interfacial contact with bone tissue. The porosity of the biomaterial with added microcapsules may contribute to the bone regeneration.

Keywords – Bone grafts, kyphoplasty, biomaterials*, in situ*, hydroxyapatite

Contents

List of Figures

List of Tables

1 Introduction

1.1 Motivation

Ageing has become a global issue as a result of improved living conditions and health care. However, the increase of pathologies related to higher life expectation constitutes a common health, social and economic burden. That is the case, for instance, of osteoporosis and cancer diseases which are frequently associated with osteolytic lesions of the spine [1–6].

Osteoporosis is the most common chronic metabolic bone disease, which is characterized by low bone mass, deterioration of bone tissue, and disruption of bone microarchitecture. It can lead to compromised bone strength and an increase in the bone fragility and risk of fractures. Although it is seen in all age groups, gender, and races, osteoporosis is more common in Caucasians, older people, and women. Osteoporosis is a risk factor for fracture just as hypertension is for stroke. It is a silent disease until fractures occur, which causes important secondary health problems including severe debilitating pain, with consequent deteriorated quality of life, physical function and psychosocial performance [1–6].

According to recent statistics from the International Osteoporosis Foundation, worldwide, 1 in 3 women over the age of 50 years and 1 in 5 men will experience osteoporotic fractures in their lifetime. The annual incidence of osteoporotic fractures exceeds 1.5 million in the US, of which more than 50% are osteoporotic vertebral compression fractures (VCF), and this is twice the incidence of hip fractures. Some metastatic bone diseases are also frequently located in vertebrae, increasing their fragility and probability of fracture by compressive load [1–6].

In order to repair the fractured vertebrae, reduce the morbidity of VCF patients and improve their life quality, minimally invasive procedures have emerged as alternatives to spinal conventional surgery. Two main methods for cement application into the vertebral body have been developed, namely vertebroplasty and kyphoplasty. Vertebroplasty, developed from 1984 and kyphoplasty, from 1998, are percutaneous techniques performed under radioscopic control [1–7]. These techniques constitute increasingly important options for radiologists, orthopaedic surgeons and neurosurgeons managing spinal lesions. Kyphoplasty was developed from the concept of vertebroplasty, both being the basis of other recent developments of vertebral augmentation procedures that involve not only technical aspects of the surgery, but also progresses in bone cements` composition and properties [1–15]. Vertebral body stenting is a new method that has been developed in the last decade (from around 2010) to overcome some limitations of kyphoplasty [8,9,12].

Although vertebroplasty, kyphoplasty and vertebral body stenting may be considered medically necessary for different indications, these procedures require the injection of a radiopaque bone cement into the fractured vertebrae of patients to stabilize and repair the damages. As such, bone cement as the filling material plays an essential role in the effectiveness of these treatments. Since the preparation of the bone cements are made “at the operation table”, this calls for chemist skills from the medical team and the outcome of this step may, in part, compromise the success of the surgical procedure [1–13].

Nowadays, kyphoplasthy is considered an advanced surgical method to treat vertebral compression fractures, most often originated by osteoporosis or osteolytic lesions within a vertebral body, as well as kyphotic deformity management and spine realignment. Whereas vertebroplasty involves bone cement directly injected under pressure inside the collapsed vertebral body, kyphoplasty involves the percutaneous injection of bone cement inside a damaged vertebra, after creating a cavity with an inflatable balloon device. The initial inflation of the bone tamp with liquid allows restoration of the vertebral height. After deflation and removal of the balloon, the cavity which has been produced is filled by injection of a bone cement. It must contain a contrast agent to enable the radioscopic guidance of the surgery and posterior observation of the cured cement inside the vertebral body. This procedure recovers the biomechanical functions of the vertebrae, enables to align the spine and alleviate pain, with the convenient advantage of being a minimally invasive procedure that does not require much recovery time for the patient. On the other hand, the vertebral body stenting procedure is similar to kyphoplasty except for the application of a stent inside the vertebral body before the balloon inflation. After removal of the balloon, the expanded metal mesh stabilizes the vertebral height and the cavity volume and shape, allowing for the safer injection of a larger quantity of bone cement [1–13].

The currently available major categories of bone cements are non-biodegradable acrylic bone cements, biodegradable ceramic cements and composite cements with various degradation behaviours *in vivo*. Acrylic bone cements are the most frequently applied both in vertebroplasty and in kyphoplasty [1–13]. They are based on poly (methyl methacrylate) (PMMA) which, according to the orthopaedic community, present several drawbacks including monomer toxicity, flowability problems, leakage, high polymerization temperature, inappropriate mechanical properties and osteointegration limitations [1-10,14–17]. On the other hand, the ceramic bone cements, often composed of calcium phosphate or minerals, have advantages regarding biocompatibility, osteocondutivity and non-exothermal setting, but poor mechanical performance and inconsistency of

degradability [14–20]. Finally, most of the composite bone cements available in the market are based on mixtures of acrylic polymers with calcium phosphate minerals. This type of composite cements has been developed to combine the injectability potential and the bone augmentation characteristics of acrylic cements with the biodegradability of ceramic cements, but the limitations of these composites components are also reflected in the resulting materials. [20–30].

1.2 Objectives and research significance

Most bone cements that have been used so far in kyphoplasty (as well as in its preceding simpler technique, vertebroplasty) present diverse risks and limitations that stimulate the search for improvements in biomaterials for these applications. This research must rely on innovative concepts and interdisciplinary knowledge. It may lead to new biomaterials for injectable bone grafts with better performance and less secondary effects compared to the currently used materials. It may also lead to different technical applications such as 3D-printed scaffolds, to apply as solid bone grafts. Globally, depending on the set of properties obtained from these new biomaterials, the range of clinical applications may be enlarged not only in the orthopaedic field, but also in dentistry. Thus, the research significance of this scientific area is very high, as well as the potential impact of these biomaterials in health care and in the pharmaceutical industry.

The driving concern of this project is the development of a new injectable biomaterial for kyphoplasty, aiming to obtain to a viable and safer alternative to the conventional acrylic-based bone cements currently used [1–17].

With that intention in mind, the objective of the present work is the synthesis of an *in situ* solidifying composite material which is meant to mimic the bone matrix and to comply, as much as possible, with high biocompatibility and with low toxicity of all components, from the starting reagents to the final solid composite. The new biomaterial should combine a solid phase with a liquid phase, necessary to obtain a starting injectable composition. The solid phase should be of mineral origin and the liquid phase should be a polymeric solution, being water the most adequate solvent. In addition to these main component types, the composition should include specific reagents to trigger the solidification of the precursors inside a vertebral body, in an adequate time frame.

In order to meet some practical requirements, the preparation method of the new biomaterial should require simple manipulation skills before injection into the vertebral body, and it should be administered under technical conditions similar to the currently applied.

Regarding the clinical outcome of performing bone grafting procedures with the new biomaterial, this composite should enable not only bone repair, but also new bone formation for some clinical cases. The main objective is to obtain tailored biomaterials for injectable bone grafts to apply in different pathological indications through kyphoplasty procedures.

1.3 Thesis structure

The research reported in this thesis is organized in ten chapters. After Chapter 1 with a brief introduction regarding the objectives and motivation of this study, the state of the art is reviewed in Chapter 2. In Chapter 3, the objectives are described with greater detail and the experimental strategies that were adopted are explained, providing an overview of the next sections that contain the obtained results. Chapter 4 is dedicated to the selection and characterization of mineral components for the composite, namely bone-derived hydroxyapatite and barium sulphate. Chapter 5 describes the selection and characterization of organic components for the composite, focusing poly (vinyl alcohol) as the main polymer for the matrix and poly (lactic acid)-based microcapsules. Chapter 6 reports the synthesis and characterization of *in situ* solidifying composites with diverse compositions, being selected a specific formulation with adequate properties to proceed to a test with an *in vivo* model. This test is described in Chapter 7. The main conclusions from the experimental work are presented at the end of the respective section and the final remarks are presented in Chapter 8. The instrumental conditions are included as appendix in Chapter 9, and the bibliography is presented in Chapter 10.

2 State of the art

2.1 Introduction

Pathologies related to human ageing represent an increasing problem to society and have resulted in numerous research works involving interdisciplinary skills, from physical to life sciences. The incidence of age-related bone fractures, leading to significant morbidity and mortality, represents an important and onerous public health concern. Spine fractures, particularly those derived from osteoporotic vertebral compression fractures (VCF) or originated by osteolytic lesions, led to the development of sophisticated surgical techniques and concomitant progress on biomaterials for bone repair [1–14].

Bone defects originated by VCFs constitute specific conditions for orthopaedic intervention. The clinical indications for vertebral augmentation procedures have been broadened as technical advances occur, and as innovative concepts of bone cements are developed. Nowadays, percutaneous minimally invasive techniques, namely vertebroplasty, kyphoplasty and vertebral body stenting, constitute some of the most advanced surgical methods to repair collapsed vertebrae. These methods involve the injection of a radiopaque bone cement into the vertebral body, being acrylate-based compositions the most commonly used [1–17]. Although poly(methyl methacrylate) (PMMA) has been applied from the origin of these techniques , and despite diverse improvements on the composition of acrylate-based bone cements, the permanence of adverse secondary effects motivates the use of other types of materials and the search for better alternatives [1–31].

The quest for alternative biomaterials for vertebral body repair procedures, particularly through kyphoplasty, requires understanding not only the technical aspects of the surgery that imply specific properties for the material, but also the environment where it is applied. This involves considering the bone structure and composition, as well as the biological activity of this tissue. Moreover, given that the aimed alternative biomaterials need to act as bone substitutes, it is also essential to review the general properties required for bone graft materials and to learn about bone cements.

In order to recognize the main factors assisting the research in the present study, a review about the following topics is presented in this chapter: kyphoplasty and bone cements (acrylics, ceramics and composites) currently used, bone and bone tissue (composition, structure, evolution with age), and bone substitutes (material requirements).

2.2 Kyphoplasty

In the last three decades, minimally invasive percutaneous surgical techniques, namely vertebroplasty, kyphoplasty and vertebral body stenting have been adopted to treat and repair vertebral compression fractures (VCF), to alleviate pain and to restore the vertebral lost height and spinal biomechanics. These procedures involve radioscopic guidance, being each of them recommended for specific medical conditions, particularly when conservative therapy which includes analgesics, bed rest, orthoses and rehabilitation, are not effective. Vertebral augmentation surgery has been widely adopted to treat vertebral body compression fractures caused by varied pathologies including hemangioma, multiple myeloma, osteolytic metastases, and primary or secondary osteoporosis. In western countries, the osteoporotic vertebral compression fractures account for over 50% of the osteoporotic fractures [1-13].

The materials used in both vertebral augmentation procedures are bone cements, self-curing compounds that are applied in a flowable state and become solid (fully cured) inside the vertebral body, providing adequate support to the fractured vertebra. The general requirements for the vertebroplasty or kyphoplasty (with or without vertebral body stenting) bone cements make these materials a special category, which largely differs from the cements for other purposes such as total hip arthroplasty or total knee arthroplasty. Bone cements for VCF treatment require specific biomechanical and biological properties to support the spinal column. Because this procedure is performed under fluoroscopy, the material must be radiopaque to track filler material movement and detect or avoid material leak that may cause neurological or other tissue injury [1-13].

Percutaneous vertebroplasty, first conceived in 1984, is a minimally invasive method that traditionally involves the injection of the precursors of poly (methyl methacrylate) (PMMA) directly into the collapsed vertebral body. The injection of low viscosity components, the liquid monomer (MMA) and other reagents, is made under pressure, often causing additional fissures in the vertebra, leakage problems and increasing the risk of embolism, among others. The high exothermal reaction of PMMA polymerization is another undesired effect [1-7,13-16].

Kyphoplasty, developed in the 1990s, involves the introduction and expansion of an inflatable balloon into the fractured vertebral body, creating a cavity which is subsequently filled with an adequate material (Figure 2.1), being partially cured PMMA, more viscous than that applied in vertebroplasty, the most widely used material. Compared to the first method, kyphoplasty presents lower risk of cement extravasion

(since the pressure to inject the material into the created void is not so high) and better restoration of the vertebral body and spinal biomechanics [1-17].

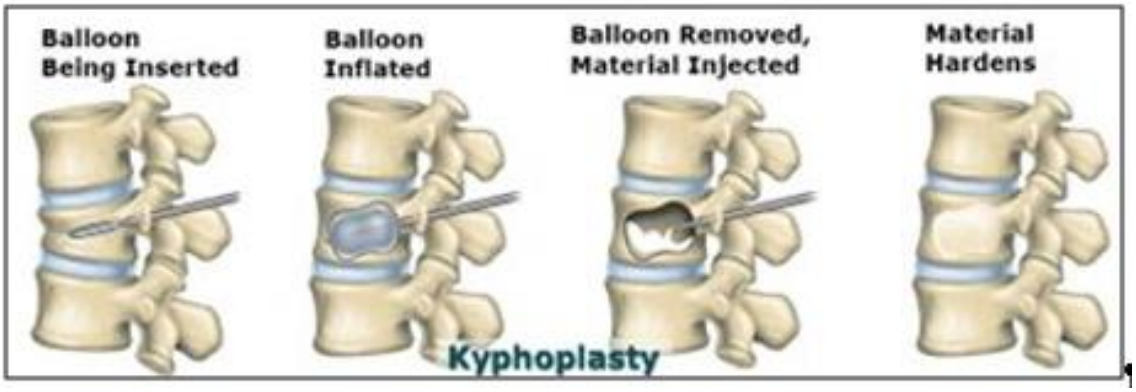

Figure 2.1 – Central stages of the kyphoplasty procedure: transpedicular insertion of a balloon tamp into the fractured vertebral body, inflation and posterior removal of the balloon device, injection of a bone cement inside the enlarged cavity and hardening of the inserted material.

Vertebral body stenting consists of a method that combines kyphoplasty with an intermediate additional procedure to insert an expandable stent inside the bone defect, before the balloon inflation. After removing the balloon, the expanded stent remains within the newly created vertebral cavity, preventing the vertebral body from collapsing so that, in an ideal scenario, a virtually physiological vertebral body height and shape can be restored and preserved. Then, the bone cement is injected inside the cavity and the solidification enables the vertebral repair [8,9,12]. Figure 2.2 shows fluoroscopic images illustrating a vertebral body stenting procedure during a surgery in the Orthopaedic Service of Centro Hospitalar e Universitário de Coimbra in 2017.

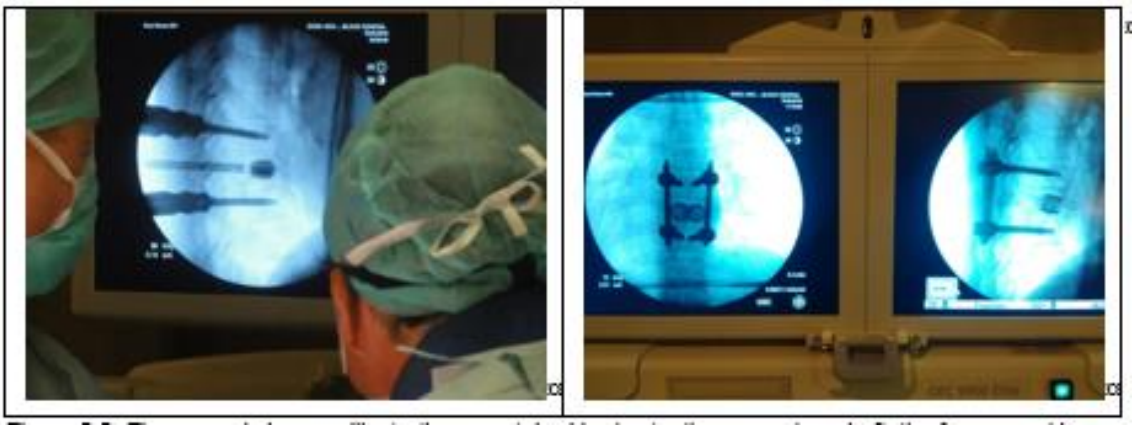

Figure 2.2- Fluoroscopic images illustrating a vertebral body stenting procedure. Left: the foreground image shows an intact stent inside a vertebral body and the background, an expanded stent containing an inflated balloon. Right: orthogonal images displaying two expanded stents. The spine is also stabilized with special connected screws. Surgery performed in Centro Hospitalar e Universitário de Coimbra in 2017.

The surgical application of bone cements by vertebroplasty and kyphoplasty requires multiple instruments, specifically designed for the injection of bone cements into vertebrae. The appropriate set of instruments is often supplied as a kit tray. These kits contain some items that are intended for single-time use and include, among other specific tools, cannulae, special syringes and needles of various size ranges. The section of the spinal needles is usually around 11 to 15 gauge (corresponding to diameters around 3.0 to 1.5 mm, respectively) [8]. Normally, the material volume injected into the vertebral body is approximately 1-4 cm^3 per side in vertebroplasty, and 2-6 cm^3 per side in kyphoplasty [1]. A set of the main instruments that are required to perform these surgical procedures is illustrated in Figure 2.3, that also shows the fluoroscopy equipment to monitor the process at diverse angles relative to the patient position.

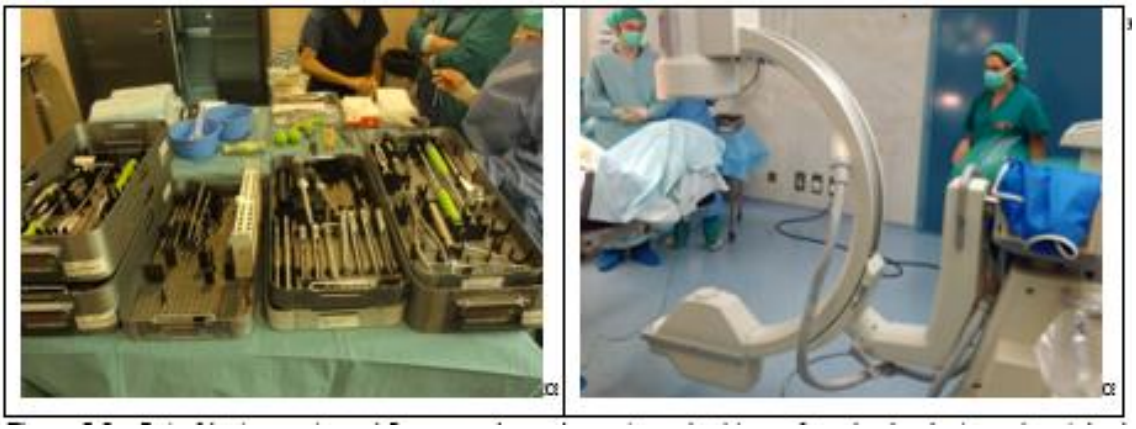

Figure 2.3 - Set of instruments and fluoroscopic equipment required to perform kyphoplasty and vertebral body stenting procedures. Images obtained during a surgery performed in Centro Hospitalar e Universitário de Coimbra in 2017.

As for the filling materials, acrylic bone cements based on PMMA are the most usually applied. Commercially available bone cements are made of (a) a powder component consisting of PMMA polymer or related block copolymers and (b) a liquid component made of methylmethacrylate (MMA) or related monomer liquids. Just before the clinical procedure, the bone cement is fabricated by combining the powder and the liquid component together. In fact, the monomer phase dissolves the powder component and, thereafter, it autopolymerizes within 10 – 15 min, resulting first in a mouldable viscous dough after 3-7 min, and then a very dense cured PMMA-based bone cement [1-5,13-16,32,33]. The preparation of the bone cement involves the mixture of the components with a specific device that has a closed chamber often connected to a vacuum source. This enables the protection from the noxious monomer fumes and prevents the entrapment of air in the mixture that could cause undesired porosity in the cement.

Nowadays, two types of PMMA bone cements are commonly applied for spinal column fractures: low viscosity compositions for vertebroplasty and high viscosity for kyphoplasty [3,7,13–15,30]. The differences between both surgical techniques dictate different characteristics for the filler material and accordingly, for its handling procedures. However, no matter the specific surgery, the bone cement is always prepared inside the operating room, meeting the same high standards that are demanded for any other material supplied by the industry. In addition, due to its composition, PMMA has unique safety considerations that are related to its preparation and application. Accurate bone cement mixing and precise application techniques are critical in ensuring that the potential health risks to both patients and healthcare professionals are minimized.

The main complications derived from the application of PMMA bone cements derive from incomplete polymerization of MMA causing monomer toxicity, high temperature reaction causing tissue necrosis, volume contraction leading to lack of cohesion between bone and the material, as well as excessive stiffness, which constitutes the probable cause of fracture of untreated adjacent vertebrae. Moreover, cement leakage into adjacent tissues, disk spaces, vascular vessels and spinal cord have also been reported, causing a wide range of serious health problems including cardiovascular episodes due to embolism [1-11]. To address these concerns several approaches have been proposed namely mixing PMMA with other products or replacing it by other cements. Currently, most alternative bone cements may be chosen from a variety of ceramic compositions (mainly calcium-phosphate cements) and composites[4,13,14,16,23,30,33,34].

2.3 Bone cements currently used in vertebral augmentation

According to the International Union of Pure and Applied Chemistry (IUPAC) definition, bone cements consist of self-curing organic or inorganic materials, used to fill up cavities or create a mechanical fixation [35]. This definition brings to attention that self-curing processes can be the source of release of reagents that may cause local and/or systemic toxicity, as in the case of the monomer released from methacrylics-based bone cements used in orthopaedic surgery. It is also mentioned that polymer-based cements used in dentistry are usually cured photochemically using UV radiation, in contrast to bone cements (that require a chemical initiator).

Currently, the most widely used bone cement is poly (methyl methacrylate) (PMMA), the base composition of acrylic bone cements [1-5,13-16,32,33]. However, the most ancient bone cement is a ceramic composition based on calcium sulphate. Meanwhile, other ceramic bone cements were developed, particularly those with similar properties to the bone mineral, that is, the calcium-phosphate cements [16,17,33,34,36–38]. Other alternatives, combining organic and mineral components, have also emerged. The self-curing or *in situ* crosslinkable composites constitute additional options relative to PMMA [4,16,24,28,30,34,39–45].

In vertebral augmentation procedures, no matter the type of bone cement, all have a common ingredient: the radiological contrast agent, which is mandatory to monitor the application procedure and allow the observation of the material after implantation. So far, the contrast agents can be selected from non-resorbable additives (such as Tungsten, Tantalum, Bismuth oxide or Barium sulphate particles), resorbable additives as Strontium carbonate or iodine-based liquids. The most commonly used has been Barium sulphate, although the fact of being non-resorbable has been pointed out as a probable cause of release of undesirable particles into the organism. Strontium carbonate, on the other hand, has the advantage of being bioresorbable, but is not as radio-opaque as calcium phosphates (such as hydroxyapatite). Finally, iodine-based liquids may cause allergic reactions days after the material implantation, with potential dramatic consequences for the patient [2] [4].

2.3.1 Acrylic bone cements

Acrylic bone cements based on the polymerization of MMA constitute the most frequently used filler materials in vertebral augmentation procedures.

The chemical reactions involved in the synthesis of PMMA result from a free radical polymerization mechanism that involves several stages. The process starts with the initiation (or induction) of reactive species: the free radicals result from the thermally or light induced reaction of the initiator (benzoyl peroxide, for instance). Then, the addition of primary radicals to the double bond of the monomer occurs, forming a new starting active component to the reaction (Figure 2.4)

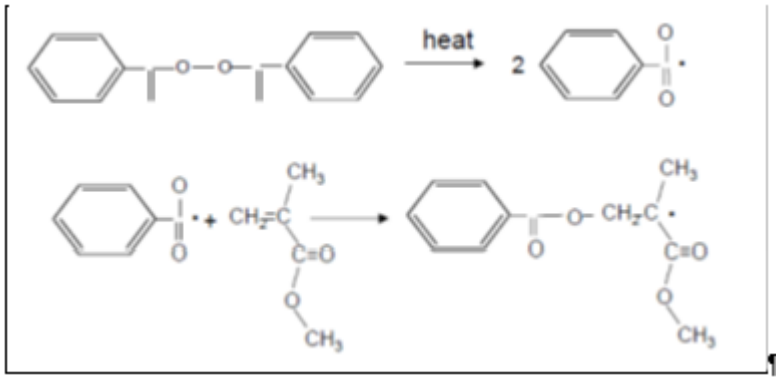

Figure 2.4 – Initiation mechanism.

The stage of propagation (Figure 2.5) involves the successive addition of monomer molecules to the new free radicals, forming new active centers with growing molecular weight.

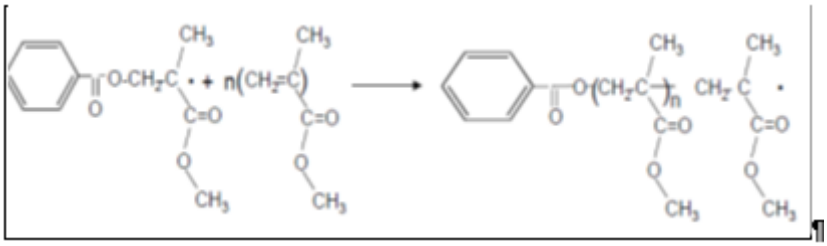

Figure 2.5 – Propagation mechanism.

Finally, the termination of the polymerization reaction occurs (Figure 2.6) due to radical coupling or recombination, stopping the growing of the molecular chain.

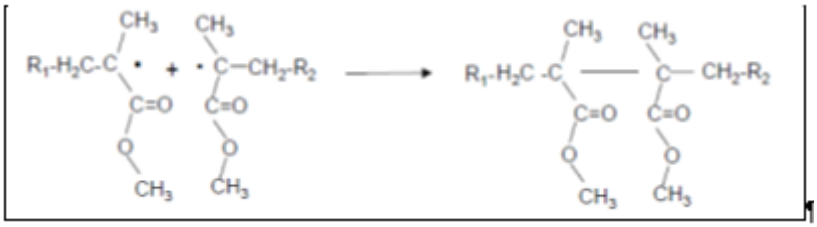

Figure 2.6 - Termination mechanism.

Acrylic bone cements consist of two primary components: a powder commonly consisting of copolymers based on PMMA and styrene, and a liquid monomer, methyl

methacrylate (MMA). These two components are mixed at an approximate weight ratio of 2:1 to form a poly (methyl methacrylate) cement. However, other components are also part of the cement composition, being most of them toxic. Hydroquinone is often added to the liquid component, acting as a stabilizer or inhibitor to prevent premature polymerization because exposure to light or high temperatures can cause premature polymerization of the MMA monomer. Di-benzoyl peroxide (an initiator) is often added to the powder and N,N-dimethyl-p-toluidine (a cataliyst) is added to the liquid, to encourage the polymer and monomer to polymerize at room temperature (cold curing cement) [4,13,46].

In order to make the cement radiopaque, a contrast agent is added. Commercially available cements mostly use either zirconium dioxide (ZrO2) or barium sulphate ($BaSO_4$). Zirconium dioxide is one hundred times less soluble than barium sulphate and has less effect on the mechanical properties of the cement [4,13-15].

Some formulations also contain a dye such as Chlorophyll. The colour makes the cement more easily visible in the operating room, especially during revision procedures. Additionally, the powder component usually contains an antibiotic (such as gentamicin) or a combination of antibiotics (such as gentamicin and clindamycin) [4,13-15]. The common qualitative composition of PMMA bone cements is presented in Table 2.1.

Table 2.1 - Typical composition of the powder and liquid components of PMMA bone cements.

Powder	**Composition**	**Liquid**	**Composition**
Polymer	PMMA-co-Styrene	Monomer	MMA
Initiator	Benzoyl Peroxide	Catalyst	N,N-dimethyl-p-toluidine
Radiopacifier	ZrO_2/$BaSO_4$	Inhibitor	Hydroquinone
Antibiotics		Colouring agent	Chlorophyll

When the polymer powder and monomer liquid meet, the polymerization process starts. During the polymerization of the monomer, the original polymer beads of the powder are bonded into a doughlike mass. The mass hardens approximately 7-15 minutes after the start of mixing, depending on the temperature. The polymerization process can be divided into four different phases: mixing, waiting, application and setting. In the mixing phase, the cement should be mixed homogeneously, minimizing the number or pores. Vacuum mixing has been shown to reduce the cement's porosity and increase its mechanical strength. During the waiting phase, the cement achieves a suitable viscosity for delivery, being a sticky paste. The working phase is the period during which the cement can be introduced with ease. The cement must not be sticky anymore, and its viscosity should be suitable for application. If the viscosity is too low,

the cement may not be able to withstand the bleeding pressure and to prevent the blood from entering the cement. Finally, during the hardening phase, the cement hardens and sets completely. Hardening of the acrylic cements is strongly influenced by the temperature (material, body and environment) [30,47].

Gathering the basic information about acrylic cements, it can be stated that conventional PMMA processed in its current two-part form, the cement precursors, is mainly composed of a powder component containing PMMA microspheres and a benzoyl peroxide initiator, and the liquid monomer MMA. Mixing these components leads to an exothermic polymerization reaction, producing a doughlike material that slowly hardens into a glasslike state. This base composition has been used in orthopaedic surgery as bone cement from the 1940 decade, mostly for implant/prothesis fixation. The range of specific applications increased with time, leading to numerous formulations adapted from the starting MMA/PMMA binary. Nowadays, whereas the powder component of acrylic bone cements typically includes pre-polymerized PMMA microspheres, barium sulfate or zirconium dioxide for radio-opacification and dibenzoyl peroxide (BPO) as an initiator, the liquid component typically consists of MMA monomer, N,N-dimethyl-p-toluidine (DMPT) as an accelerator, and hydroquinone (HQ) to prevent premature polymerization. Other components that can be included with the powder are tri-n-butylborane as an initiator, 2,5-dimethylhexane-2,5-dihydroperoxide as an accelerator, ascorbic acid, antibiotics, and dyes such as chlorophyll [30,47]. The main reasons for such two-component mixtures include finding a balance between the polymerization rate of the MMA monomer, the possibility of monomer diffusion into bloodstream, the high temperature produced from the polymerization reaction and the high volumetric shrinkage of PMMA from its monomer. The volume contraction that occurs as curing proceeds may be the cause of low interfacial contact between the polymer and the surrounding bone tissue, leading to increased risk of mechanical failure. After curing, the resulting PMMA may be classified as an *in situ* forming hydrogel, although its water absorption ability is decreased as result of using pre-polymerized PMMA, known to enhance the crosslinking density of the final product. Typically, this originates very hard and brittle materials, with low water swelling potential [27,30,48]. Due to spinal biomechanics, the increased hardness of PMMA may be related to fissures and fractures of other vertebrae, adjacent to the repaired one [7][14].

The chemical composition of acrylic cements may vary qualitatively and regarding the relative concentrations of the components. Table 2.2 displays the details of multiple commercially available acrylic cements [4]. It is worth mentioning that

typically, the pre-polymer constitutes around 88 % of the total weight of the solid components, the contrast agent to nearly 10% and the initiator, to 2%. As for the liquid components, the monomer accounts for 97-99% of the composition, being the remaining weight due to the accelerator (DMPT) and to the inhibitor (HQ). The ratio between the solid and liquid phases, as mentioned earlier, is usually 2:1. The technical information from the suppliers of each brand described in Table 2.2 shows that the working time is between 3 and 12 minutes and the setting time is in the 6-20 minutes interval. The data also show that before setting, the viscosity of the bone cements may be low, medium or high. After solidification, the mechanical strength of the cements under compressive forces correspond to values between 70 and 111 MPa.

Table 2.2 - Trade name and chemical composition of diverse acrylic bone cements expressed in weight percentages of solid (pre-polymer, radioopacifier, BPO) and liquid (monomer, DMPT) components, handling (working time, setting time, viscosity) mechanical properties (bending modulus, bending strength and compressive strength) and respective supplier [4].

Brand	Prepolymer	Monomer	Radiopacifier	Initiator and additives	Working time (min)	Setting time (min)	Viscosity	Bending modulus (MPa)	Bending strength (MPa)	Compressive strength (MPa)	Supplier
CMW1	PMMA: 88.85%	MMA: 99.18%	$BaSO_4$: 9.1%	BPO: 2.05% DMPT: 0.82% HQ: 0.0025%	6.5	11	High	2634	67.81	94.4	Depuy
CMW2	PMMA: 86.7%	MMA: 99.18%	$BaSO_4$: 11.3%	BPO: 2.0% DMPT: 0.82% HQ: 0.0025%	3	6	High	3008	74.3	97.8	Depuy
CMW3	PMMA: 88.0%	MMA: 97.5%	$BaSO_4$: 10%	BPO: 2.0% DMPT: 2.50% HQ: 0.0025%	5.5	11	Medium	2764	70.3	96.3	Depuy
Smartset HV	PMMA-co-PMA: 84%	MMA: 97.5%	ZrO_2: 15%	BPO: 1% DMPT: 2.5% HQ: 0.0075%	8.0	12.5	High	3010	64.32	86.54	Depuy
Endurance	PMMA: 67.5% PMMA-co-PS: 21.1%	MMA: 98.0%	$BaSO_4$: 10%	BPO: 1.85% DMPT: 2.0% HQ: 0.0011%	8.0	14	Low	2896	76.1	94	Depuy
Smartset MV	PMMA-co-PS: 15–30% PMMA: >50.0%	MMA: >50.0%	$BaSO_4$: 5–10%	BPO: 1–3% DMPT: ≤2.0%	8.0	14	Medium	3010	64.32	70	Depuy
Simplex P	PMMA-co-PS: 73.5% PMMA:15%	MMA: 97.45%	$BaSO_4$: 10%	BPO: 1.5% DMPT: 2.55% HQ: 0.008%	7	14.3	Medium	2681	71	90.32	Stryker
Spineplex	PMMA: 8.51% PMMA-co-PS: 58.3%	MMA: 97.5%	$BaSO_4$: 30%	BPO: 1.5% DMPT: 2.5% HQ: 0.0079%	10–12	8.7	Low		55.1	80.91	Stryker
Palacos® R	PMA: 83.9%	MMA: 97.98%	ZrO_2: 15.3%	BPO: 0.8% DMPT: 2.0%	5.0	12.5	High	2628	72.2	79.6	Heraeus
Osteopal V	PMMA-co-PMA: 54.6%	MMA: 97.87%	ZrO_2: 45%	BPO: 0.38% DMPT: 2.13% HQ	8	14	Low	3504 ± 235	46 ± 8	82 ± 3	Heraeus
Cobalt HV	PMMA-co-PMA: 83.55–84.65%	MMA: 98%	ZrO_2: 14.9%	BPO: 0.5–1.6% DMPT: 4.27%	5	10	High		67.84	96.04	Biomet
Osteobond	PMMA-co-PS: 88.75%	MMA: 99.26%	$BaSO_4$: 10%	BPO:1.25% DMPT: 0.745% HQ: 0.008%	5	14.5	Low	2828	73.7	104.6	Zimmer
KyphX HV-R	PMMA-co-PS: 68%	MMA: 99.11%	$BaSO_4$: 30%	BPO: 2% DMPT: 0.888% HQ: 0.0075%	8	20	High			111	Kyphon
ABC	PMMA-co-PS: 99.55%	MMA: 99%		BPO: 4.5% DMPT: 1% HQ: 0.006%	4.5–6.5	12	Medium	3300	68	93	Tianjin Institute of Synthetic Materials Industry

$BaSO_4$ = barium sulphate; BPO = benzoyl peroxide; DMPT = *N*–*N*-dimethyl-*p*-toluidine; HQ = hydroquinone; HV = high viscosity; MMA = methyl methacrylate; MPa = megapascals; MV = medium viscosity; PMA = polymethyl acrylate); PMMA-co-PMA = methyl methacrylate-methylacrylate copolymer; PMMA-co-PS = methyl methacrylate-styrene copolymer; ZrO_2 = zirconium dioxide.

In addition to the classic PMMA, other acrylic cements that obey to the same principles and reaction mechanisms are also used. The mixture of different monomers and the use of co-polymers as monomers are used as strategies to modify some of the properties of the PMMA polymeric system. That is the case of bifunctional acrylic resins which contain monomers with two active bonding positions as, for instance, bisphenol-A-glycidyldimethacrylate (BisGMA) and triethylene glycol dimethacrylate (TEGDMA).

The BisGMA polymers may be highly crosslinked, originating products with very strong mechanical properties (compression strength superior to 100 MPa) adequate for demanding applications as in some dentistry applications. However, for vertebral augmentation procedures, the excessive stiffness may be damaging.

2.3.2 Ceramic bone cements

Ceramic bone cements are usually composed of a mixture of low and high soluble ceramics, being the latter normally supplied already dissolved in a liquid phase that may be water, or not. These ceramics react with each other, forming a paste that latter hardens *in vivo.* This process is known as setting reaction and results from the precipitation of a new salt, constituting a new interlocked structure. This type of cement is typically used for low to medium load-bearing applications [9], [13], [30], [31]. Being usually composed by low or non-toxic components, ceramic bone cements are usually prepared with no special precautions besides sterilization and centrifugation of the mixture to eliminate air bubbles.

The most ancient ceramic bone cement, with over 100 years of clinical history, is the well-known Plaster of Paris. It combines two different forms of calcium sulphate (anhydrous and hemi-hydrated salts) which, after being mixed together, precipitate into calcium di-sulphate (gypsum) entangled crystals. Though gypsum presents very low solubility, it is fast resorbed under physiological conditions thus limiting its application in clinical practice. Calcium sulfate cement is mostly used in the treatment of oral maxillofacial syndromes, including periodontal disease and maxillary sinus augmentation.

Calcium phosphate cements (CPCs) begun being used in the 1980s, opening a new era on bone substitute materials. These cements have shown some promise in applications such as vertebral augmentation, osteoporosis related fractures, unstable fractures, skull reconstruction, and maxillofacial deformities. The main driving force behind the use of CPCs as bone substitute materials is, as previously mentioned, their similarity to the mineral component of bone. As a result, in addition to being non-toxic, they are biocompatible, not recognized as foreign in the body and most importantly, exhibit bioactive behaviour, being integrated into the tissue by the same processes active in remodelling healthy bone [17-19,36–38,48–50].

The mechanism of CPCs may involve diverse orthophosphates (as those exemplified in Table 2.3), combining minerals with different solubilities. This description

is, however, a very simplified model relative to the products currently commercialized. In fact, these types of cements frequently include other components to overcome multiple unfavourable situations arriving from injectability and viscosity problems, lack of cohesion, variable setting time, inadequate resorption and poor mechanical properties [17-19,36–38,48–50]. Changing the particle size and shape of the ceramics may be helpful in controlling some of these issues. In fact, in most systems, viscosity usually increases when the dispersed particles are smaller. However, if the viscosity is too high, it may be necessary to include dispersive components. On the other hand, the cohesion between the liquid phase and the particles must be also controlled in order to avoid phase separation and consequent blocking of the injection devices. This may involve the use of additional salts in the solution or even adequate organic components. A large number of strategies are also commonly used to control the setting rate, including the addition of nucleating agents, retarders or accelerators into the mixture [18,48].

Another approach may also be considered. Some bone cements combine calcium sulphate with calcium phosphates. Since gypsum is relatively fast dissolved under physiological conditions, leading to the rapid decrease of mechanical properties, it is often combined with less soluble minerals, such as β-TCP or hydroxyapatite [51].

Table 2.3 - Density and solubility at 25 ºC of some calcium phosphate minerals.

Compound (*)	**Density (g/cm^3)**	**-log K_s (**)**
$Ca(H_2PO_4)_2.H_2O$	2.23	1.14
$CaHPO_4.2H_2O$	2.32	6.59
$CaHPO_4$	2.89	6.90
$Ca_8H_2(PO_4)_6.5H_2O$	2.61	96.6
α-$Ca_3(PO_4)_2$	2.86	25.5
β-$Ca_3(PO_4)_2$	3.07	28.9
$Ca_{10}(PO_4)_6(OH)_2$	3.16	116.8
$Ca_4(PO_4)_2O$	3.05	38-44

* Tricalcium Phosphate α-$Ca_3(PO_4)_2$ and β-$Ca_3(PO_4)_2$ are commonly designated by α-TCP and β-TCP, respectively.

** K_s is the solubility product; concentrations are given in mol.dm^{-3}

There are diverse ceramic bone cements commercially available, as illustrated in Table 2.4 [4]. In these examples, the end products are mostly apatite salts with variable porosity (2-80%) and diverse pore sizes (maximum is 300 μm). These parameters have great influence in the biodegradation rate of the cement and in the new bone formation potential. Other characteristics include initial setting time (3-20 minutes), full hardening

time (1-72 hours), injectability and degradability. Additionally, compressive strength ranges between 0.24 and 80 MPa.

Table 2.4 - Trade name, supplier and chemical composition of diverse ceramic bone cements. The salts concentration is expressed in weight percentage of the solid components. The respective end-products are described relative to the initial setting time and the full hardening time, porosity and pore size, degradability, injectability and compressive strength [4].

Brand	Powder composition	Initial setting time	Full hardening time	End product	Porosity	Pore size (μm)	Degradability	Injectability	Compressive strength (MPa)	Supplier
BoneSource	72.3% TTCP, 27.7% DCPA	7 min	4 h	Apatite	5–10%	33.4 ± 6.2	Minimal	No	26	Stryker
Norian SRS	α-TCP, $CaCO_3$, MCPM	10–15 min	12 h	Carbonated apatite	50%	47.2 ± 21.9	Yes	Yes	50	Synthes
α-BSM	ACP, DCPD	15–20 min	1 h	Apatite	80%	<1	Yes	Yes	4	ETEX
Biopex	75% α-TCP, 18% TTCP, 5% DCPD, 2% HA	7–10 min	24 h	Apatite	40–50%		Yes	Yes	80	Mitsubishi
Calcibon	α-TCP, DCPA, $CaCO_3$, HA	10 min	6 h	Carbonated apatite	30–40%	41.6 ± 22.0	Yes	Yes	60	Biomet-Merck
Cementek	α-TCP, TTCP, $Ca(OH)_2$	3–15 min	24–48 h	Apatite	50%	26	Yes	Yes	13	Teknimed
Graftys HBS	HA, TCP	15 min	72 h	Apatite	65–70%	100–300	Yes	Yes	12	Graftys
Graftys Quickset	HA, TCP	8 min	24 h	Apatite	70%	10–100	Yes	Yes	24	Graftys
Ostim	HA	20 min		Apatite	53%	70	Yes	Yes	0.24	Hereaus
chronOS Inject	β-TCP, DCPD	6–12 min	24 h	Brushite	60–75%	70–170	Yes	Yes	3	Synthes
Embarc	ACP, DCPD			Apatite			Yes			Lorenz Surgical
Fracture Grout	α-TCP, $CaCO_3$			Apatite			Yes			Norian
Eurobone	TCP, DCPD	3–15 min		Apatite	2%	162.2 ± 107.1	Yes		17	FH Orthopedics
KyphOs FS		5 min	24 h	Apatite			Yes		61	Kyphon

ACP = amorphous calcium phosphate; DCPD = dicalcium phosphate dihydrate; HA = hydroxyapatite; MCPM = monocalcium phosphate monohydrate; TCP = tricalcium phosphate; TTCP = tetracalcium phosphate.

According to the values described by the producers, this type of bone cements may present a very broad range of properties. The selection of these products may be complicated due, in addition, to the influence of the preparation conditions.

Other classes of ceramic materials have been used in bone grafting. That is the case of bioactive glass, also known as Bioglass, that shows interesting results in the conventional application of solid grafts inside bone defects or as the mineral phase of injectable composites [4,5,19,21,29,30,52-54]. Bioglass refers to a group of synthetic silicate-based ceramics and was originally constituted by silicon dioxide (SiO_2), sodium oxide (Na_2O), calcium oxide (CaO), and phosphorus pentoxide (P_2O_5) when first developed in 1970s. This was later modified to a more stable composition by addition potassium oxide (K_2O), magnesium oxide (MgO) and boric oxide (B_2O); the key component, silicate, constitutes 45-52% of its weight.

Calcium carbonate from corals, sometimes combined with hydroxyapatite, has also been used as mineral phase of composites, combined with injectable acrylic polymers. Magnesium-based ceramics, too. These ceramics may enhance new bone formation [5,14,30,54,55], being interesting options to use in grafting procedures.

2.3.3 Composite bone cements

A solid composite material consists of at least two chemically identified phases (usually named as matrix and filler) which are separated by interface(s). Composite bone cements combine the concept of bone cement with that of a composite material. This implies that its multiple phase composition must undergo a self-curing or hardening process, from a viscous condition to the solid state. In accordance to the dual-phase composition of bone (hydroxyapatite and collagen), the matrix of composite bone cements is commonly a polymer, and the filler is usually a ceramic. Mineral dispersions of calcium phosphates (or other ceramics based on silica, as bioglass) in a polymeric matrix represent the strongest fields of research for bioactive composite bone cements [4,5,14,16,19-24,28-30,34,38,52–54].

The composite bone cements commercially available are mostly based in acrylic polymers and calcium phosphate minerals or Bioglass. For instance, a composite from Kuraray composed of an acrylic monomer (bis-phenol-A glycidyl methacrylate 2.2-bis-(4-methacryloyl- ethoxyphenyl) propane/ TEGDMA) combined with hydroxyapatite. Another example is Cortoss from Orthovita, a composite based in bis-GMA/bis-EMA/ TEGDMA resins combined with Bioglass [4,13–15,26,30,54].

Traditionally, the mechanism for obtaining a solid composite material from a dispersion of minerals in a liquid polymer (or in a polymer solution) may either involve the curing process of the polymer with simultaneous entrapment of the minerals, or the interlocking reaction and precipitation of the ceramic salts within a fluid environment containing the polymer [4,5,18,19,48,51]. The former option is the most commonly used in the currently commercialized materials, taking advantage of self-curing acrylate systems combined with varied ceramic compositions. The so-called composite resins constitute an example of such systems [5,13,20,27,30]. Given the acquired experience with acrylate bone cements, the medical staff may easily adapt to this alternative. However, the disadvantages regarding the polymeric component (previously described in 2.4-a)) are not overcome by using this type of composite, not only due to the qualitative composition of the acrylate-based organic phase, but also because the proportion of minerals in these composites is relatively low. On the other hand, the latter option of using precipitating salts dispersed in a polymer solution does not constitute a very efficient alternative. This option makes good use of the principles of the ceramic bone cements, combined with water soluble polymers (the most usual type) that show a strong attractive interaction with the salts. This is the case of alginate, which may link to the calcium ions of the hydroxyapatite precursors. However, such type of composites usually

degrades too fast, leaching out the polymer component and causing undesired reactions [18,48,51]. Adding these disadvantages to the common limitations of the ceramic bone cements has contributed to further investigate other types of composites [4,5,48,52,55–57]. The use of biopolymers as the organic phase of cement composites may seem an attractive option but these present diverse limitations to comply with the multiple requirements of this application [28].

Lately, another alternative has gained special attention for building up composite bone cements. It consists of promoting crosslinking reactions (between a crosslinkable polymer and respective crosslinking agent) to build up the organic component of the composite, being the mineral component a non-reactive dispersion of ceramic particles [21,30,55–57]. Although liquid organic compounds can be used, the matrix composition is normally selected among water soluble polymers, since organic solvents should be avoided. The presence of a liquid phase in the initial composition is obviously mandatory in order to enable the injection of the material. Water-soluble gelatin, the product of collagen hydrolysis, is often considered as most appropriate due to its resemblance with the organic matrix of bone. However, the crosslinking agents for gelatine are most often toxic or/and carcinogenic agents (e.g. glutaraldehyde, epichlorohydrin) which require special conditions to react. For instance, crosslinking gelatine (alone or mixed with other polymers) with glutaraldehyde typically requires acid conditions, whereas crosslinking with epichlorohydrin usually occurs in alkaline medium [61]. The addition of this type of molecules to the material composition increases undesired risks, not only due to their concomitant toxicity before reacting with the polymer, but also because the reaction may be incomplete, and it is not possible to remove any product from the implantation site. In fact, many of the crosslinking reactions of polymers require high temperature, long reaction time and solvent extraction to originate a fully crosslinked structure. Similarly to the other types of bone cements, the crosslinking reaction should start with the addition of an appropriate agent to the crosslinkable polymer (blended with the ceramic particles), being this step performed before injection. From this point, the composition cannot be further manipulated, being injected into the bone defect while viscosity permits it. The implanted material should evolve to a solid composite and become indefinitely insoluble in the physiological medium to enable bone repair, or temporarily insoluble to allow for bone regeneration. As previously mentioned (section 2.3), the material composition and structure are determinant factors for achieving such faculty. The role of the mineral component of the composite is of utmost importance not only regarding chemical composition, but also physical properties including particle size (that influences viscosity and injectability). The interaction between the mineral particles and the polymer must be

carefully evaluated, since it may block the polymer crosslinking reaction and/or compromise the rheology and dynamics of the upcoming solid composite system.

2.4 **Bone and bone tissue– composition, structure and evolution with age**

Most animal species are provided with an internal skeleton that plays not only structural functions (protection, support and locomotion) but also metabolic ones (mineral reservoir and hematopoietic site). The skeletal bones constitute complex organs and may comprise many shapes and sizes, according to their particular mechanical function and anatomic location.

Being the terms bone and bone tissue sometimes mistakenly applied, it is convenient to clarify that while the former refers to an organ made of bone tissue as well as marrow, blood vessels, nerves and epithelium, the latter refers specifically to the mineralized matrix and cells that build up and transform the rigid sections of that organ. Thus, being bone tissue a constituent of bone (organ), it is natural that they share certain characteristics such as chemical and structural features, as summarized in Figure 2.7. The following descriptions enable the full understanding of this diagram.

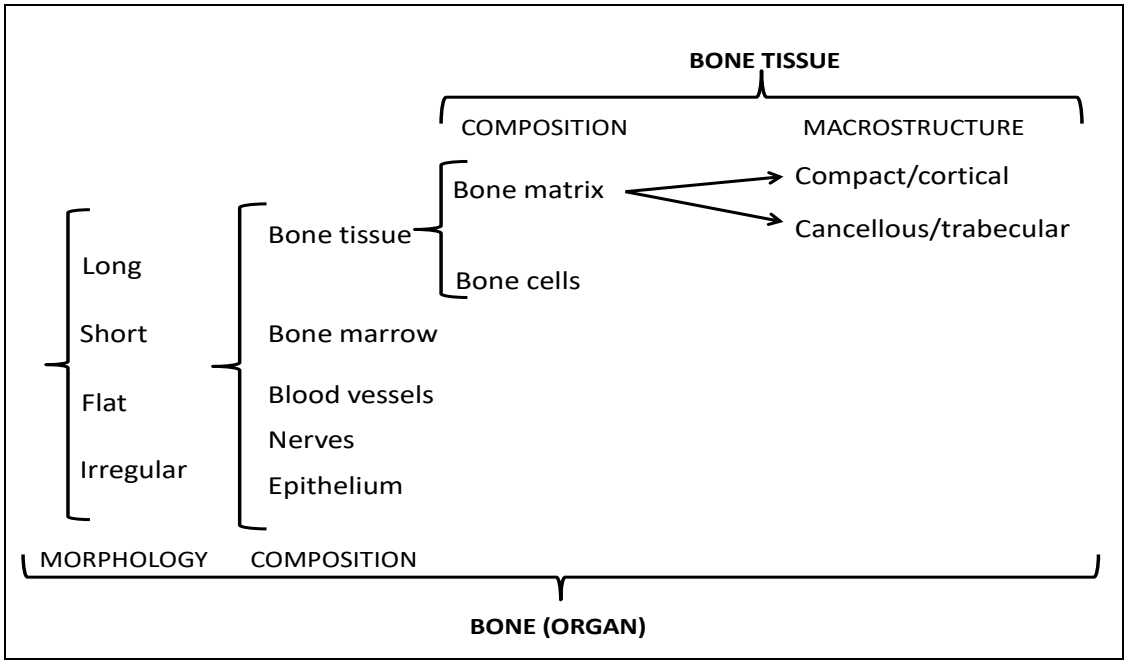

Figure 2.7 – Composition and structure of bone (organ) *versus* bone tissue.

2.4.2 Bone – structure and composition

2.4.2.1 Macrostructure

Based on their size and morphology, bones are commonly classified as long, short, flat and irregular. Examples of each kind include the long bones of the leg, such as the femur; the short bones of the fingers, the phalanges; the flat bones of the skull, as the occipital; and the irregular bones of the spine, the vertebrae. Figure 2.8 illustrates the morphology of the femur and of a lumbar vertebra, being also represented additional details about the internal structure and composition of the long bone.

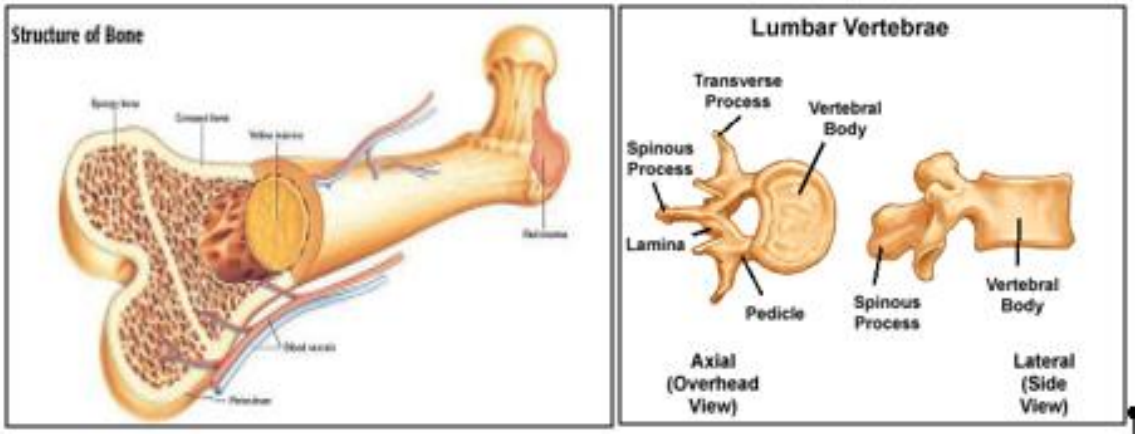

Figure 2.8 - Morphology and structural details of the femur, an emblematic long bone, and of a lumbar vertebra, an irregular bone (axial and lateral view).

Considering the internal architecture, bones can be divided into two types of structures, being named after the respective types of bone tissue: whereas the peripheral region is a very dense and hard structure, the inner region is composed of numerous trabeculae that form an interconnected porous structure. Accordingly to its relative position and appearance, the first type is named as compact or cortical bone and the latter, as trabecular, cancellous or spongy bone. Moreover, some bones (like femur) possess a medullary canal in the centre of the diaphysis (Figure 2.8). This canal contains bone marrow, which also occupies the pores of the cancellous region of the epiphyses. Other bones (like vertebrae) are not provided with any canal and the bone marrow is interspersed within all the internal porous structure (Figure 2.9).

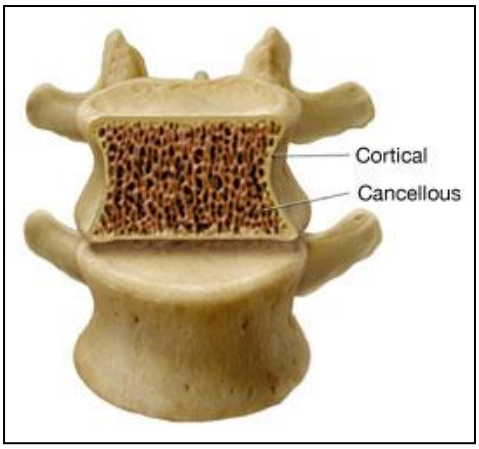

Figure 2.9- Macrostructure of the vertebral body where cortical bone constitutes the periphery and cancellous bone occupies all the inner space. Bone marrow is not represented.

2.4.2.2 Bone Composition

As mentioned, bone tissue, bone marrow, blood vessels, nerves and epithelium are the main constituents of bone, considered as an organ. Given the particular relevance of bone tissue and bone marrow for the present work, this review focuses these two components, although the remaining ones are also briefly mentioned, particularly in the context of bone matrix structure.

a) Bone marrow

Bone marrow, being a component of the bone organ, is the body tissue where most of the blood cells of the entire organism are formed in a process named hematopoiesis. In the parenchyma, bone marrow contains hematopoietic stem cells which, after differentiation and maturation, originate erythrocytes (red blood cells), leucocytes (white blood cells), thrombocytes (platelets) and also lymphocytes (key elements of the immune system). The stroma (or mesenchima) of the bone marrow constitutes the part of the tissue that is not so directly involved in the hematopoiesis. However, the stroma is also crucial for that process since it provides a convenient microenvironment and generates stimulating factors which facilitate blood cells formation. The stroma contains numerous cell types at different stages of development, including fibroblasts, osteoblasts, osteoclasts, macrophages, adipocytes and others. Endothelial cells, related to the vasculature of the marrow, are also present. The main constituents of the bone marrow are represented in Figure 2.10.

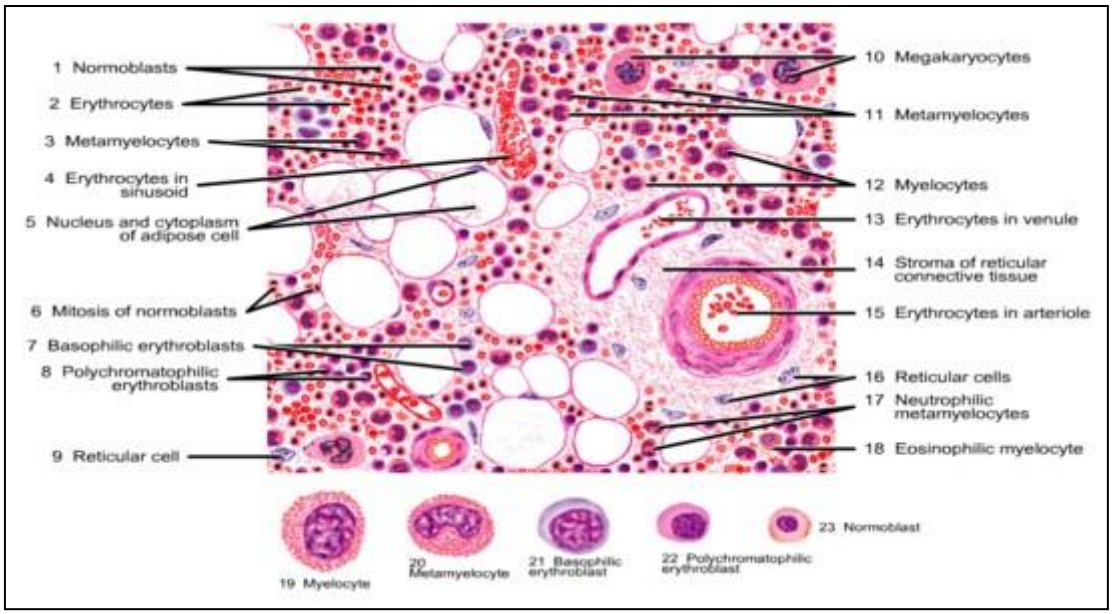

Figure 2.10 – Schematic representation of the main constituents of the bone marrow.

b) Bone tissue

Bone tissue constitutes the major fraction of bone constituents, accounting for the major weight contribution of those organs. The detailed composition and structure of the bone tissue are presented hereafter.

2.4.3 Bone tissue – composition and structure

Bone tissue is mainly composed of a solid composite material (the bone matrix) and bone cells (fundamentally osteoblasts, osteoclasts and osteocytes) that represent less than 2% of the total bone tissue weight. Thus, naturally, the structure of the bone tissue is coincident with that of the bone matrix (described in 2.2.3.1).

2.4.3.1 Composition

a) Bone cells

The bone tissue metabolism is regulated by the combined activity of two principal cell lineages: the bone forming cells (mainly osteoblasts and osteocytes) and bone resorption cells (osteoclats).

Osteoblasts, which are mononucleated cells, are responsible for the formation and deposition of layers of new bone matrix. After becoming entrapped in the mineralized

and rigid matrix inside lacunar spaces between lamellae, osteoblats differentiate into osteocytes. At this stage, these cells act mainly as chemical and mechanical sensors, enabling the transduction of signals and communication with the other cells [55,62,63].

On the other hand, osteoclasts are large and multinucleated cells belonging to the macrophage cell lineage. Osteoclasts are asymmetric cells, possessing a membrane region with a ruffled border that greatly increases the corresponding surface area. Putting this membrane region in touch with the bone matrix and sealing the periphery of the contact area, osteoclasts locally destroy the matrix by creating an acidic environment that degrades both the mineral and the organic bone components [55,62–64].

Diverse enzymes and many other molecules, such as the important bone morphogenetic proteins (BMP´s) and various hormones, also participate in those dynamic and highly complex cellular processes [17,55,62,65,66]. Additionally, the cascade of events leading to new bone formation also involves neovasculation of the bone defect. Thus, various other cell types and biological mechanisms participate in the whole process. Ultimately, bone structure and composition are dictated and directly influenced by the smallest and less abundant components of the bone tissue.

b) Bone matrix

The bone matrix constitutes the mineralized extracellular material derived from the bone cells activity.

2.4.4 Bone matrix – Structure and composition

2.4.4.1 Structure

The structure of the bone matrix results from a complex biological building process originating several highly organized architectures that, at growing hierarchical stages, start at molecular level and finally, are reflected on the physical appearance of compact and cancellous bone. Although this classification may suggest material discontinuities, it should be mentioned that most structural features at lower levels of organization are identical since they derive from a shared formation mechanism. Moreover, the interface between both types of structures reveals a gradual transition and in both cases, the multi-level structures provide multifunctional properties to the bone

matrix including mechanical features as high compression strength, moderate elasticity and important resistance to microdamage propagation [67–69].

The bone matrix structure is deeply related to its chemical composition. In fact, the matrix organization starts with the biomineralization of the organic collagenous matrix, preserving its characteristic geometry and structure (Figure 2.11). The mineralization results from the deposition of nanoscopic crystals of hydroxyapatite into specific sites of the collagen molecules. It mainly occurs in the regularly spaced gap regions of collagen telopeptides and the crystals are usually laid down oriented and aligned within the collagen molecules, towards its long axis. From a self-assembly process, the mineralized molecules organize into fibrils, which possess a characteristic band pattern resulting from the overlapped regions of the mineralized molecules. On the other hand, the fibrils become associated into fibres which usually adopt a parallel arrangement with an alternate oriented “plywood” appearance, constituting the lamellae [67,68,70–74].

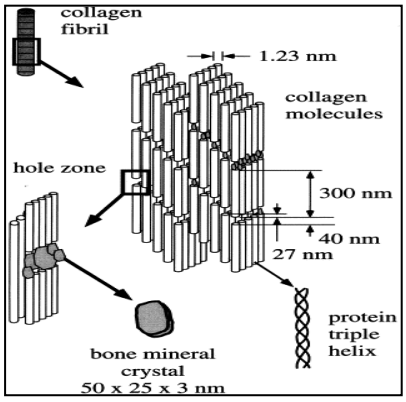

Figure 2.11 – Nanostructure of natural bone.

Lamellar bone may be disposed concentrically around blood vessels and nerves, like rings of a tree, to form osteons (Havers Systems) or occur interstitially between osteons (Figure 2.12). This organization, from a nano to a macroscopic level, leads essentially to two distinct morphologies: compact bone, composed of densely packed osteons, and cancellous bone, wherein lamellae are assembled as spaced spicules (trabeculae), originating an interconnected microporous structure.

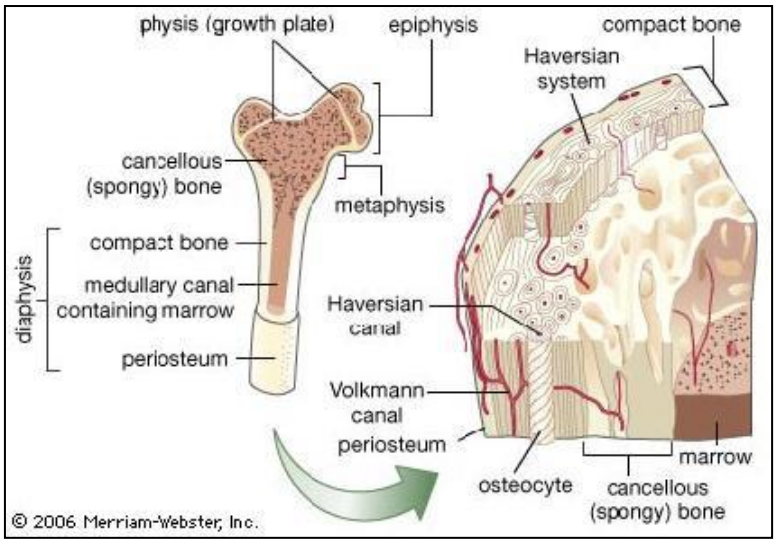

Figure 2.12 - Detailed macrostructure of the femur and representation of the corresponding microstructure of compact and cancellous bone.

It is interesting to perceive that each hierarchical structure of this anisotropic composite material is optimised to achieve a remarkable mechanical performance, from its basic building block (the mineralized collagen fibril wherein hydroxyapatite crystals have the long axis parallel to the longitudinal axis of the collagen molecules) to the tri-dimensional architecture of compact and cancellous bone [64,67]. Moreover, each structural level may undergo minor but fundamental modifications, to better adapt and respond to various biomechanical forces. As stated in a basic rule of skeletal biology known as Wolff´s law, “the bone´s morphology is a reflection of what function the bone has been built to do or adapted to perform”.

Moreover, despite the rigid structure of the bone matrix, it is provided with communication routes at various levels, enabling nutrients flow and also chemical signaling molecules, between bone cells. Havers canals, Volkman´s canals and canaliculli constitute the main existing types. Whereas blood vessels and nerves break through the bone matrix mostly inside the larger canals, the microscopic canaliculli get across successive lamellae, constituting a network that irrigates and feeds the all matrix, simultaneously allowing for osteocyte communication through gap junctions between their cytoplasmatic extensions [40,48–52].

2.4.4.2 Composition

The composition of the extracellular matrix of bone is often described as a two-phase composite of interlinked inorganic and organic components. The total weight of the bone matrix includes nearly 65% mineral component (carbonated hydroxyapatite),

25% organic components (mainly type I collagen) and 8% water, being the remaining 2% non-collagenous proteins (Figure 2.13). These components have extremely different mechanical properties: the mineral is stiff and brittle while the protein, when hydrated, is much more elastic and also much tougher than the mineral. Bone combines both the stiffness and the toughness in an unusual arrangement of material properties that result on a remarkable tensile strength and resistance against fracture, namely by compressive load [64,78,79].

Typically, the mechanical strength of cortical bone under compressive forces is 130-180 MPa and 4-12 MPa for cancellous bone. These are reference values since both composition and structure influence the mechanical performance of bone. In addition to variables as age, nutrition, health condition, hormonal equilibrium and physical activity that affect the bone composition, the architecture and anatomical position are clearly related to the mechanical properties of bone.

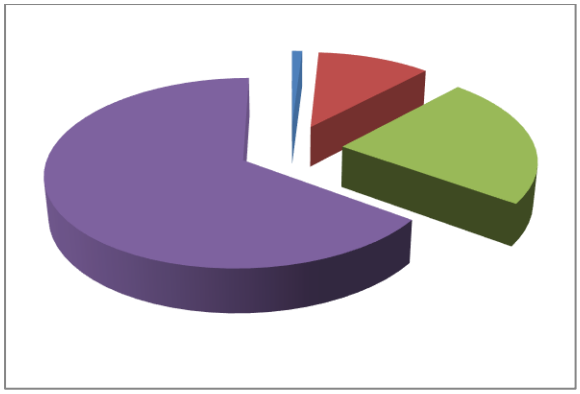

Figure 2.13 - Chemical composition of the bone matrix (65% hydroxyapatite, 25% type I collagen, 8% water and 2% non-collagenous proteins).

The bone components are so tightly embedded that they require the use of chemical procedures to obtain an effective separation of the mineral from the organic phase. The mineral component may be obtained by using thermal treatment at high temperatures (calcination) in order to eliminate the organic component [48,80]. Conversely, the latter may be isolated by using acid demineralization processes [81,82].

a) Mineral phase

Bone mineral is a poorly crystalline calcium-deficient apatite, with a Calcium-to-Phosphorous atomic ratio lower than 1.67, which is the theoretical value for pure hydroxyapatite [$Ca_{10}(PO_4)_6(OH)_2$]. The nonstoichiometric biological apatites contain several ion substitutions. For example, Na^+ and Mg^{2+} may substitute Ca^{2+} ions, HPO_4^{2-}

ions may substitute phosphate ions, and Cl^- and F^- may replace OH^-. Additionally, carbonate ions, the most abundant substitutions (3-8 % wt), may occupy either the OH^- (type A apatite) or PO_4^{3-} (type B apatite) positions in the crystal lattice. The mineral component of bone is usually closer to B-type apatite.[83–86]

The crystalline structure of carbonated hydroxyapatite belongs to the hexagonal system, although a portion of the bone mineral remains amorphous. In fact, the apatite crystals comprise two different environments: a non-apatitic hydrated domain, containing diverse labile and reactive ions, surrounds a relatively inert and more stable apatitic domain (Figure 2.14). In the interface between these domains, labile anions (PO_4^{3-} , HPO_4^{2-} and CO_3^{2-}) and cations (Ca^{2+}, Mg^{2+}) are easily and reversibly exchangeable. During initial crystal formation, ionic exchange occurs and ions gradually incorporate into the interior unit cell. The maturation of the mineral is associated with reduction of labile non-apatitic environments while stable apatitic domains augment. Moreover, as bone mineral becomes more mature, it contains less structural defects, both the size and number of crystals increase and its composition becomes closer to the stoichiometric hydroxyapatite. For this reason, crystal maturity is often associated with crystallinity (that augments with crystal size and perfection of the mineral) [55] [86–88].

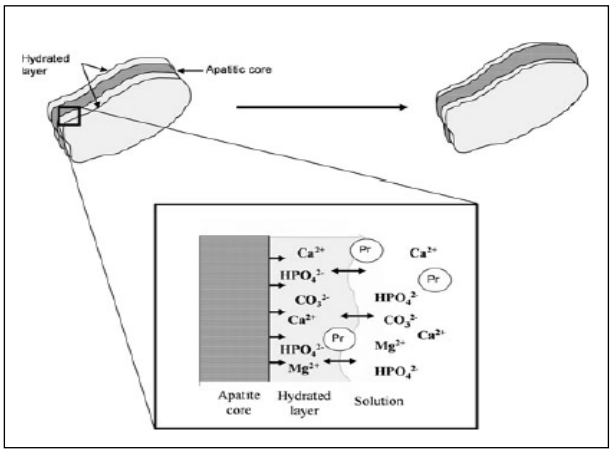

Figure 2.14 - Evolution of the apatite crystal and of the surrounding hydrated layer. During maturation and growth of the mineral, the apatitic domain of the crystal increases whereas the hydrated layer decreases, due to continuous ionic exchange between these domains and the bathing environment. Soluble charged groups of proteins (Pr) can also participate in the ionic equilibrium of the non-apatitic domain.

b) Organic phase

The organic matrix of bone consists of collagen and a series of non-collagenous proteins and lipids. Some 85%–90% of the total bone protein weight consists of Type I collagen fibers, being other collagen types also present. Despite the amount of non-colagenous proteins (such as BMPS, osteocalcin, osteopontin or osteonectine) being

very low (around 3 % wt), they provide active sites for biomineralization and cellular attachment. As for the role of collagen matrix, it has been long considered to be just a passive template for the mineralization process. However, recent investigations revealed the direct influence of some specific molecular fragments of collagen on the osteoblastic activity, activating and directing the deposition of amorphous crystals of hydroxyapatite and subsequent evolution into more crystalline minerals. The preferential sites for biomineralization include, among others, both of the 67 nm length extremities of the individual collagen molecules. Many of the cross-linking bonds between adjacent collagen molecules occur in those regions [70,89,90].

Type I collagen, the principal component of the organic matrix of bone, is a large fibrous protein with a highly repetitive amino acid sequence [Gly (glycine)–X–Y]n (often X is proline and Y is hydroxyproline). Other amino acids may also be found, such as alanine, lysine and hydroxylysine. These monomers are bound together by peptide bonds (between the carboxyl and amino groups of adjacent amino acids), constituting three polypeptide chains (two α1 and one α2 chains) that fold into a unique structure (Figure 2.15): it consists of a single uninterrupted triple helix which represents more than 95 % of the molecule (tropocollagen) and two non-helical domains (the telopeptides) containing the – COOH and – NH_2 terminals of the protein. The characteristic arrangement of the multiple collagen molecules, staggered but with some overlapped regions, originates the typical band pattern in fibrils. As observed by microscopy, fibrils have regularly spaced (40 nm) dark stripes with 27 nm length [78,89,91].

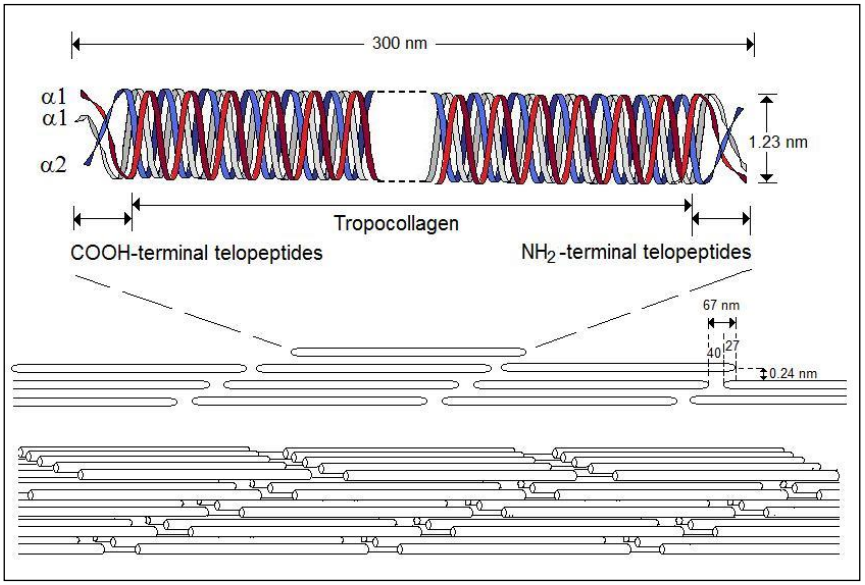

Figure 2.15 - Structure of the collagen molecule: three intertwined polypeptide chains (two α1 and one α2) constitute a major triple helical domain (tropocollagen) and two non-triple helical domains (telopeptides) at the –COOH and –NH_2 terminals of the protein. The typical staggered arrangement found in the collagen fibrils is displayed both in 2D and 3D configurations. The gap regions between the molecules are nucleation sites for hydroxyapatite.

The integrity of the collagen molecule is attributed to the formation of intra- and inter-molecular cross-linking which contribute to the mechanical strength of the bone organic matrix. Inter-molecular collagen cross-links, which may contain diverse chemical functional groups (including imine fragments), can be divided into two types: lysine hydroxylase/lysyl oxidase-controlled cross-links (enzymatic cross-links) and glycation/oxidation-induced cross-links. In both cases, cross-linking sites are at specific Lys (lysine) or Hyl (hydroxylysine) residues of the collagen molecule. Concerning the first type, the enzymatic activity leads to the formation of Lys and Hyl aldehyde-derived covalent cross-links, in which a molecular fragment binds a telopeptide and a triple helix of adjacent molecules (divalent cross-link). As a consequence of chemical reactions and rearrangements, divalent cross-links may be converted into trivalent cross-links, in which a helix is bound to two telopeptides, each from a different collagen molecule. As suggested by the sequence of the mechanism of formation, divalent cross-links are classified as immature, whereas trivalent are considered as mature. These cross-links are also commonly named after their reactivity with sodium borohydride: typically, divalent cross-links are reducible fragments whereas trivalent are non-reducible. As for the second type, glycation cross-links, these are formed between collagen helices (telopeptides are not involved), being frequently associated with the ageing process that is generally deleterious to the function of the bone tissue. In fact, the extent and type of collagen cross-linking are known to change throughout life, leading to less flexible and less elastic properties. Besides the usual bone mass loss associated with age, the accumulation of glycation cross-links and mature enzymatic cross-links in collagen is also thought to contribute to the fragility and brittleness of bone [70,78,89,90,92].

2.4.5 Bone and bone tissue - evolution with age

Bone and bone tissue properties, both structural and metabolic, depend and change with age, nutrition, hormonal equilibrium and health condition, in addition to other factors such as biomechanical environment [17,64,93,94].

The most important changes in bone structure and composition of vertebrates occur during the embryonic stages of development and posterior growth until adult phase. In fact, before reaching this phase, the osteoblastic activity exceeds that of the osteoclasts, thus promoting bone growth. Afterwards, during adulthood, despite a static appearance, bone metabolism is mostly based on the active equilibrium between the resorption of the existing matrix and the formation of new bone tissue. This process, named as remodelling (or turnover), enables the replacement of microdamaged regions

with restricted changes in their shape and size. It constitutes a dynamic response to multiple local and systemic factors, re-establishing the metabolic equilibrium of bone tissue.

However, from adulthood, bone quality usually deteriorates throughout life. Bone quality is a broad term that encompasses factors affecting the geometric and material factors that contribute to fracture resistance. Geometric factors include the macroscopic geometry of the whole bone and the microscopic architecture of the trabeculae. On the other hand, material factors include properties of the bone tissue, namely the composition and arrangement of the primary constituents (collagen and mineral) as well as microdamage and microstructural discontinuities. In general, as age increases, the osteoblastic activity becomes less efficient due to multiple factors and conversely, the osteoclasts action becomes predominant, leading eventually to excessive bone resorption and increased facture risk [83,95–100].

The most common disorder of bone associated with aging is, undoubtedly, osteoporosis. Above the age of 50 years, the incidence of this disease reaches more than 50% of the male population and over 80% of the female population of the United States of America, an emblematic example of a developed country. Osteoporosis is mainly characterized by the decrease of bone mineral density and deterioration of bone microarchitecture, particularly in the cancellous regions, leading to increased bone fragility and risk of fracture [7,11,67,69,83,86,97,101]. However, additional and more subtle alterations may also be involved. Recent progresses on diverse techniques have shown that bone fragility may also derive from the increase of rigidity of the organic matrix, due to the evolution of its crosslinking fragments.

Given the structure of the vertebrae, mostly composed of cancellous bone, the incidence of osteoporosis in spine is of utmost importance, being statistically very significant. Osteoporotic vertebral fractures, the most common complication of osteoporosis, account for over 50% of the osteoporotic fractures. They frequently occur by compressive load (Figure 2.16), causing pain problems and deformity [1,2,6,7,11].

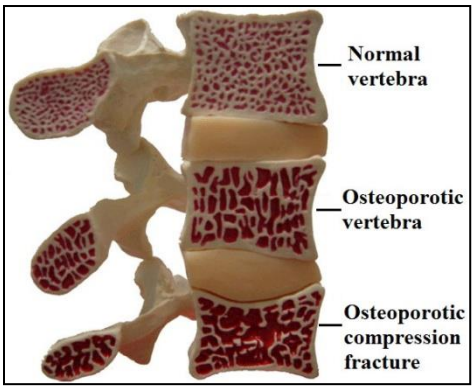

Figure 2.16 - Evolution of the cancellous bone structure of the vertebrae with osteoporosis.

In addition to osteoporosis, vertebral compression fractures may also be caused by varied pathologies including hemangioma, multiple myeloma and osteolytic metastases. Many of these cases are recommended for surgery by vertebroplasty or kyphoplasty.

2.5 Bone substitute materials

2.5.1 Material requirements

Just as the distinction between bone and bone tissue was previously presented to clarify the respective meaning, a parallel differentiation regarding bone substitutes should be considered. In fact, the “bone substitute” expression may be used whether concerning the replacement of the bone organ (using prosthesis, for instance), or the bone tissue (using bone grafts). A very important difference between the material properties of each of these kinds of bone substitutes is that while the former cannot be biodegradable, the latter should be so. It is obvious that bone prosthesis should remain intact as long as possible being, for this reason, usually made of metal alloys based on stainless steel or titanium, for instance. On the other hand, bone grafts should remain only temporarily in the organism, gradually degrading into non-toxic residues and allowing for the simultaneous replacement of the material by newly formed bone tissue [14,16,21,23,36,51,56,65,102–104].

As an aside and having these differences in mind, since the PMMA applied in vertebral surgery is a non-biodegradable material and is bio-inert regarding bone regeneration, acting merely as a repair material, it should be considered mostly as a kind of prosthesis rather than a bone tissue substitute. As a matter of fact, PMMA based cements started being used in orthopaedics as glues to enable the adhesion between metallic prosthesis and the surrounding bone. Only recently, PMMA has been applied in

vertebral augmentation procedures, remaining nevertheless as a structural repair material. Although this may be totally adequate for many of the clinical conditions recommended for kyphoplasty (particularly for elder individuals), some cases could beneficiate from the application of a true bone substitute that would enable not only repair, but also bone regeneration [5,52,54,105]. Such a biomaterial would be more appropriate for the vertebral surgery of younger individuals (due to their naturally higher bone metabolism), particularly to repair relatively small bone defects (including osteolytic lesions).

Despite bone tissue posses a remarkable capacity to self-repair microdamages, when a bone defect reaches a critical size, healing usually requires the introduction of grafting materials. In addition to the general obligatory requirements for any biomaterial, which include biocompatibility, non-toxicity and non-immunogenicity, bone grafts should meet other properties in order to enable an active recovery of the damaged region. Combined with a predictable biodegradation profile, these materials need osteocondutive properties to enable the progressive deposition of layers of new bone tissue, osteoinductive properties to stimulate the osteoblastic activity and eventually osteogenic properties which provide the ability of bone formation even in dissimilar environments. The material properties of the bone grafts result from the combination of chemical and structural features, being interconnected porosity a most relevant structural requirement. The pore sizes (100-500 μm are typically recommended) and even the thickness (around 50 μm) of the material walls between pores may be determinant factors for bone regeneration [17,28,29,42,44,106–108].

In practical and simplified terms, an ideal bone substitute material should be able to provide a porous scaffold to enable cell invasion and attachment, and the subsequent formation of new bone tissue, as well as blood vessels. At the same time, the biomaterial should undergo a gradual degradation process, allowing for its substitution with new bone. During this osteointegration process, the mechanical stability should not be compromised. [25]

Usually associated to conventional surgery, a standard strategy applied when a bone loss occurs is using natural bone grafts (autografts, allografts and xenografts), normally in particulate or granule form, making use whether of the cancellous or the compact bone regions. An autograft consists of a tissue that is transferred from one site of the organism of an individual to a different place, an allograft represents a tissue transfer between individuals of the same species, and xenografts, between different species. Bone autografts, the “gold standard” in bone grafting procedures, have the

advantage of no adverse immunological response and thus represent the best for inducing new bone formation. However, they are usually available in limited quantity (depending on donor site anatomy) and harvesting requires additional surgery, resulting in increased morbidity for the patient. Human allografts, which can be appropriately preserved in bone banks, being thus available in greater abundance, represent a valuable alternative to autografts. Even so, the application of allografts is often limited due to uncertainty on compatibility and risk of disease transmission. Xenografts, most often of bovine or porcine origin, have no limitations regarding availability but, similarly to allogenous bone, can introduce risk of rejection and disease transmission [5,52,54,105].

A given type of graft can function by more than one mechanism. For instance, autografts are osteoconductive, osteoinductive and osteogenic whereas allografts and xenografts are mainly osteoconductive. Evidences that natural apatites also possess osteocondutive properties has stimulated their application as grafting materials, alone or combined with other materials. Currently, this mineral component of bone is usually obtained from calcined xenografts, being commercially available from different animal origins, under various formulations. Corals may also be a source of natural hydroxyapatite, after applying hydrothermal conversion procedures to their calcium carbonate skeletons. On the other hand, in addition to osteocondutive properties, demineralized bone grafts have demonstrated to also possess osteoinductive capacities [14,16,25,56,81,82,109–113]. These are mainly attributed to the exposure of bone morphogenetic proteins (BMPs), caused by the demineralization procedure. Thus, not only natural bone grafts, but also calcined and demineralized bone grafts constitute very important options that require extensive research regarding materials characterization, processing conditions and application methods, in order to help the prediction of their clinical performance.

As described, these strategies of processing natural bone allow improving the non-autograft materials, while maintaining their advantages regarding chemical and physical properties. Natural hydroxyapatite obtained by heat treatment (calcination) has the advantage of inheriting the chemical composition and structure of the raw material, being therefore an alternative solution for numerous applications based on its analogous synthetic products. As compared to allogeneic bone, hydroxyapatite derived from xenogeneic bone (usually of bovine origin) is considered a good option because it is easier to obtain at lower cost and is available in unlimited supply. However, particularly regarding bovine derived hydroxyapatite, high temperature treatments (above 800 ºC)

are usually recommended to eliminate eventual existing pathogens, especially prions that transmit bovine spongiform encephalopathy (BSE). Diverse combined sterilization procedures have been proposed in order to obtain safe materials. The problem that arises with heat treatment at elevated temperatures, the most common sterilization method, is that the biogenic composition and structure of bone mineral can change and this may affect the efficacy of this material. Although there is some controversy regarding the onset of chemical and structural changes as a consequence of heat treatment, it has been reported that changes in the mineral phase of bone are not significant until degradation and combustion of most of the more labile organic components occurs (around 500 ºC). Regarding sample mineralogy, it is generally accepted that heat treatment promotes the crystallinity of bone derived hydroxyapatite and increases the crystallite size [80,112–115].

2.5.2 Composite materials as alternatives to natural bone grafts

Currently, the most common alternatives to natural bone grafts are composite materials which are designed and produced after taking inspiration from the composition and structure of natural bone. Different approaches have been considered, including using natural or synthetic polymers as matrix components and bone-derived or synthetic ceramics (often Ca/P minerals) as fillers. Thus, these composites may be entirely composed of natural or of synthetic products or, alternatively, contain both kinds of components. The starting materials of these composites are usually selected to fulfil the usual requirements (such as biocompatibility, osteoconductivity and non-toxicity), being the synthetic ones often modified to mimic some of the characteristics of natural bone. The natural products, on the other hand, are sometimes manipulated in order to enhance a specific property (e.g. osteoinductivity). The application of synthetic biomaterials represents a growing trend, mostly because they provide more consistent and predictable properties. However, they still present numerous limitations that challenge the scientific community on the quest for more convenient products. In fact, despite all the advances, the best clinical results still derive from the application of autografts [16,23,30,116,117].

2.5.2.1 Mineral phase of the composites

Hydroxyapatite, the mineral and most abundant component of natural bone, is probably the most studied ceramic for being applied as bone graft (alone or combined with a polymer matrix). Synthetic hydroxyapatite and diverse calcium phosphate salts have also been commonly applied, taking advantage not only of their resemblance with the natural bone mineral (including its osteocondutive potential), but also of the differences regarding the kinetics of dissolution. However, for the time being, synthetic apatites are not yet able to duplicate the characteristics of the bone mineral, known to influence the grafts osteointegration, nor to overcome some limitations as poor mechanical properties (particularly when exposed to wet environments) and lack of osteoinductive properties [16,18,50,115–118].

As for the *in vivo* behavior of calcium phosphates, it should be recalled that their chemical composition is one of the main factors that influences the rate of mineral dissolution. Taking the natural hydroxyapatite as a model, it is well known that the fact of containing several ions incorporated into its crystal structure is very important for the bone metabolism. In fact, although the presence of these ions is very low, they play a vital role in biological activity. It has been shown that carbonate incorporation tends to decrease the crystallinity and to increase the solubility of hydroxyapatite, enhancing its biodegradation rate. Thus, not only synthetic hydroxyapatite is often chemically modified in order to include additional properties favorable to bone grafting, but other calcium phosphates with different dissolution rates (Table 2.2) are frequently combined to achieve an adequate degradation profile for a given system. That is the case of some bi-calcium phosphates that combine hydroxyapatite (which degrades very slowly) with tricalcium phosphate (usually β-TCP), which is less stable and much more soluble at physiological conditions. The ratio of the two mineral phases can be varied to tailor adequate degradation properties. Another decisive factor affecting the life-time of the mineral is the material structure, particularly its porosity, by enabling the fluids penetration into the scaffold and consequentially, enhancing its dissolution [18,38,44,117].

2.5.2.2 Organic phase of the composites

Concerning the selection of a polymer (or polymeric system) to build up the matrix for a bone substitute composite containing mineral components, the wide range of available products and methods of production make this subject a very extensive issue. In fact, the composite matrix may be composed of a single polymer or multiple ones.

These may natural or synthetic products, or even a combination of both. This includes not only mixtures of the different kinds of polymers, but also chemical modifications of the natural and synthetic starting materials, as well as of the subsequent derived products (*e.g.* through chemical or physical crosslinking). Moreover, while some polymers may be water soluble, others require the use of organic solvents. Anyway, the selected polymers should be biocompatible and non-toxic, as well as their degradation products. They should also be compatible with the ceramic filler, promoting the interaction between the different phases of the composite [16,28,30,38,40,42,43,51,115].

The most commonly applied natural polymers have been gelatin (partial hydrolysis product of collagen) and polysaccharides (such as chitosan, starch, dextran, hyaluronic acid). As for synthetic polymers, polylactides and their co-polymers with polyglycolides, polycaprolactone and others have also been frequently used, as well as diverse polyurethanes, polyphosphazenes and multiple hydrogels, mostly based in acrylic systems (as PMMA). Some of these polymers may be produced as *in situ* forming hydrogels, being often tailored to provide the most suitable chemical or mechanical properties. Moreover, sometimes these polymeric systems are produced in the form of interpenetrated networks (IPN) [16,24,28,30,39,42,44].

Whereas some of these polymers are able to bind with the ceramics, others are usually crosslinked to hold the fillers within the matrix. The crosslinking reactions occur by using appropriate reagents before or after adding the ceramic particles to build the composite. It should be mentioned that although many of the reagents and solvents involved in the reactions of the polymeric components may be toxic, they are usually extracted from the scaffold prior to its application *in vivo*. Naturally, this applies to the production of solid scaffolds which are meant to be used in conventional surgery. In addition to the advantages coming from the possibility of extracting solvents or other reagents, the previous synthesis of a solid scaffold enables multiple optimization procedures regarding material properties (as mechanical strength, porosity or surface topography). The production of porous scaffolds is attainable by using porogen substances, whether by the introduction of soluble leaching salts or gas-forming agents. Another frequent strategy consists of producing a transitory composite which, after eliminating its organic phase, originates a porous dense body, only composed of minerals [17,22,25,29,30,41,119,120].

2.5.2.3 In situ forming hydrogels

For minimally invasive surgical procedures, *in situ* forming hydrogels may be adequate alternatives because this type of hydrogels can form in the body, near physiological conditions, from fluid precursors. However, these should be non-toxic and the gelation reaction should not cause any toxicity or substantial temperature rise.

The precursors of *in situ* forming hydrogels are injectable fluids that can be introduced into the desired tissue, organ or body cavity in a minimally invasive manner prior to gelation, enabling a good fit and contact with surrounding tissues. Since hydrogels are fluid prior to gelation, bioactive components, such as cells, proteins and drugs can be easily mixed with the polymer solutions, ensuring high loading and homogeneous distribution. After mixing the precursors solutions, gelation occurs as the result from chemical or physical crosslinking reactions. The variables involved must be carefully controlled because gelation should occur within a few minutes to minimize the length of the procedure, preventing leakage of the gelling solution to the surrounding tissues. On the other hand, the gelation process should simultaneously allow enough time for placement of the hydrogel before hardening. This coordination is very important to enable the application of the hydrogel with a single chamber injection device [121–126].

Chemically crosslinked hydrogels may be formed through different mechanisms as radical chain polymerization (initiated by photoirradiation or a redox system) or through reactions between complementary groups. The main issue is that photoirradiation and/or reactive compounds are needed, which may cause toxicity problems, aggravated from the fact that reagents cannot be removed from the injection site. Photopolymerization has not yet proven suitable for gelation after injection delivery due to the toxicity of most photoinitiators, generation of highly reactive radicals *in vivo*, limited accessibility of light, and eventual exothermic effect of photoreactions. On the other hand, the crosslinking reactions between complementary groups may be a valuable alternative. The most used mechanisms include Michael-type addition reactions between thiols and acrylates or vinyl sulfones, and amines and activated esters or aldehydes [39,61,121,125,127–129].

Physically crosslinked hydrogels may be formed by thermal gelation, stereocomplexation or physical self-assembly, as a result from ionic, van der Waals and/or hydrophobic interactions. Physical crosslinking generally proceeds under mild conditions, thus allowing for the immobilization of labile compounds, such as proteins. However, in general physically crosslinked hydrogels are mechanically weak and less

stable (they are often reversible) than those chemically crosslinked [39,61,121,125,127–129].

Over the past decades, a variety of naturally- and synthetically-derived materials have been used to form injectable hydrogels for biomedical applications. Natural polymers such as collagen, starch, agarose, carboxymethyl cellulose, chitosan, alginate, hyaluronic acid, chondroitin sulphate and fibrin have been often selected, among many others, for the synthesis of substrates that mimic the chemical and physical environment of the extracellular matrix. Despite natural polymers have been often preferred due to excellent biocompatibility and biodegradability, a wide range of synthetic polymers have also shown similar potential properties. That is the case of polyesters such as poly(ethylene glycol)/PEG, poly(lactic acid) [PLA], poly(glycolic acid) [PGA], poly(propylene fumarate) [PPF] and poly(caprolactone) [PCL]. These synthetic polymers have been widely explored both alone or combined as co-polymers, maintaining the hydrolysis potential of the ester linkages. As an example, PEG, which remains one of the most widely studied systems, may form biodegradable hydrogels by copolymerization with PLA, PGA ad PPF. The copolymerization with selected polymers may originate additional properties, as thermosensitivity in tri-block co-polymers of PEG-PCL-PEG and PLGA-PEG-PLGA (where PLGA derives from PLA+PGA). PEG has also been combined with many naturally occurring biopolymers (as those previously mentioned), resulting in new biodegradable hydrogels [13,21,39,43,121,125,126,130].

Other synthetic polymers may, however, lack informational structure for positive cell biological response. As a consequence, modification of synthetically derived hydrogels may be required, mostly in order to elicit a biodegradation response or to introduce cell-specific domains such as RGD (Arg-Gly-Asp) sequence [21,43,121,125,126][21,39,43,66,104,121,125,130,131]. The synthesis of hybrid polymers through grafting of molecular sequences from natural polymers is a frequent strategy to achieve better interaction with the host tissues. Those molecular sequences include carboxyl, amino or vinyl groups, frequently at terminal positions of the molecular structure. The modified polymers may then be coupled into biomacromolecular or peptides sequences, or participate in other polymerization reactions [21,28,39,56,66,104,132–134]. Another strategy consists in blending synthetic and natural polymers, promoting the formation of interpenetrating netwoks (IPN). Poly (vinyl alcohol) [PVA] is a hydrophilic synthetic polymer which has been widely investigated regarding the synthesis of hydrogels by diverse of the mentioned processes.

2.5.2.4 Hydrogels based in Poly (vinyl alcohol)

Since the early days of its discovery (in 1924), PVA has been used in various industries, being gradually introduced in the field of biomedical applications. For instance, it has often been used as protective colloid in emulsion or suspension polymerizations, in the paper-making industry, in waste water treatments (including in the removal of nuclear wastes), in food industry (approved by FDA in 2003) and in the synthesis of hydrogels for medical applications [133,135–141].

PVA based hydrogels, in particular, are classified as biomaterials that have been gaining increasing importance in view of its low toxicity, non-carcinogenicity, and high biocompatibility. The main areas of hydrogels application include: topical uses as wound dressings; drug-delivery systems; transdermal systems; dental applications; injectable polymers; implants; soft contact lenses; superabsorbents; and stimuli-responsive systems. This wide range of applications is related to the fact that PVA can be modified into multifunctional macromers through its numerous hydroxyl pendant groups, which can be derivatized by a variety of substituents. Moreover, PVA hydrogels may be obtained by chemical crosslinking (e.g., with glutaraldehyde or epychlorohydrin) or by physical crosslinking (e.g., by applying freezing/thawning cycles). It may also be blended with numerous water-soluble polymers, both of natural and synthetic origin, to form IPN structures [24,45,103,122,137,142–148].

Poly (vinyl alcohol)/PVA is produced commercially from poly (vinyl acetate)/PVAc (Figure 2.17), generally by a continuous process. It starts from the polymerization of vinyl acetate monomer, the primary raw material, into poly (vinyl acetate), followed by partial or complete hydrolysis of this polymer. The process of hydrolysis is based on the gradual replacement of the ester group in vinyl acetate with the hydroxyl group, by ester interchange with methanol, and is completed in the presence of aqueous sodium hydroxide. Following gradual addition of the aqueous saponification agent, PVA is precipitated, washed and dried. The degree of hydrolysis is determined by the time point at which the saponification reaction is stopped.

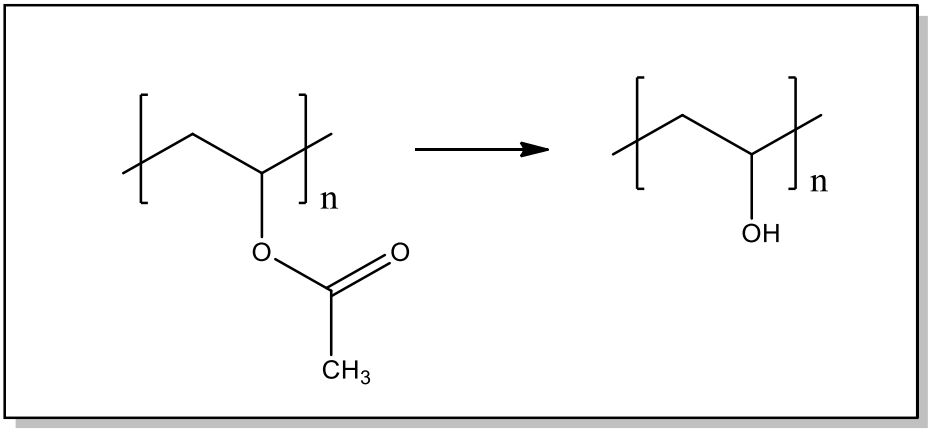

Figure 2.17 - Chemical structure of PVA ($[C_2H_4O]_n$), derived from the hydrolysis of PVAc ($[C_4H_6O_2]_n$).

The physical characteristics and the specific functional uses of PVA depend at great extent on the degree of polymerization and on the degree of hydrolysis. Given the relevance of the latter factor, PVA is usually classified into two classes, namely partially hydrolyzed and fully hydrolyzed. Its designation normally specifies the hydrolysis level; for instance, PVA 80% hydrolyzed, PVA 90% hydrolyzed and so on, until PVA fully hydrolyzed.

Typically, PVA is soluble in water and slightly soluble in ethanol, but insoluble in other organic solvents. Within the same range of molecular weight distribution, the solubility of PVA decreases with the hydrolysis degree. Whereas fully hydrolyzed PVA is only soluble in hot water (it is recommended a temperature not higher than 90 ºC), PVA 80% only needs 25ºC. On the other hand, within the same hydrolysis degree, the solubility of PVA decreases with the increase in molecular weight. These combined factors have strong influence not only on the viscosity of the PVA solutions, but also on the pH values which, depending on the polymer concentration, typically range from 5.0 to 6.5. Furthermore, they also influence some properties related to the thermal behavior of PVA such as the glass transition temperature (50-70 ºC), the melting temperature (180-220 ºC) and the intervals of combustion temperatures (typically, 280-320 ºC and 400-450 ºC) [133,135–141,149,150].

Commercial grades of PVA are usually characterized by a number of quality tests, chief of which are vinyl alcohol/vinyl acetate content and relative viscosity in aqueous solution. However, these quality control tests are known not to be entirely adequate since similar grades of partially hydrolyzed PVA may behave differently in chemical practice. This happens because PVA can differ in terms of sequence distribution of vinyl acetate residues, tacticity, branching, molecular weight, unsaturation and frequency of head-to-head monomer residues [151–154].

Taking fully hydrolyzed PVA as a model to understand some of its structural characteristics, this polymer is usually represented as an atatic linear molecule possessing alternate -CH_2 and -CHOH groups wherein –OH substituents are randomly oriented along the chain (Figure 2.18). The tacticity, which reflects the stereochemistry of adjacent chiral centers, is usually described in terms of a number of adjacent structural units such as dias, triads, tetrads, pentads or even higher order ads when information on long-range ordering is desirable. The terms meso (m) and racemo (r), referring to similar or different orientation respectively, are used as follows: for the simplest case, a diad, whereas a meso (m) diad consists of two identically oriented units, a racemo (r) diad consists of units oriented in opposition. As for a triad, an isotactic triad (mm) is made up of two adjacent meso diads, a syndiotactic triad (rr) consists of two adjacent racemo diads and a heterotactic triad (rm) is composed of a meso diad adjacent to a racemo diad. Tacticity measurements obtained by Carbon-13 NMR are typically expressed in terms of the relative abundance of triads (mm, rm, rr), tetrads (*e.g.* mmm, mrm) or pentads (*e.g. mmmm*, *mrrm*) within the polymer molecule.

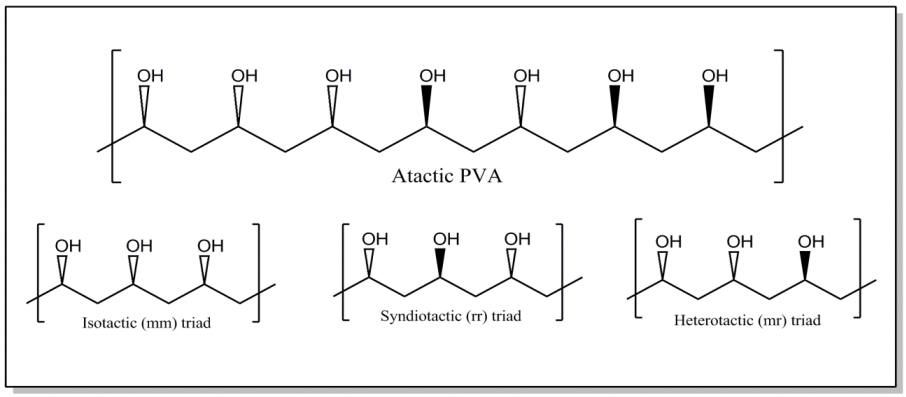

Figure 2.18- Isotatic (mm), syndiotactic (rr) and heterotactic (mr) triads in the atactic structure of PVA.

Moreover, it is well known that the backbone of PVA usually contains small amounts of structural defects that derive from its synthesis process, leading to changes into the usual heal-to-tail configuration. These defects consist on adjacent CH-OH bonds (usually named as diol or 1,2 - glycol units) that correspond to head-to-head configurations, or adjacent CH_2-CH_2 groups, characteristic of tail-to-tail configurations (Figure 2.19).

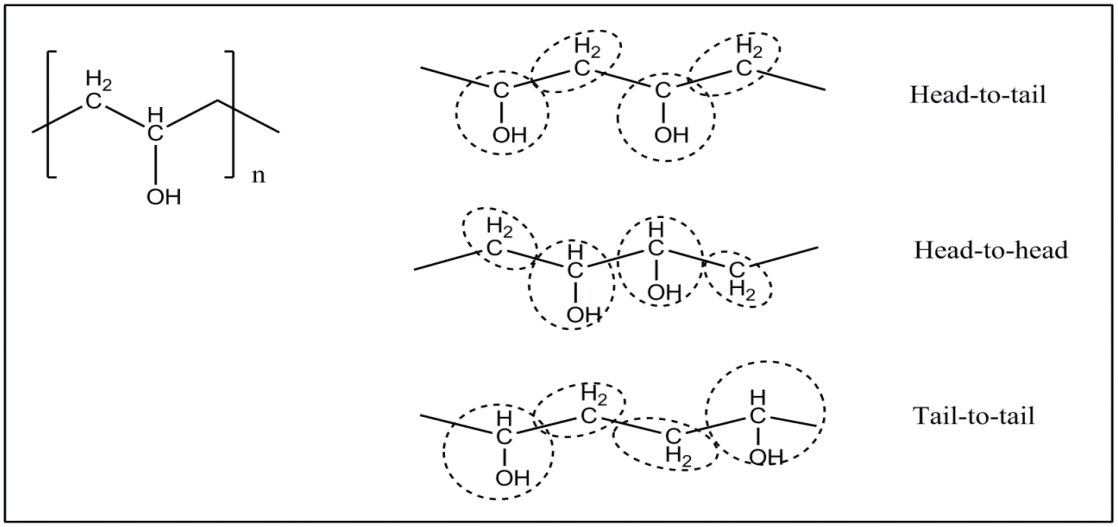

Figure 2.19 – Structure of the head-to-tail, head-to-head and tail-to-tail configurations in PVA.

Although it is recognized that variations in these properties (degree of polymerization, degree of hydrolysis, distribution of hydroxyl groups, stereoregularity and crystallinity) may exert an important influence on the practical uses of this polymer, it is nevertheless not possible to determine the significance of a specific characteristic of PVA until the property in question has been quantified accurately. For PVA and PVA-based systems, the assessment of the relationship between biodegradability and polymer structure is also a fundamental instance to be ascertained [149,151,155,156].

Despite the overall number of PVA-degrading microorganisms is rather limited in comparison with the widespread species able to degrade aliphatic polyesters, PVA is known to be a truly biodegradable synthetic polymer, namely in peculiar environments, such as PVA-polluted textile or paper mill effluents. Since the early thirties, diverse microorganisms and symbiotic mixed cultures able to degrade PVA have been identified and many degradation pathways have been proposed to explain the biodegradation process [103,122,142,155–157]. However, for *in vivo* applications, PVA is usually modified in order to introduce molecular fragments and/or molecular bonds that are typically biodegradable. Alternatively, PVA may also be blended with natural biodegradable polymers, constituting interpenetrating networks with higher *in vivo* degradation potential than PVA alone.

2.5.3 Controlled drug delivery

Nowadays, many biomaterials are formulated so as to include drug delivery systems. Antibiotics and anti-inflammatory drugs are usually applied directly in the

biomaterial formulation or through encapsulation devices to enable a controlled release profile into the targeted environment [61,127,158,159,160] [160–163].

The same applies to many other additives (e.g. growth factors, osteoinductive molecules as BMPs) but care bust be taken to ensure that the drugs keep their biological activity despite the global environment and application conditions [160,164].

2.5.4 Sterilization of bone substitute composite materials

A very important aspect that should be mentioned regarding all types of bone substitutes is the sterilization of the applied materials. The most used standard procedures involve temperature (from cryo-treatments/preservation to autoclaving), ethylene oxide (a gas that eliminates pathogens) and ionizing radiation (such as ^{60}Co). The fact that polymers and ceramics often require different sterilization methods may represent a complicated problem, which must be solved in order to obtain non-contaminated composite materials. In fact, the properties of most polymers vary with temperature and gamma irradiation often affects the polymers integrity. On the other hand, many ceramics (such as hydrated salts) are often unstable during autoclaving. As a result, some composites can only be supplied in sterilized form by acquiring sterile products and preparing them under aseptic conditions [18,48,81,82,105].

2.5.5 Shelf-life of bone substitute composite materials

The shelf-life of a material refers to the period of time that guaranties the quality of the product from the moment of its production. In biomedical applications, the recommended shelf life of a material must always be taken into consideration.

The factors that affect the stability of bone substitute composite materials depend not only of the selected components, but also on the conditions involved in the preparation of those products. The control of the shelf life of dynamic wet systems, as different types of bone cements, may offer additional difficulties compared to most solid scaffold composites.

As an example, the ceramic particles of ceramic or composite bone cements may dissolve and precipitate in solution, leading to a change of the mean crystal/particle size, or even to the formation of agglomerates. As a consequence, the rheological properties of the cement may be significantly altered and affect the injectability and posterior

dynamics of solidification. On the other hand, regarding the use of biodegradable polymers in injectable composites, the potential degradation of these polymers in aqueous solution may compromise the whole system, becoming impossible to obtain a product according to its initial design [18,39].

3 Objectives and Strategies

3.1 Introduction

The aim of the present work consisted of obtaining a new biomaterial to be applied in kyphoplasty procedures. The main purpose has been to build a viable alternative to the most commonly used bone cements (mainly based on poly methyl methacrylate (PMMA)). This involved the search for a biomaterial that would not present as many disadvantages as acrylic bone cements do, being able to provide convenient properties for bone repair and ideally to allow, in addition, for bone regeneration. Thus, the new biomaterial should not be biologically inert (as PMMA) but conversely, should be bioactive, promoting the interaction with natural bone and bone marrow. Building up an injectable composite biomaterial made of non-toxic components that share some of the properties of natural bone after hardening *in situ*, was taken as the main objective of this study. The characterization of the new biomaterial and its application using an *in vivo* model were the other major objectives.

To accomplish these tasks, some assumptions had to be made regarding some of the technical aspects of the kyphoplasty procedure, and also about the biomaterial characteristics. The adopted experimental strategies resulted from the effort to combine the established goals with a set of restrictions from the surgical method and from the materials properties.

It should be kept in mind that in order to maintain the surgical procedure, some of the characteristics of the alternative material should not be modified relatively to the PMMA system. First of all, the most important idea to retain is that the new biomaterial must behave as a bone cement. As for acrylic and ceramic based cements, both are supplied in separate solid and liquid phases that have to be mixed before application. In the acrylic systems, this initiates a polymerization reaction which is evidenced mostly by the increasing viscosity of the intermediate products until obtaining a hard material. In the ceramic systems, the increase in viscosity is due to dissolution and precipitation processes associated to chemical reactions that originate new interlocked species. In both cases, short after mixing the reagents and while the viscosity is still low, the intermediate material has to be transferred to the injection device and be applied inside the vertebral body when the surgeon considers that the viscosity of the cement has reached an adequate level, enough to minimize leakage problems. The material properties of the cement components must be appropriate for a rapid preparation during surgery, which means that the reaction must occur at room temperature and oxygen atmosphere, without a complicated equipment.

Regarding the procedure to inject the material inside the vertebral body, it should be recalled that this step is performed using a single chamber injection device, even when the material is initially composed of more than one component. The explanation for the need of a typical syringe (and for the exclusion of a double chamber device) is very simple. Since it is not possible to mix the material components inside a vertebra, these must be previously blended and then injected in the form of a homogeneous and stable fluid. The requirement of pre-mixing the cement components derives from the need to avoid the premature solidification of the material inside the storage packing, either if the reaction mechanism involves a polymerization (acrylic cements) or the precipitation of selected salts (ceramic cements). For similar reasons, the use of any other system composed of multiple components (as crosslinkable polymers) also calls for a preliminary mixture step to enable the injection of the fluid with a conventional device.

Secondly, another issue to attend is the hardening phase of the injected material that must occur within a few hours after injection, inside the vertebral body. Using the PMMA system, this objective is attained by adding the monomer as the last element of the formulation, a few minutes before injecting the blended reagents. This way, the polymerization reaction of MMA starts outside and is completed inside the vertebral body. This step of the procedure may be considered as critical, since it can originate diverse harmful secondary effects, mostly related to the toxicity of the components, the high polymerization temperature, the eventual low extent of the reaction and difficulties on controlling the viscosity of the cement. Anyway, after injection, the hardening stage implies a dramatic change of the material properties inside the vertebral body, under very mild temperature conditions (around 37 ºC) and inside a closed environment that hinders the possibility of extracting undesired reaction products. The body temperature does not constitute a very strong limiting factor for acrylic cements, since they typically contain a pre-polymerized PMMA fraction and are usually injected only after the reaction with MMA has shown some progress. Moreover, the polymerization reaction is highly exothermic (it can reach around 70 ºC), which motivates the addition of catalysts to lower both the activation energy of the reaction and the subsequent energy release. The initiators for these reactions must not be obtained from photochemical reactions to produce the starting radicals. Instead, the initiators must be chemical reagents that produce radicals by dissolution with appropriate solvents. The photochemical option is not adequate for preparing materials at the operation table since the reagents may not be exposed under controlled conditions for enough time. As for ceramic bone cements, the influence of the temperature inside the vertebral body is not very relevant since the

process of dissolution and precipitation of the salts is usually able to proceed regularly. However, for other alternatives, as some crosslinkable polymers that form hydrogels, the body temperature may be too low to enable the crosslinking reaction to occur, or too high to enable the gelation of the obtained composition. To summarize, these problems associated to the environment of the vertebral body constitute limiting factors for diverse reasons. Since the biomaterial must be injected in a liquid or paste form, it needs a solvent, preferably water. Thus, the biomaterial should start as a water-soluble material. However, as explained before, it needs to become solid and insoluble in water after a certain time period, inside the vertebral body. This means that the solvent extraction is not possible, and the hardening of the material must proceed at body temperature, inside a closed space.

The third aspect regarding technical implications over the material composition is the mandatory addition of a radio-contrast agent, in order to permit X-ray guidance during the surgery. The contrast component must be compatible with the other requirements of the material so that the chemical reactions and the injectability will not be negatively affected.

To summarize, the conditions that could not be changed in this work relative to the currently used systems (based on acrylic or ceramic cements) are the following:

a) the temperature and atmosphere of the preparation site;
b) the use of water as a solvent or as a liquid support;
c) the inclusion of a contrast agent in the initial composition;
d) the use of reagents that behave as a cement after their mixture, originating a viscous material that hardens progressively until reaching the solid state;
e) the use of a syringe with a single chamber device to perform the injection of the blended components;
f) the application site, the vertebral body, as a closed and mild environment where solidification must occur.

In contrast to the operational aspects of the procedure that must be kept, those concerning the chemical composition of the current bone cements (and respective hardening mechanisms) had to be changed in order to find a competitive new product.

A direct competitive product would mainly correspond to a new (but eventually less toxic) structural and non-biodegradable biomaterial. The advantage of such biomaterial would be the ability of inducing bone regeneration, rather than just acting as a repair structure. It should also have an adequate biodegradation rate to enable its

gradual substitution by newly formed natural bone. The biodegradability of the new bone graft raises some important questions about the clinical application of such materials. Whereas a material with a controlled biodegradation profile may be adequate for a young patient that has naturally a great potential for new bone formation, an inert material may be a better option for elderly patients. They usually have limited bone regeneration and low mineral density, frequently associated with osteoporosis, being this one of the main causes for the vertebral fractures for which this study aims at developing new biomaterials.

As mentioned, this work aimed at the *in situ* regeneration of bone tissue, the so-called bone tissue engineering, which requires materials with properties different from those of permanent implants. In addition to biocompatibility and non-toxicity, these properties include an adequate biodegradation profile, compatible with the processes of bone remodeling, that implies resorption due to interaction with osteoclasts and biomineralization from the action of osteoblasts. Other requirements such as adequate porosity, both in terms of pore size and interconnection, are also important. The interconnected porosity would enable the movement and progression of the bone cells through a solid biomaterial.

3.2 **Strategies**

The adopted strategy to find an alternative material was based on the synthesis of an injectable and hardenable composite material that would mimick bone (a natural composite of hydroxyapatite and collagen) for a certain extent. The objective was to ultimately obtain a composite material with a mineral phase containing natural hydroxyapatite and a contrast agent, both embedded in an organic phase composed of an initially water-soluble polymer, which had to become insoluble after an appropriate reaction. Water was selected *ab initio* as the liquid phase to enable the injection of the composition. The functional properties of the mineral and organic components and, above all, those of the composite, were also a matter of concern. The chemical and structural characteristics of the composite needed to be tailored with the objective of producing a material with osteocondutive and osteoindutive properties, able to help bone repair and to stimulate bone regeneration. This implies adequate composition and porosity for interactions with specific cells, and adequate mechanical properties to withstand load forces.

Bone-derived hydroxyapatite was readily selected as one of the ceramic components of the composite because that is the base composition of the mineral phase

of bone and constitutes the nearest material to the gold standard that autologous bone represents. Natural hydroxyapatite is biocompatible, bioactive and possesses particular structural properties due to the natural biomineralization process on its origin. Nevertheless, hydroxyapatite obtained from bone may present different characteristics, not only derived from the variations that naturally occur in any living tissue, but also because of the process (usually bone calcination) to obtain this mineral. Thus, a thorough characterization of bone samples of diverse origins, before and after calcination at different temperatures, was performed to enable the most suitable choice. The selected mineral was subsequently produced in large scale to provide a homogeneous supply of natural hydroxyapatite for the whole study. The calcined bone blocks had to be reduced into particles with a size range adequate for the proposed application: small enough to enable the injection of the minerals through the syringe, but larger than red blood cells, the diameter size limit of the capillaries. The second mineral ingredient that was selected for the composite was barium sulphate due to its radiologic contrast ability. This component is probably the most frequently used in materials for medical procedures that require x-ray monitoring. In addition to the qualitative selection of ceramic components, the quantification of each mineral was also performed in order to determine an appropriate mineral proportion for the inorganic phase of the composite. The experimental methods and the results regarding the mineral phase of the composite are presented in Chapter 4.

As for the organic component of the composite, many strategies were tested, always avoiding the use of a polymerization process similar to that of acrylate-based systems. Although there are commercially available materials based on acrylic cements mixed with ceramic particles, mostly calcium phosphates and Bioglass, these solutions would not provide the intended innovation for this study. The preferred alternative was using other types of materials, selected from biocompatible biopolymers able to produce hydrogels *in situ* through crosslinking mechanisms. This option was considered very interesting due to the potential high compatibility with cells, despite the limitations related to inadequate mechanical properties for load bearing applications. However, theoretically, this limitation could be solved by incorporating the ceramic particles into the polymeric components, as a suspension.

Following this approach, diverse binary systems (crosslinkable polymers and respective crosslinking agents) were tested, using natural and synthetic polymers, in the as supplied or modified forms, to enable the crosslinking reactions between the polymeric precursors. The most promising polymeric systems preliminarily tested

involved biopolymers as dextran and chitosan, and also the synthetic poly (vinyl alcohol), each with diverse specific methodologies to obtain crosslinked structures. The experiences showed that the selection of an adequate polymer matrix could be a difficult task for multiple reasons. According to the literature, there are not so many systems that crosslink at body temperature and reach adequate mechanical strength without solvent extraction, in a timeframe of a few hours. Moreover, the preliminary results showed that the gel formation could be controlled in most isolate polymeric systems, but that the addition of minerals to any of the biopolymer´s gel precursors would hinder their chemical reactions. This constituted a great limitation for this study since the presence of minerals in a polymer solution was mandatory. Indeed, even before the determination of the appropriate concentrations of hydroxyapatite and barium sulphate, given their very low solubility in water, it was decided that these minerals would have to be suspended in a polymer solution. To obtain a homogeneous suspension, that polymer solution would have to be chemically compatible with the mineral particles and would need a high viscosity to sustain their weight, preventing phase separation and particle agglomeration. Besides, the crosslinking agent (in solid or liquid form) would need to be blended into that suspension without damaging the injectability of the mixture. Then, the obtained mixture would be transferred to the injection device. The hardening process of the material should already have started before the transfer.

Some biopolymers were tested, as mentioned, but they were not adequate for the proposed application. For instance, dextran was oxidized with periodate solution to produce new acetal bonds due to ring-opening reactions, being necessary to use a dialysis procedure to separate this product from the reaction medium. Then, it was lyophilized and kept at low temperatures to preserve the composition. Afterwards, the oxidized dextran could be crosslinked with diverse amines, as adipic acid dihydrazide, to obtain a new hydrogel after some hours. However, despite the adjustment of different variables, the obtained hydrogels were not strong enough to obtain a homogeneous viscous fluid after the addition of the mineral components, nor the final blend ever achieved a solid material, as required. With chitosan, no matter the applied method to crosslink the polymer, the addition of hydroxyapatite resulted always on the precipitation of the minerals and formation of agglomerates that would never allow the injection of the blended materials. The experimental procedures and results obtained with these (and other) natural polymers are only briefly mentioned to avoid a large volume of information that did not allow to proceed to the objectives of the study. The problems with the polymers of natural origin that were tested had some influence on the decision of adopting preferably polymers of synthetic origin. The other main reasons are related to

the well-known difficulties on controlling the properties of natural biopolymers, in order to have homogeneous and reliable supplies to use in medicinal applications.

On the other hand, the synthetic poly (vinyl alcohol) (PVA) presented more promising properties regarding most of the described requirements. This polymer was selected as the main component of the organic matrix of the composite, as described in Chapter 5. In this section, PVA with different hydrolysis degrees and molecular weights are characterized and their crosslinking potential under diverse conditions is analyzed. One of these conditions regards the crosslinking of PVA with borax that occurred always very suddenly, no matter its concentration. This led to the development of biodegradable microcapsules based on poly (lactic acid) (PLA), charged with that salt, to use as a delivery device of borax to the PVA suspension with minerals. Theoretically, this would retard the crosslinking and help to control the rate of the chemical reaction. The PLA microcapsules were studied to enable its use not only as a delivery device for crosslinking reagents or other chemicals, as antibiotics, but also for the chance of creating porosity in the composite. The conventional methods of salt leaching or gas formation could not be applied inside the closed environment of the vertebral body. In addition to the characterization of PVA, Chapter 5 also includes the synthesis and characterization of diverse PLA microcapsules.

Following the selection and characterization of diverse mineral and organic reagents that were tested in the synthesis of composites based in the literature, a critical analysis of the results was made. The practical experience with the obtained bone-derived hydroxyapatite and diverse polymeric materials has detected many difficulties to meet the total set of desired requirements, particularly regarding the crosslinking of the organic matrix of the composite bearing a suspension of minerals. The strategy to obtain a hardenable composite biomaterial had to be changed.

The design of a new strategy was based on the acquired experience with the previously studied systems, being selected the most promising polymer (poly (vinyl alcohol) from that latter stage of the work to constitute the main organic component of the new composite material. In addition to bone-derived hydroxyapatite and barium sulphate, diverse other reagents were added in order to obtain a composite that fulfilled the necessary requirements. Collagen, for instance, was also used. Since collagen is not soluble in water, it had to be hydrolyzed into gelatin. Without revealing too much at this moment, some details can already be mentioned to illustrate the experimental methodology that is presented in Chapter 6.

The synthesis of a new crosslinked composite started with the modification of PVA with a carbodiimide (CDI), originating functional groups which were able to react with natural hydroxyapatite. From the synthesis of such a hybrid (organo-ceramic) composition, the whole process involved diverse additional reagents and multiple synthesis steps, being each one optimized by varying some characteristics of the reagents (*e.g.* the hydrolysis degree of PVA, the type and composition of hydroxyapatite and the hydrolysis method applied to collagen). The amount and the order of addition of some of the products were also altered at certain phases of the process. Despite all efforts to avoid acrylic monomers, it became necessary to use a reagent (hydroxy ethyl methacrylate/HEMA) from that family, associated to an innocuous chemical initiator (potasium persulphate/$K_2S_2O_8$). Microcapsules mostly made of poly (lactic acid) (PLA) were also tested in this system, either containing HEMA or not. The optimization of the applied microcapsules was previously made.

The global synthesis path adopted in the building process of the injectable composite is represented in the diagram of Figure 3.1. Starting with a PVA solution, the reagents represented in the left side of the reaction path were sequentially added, originating intermediate products. The variables in the process are represented in the right side. In addition to meaning of the abbreviations already mentioned, PVA80 and PVA98 stand for 80% and 98% hydrolyzed PVA and HA stands for hydroxyapatite. The different types of HA were natural (nat) and synthetic (syn), being each kind carbonated (CO_3^{2-}) or non-carbonated minerals. Collagen (COL) was also a necessary reagent which required a previous hydrolysis process to become water-soluble. The different procedures applied in the hydrolysis process, in acid and alkaline media, are also represented in the diagram. HEMA was added in two different ways, in aqueous solution and encapsulated. Before the addition of HEMA, the material is named of pre-composite. Afterwards, solidification occurs and the product is classified as a true composite material.

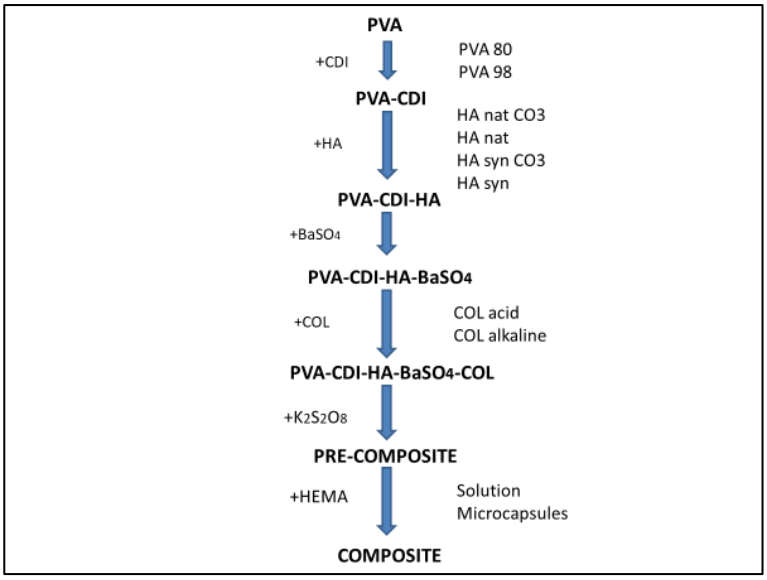

Figure 3.1 - Main steps for the synthesis of the composites and variables in the process.

The introduction of variables allowed for a consecutive process of optimization, being the most suitable products submitted to *in vitro* tests concerning injectability, swelling, degradation in phosphate buffered saline (PBS) solution, mechanical strength, as well as biocompatibility with bone cells (namely, osteoblasts) and blood. Chapter 6 presents all these results concerning the composite optimization and characterization of material properties.

The series of tests led to the selection of a particular composite which was subsequentially used in a preliminary *in vivo* study, using a rabbit animal model. This study was periodically monitored by x-ray images and finally, the histological analysis enabled the detailed observation of the main local biological events, derived from the interaction with the implanted composite. These results are presented in Chapter 7.

To conclude the strategy description that intentionally did not reveal all the details in this chapter, it should be mentioned that multiple techniques and experimental methods (Table 3.1) were applied during this study. In addition to the usual characterization of starting reagents and reaction products, the consecutive intermediate compounds of each studied system were, as much as possible and when considered relevant, also characterized. The multi-phase composition of the intermediates and final composite products originated increased difficulties to the chemical characterization of the materials, particularly to determine minor alterations derived from consecutive chemical reactions. Thus, the measurement of physical properties or the use of model compounds was also adopted. Finally, the overall experimental results were used to

build up a theory relative to the applied synthesis path and respective products at diverse stages of the process. On the other hand, the biological tests enabled to extract important information to explore in future work.

Table 3.1 - Summary of the experimental methods applied in the characterization of the individual components/intermediates of the composites, of the microcapsules and of the obtained composites.

	Method *	**Components**	**Microcapsules**	**Composites**
1	Rheometry	X		
2	SEC	X		
3	Volumetric Titration	X		
4	NMR D_2O	X		
5	IGC	X		
6	XPS	X		
7	NMR CP-MAS	X		X
8	DMTA	X		X
9	XRD	X		X
10	Optic microscopy		X	X
11	Hg Intrusion	X	X	
12	DLS	X	X	
13	AA (Na^+)		X	
14	FTIR-ATR	X	X	X
15	DSC-TGA	X	X	X
16	SEM	X	X	X
17	Radiology	X		X
18	Swelling			X
19	Degradation in PBS			X
20	Biocompatibility			X
21	Haemocompatibility			X
22	Implantation *in vivo*			X
23	Histological analysis			X

(*) Abbreviations: size exclusion chromatography (SEC), nuclear magnetic resonance in deuterium (NMR D_2O), inverse gas chromatography (IGC), x-ray photoelectron spectroscopy (XPS), nuclear magnetic resonance with cross-polarization and magic angle spinning (NMR CP-MAS), dynamic mechanical and thermal analysis (DMTA), x-ray diffraction (XRD) spectroscopy, diffraction laser spectroscopy (DLS), atomic absorption (AA) spectroscopy, Fourier transform infrared spectroscopy in attenuated total reflection mode (FTIR-ATR), differential scanning calorimetry coupled to thermal gravimetric analysis (DSC-TGA), and scanning electron microscopy (SEM). PBS stands for phosphate buffered saline solution.

4 Selection and characterization of mineral components for the composite

4.1 Introduction

Bone-derived hydroxyapatite was selected, *ab initio*, as the most appropriate mineral component to incorporate into the aimed bone substitute injectable composite. This decision, based on the current knowledge of the advantages of the bone-derived minerals as compared to synthetic ones, motivated the detailed study of the process that should be applied to obtain (and to produce in larger scale) natural hydroxyapatite with the most suitable properties for the proposed application.

This research involved the comparative study of natural cortical bone of different origins (human, bovine and porcine), before and after thermal treatment at different temperatures (600, 900 and 1200 ºC). The calcined samples were thoroughly characterized by diverse techniques (FTIR, DSC-TGA, XRD, SEM, Hg Intrusion, IGC, XPS), being most part of this work recently published [165–170].

Among the various types of bones, femur, the longest skeletal bone, was selected as the best hydroxyapatite source because of its relative large size and concomitant higher material content (mostly cortical bone). The choice for cortical bone resulted from a preliminary study (data not shown) that revealed, as expected, a great similarity between the composition of cortical and cancellous bone.

The effects of the methodologies which were followed in the preliminary treatment of the bone samples were also evaluated, in order to determine the most efficient and less deleterious process. The purpose of this evaluation was the selection of a method that could contribute to the competitive production of bone-derived hydroxyapatite, since the pre-treatment of bone may limit the overall process.

As for the natural hydroxyapatite obtained from the thermal treatment of bone, the temperatures that were selected for this study resulted from preliminary thermogravimetric analyses of the different samples. The detailed characterization of all samples was performed in order to determine their properties and respective relation to the calcination temperatures. It also served the objective of finding which type of mineral would be more appropriate to apply in the composite synthesis.

Synthetic carbonated and non-carbonated commercial hydroxyapatites were also characterized, though less extensively, since these two types were tested as possible (but less probable) alternatives to the natural mineral, at latter stages of this study.

In addition to hydroxyapatite, another mineral substance was also selected *ab initio* to become part of the inorganic phase of the projected composite. Barium sulphate was selected based on its well-known radio-contrast properties, low solubility and high biocompatibility. It was characterized using the same techniques that were applied in posterior phases of this study, to enable the comparative analysis of results.

The criterion to determine the appropriate proportion of the selected hydroxyapatite and Barium sulphate in the composite was based on the radiologic contrast of compositions that combined both minerals. This study required the use of radiology to acquire images of animal vertebrae with artificially created bone defects, which were filled with various ratios of the selected minerals. The design of these experiments was meant to simulate *in vitro* some key features of the kyphoplasty procedure.

4.2 Hydroxyapatite

4.2.1 Bone-derived hydroxyapatite

In order to obtain natural hydroxyapatite, natural bone (femur) of different origins (human, bovine and porcine) was processed under similar conditions, being submitted to thermal treatment at 600, 900 and 1200 ºC. The respective samples were characterized before and after calcination at the mentioned temperatures, which were selected based on the preliminary thermal analysis of natural bone.

The human bone used in this study was a biologically no longer active femur from a 39-year-old male donor, supplied by the bone bank of Coimbra University Hospital (Portugal). The bovine and porcine femurs were acquired at local markets of fresh supplies.

It should be mentioned that the initial steps of bone preparation may be time consuming operations that require much manipulation in order to obtain well cleaned samples, free from surrounding organic tissues and internal bone marrow. Thus, two methodologies were tested concerning bone preparation (BP). The results presented in this chapter correspond to samples prepared using Method BP-I, with the exception of those regardind FTIR, IGC and XPS analyses whose bovine samples were prepared using Method BP-II. The detailed characterization of all samples prepared by the latter method is not presented in this chapter, since such an exhaustive comparison would

seem almost a repetition. In fact, a comparative study was preliminarily performed and the results showed that bone samples characteristics were essentially preserved by applying any of these methods. This allowed choosing the second method as the most convenient to prepare high amounts of bone samples, getting them ready to posterior calcination. Thus, the initial bone treatments used to prepare most of the hydroxyapatite that was used during the whole study derived from Method BP-II.

Regarding bone calcination (BC), three different procedures have been adopted (Methods BC-I, BC-II and BC-III), involving diverse sample manipulation processes and slightly different thermal treatments. Moreover, whereas BC-I was applied to bone samples prepared by Method BP-I, BC-II was relative to BP-II. On the other hand, Method BC-III involved only bovine samples, previously prepared by the BP-II methodology.

The application of different calcination procedures was dictated by the following characterization techniques and/or applications of the obtained hydroxyapatite minerals. While the first method (BC-I) was essentially applied for the study of the influence of the calcination temperature in the properties of bone-derived hydroxyapatite, the second one (BC-II) was mostly used for a larger scale production of hydroxyapatite, enabling to obtain enough material for the whole study. While some of the respective characterization results will naturally be presented in this chapter, others will be included in Chapter 6 as references for diverse chemical compositions. As for the third calcination method (BC-III), it was applied due to the sample requirements for IGC analysis.

4.2.1.1 Samples preparation procedures

i) Bone preparation

Method BP-I

The fresh bones of each specimen were cut into smaller pieces and well cleaned to remove most adhering impurities. Afterwards, the bones were boiled in distilled water for 30 minutes, for most external degreasing and easier removal of tissues and impregnated bone marrow. This procedure was repeated twice with fresh water.

After the boiling step, each diaphysis was transversely cut into 1.5 cm thickness slices and in order to obtain only compact bone samples, the cancellous bone inside was carefully removed from most pieces. Some slices were left intact to enable the observation of the trabecular structure.

Subsequently, the bone samples were totally degreased through immersion in an alcohol series (ethanol at 70%, v/v), followed by washing with distilled water. Then they were kept in hydrogen peroxide (30%, v/v) for at least 48 h and rinsed again. Finally, they were stored in formaldeyde solution (4%, v/v) at 4 ºC. Before use, the samples were thoroughly rinsed with distilled water and subsequently dried in a vacuum oven at 50 ºC for 3 days. Then, samples were placed inside a desiccator.

These dry cortical non-calcined bone samples represent the controls in the following study. According to the techniques applied in their characterization, these reference samples were transversely cut into smaller parts (blocks) or “scratched” with a scalpel to obtain particles.

Method BP-II

Following the removal of most external tissues, the bone samples were transversely cut into four/five smaller pieces, enabling the extraction of the bone marrow from the respective cavity. Then, the bone pieces were washed with abundant distilled water and immersed in a 0.1 M NaOH bath solution for at least 72 hours, depending on the samples dimensions. The alkaline bath enabled the elimination of the remaining surface tissues, as well as of the bone marrow impregnated in the cancellous parts. Afterwards, the bone samples were thoroughly rinsed with ethanol and water, until no alkaline reaction was denoted using pH indicator strips. The way of drying and preserving the bone samples was similar to that of Method BP-I.

Obtaining only cortical parts from some of the cleaned bone samples required the removal of the cancellous structures after the pre-treatment process. Others were left intact. Finally, an identical procedure to that already mentioned (preparation of blocks and particles) was also applied, in order to get appropriate samples for diverse characterization techniques.

ii) Bone calcination

Method BC-I

Natural hydroxyapatite was obtained after calcination of the human, bovine and porcine bone samples at 600, 900 and 1200 ºC. A systematic series of test samples was prepared by heating the cortical bone slices in a muffle furnace at each temperature for

18 hours, under air atmosphere. After calcination, the samples were placed inside a desiccator at room temperature and naturally cooled.

Depending on the characterization techniques, samples were used as blocks (the whole slice/half-slice) or as particles (obtained by crushing the slices into smaller pieces and reducing the fragments to powder form by hand grinding in an agate mortar).

Method BC-II

The complete (cortical and cancellous bone) femur pieces of different origins (human, bovine and porcine) were calcined under air atmosphere, in a muffle furnace, using a heating ramp rate of 10 ºC/min from room temperature until reaching constant weight at each selected temperature (600, 900 and 1200 ºC).Then, they were naturally cooled and kept in a desiccator. After combustion of the organic components of bone, the cancellous parts from the obtained hydroxyapatite pieces were easily discarded.

Most blocks were reduced to particles using an electric mill. The hydroxyapatite particles were subsequently sieved to different size ranges (namely 0.077-0.088, 0.088-0.150 and 0.250-0.500 mm) and stored inside a desiccator.

Method BC-III

The starting material for this method was obtained from a particular set of samples from the previously described BC-II method. These samples consisted of hydroxyapatite derived from bovine bone calcined at 600 ºC, reduced to particle form and sieved to 0.250-0.500 mm. These starting mineral particles were submitted to an additional thermal treatment at 900 ºC, using a heating ramp of 10 ºC/min from room temperature. The calcination procedure was performed under air atmosphere in a muffle furnace, until samples reached constant weight.

As described, this BC-III method is characterized by two main differences relative to the other calcination methods: the starting samples were composed of bone-derived hydroxyapatite instead of natural bone, and the mineral samples were in particle form instead of blocks. This method was specifically designed to obtain (at 600 and 900 ºC) two types of hydroxyapatite particles, both with the exact same origin and identical dimensions, in order to perform comparative IGC analyses of these minerals. One of the samples was also used for XPS analysis (a complementary technique to IGC, both

regarding surface characterization). The combined techniques were used to evaluate the influence of the calcination temperature on the surface properties of natural hydroxyapatite.

iii) Characterization methods

Before calcination, cortical bone was characterized using DSC-TGA, FTIR spectroscopy, Hg Intrusion Porosimetry and SEM. After calcination, identical techniques were applied to all samples, as well as XRD. Some of the bovine calcined samples were characterized, in addition, by IGC, XPS, LDS and CP-MAS solid state NMR spectroscopy. The results from LDS and NMR will only be presented in Chapter 6, where they constitute relevant data. The first ones, in the context of the hybrid composition derived from the hydroxyapatite reaction with a polymer, and the second ones, in the characterization of the obtained composites.

Though most of these characterization techniques required samples in particle form, porosity measurements and SEM analysis were intentionally performed using bone samples (natural or calcined ones) under block form. For SEM observation, in particular, the block samples were submitted to fragile fracture under the perpendicular direction to the long axis of the original bone. This enabled the exposure of the cross-section surface, without tool marks.

The instrumental details concerning each experimental method will be presented in the Appendix.

4.2.1.2 Samples characterization before calcination

This section reports the characterization of the natural bone samples, after the preparation procedures to remove the surrounding tissues.

DSC-TGA

The thermogravimetric curves of the human, bovine and porcine bone samples are shown in Fig. 4.1, together with the corresponding heat flow profiles, from 20 to 1400 ºC. The most relevant results obtained from the TG analysis are presented in Table 4.1.

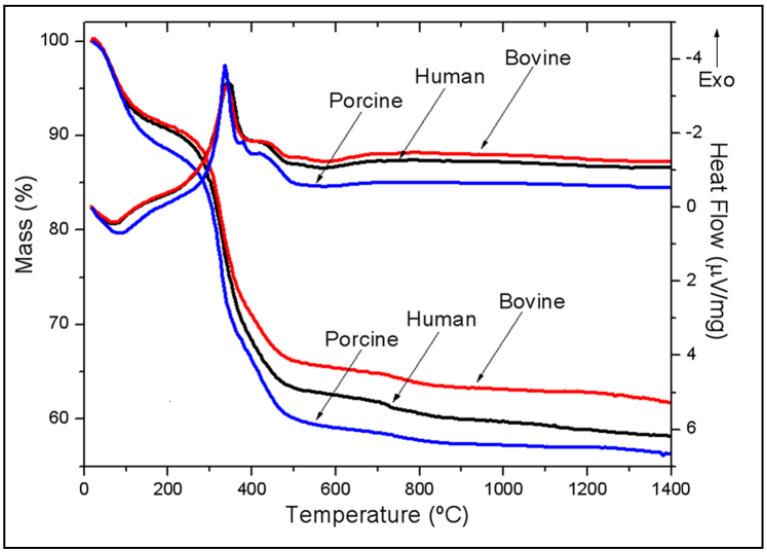

Figure 4.1– TG and DSC plots of human, bovine and porcine bone samples in the 25-1400 ºC temperature range.

The thermograms of the control samples present similar profiles, showing typically three successive steps of weight loss: one below 200 ºC, another between 200 and 600 ºC, and a third step between 700 and 900 ºC. Above this temperature, the weight variation is not significant. The former is attributed to the dehydration of bone (surface and bound water). The second step corresponds to the greatest weight loss and is due to the combustion of the organic component of bone (mainly collagen) [80,171-173]. The latter step of weight loss, observed at temperatures above 700 ºC, is mainly caused by the release of CO_2 from the apatite lattice, due to carbonate decomposition [80,171-173]. The DSC results show, for each bone sample, one endothermic peak at about 90 ºC followed by a strong exothermic peak with maximum near 335 ºC and a shoulder around 420 ºC.

Table 4.1 – Weight percentage of the main constituents of bone samples of different origins (human, bovine and porcine) estimated from the curves of Figure 4.1.

	Human	Bovine	Porcine
H_2O (wt%) (T< 200 ºC)	9.3	8.9	11.6
Collagen (wt%) (200 ºC< T <600 ºC)	28.1	25.7	29.4
Carbonate apatite (wt%) [a]	62.6	65.4	59.0
CO_3^{2-} (wt%) [b] (700 ºC< T <900 ºC)	5.5	4.2	3.8

[a] $\%=100-[(m_{20\,^oC}-m_{600\,^oC})/m_{20\,^oC}]x100\ \%$

[b] $\%=1.36x[(m_{700\,^oC}-m_{900\,^oC})/m_{700\,^oC}]x100\ \%$

Table 4.1 illustrates that human and bovine samples have similar water content, but slightly inferior to that of porcine bone, and that the organic content differs at most by 4% among all specimens. Carbonated hydroxyapatite corresponds to 59-65 wt% of

the bone samples and the relative amount of carbonate (estimated from the weight loss between 700 and 900 ºC, as suggested by the literature [80,84,171-173]) is also very alike, being the human bone sample that with a slightly higher content. The differences in carbonate content may be explained based on metabolic factors.

The above results allowed selecting the set of calcination temperatures: 600, 900 and 1200 ºC. In fact, besides corresponding to stable chemical compositions (i.e., plateaus in TG profiles), at 600 ºC the bone samples are composed of carbonate apatite and at 900 and 1200 C, mainly of stoichiometric hydroxyapatite.

FTIR

The FTIR spectra of human, bovine and porcine bone is presented in Figure 4.2, together with those of reference samples of collagen and stoichiometric synthetic hydroxyapatite.

The human, bovine and porcine bones present quite similar FTIR spectra, which reflect their identical chemical composition. As expected, each spectrum shows the characteristic peaks of hydroxyapatite (at 557, 600, 960 (shoulder), 1012 and ~1060 (shoulder) cm^{-1} due to phosphate vibrations) and collagen (C=O stretching vibration at 1634 cm^{-1}; N-H in-plane bending at 1548 cm^{-1}; C-H and N-H stretching modes in the 2800-3400 cm^{-1} region) [79,92,172-174]. It should be noted that the weak band observed in the spectrum of hydroxyapatite at ~630 cm^{-1} could not be identified in the spectra of the bone samples (Fig. 2). Additionally, the typical bands of carbonate substituting for phosphate site (type B) in the apatite lattice are also observed: peak at 871 cm^{-1} and double band at 1410/1445 cm^{-1}. Type-A carbonate may also be present, but in smaller amounts comparing to type B, since a shoulder around 880 cm^{-1} is observed in the FTIR spectra of all bone samples [79,92,172-174].

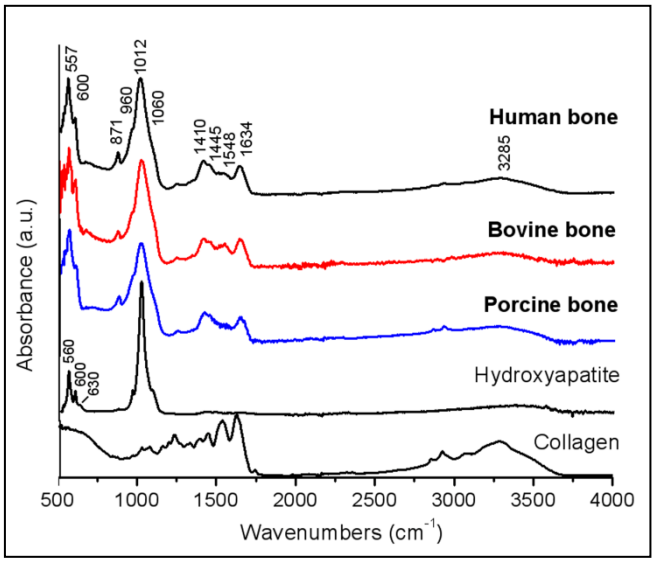

Figure 4.2 - FTIR spectra of Human, Bovine and Porcine bone samples: comparison with hydroxyapatite and collagen, the major bone components.

The composite nature of the bone matrix becomes very clear when its FTIR spectrum is compared with those of the model compounds of its components, hydroxyapatite and collagen (Figures 4.2 and 4.3). In fact, as mentioned, the spectrum of bone exhibits all the most intense bands observed in the spectrum of hydroxyapatite (at 500-700 cm^{-1} and 900-1200 cm^{-1}) and that of collagen (in the 1200-1700 cm^{-1} and 2800-3700 cm^{-1} regions), being nearly coincident with the sum of the respective profiles. Nevertheless, there are some new bands (namely at around 870 cm^{-1} and 1400-1450 cm^{-1}) originated from carbonate substitutions in the crystal lattice of hydroxyapatite.

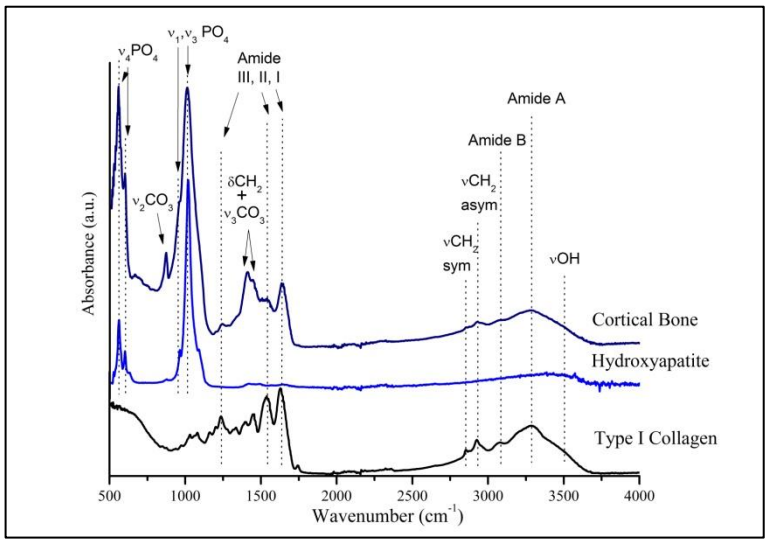

Figure 4.3 - Spectral assignment of the major bands in the FTIR spectra of cortical human bone, hydroxyapatite and collagen.

From the detailed spectral assignments presented in Table 4.2, some bands must be discussed, particularly in the 500-1700 cm^{-1} region of the spectrum of bone. The

most intense bands are originated from the mineral phase, in accordance to its larger proportion in the composite. In particular, the bands at 557 and 600 cm^{-1} correspond mainly to ν_4 PO_4^{3-} bending vibrations, despite some contribution from collagen in that region. Moreover, the absorptions at 961 and 1012 cm^{-1} correspond to the symmetric (ν_1) and asymmetric (ν_3) stretching of phosphate, respectively. Thus, most of the absorptions from phosphate vibrations are clearly observed both in the spectra of bone and of hydroxyapatite. It should be also mentioned that acidic phosphate (HPO_4^{2-}), a frequent anionic substitution in the crystal lattice of hydroxyapatite, usually originates a band at *ca.* 1110 cm^{-1}, which is normally overlapped with that from ν_3 PO_4^{3-} vibration.

Table 4.2 - Band assignments for the FTIR spectra of bone, hydroxyapatite and collagen.

Wavenumber (cm^{-1})	Vibrational modes		
	Bone	Hydroxyapatite	Collagen
557	ν_4 PO_4^{3-} bending (mineral) +Amide (organic)	ν_4 PO_4^{3-} bending	Amide
600	ν_4 PO_4^{3-} bending (mineral) +Amide (organic)	ν_4 PO_4^{3-} bending	Amide
630	ν_4 PO_4^{3-} bending (mineral) +Amide IV (organic)	ν_4 PO_4^{3-} bending	Amide IV
871	ν_2 CO_3^{2-} bending	ν_2 CO_3^{2-} bending	-
961	$\nu_1PO_4^{3-}$ sym stretching	$\nu_1PO_4^{3-}$ sym stretching	-
1012	$\nu_3PO_4^{3-}$ asym stretching	$\nu_3PO_4^{3-}$ asym stretching	-
1250	Amide III	-	Amide III
1410	CH_2 bending (organic)+ ν_3 CO_3^{2-} (mineral)	-	CH_2 bending
1445	CH_2 bending (organic)+ ν_3 CO_3^{2-} (mineral)	-	CH_2 bending
1548	Amide II	-	Amide II
1634	Amide I	-	Amide I
2850	-	-	CH_2 sym stretching
2930	-	-	CH_3 sym stretching
3072	-	-	Amide B
3278	-	-	Amide A
3500	-	ν OH	ν OH

On the other hand, the collagen moiety of bone originates the typical Amide I and Amide II bands at 1634 and 1548 cm^{-1}, respectively. Furthermore, the bands at 1410 and 1445 cm^{-1} show a different profile and higher intensity in the spectrum of bone relative to its organic model compound. These bands correspond, in fact, to absorptions from CH_2 wagging and bending vibrations superimposed with those from asymmetric stretching (ν_3) vibrations of CO_3^{2-} groups, present as ionic substitutes in the apatite crystal. Carbonate also originates a single band at *ca.* 870 cm^{-1}, which is assigned to ν_2 bending vibrations. This band is characteristic of a Type-B apatite.

SEM

SEM was used to observe samples of cortical bone and samples of cancellous bone from different origins (human, bovine and porcine). Despite the different origins of the analyzed bone samples, SEM observations showed that all share similar microstructural features. Thus, the exact origin from which each image was obtained is not emphasized in the description of the various bone samples.

In fact, at low magnification (75x) all samples present the typical morphology and structure of the bone matrix (Figure 4.4). As observed in cross section view, while cortical bone shows a very compact organization, cancellous bone constitutes a macroporous structure. The numerous Havers systems that make up cortical bone are illustrated, as well as a Volksmann canal crossing through the compact bone matrix. On the other hand, the cancellous structure is quite less dense, possessing randomly oriented trabecullae which define large interconnected pores.

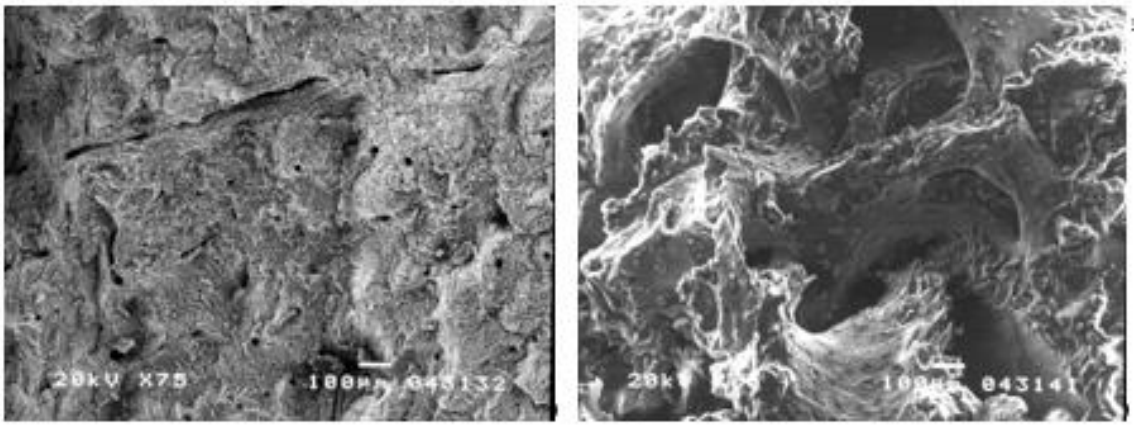

Figure 4.4 - Microstructure of cortical bone (left) *versus* cancellous bone (right).

Increasing SEM magnification and focusing the attention in cortical bone, additional details may be observed (Figure 4.5) regarding its lamellar organization. At 200x, the characteristic Havers systems comprising a multilayer structure of concentric lamellae around each Havers canal, as well as interstitial lamellae, are clearly observed. At 400x magnification, the concentric lamellae reveal their fine structure, being the alternate high and low configuration probably related to the different orientation of consecutive layers of the mineralized fibres. Moreover, the blood vessels inside Havers canals could also be observed, although very rarely, in some of the bone samples.

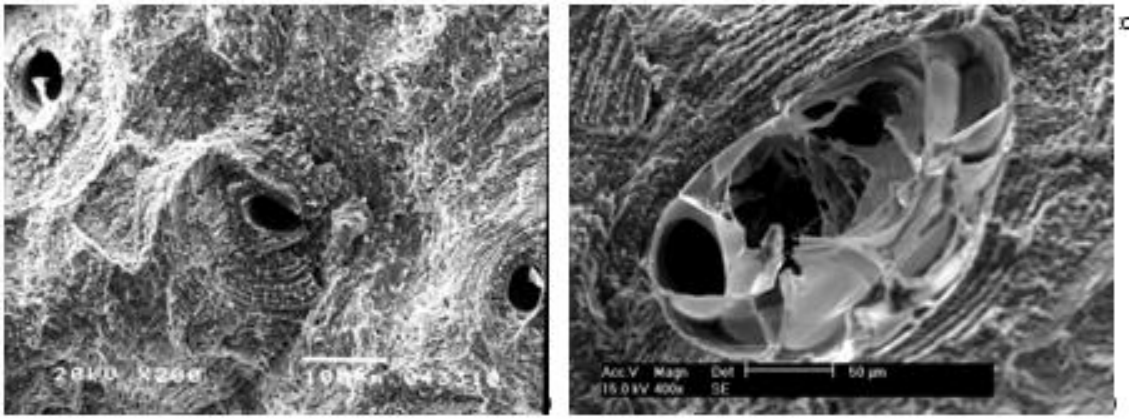

Figure 4.5 - Microstructure of cortical bone: numerous Havers systems (left) and detail of a Havers canal containing vascular vessels and surrounded by the typical concentric lamellae of mineralized fibres (right).

It should be mentioned that the observed details varied among the diverse samples. For instance, in the 500x magnification image of Figure 4.6, the individual lamellae are not distinguishable (as in the 400x image of the previous figure). However, multiple osteocyte lacunar spaces are clearly observed. Using a higher magnification (7500x), the characteristic eye shape of a lacuna is also illustrated in Figure 4.6. Moreover, a very unique detail was also caught by SEM imaging: the interior of this lacuna, containing bundles of numerous entangled nanofibres, distributed around circular micropores.

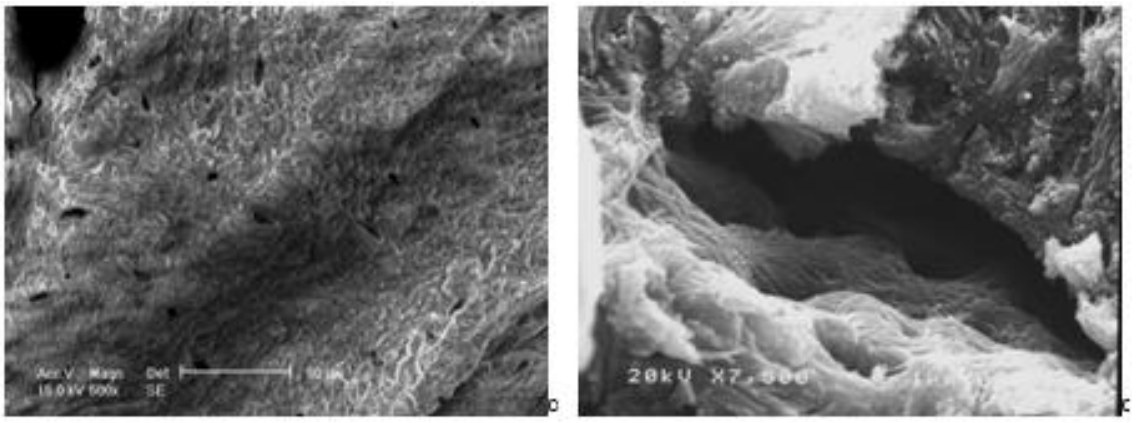

Figure 4.6 - Osteocyte lacunar spaces spread in the bone matrix (left) and detail of the interior of a lacuna (right) showing an entangled fibrous environment which defines the entrance geometry of the canaliculli where nutrients flow, and where to osteocytes launch cytoplasm extensions, enabling short range cell contacts through gap junctions.

The special environment inside the lacunar space is most probably related to the metabolic functions of bone tissue. In fact, the lacunae are the matrix sites where osteocytes become entrapped, after differentiating from osteoblasts. Since the bone matrix is a rigid material where cells are not able to move across, the communication between the latent osteocytes is only possible due to an ingenious process. These cells send cytoplasm extensions through microscopic channels (the canaliculli) comprising a

true web that enables fluid circulation, nutrient exchange and chemical signaling between cells. The size and shape of the pores between the fibres inside the lacuna illustrated in Figure 4.6 are consistent with canaliculli arriving to that cellular space. The osteocytes make use of those channels, meeting at short range distances other osteocytes that employ an identical strategy. The cell contacts usually occur through gap junctions, facilitating the communication through the bone matrix.

Hg Intrusion Porosimetry

Mercury porosimetry was used to evaluate the porosity of the diverse compact bone samples, as well as the respective pore size distribution. This parameter is determined by applying the Washburn equation (Eq. 4.1) where d is the pore diameter, P is the applied pressure necessary for the mercury to penetrate the sample pores, γ is the mercury surface tension (0.48 Nm^{-1}) and θ is the contact angle between mercury and the solid surface (130º). The total porosity was calculated as the ratio of the total intruded volume and the sample bulk volume.

$$d = \frac{4\gamma\, cos\theta}{P} \qquad \text{Eq. 4.1}$$

The Hg intrusion curves (cumulative and differential) of human cortical bone block samples presented in Figure 4.7 are representative of the corresponding results (data not shown) relative to bovine and porcine samples before calcination.

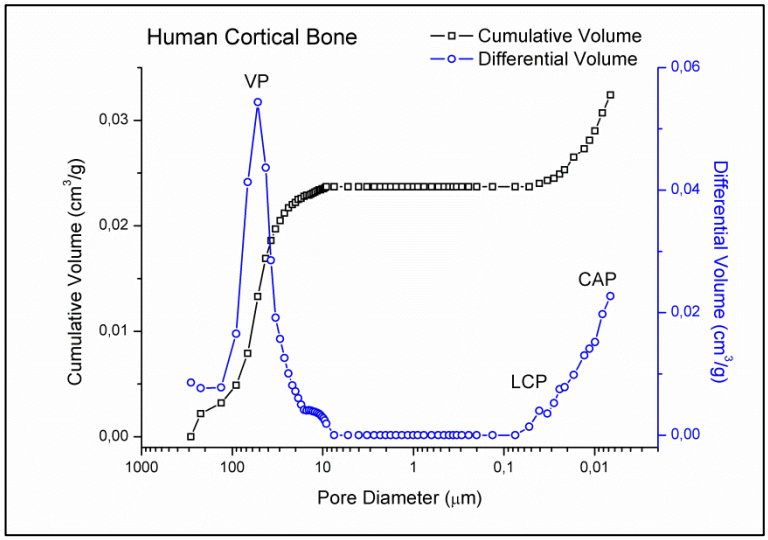

Figure 4.7 – Cumulative and differential intrusion curves of non-calcined human cortical bone, measured by mercury porosimetry. VP,vascular porosity; LCP, lacunae-canaliculi porosity; CAP, collagen-apatite porosity.

In fact, all samples analysed exhibit pore size distributions which denote the three types of porosity typical of a compact bone: vascular porosity (VP), related to average pore diameters around 50 μm; lacunae-canaliculi porosity (LCP), corresponding to an average pore size of 0.1 μm; and collagen-apatite porosity (CAP), with only a few nanometers in diameter. VP corresponds to Harvers and Volkmann canals; LCP, as the name suggests, results from the osteocyte lacunar spaces and the interconnected network of canaliculi that enables the communication within the bone matrix; and CAP corresponds to the empty spaces between collagen fibres and apatite crystals. The results in terms of total porosity and bulk and skeletal density will be discussed along with the calcined samples.

4.2.1.3 Samples characterization after calcination

This section reports the characterization of bone-derived hydroxyapatite, obtained by calcination at 600, 900 and 1200 ºC.

Macroscopic and microscopic changes (general considerations)

Before describing in detail the effects of the calcination temperature on the chemical composition and structure of the diverse bone samples, the most notorious changes that are observed at macro scale are illustrated in the Figure 4.8.

Provided that the applied temperature is high enough (above 600 ºC) and for enough time to enable the combustion of collagen, bone samples undergo common changes from their natural appearance to totally white materials. At intermediate stages of calcination, bone acquires different colors from pale yellow, to diverse grades of brown and to black, losing the darkest tones to consecutive grades of grey before achieving the white color. The starting and ending points of this process, relative to a bovine bone piece comprising both of its cortical and cancellous structures, are shown in Figure 4.8. The left image corresponds to a block of natural bone and the right one, to a block of bone-derived hydroxyapatite. Interestingly, the macrostructure of bone maintains its integrity after calcination, allowing for a better distinction between the compact and the trabecular structure, whose macroporosity becomes clearly observable. Despite its structural integrity, the calcined block may be easily fractured since being only composed of bone´s ceramic component, it is hard but simultaneously fragile. This shows the relevance of collagen on the mechanical properties of natural bone, providing tenacity (shock absorption capacity) and also some elasticity.

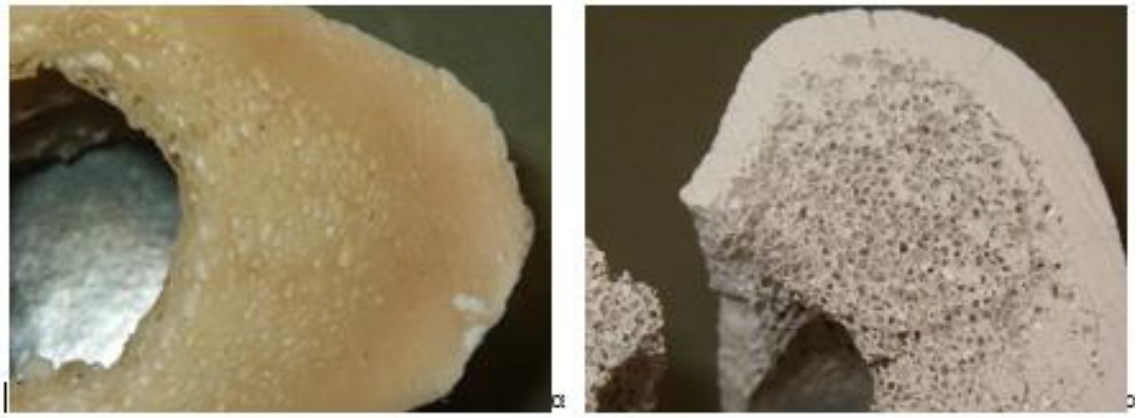

Figure 4.8 – Macrostructure of bovine bone blocks before (left) and after (right) calcination. After complete combustion of the organic components, bone blocks become white and the macroporosity of the cancellous structure becomes apparent. Although the macrostructure maintains its integrity, calcined bone loses much of its tenacity and can be easily fractured.

Using low magnifications (around 100x) in SEM observation to compare cortical sections of natural and calcined bone samples, as shown in Figure 4.9, two main features must be emphasized. While the calcination process preserves the Havers canals of the bone matrix, the most significant difference concerns the characteristic lamellae around and between these canals. These images demonstrate that the lamellar configuration derives from the collagen arrangement since after elimination of this organic component, the lamellae also disappear.

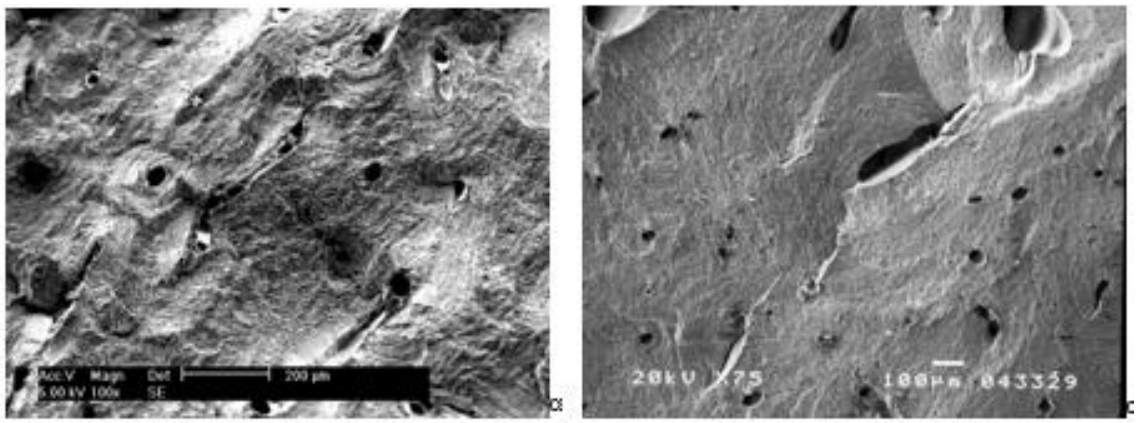

Figure 4.9 - Microstructure of cortical bone before (left) and after (right) calcination. The Havers canals maintained their morphology, but the lamellae are no longer observable after calcination

Increasing SEM magnification to observe the matrix surface (Figure 4.10), a calcined Havers system can be identified (at 800x) by the circumferential distribution of the osteocyte lacunar spaces around a Havers canal, although the typical concentric lamellae no longer exist. The fissures observed in the left image are probably effects from the heat treatment process. Another outcome is the loss of material´s smoothness, as evidenced at 1500x magnification. The multiple lacunae still present their typical morphology, but the collagen-free matrix shows an irregular and rough surface.

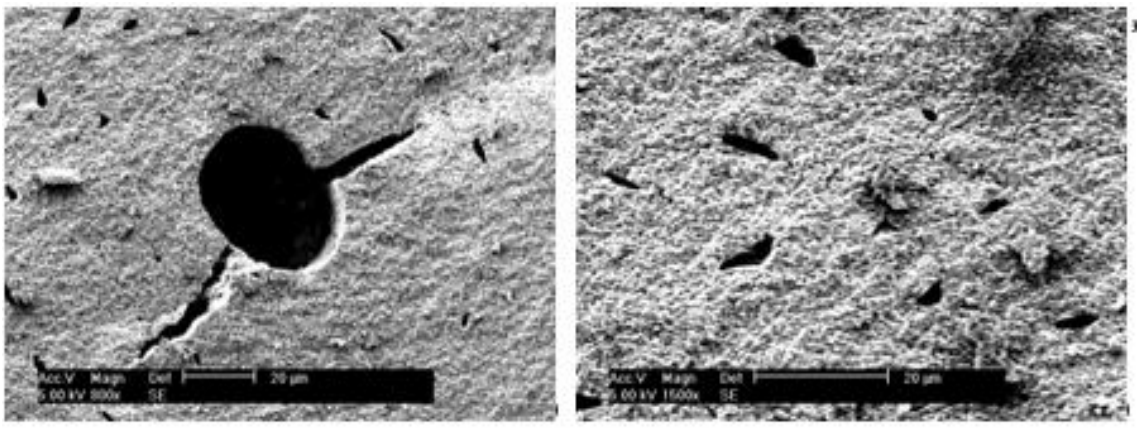

Figure 4.10 - Details of the calcined surface of cortical bone: a Havers canal surrounded by osteocyte lacunar spaces (left) and a higher amplification (right) showing the typical shape of lacunae and the roughness of the organic-free matrix.

FTIR

Figure 4.11 shows the FTIR spectra in the 500-1800 cm^{-1} range of the human, bovine and porcine bone samples, before and after thermal treatment at 600, 900 and 1200 ºC.

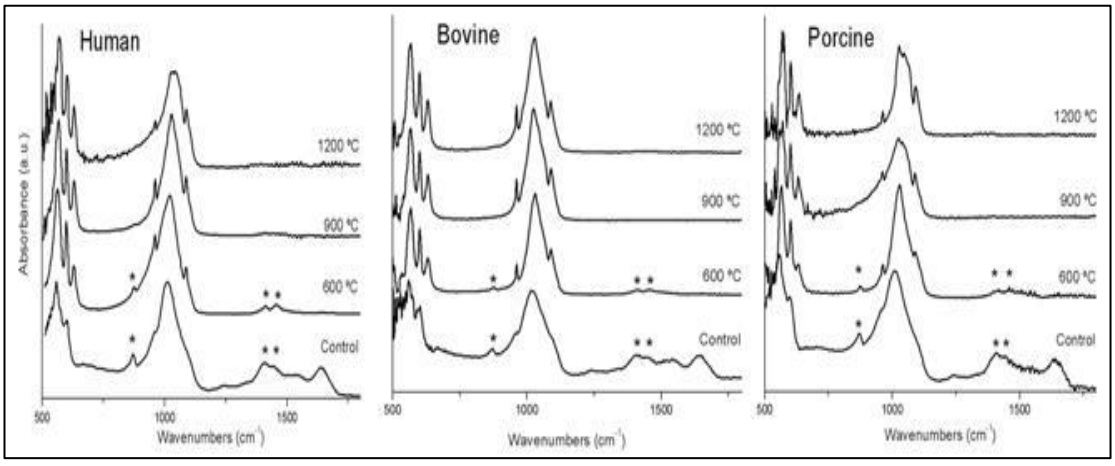

Figure 4.11 – FTIR spectra of human, bovine and porcine bone samples, before and after calcination at 600, 900 and 1200 ºC. *Bands attributed to lattice carbonate vibrations.

All absorption bands originated by the collagen, namely those at 1548 and 1634 cm^{-1} (and also those in the 2800-3400 cm^{-1} region), disappear after calcination at 600 ºC, which suggests that the organic component has been removed from the bone samples. In addition, most of the bands due to the phosphate vibrations of hydroxyapatite have largely increased in intensity after calcination. This behavior has been described by other authors as a consequence of the thermal treatment of apatites. In particular, in addition to the most intense peak at 1012 cm^{-1}, there are now three bands

in the spectra in the 500-700 cm^{-1} region of the calcined samples (561, 600 and 629 cm^{-1}) whereas in the spectra of the original samples only two were clearly discernible (557 and 600 cm^{-1}). Despite its low intensity, the band at ~630 cm^{-1} is clearly resolved in the spectra of the calcined samples.

The obtained spectra of the diverse bone-derived apatites agree well with the theoretical predictions for phosphate vibrations. In fact, concerning the phosphate anions in tetrahedral geometry, there are four fundamental vibrations distributed as ν_1 (symmetric stretch), ν_2 (bend), ν_3 (asymmetric stretch), and ν_4 (bend) and these vibration modes (except ν_2) give rise to medium to strong bands. Typically, in hydroxyapatite, ν_1 (a non degenerate vibration mode) originates one intense band at around 960 cm^{-1}, and ν_3 and ν_4 (triply degenerate modes) originate up to three bands each in the 1000-1100 cm^{-1} and 500-650 cm^{-1} regions, respectively. Finally, the doubly degenerate mode ν_2 may be observed at less than 500 cm^{-1} but given to instrumental limitations, spectra were not acquired in that region.

The FTIR spectra also show bands of small intensity at 871, 1410 and 1445 cm^{-1} attributed to lattice carbonate vibrations [79,84,92,172-174]. Although the relative intensity of these carbonate bands is similar in the various samples spectra, they are more pronounced in the spectrum of the human sample, confirming a higher carbonate content. After calcination at 900 ºC, the bands due to carbonate are no longer observed in the spectra of the bone samples. The spectra of the samples calcined at 1200 ºC were similar to those at 900 ºC, corresponding also to non-carbonated hydroxyapatite.

The attribution of the described bands to carbonate vibrations also finds good agreement with theory. Carbonate anions may also show up to four normal modes of vibration: symmetric stretch (ν_1), out-of-phase bending (ν_2), asymmetric stretch (ν_3) and in-plane CO_2 bending (ν_4). ν_3 and ν_4 constitute doubly degenerate modes and ν_1 is not an active vibration in the infrared because it does not change the dipole moment of the molecule. In carbonated apatites, the CO_3^{2-} characteristic bands appear at 870-880 cm^{-1} (ν_2, as a single band) and at 1400-1450 cm^{-1} (ν_3, usually as a double band). Depending on the type of carbonate substitution in the crystal lattice, bands may appear at slightly different wavenumbers: type *A* carbonate apatite is characterized by a ν_2 band at 880 cm^{-1} and a ν_3 double band around 1450 and 1540 cm^{-1}, whereas type *B* configuration has these bands at about 870, 1430 and 1450 cm^{-1}, respectively. The ν_2 band is often used to estimate the CO_3^{2-} content of the sample, by calculating the respective area underneath. Moreover, this band may also contain a component at *ca.* 866 cm^{-1}, due to

the contribution of non-apatitic (labile) carbonate. As mentioned before, the carbonate bands of the diverse analysed samples reveal that the obtained hydroxyapatite minerals are mostly of type B, although there may as well exist some contribution of type A substitution. The AB-type, corresponding to minerals that contain both phosphate and hydroxide ions substituted by carbonate, is another possibility that would require further analysis.

The results illustrated in Figure 4.11 are fairly consistent with those of thermogravimetric analysis (Table 4.1) and confirm that the chemical composition of human, bovine and porcine bone samples is quite similar. Moreover, heat treatment at 600 ºC causes the elimination of collagen from bone samples, originating a carbonated apatite, and calcination at higher temperatures (900-1200 ºC) results in the complete removal of carbonate from the mineral.

Whereas the above results concerned samples prepared by using methods BP-I and BC-I, additional FTIR spectra were also acquired relatively to equivalent samples prepared by methods BP-II and BC-II, as mentioned at the beginning of this chapter. From these last samples, the vibrational spectra of hydroxyapatite (HA) obtained from bovine (Bov) bone calcined at 600 and 900 ºC (respectively designated as HA Bov 600 and HA Bov 900) are presented in Figure 4.12. These spectra are similar to the ones obtained with the first group of samples, showing that both of the applied pairs of methods (BP-I+BC-I; BP-II+BC-II) are adequate to obtain hydroxyapatite (carbonated or not) from natural bone.

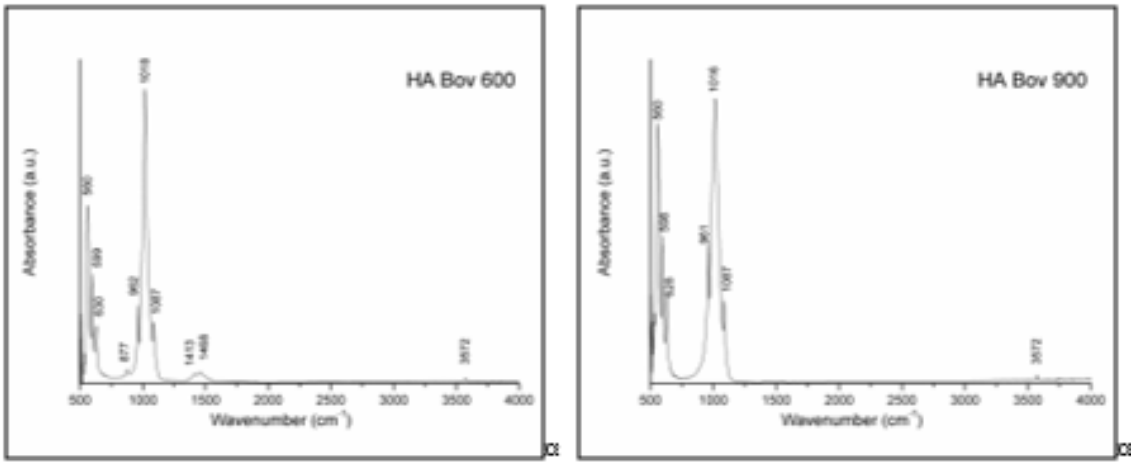

Figure 4.12 - FTIR spectra of bovine bone after calcination at 600 ºC (left; HA Bov 600) and 900 ºC (right; HA Bov 900). Both spectra correspond to hydroxyapatite but whereas HA Bov 600 is a carbonate susbstituted apatite (carbonate bands at 877 cm^{-1} and in the 1400-1500 cm^{-1} region), HA Bov 900 is a non-carbonated mineral.

In the FTIR spectra of Figure 4.12, HA Bov 600 corresponds to carbonated hydroxyapatite and HA Bov 900 to non-carbonated hydroxyapatite, as discussed before. Both spectra show the typical hydroxyapatite phosphate bands (three peaks at 500-650 cm^{-1} and a very intense peak at 1018 cm^{-1} with two shoulders at each of its sides), as well as the small intensity peak at 3572 cm^{-1} due to hydroxide stretching. HA Bov 600 spectrum shows, in addition, an isolate peak at 877 cm^{-1} and two other bands in the 1400-1500 cm^{-1} region, being these additional peaks characteristic of carbonate vibrations. It is worth mentioning that the spectra of Figure 4.12 are better resolved then those of Figure 4.11 and although some vibration frequencies are slightly shifted for higher values, the respective assignments (Table 4.3) are identical to those concerning the first group of samples.

Table 4.3 – Assignments of the FTIR absorption bands of HA Bov 600 and HA Bov 900.

Vibrational Mode	Wavenumber (cm^{-1})	
	HA Bov 600	HA Bov 900
ν_4 PO_4^{3-} bending	560	560
ν_4 PO_4^{3-} bending	599	598
ν_4 PO_4^{3-} bending	630	628
ν_2 CO_3^{2-} bending	877	-
$\nu_1 PO_4^{3-}$ sym stretching	962	961
$\nu_3 PO_4^{3-}$ asym stretching	1018	1016
ν_1 HPO_4^{2-} sym stretching	1087	1087
ν_3 CO_3^{2-} asym stretching	1413/1458	-
ν OH	3572	3572

XRD

X-ray diffraction was employed to evaluate the phase purity and the crystallographic structural properties of the mineral component of bone after calcination at the three selected temperatures (600, 900 and 1200 ºC). Spectra from the human and bovine samples are depicted in Figure 4.13 and quantitative structural parameters (crystallinity degree and crystallite size) derived from XRD analysis for the samples tested are presented in Table 4.4.

The crystallinity degree (X_c), corresponding to the fraction of crystalline phase present in the examined volume, was estimated from Eq.4.2, where I_{300} is the intensity of (300) reflection and $V_{112/300}$ is the intensity of the hollow between (112) and (300) reflections.

$$X_c = 1 - \frac{V_{112/300}}{I_{300}} \quad \text{Eq. 4.2}$$

For microstructural analysis, microstrain was assumed to be negligible and all the diffraction peaks broadening attributed to crystallite size. Scherrer equation (Eq. 4.3) was used to calculate crystallite size (τ). In this expression, λ is the wavelength of the radiation, θ is the Bragg angle and B, the line broadening at half the maximum intensity (FWHM) of the selected peaks in the diffractogram. The (002) reflection of the calcined samples was used for determining the FWHM data.

$$\tau = \frac{K\lambda}{B\cos\theta} \quad \text{Eq. 4.3}$$

The diffractograms of all calcined samples show only the characteristic pattern of hydroxyapatite (as deduced by comparing to the reference ICDD data file nº 84-1998). These results confirm that the amorphous organic component (collagen) of bone was removed after calcination at temperatures superior to 600 ºC.

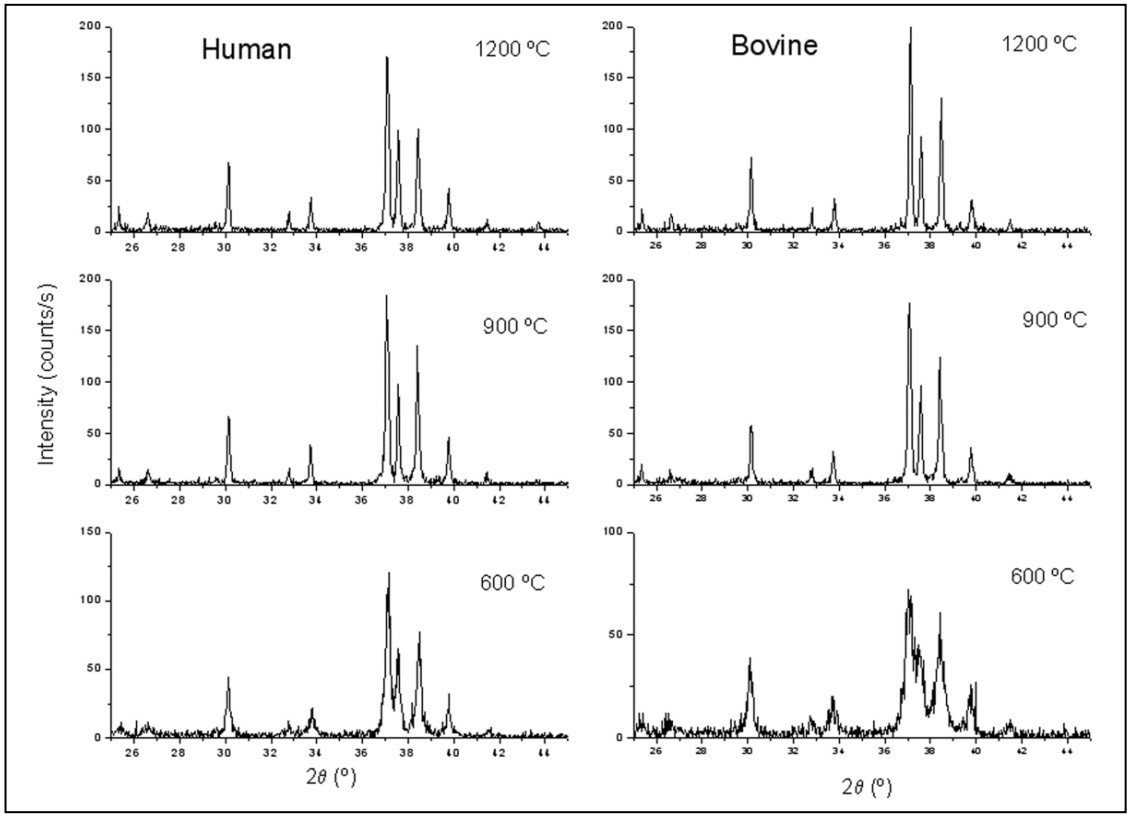

Figure 4.13 - Diffractograms of human (left) and bovine (right) bone samples calcined at 600, 900 and 1200 ºC.

For 2θ between 25º and 45º, the main lattice reflections originate peaks at 30.1, 32.8, 33.7, 37.0, 37.5, 38.4 and 39.7º, being respectively assigned to the (002), (102),

(210), (211), (112), (300) and (202) Miller plans of hydroxyapatite. A few peaks of lower intensity are also observed matching, all together, the hydroxyapatite characteristic diffractogram. The formation of other mineral phases (such as β-TCP and CaO) is not identified in any of the X-ray profiles. Nonetheless an additional study was performed to investigate the possibility of CaO formation. The calcined samples were washed with de-carbonated and distilled water and the respective filtrates were chemically analyzed. The results revealed that only the samples heated at 1200 ºC contained traces of CaO (0.1-0.2%). Such low percentages justify the non-detection of the respective peaks in the diffractograms.

The XRD results also denote a generalized trend concerning the crystallinity of the calcined samples (Table 4.4): i) the relatively broad peaks resultant from heating at 600 ºC reflect a poor crystalline apatite, probably due to the carbonate substitution into the mineral; ii) increasing the temperature to 900 ºC originates more intense and sharp peaks, corresponding to an increase in the mineral crystallinity, which is compatible with crystallite growth and with the elimination of carbonate from the lattice; iii) further increase of the calcination temperature to 1200 ºC practically has no influence on the crystallinity [79,115,174,175].

As expected, the observed narrowing of the diffraction peaks is also related to changes in the crystallite size that increases with calcination temperature. Additionally, estimates of the crystallite size (Table 4.4) show that close values are obtained for the various samples at each calcination temperature. These results are consistent with the most significant structural changes of the bone mineral occurring between 600 ºC and 800 ºC, as previously reported [79,80].

Table 4.4 – Crystallinity degree (X_c) and crystallite size (τ) of bone samples of different origins, calcined at 600, 900 and 1200 ºC.

Sample	Temperature (ºC)	X_c (%) [a]	τ (nm) [b]
Human	600	91	63
	900	96	76
	1200	96	105
Bovine	600	80	44
	900	94	82
	1200	95	95
Porcine	600	85	50
	900	95	89
	1200	96	104

[a] From Eq. 4.2.
[b] From Eq. 4.3 for the (002) diffraction peak.

SEM

Representative SEM pictures of human and bovine bone block samples calcined at 600, 900 and 1200 ºC are respectively depicted in Figures 4.14 and 4.15. These images enable the comparison of similar magnifications (3500x) that provide a new insight into structural details of calcined bone. As expected from the previous description of SEM images of lower magnifications (Figures 4.9 and 4.10), the basic microstructure of cortical bone (Havers Canals and osteocyte lacunar spaces, in particular) is preserved after calcination but the samples´ surfaces no longer present the characteristic concentric lamellae around the Havers Canals, due to the elimination of collagen with heat treatment. The detailed observation reveals, however, that crystal size and morphology display significant changes upon heating.

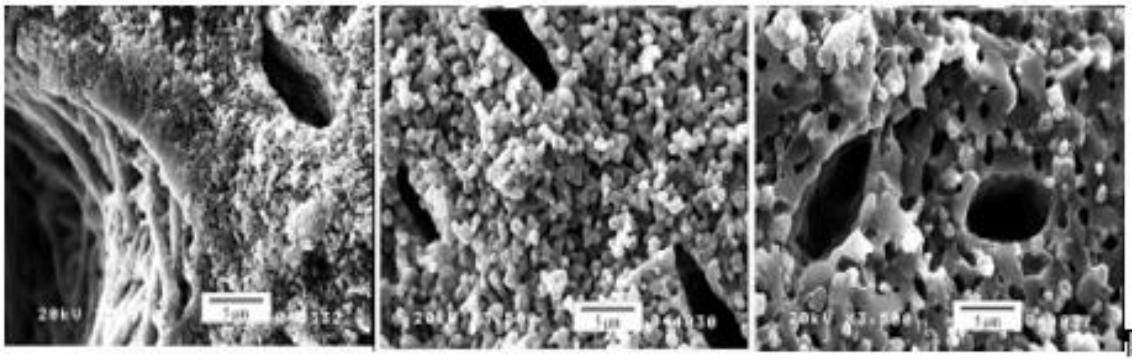

Figure 4.14 - SEM images of human bone calcined at 600, 900 and 1200 ºC (from left to right), showing the increase in crystal size with temperature.

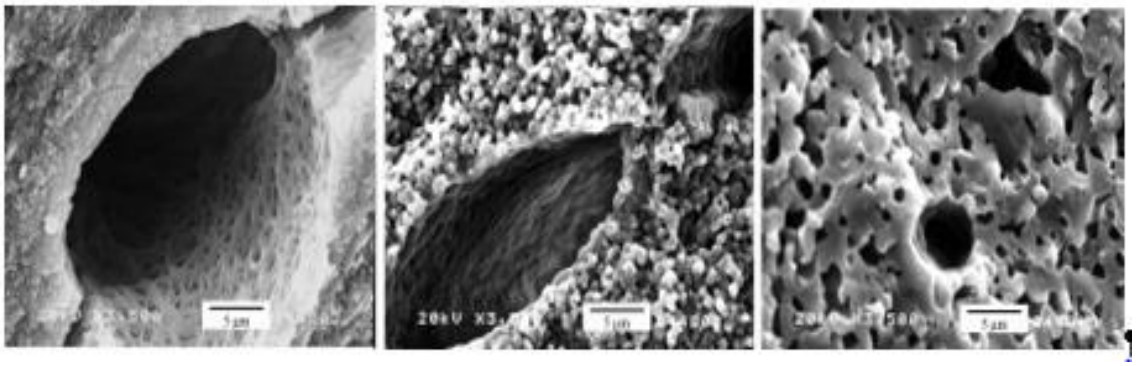

Figure 4.15 - SEM images of bovine bone calcined at 600, 900 and 1200 ºC (from left to right), showing the increase in crystal size with temperature.

As for the human bone calcined at 600 ºC, Figure 4.14 partially shows the interior of a Havers Canal where a record of the formerly existent organic structure can still be observed. Outside the Canal, a lacuna with its typical and well preserved geometry can be noticed. The other images show that as temperature augments the crystal sizes considerably increase. Moreover, at the highest temperature the sintering effect is also

obvious. Similar conclusions can be withdrawn from bovine (Figure 4.15) and porcine (data not shown) samples.

Hg Intrusion Porosimetry

This technique was used to determine the porosity and pore size distribution of the diverse bone samples in block form, before and after calcination at 600, 900 and 1200 ºC. It also enabled to determine the skeletal and bulk volume of each sample, and the respective densities. Skeletal and true densities follow from dividing the material mass by the respective skeletal and true volumes, corresponding to the sample volumes measured at the lowest and the highest intrusion pressures, respectively.

The results obtained for sample porosity using mercury intrusion are listed in Table 4.5 for all samples under investigation, including the control (non-calcined) samples. The reported values correspond to a pore range between 6 nm and 400 μm (the minimum and maximum detection limits of the equipment, respectively). As this table shows, the porosity of non-calcined samples depends on the origin of the sample, varying from around 5% for bovine bone up to 14% for porcine bone, having the human bone an intermediate value (9%).

Table 4.5 – Porosity, bulk density and skeletal density of human, bovine and porcine bone samples, before and after calcination at 600, 900 and 1200 ºC.

Bone	Parameter	Temperature (ºC)			
		Non-calcined	600	900	1200
Human	Total Porosity (%)	9.24	46.8	37.5	11.1
	Bulk Density[a] (cm^3/g)	1.89	1.61	1.83	2.62
	Skeletal Density[b] (cm^3/g)	2.08	3.02	2.93	2.95
Bovine	Total Porosity (%)	5.20	54.5	31.7	12.4
	Bulk Density[a] (cm^3/g)	2.01	1.32	2.06	2.67
	Skeletal Density[b] (cm^3/g)	2.12	2.90	3.02	3.05
Porcine	Total Porosity (%)	14.3	56.8	-	14.7
	Bulk Density[a] (cm^3/g)	1.77	1.25	-	2.49
	Skeletal Density[b] (cm^3/g)	2.11	2.90	-	2.91

[a] Includes all open pores smaller than about 400 μm (the upper detection limit of the equipment).

[b] Only includes pores smaller than 6 nm (the minimum pore size detectable by the equipment).

These differences are expected since the samples are not directly comparable. Nonetheless they all exhibit a low porosity value, consistent with a compact bone. The

effect of calcination at 600 ºC is a significant increase in porosity (which reaches values up to more than 50%) as a consequence of the releasing of water and burning of organic matter. However, the use of higher temperatures originates a systematic decrease in porosity, reaching, at 1200 ºC, values comparable to those of the control samples. This is in agreement with the increase in crystallinity as well as in crystallite size and, for the highest temperatures, with the observed sintering process (that fuses crystals and simultaneously closes many pores).

As mentioned, mercury porosimetry also provides information about sample density: bulk density, defined as the ratio of the sample mass by its bulk volume (solid + all open pores), and skeletal density, calculated from the skeletal volume (solid + pores inferior to the lower limit detected by the porosimeter (i.e., 6 nm)). According to these definitions, the bulk density values are naturally inferior to those of the skeletal density, being the former dependent upon the sample porosity (reaching the higher values for lower porosities) contrary to the latter that are practically independent of this parameter. Moreover, if the sample does not possess a considerable amount of pores below 6 nm, the skeletal density should be close to the material (solid) absolute density. Thus, it is not surprising that the calcined samples generally exhibit skeletal densities near to 3 g/cm^3, which is close to the theoretical density of hydroxyapatite (3.16 g/cm^3), being those of the control samples about 2 g/cm^3, in agreement with their water and organic content. It should also be emphasized that the value measured for the bulk density of the non-calcined human bone (1.89 g/cm^3) is close to that reported in the literature.

As interesting as knowing the total porosity, it is to be able to specify the pore size distribution. Figure 4.16 presents the pore size distribution in terms of cumulative and differential curves which clearly illustrate the effect of the calcination temperature on the porosity of the human and bovine bone samples.

The cumulative curves (Figure 4.16-a) of human samples denote a small intrusion into pores between about 100 and 20 µm, followed by a plateau and finally another intrusion of mercury into pores smaller than 1 µm. Although this trend is followed by all cumulative curves, it is apparent that the samples calcined at 600 ºC and 900 ºC correspond to the highest intruded volumes (hence the highest sample porosity) whereas the curve of the sample calcined at 1200 ºC is close to that of the control sample. The pore size ranges are more obvious in the differential curves (Figure 4.16-b) which clearly exhibit two peaks: a small peak in the 20 – 120 µm region (corresponding to the Havers Canals) and a more prominent peak between 0.1 and 1 µm (related to the lacunae/canaliculi). From the latter, it is also evident that the peak modes (i.e., most

frequent diameter) are gradually shifted to the left and are simultaneously less intense as temperatures increases. Furthermore, in comparison to the control sample, it seems that the nanoporosity has practically vanished. This is obviously related to the micro structural changes resultant from heat treatment. Similar findings were obtained for the bovine (Figure 4.16-c and –d) and porcine (data not shown) samples.

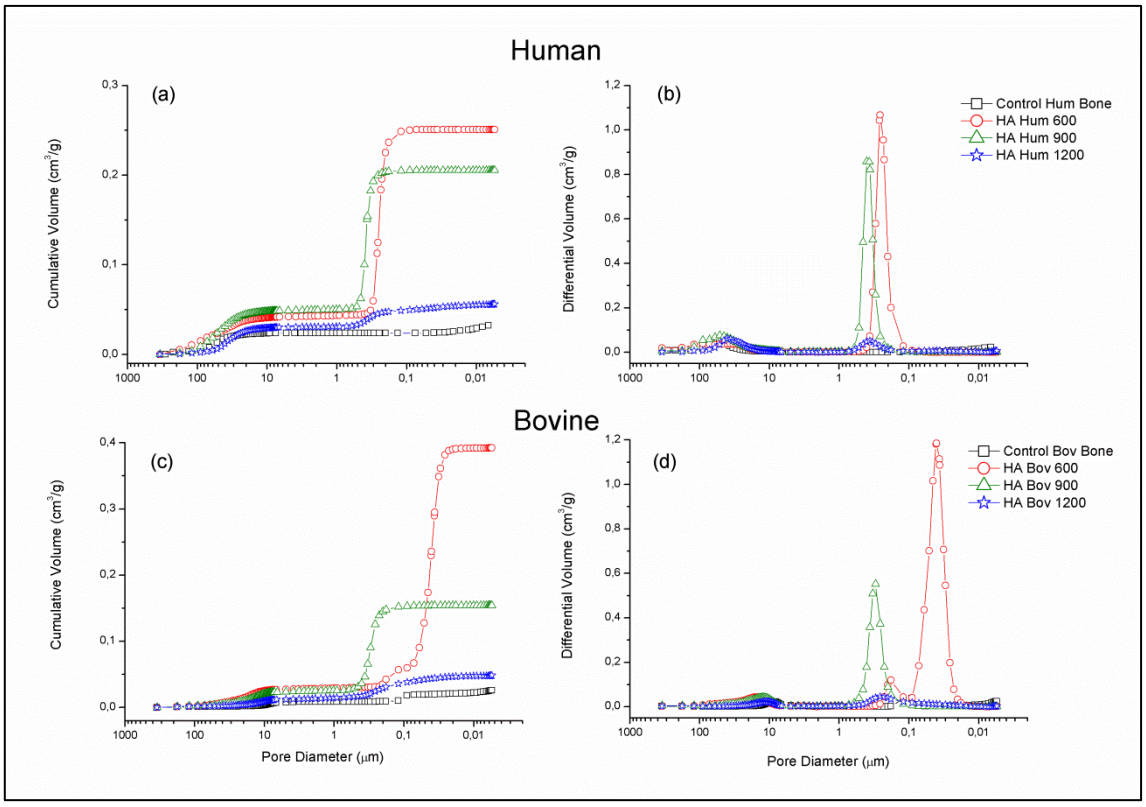

Figure 4.16 – Cumulative (a,c) and differential (b,d) intrusion curves of human and bovine cortical bone samples, before and after calcination at 600, 900 and 1200 ºC, measured by mercury porosimetry.

In the samples calcined at 600 ºC, corresponding to carbonated hydroxyapatite, the pore size distribution curves show that the most relevant contribution to the total sample porosity is in the region 0.1 - 1 µm (i.e., microporosity). According to the works published in the literature, this microporosity may be essential for inductive bone formation. Further tests performed in these samples, reduced to particulate form, confirm that the particles maintain the same microstructure as blocks. Additionally, in the form of particles, samples also exhibit high values of inter-particle porosity (with pores around 100 µm), most convenient for bone remodelling. This is obviously a convenient way of obtaining simultaneously macro and microporosity.

LDS

Laser diffraction spectrometry was used to determine the particle size distribution of the calcined bone samples after being sieved into three main fractions: 0.077-0.088, 0.088-0.150 and 0.250-0.500 mm.

Figure 4.17 illustrates the LDS results relative to carbonated and non-carbonated hydroxyapatite samples of bovine origin, sieved to the intermediate size range 88-150 μm. Samples calcined at 600 ºC are identified as HABov600 (Figure 4.17-left) and at 900 ºC, as HABov900 (Figure 4.17-right).

The particle size distribution of both samples is a bi-modal curve that covers a wide range of dimensions (from 0.4 μm to 300 μm for HABov600 and from 0.1 μm to 50 μm for HABov900), despite the use of meshes that should limit this range to narrower distributions. In both cases, however, the most frequent particle sizes are centred around 130 μm for the carbonated sample and around 20 μm for the non-carbonated ones, as a direct result from the applied meshes. The lower filter is less efficient since particles of dimensions inferior to 88 μm are detected in both samples. HABov600 has a significant proportion of particles sizes around 0.2-0.2 μm and 20-30 μm. On the other hand, the smaller particles of HABov900 measure approximately 3 μm.

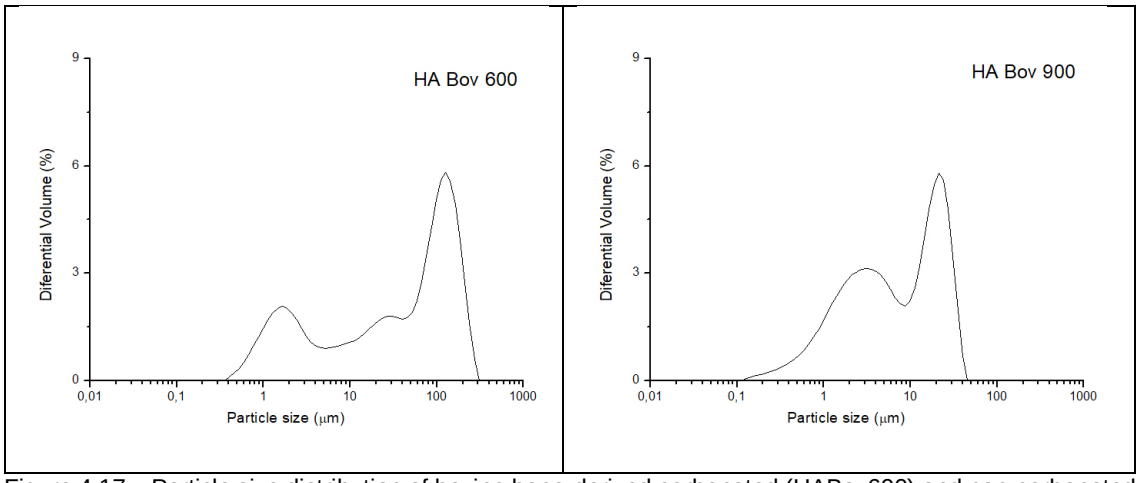

Figure 4.17 – Particle size distribution of bovine bone-derived carbonated (HABov600) and non-carbonated (HABov900) hydroxyapatite sieved to 0.088-0.150 mm.

As inferred from the distribution curves, the average size of the hydroxyapatite particles obtained by calcination at 900 ºC is inferior to that of samples calcined at 600 ºC. This is probably a consequence of the increased brittleness of the mineral due to the higher processing temperature. Using the same milling conditions (identical sample mass, time and speed of blade rotation), a brittle material crashes into smaller fragments,

IGC

Inverse gas chromatography (IGC) was used to determine the surface properties of bone derived carbonated hydroxyapatite (HA Bov 600) and non-carbonated hydroxyapatite (HA Bov 900), both obtained from calcination of bone of bovine origin at 600 and 900 ºC respectively, using the Method BC-III previously described. Since the samples were in particle form, the use of wetting methods would not be adequate because of material preparation constraints and consequent introduction of artifacts such as surface roughness, absorption of the wetting liquids into the bulk structure of the material, or contamination of the wetting liquid due to material dissolution.

Inverse gas chromatography was chosen because this technique is normally used to determine the surface properties of materials which are difficult (or even impossible) to analyze by applying more conventional techniques. IGC enables to determine various thermodynamic parameters as the surface energy and the relative affinity towards reagents with different properties, by calculating the work of adhesion between the applied gas probes and the material´s surface.

Using IGC, the material under analysis is packed inside a column and small amounts of probe gases with different properties are injected into a carrier gas stream flowing through the stationary phase. After each probe passes the detector, the equipment generates a chromatogram representing voltage intensity (proportional to the probe concentration) as a function of time. This enables to determine experimentally the retention time of a gas probe. From that value, the net retention volume (V_n) may be calculated using Eq. 4.4, where t_r is the retention time of the injected probe, t_0 is the retention time of a non-interacting probe (methane), F is the corrected flow rate of the inert carrier gas and J is the James–Martin correction factor for the carrier gas compressibility.

$$V_n = (t_r - t_o).F.J \qquad \text{Eq. 4.4}$$

The injection of gas probes is normally under infinite dilution conditions. It implies that the interactions between probe molecules themselves may be neglected. In this way, the retention time and corresponding retention volume of each gas probe reflects a dynamic interaction (adsorption and desorption) of the probe with the surface of the sample, particularly with its highest energy sites.

The free energy of adsorption (ΔG_a) of a probe into the surface of the stationary phase is a function of the net retention volume (V_n), as described by Eq. 4.5, where R is

the gas constant, *T* is the column absolute temperature and K is a constant dependent on the chosen reference state.

$$\Delta G_a = -RT\ln(V_n) + K \qquad \text{Eq. 4.5}$$

Being ΔG_a the sum of the Lifshitz–Van der Waals (γ_s^{LW}) apolar component and an acid-base (γ_s^{ab}) polar component, the free energy of adsorption may also be expressed by Eq. 4.6.

$$\Delta G_a = \gamma_s^{LW} + \gamma_s^{ab} \qquad \text{Eq. 4.6}$$

When nonpolar molecules such as *n-alkanes* are used as the gas probes in IGC, the surface energy is dominated by the Lifshitz–Van der Waals component, and the polar interactions can be neglected. Furthermore, under these conditions, although γ_s^{LW} results from the contribution of three separate interaction energies (London dispersive, γ_s^d; dipole-induced dipole (Debye, γ_s^i) and dipole-dipole orientation (Keesonm, γ_s^μ), the value of the former one is approximately equal to γ_s^d.

Briefly, if only dispersive interactions occur between sample and probe, γ_s^d may be estimated using the Schultz and Lavielle (SL) approach (Eq. 4.7), from the slope of the linear fit of $RT\ln(V_n)$ as a function of $2N{\cdot}a(\gamma_l^d)^{0.5}$, using the IGC data obtained with the apolar probes. In the equation, N is the Avogadro number, a is the surface area of the gas molecule, and γ_s^d and γ_l^d, represent the dispersive components of the surface free energy of the interacting solid and probe, respectively.

$$RT\ln(V_n) = \sqrt{\gamma_s^d}\,2N.a\sqrt{\gamma_l^d} + K \qquad \text{Eq. 4.7}$$

The Lifshitz–Van der Waals component of the surface free energy (or, as explained, the London dispersive component) can also be calculated using the method proposed by Dorris and Gray (DG). As expressed by Eq. 4.8, γ_s^d is determined from the increment in the free energy of adsorption due to the introduction of an additional $–CH_2$-group into the carbon chain of a *n*-alkane probe. a_{CH2} is the molecular area of the $–CH_2$-group, which is usually taken as 0.06 nm^2 and γ_{CH2} is the surface energy of a solid entirely composed of methylene groups. Using this approach, the free energy is graphically represented as function of the number of carbon atoms of the applied gas probes.

$$\gamma_s^d = \frac{\left[RT \ln \frac{V_n^{(C_{n+1}H_{2n+4})}}{V_n^{(C_nH_{2n+2})}}\right]^2}{4N^2(a_{CH_2})^2\gamma_{CH_2}} \qquad \text{Eq. 4.8}$$

When a polar probe is injected and a Lewis acid-base interaction occurs, there is a specific component contribution, ΔG_a^s, in addition to the dispersive component, to the overall free energy of adsorption. This parameter can be estimated by calculating the difference between the experimental value of $RT\ln(V_n)$ obtained for the polar probe and the corresponding estimation for the reference apolar probe based on the linear fitting of $RT\ln(V_n)$ *vs*. $2N{\cdot}a(\gamma_1^d)^{0.5}$ for *n-alkanes* or *vs.* the number of carbon atoms. In the present study, the former method was used to calculate the specific component of the work of adhesion (W_a^s) of two acid probes and the latter one, to determine ε_π, the separation factor corresponding to n-alkenes interactions.

As mentioned, two sets of particles of bovine derived hydroxyapatite were selected for this analysis. The first set was composed of particles derived from milled blocks calcined at 600 ºC, sieved to 0.250-0.500 mm. The second one resulted from the calcination at 900 ºC of particles from the first set. This allowed the use of particles with the exact same origin and identical size range, thus restricting the number of variables for the comparison of results. The particle size was selected to enable an operable pressure drop across the GC column. Each sample was packed inside the respective column (around 5 g of HA Bov 600 and 8 g of HA Bov 900, in accordance with the respective apparent densities) and pre-conditioned at 105 ºC overnight, under a helium flow to desorb surface contaminants, before any measurements were made. The experiments were carried out at the column temperature of 37 ºC with the injector and detector kept at 180ºC and 200ºC, respectively. This way, the results concerned the surface properties of carbonated and non-carbonated hydroxyapatite, at body temperature.

The gas probes used for the IGC data collection were methane (C1, used as reference), *n*-pentane (C5), *n*-hexane (C6), *n*-heptane (C7), *n*-octane (C8), *n*-nonane (C9), dichloromethane (DCM), trichloromethane (TCM), 1-hexene (1-Hex), 1-heptene (1-Hep) and 1-octene (1-Oct). The n-alkane series, composed of apolar probes, was used to determine the dispersive component of the surface free energy (γ_s^d); DCM and TCM, being Lewis acids, were used to determine the work of adhesion (W_a^s) of these acids with the sample surface, and the alkene series, composed of weak Lewis bases, was used to determine the specific interaction parameter (or separation factor, ε_π) with

basic probes. Some stronger Lewis bases (tetrahydrofurane and ethyl ether) and amphoteric probes (ethyl acetate and acetone) were also tested but could not be measured because the desorption from the sample surface was too slow, revealing a strong interaction with the high energy sites of the studied materials [176,177].

Helium was used as carrier gas with a flow rate of 70-80 mL/min. Small quantities of probe vapor (<1 µL) were injected into the carrier gas, allowing to work under infinite dilution conditions. The retention times (t_r) were the average of three injections and in case of asymmetric chromatograms, were determined by the Conder and Young correction method.

The IGC results are depicted in Figures 4.18 - 4.24 and the obtained surface energetic parameters are summarized in Table 4.6.

The chromatograms representative of all injected probes into the carbonated hydroxyapatite filled column (Figure 4.18) show, as expected, that the retention time increases with the chain length of each series of saturated and insaturated hydrocarbon molecules, and with the chlorine content of the acid probes. The *n-alkanes* are retained shorter than the corresponding 1-alkenes that interact more strongly with the sample surface through the π electrons of the respective double bonds. All curves except that of TCL are symmetric, suggesting that this acid probe may be involved in a chemical reaction, in addition to the physical adsorption/desorption process. The chromatogram of TCM requires Conder and Young correction to determine the retention time accurately.

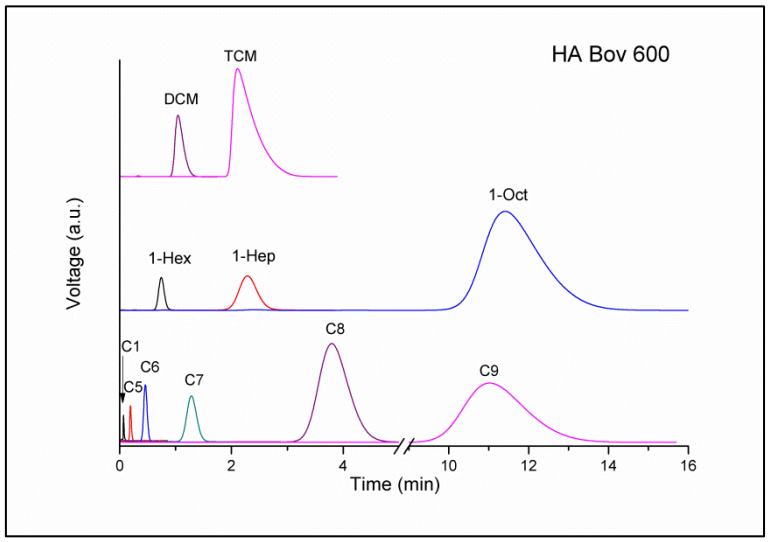

Figure 4.18 – Representative chromatograms of the different gaseous probes injected into the HA Bov 600 column at 37 ºC. Practically all curves are symmetric. Only TCM required Conder and Young correction to accurately determine the respective retention time.

The graph concerning the calculation of the dispersive component of the surface free energy of HA Bov 600 by the SL method is presented in Figure 4.19. The specific component of the work of adhesion for the DCM and TCM acid probes is also represented.

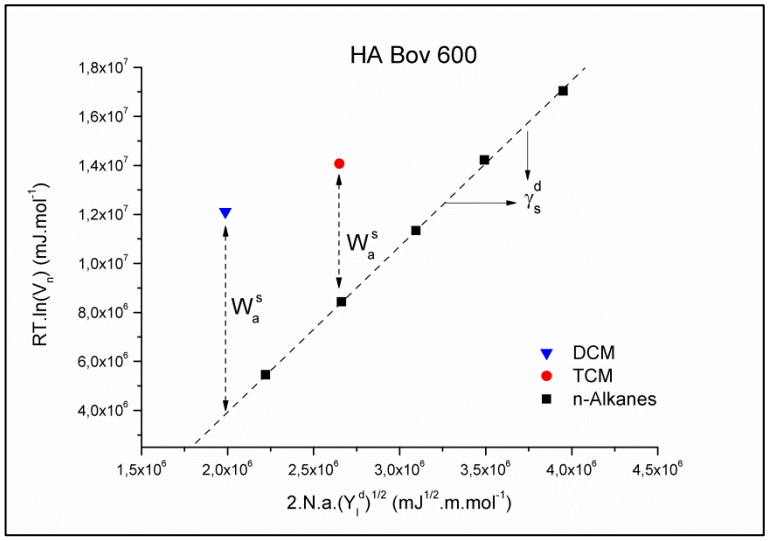

Figure 4.19 - IGC results of natural carbonated hydroxyapatite (HA Bov 600) using gaseous *n-alkanes* and two acidic probes (DCM and TCM). Determination of the dispersive component of the surface energy (γ_s^d) using the Schultz and Lavielle approach, and the specific component of the adhesion work (W_a^s) of both DCM and TCM.

Using the DG approach, the collected data enable the comparison between the adsorption of alkanes and alkenes into the HA Bov 600 sample surface (Figure 4.20). The dispersive component of the surface free energy is represented graphically, as well as the separation factor between probes with similar chain length.

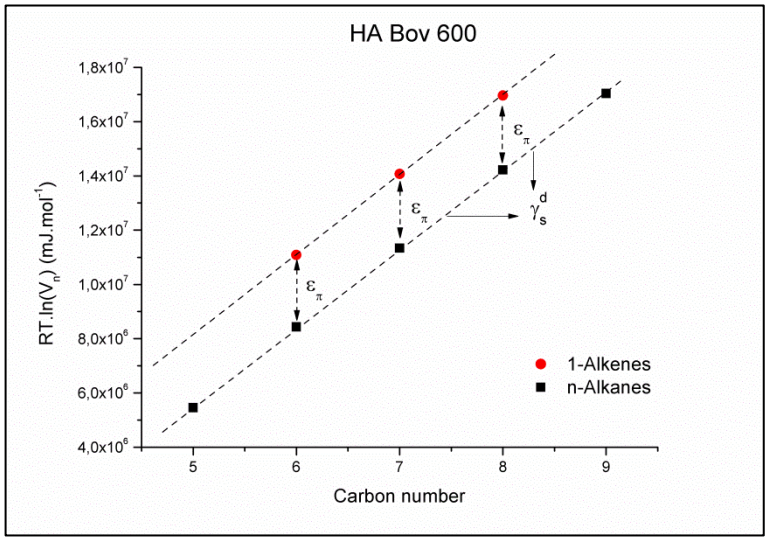

Figure 4.20 - IGC results of natural carbonated hydroxyapatite (HA Bov 600) with *n-alkanes* and 1-alkenes gaseous probes, showing the separation factor (ε_π) for C6, C7 and C8. Determination of the dispersive component of the surface energy (γ_s^d) using the Dorris and Gray methodology.

The representative chromatograms of the diverse probes injected into the non-carbonated hydroxyapatite sample are shown in Figure 4.21. The curves obtained with this sample are less symmetric, particularly those related to C8, C9, 1-Hep, 1-Oct, DCM and TCM, that require Conder and Young corrections to determine the mass centre of the asymmetric peaks.

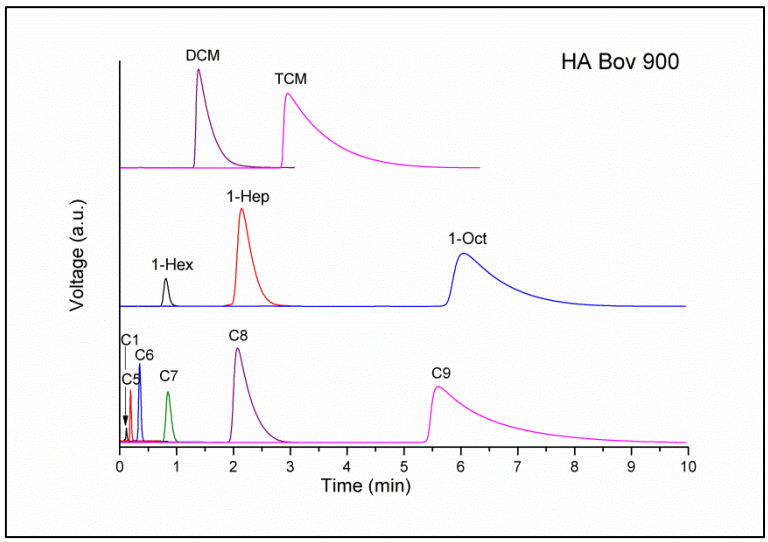

Figure 4.21 - Representative chromatograms of the different gaseous probes injected into the HA Bov 900 column at 37 ºC. The less symmetric curves (C8, C9, 1-Hep, 1-Oct, DCM and TCM) required Conder and Young corrections to accurately determine the respective retention times.

In Figure 4.22, the graphic represents the determination of the dispersive component of the surface free energy of HA Bov 900, using the SL approach. The specific component of the work of adhesion for the acid probes is also represented.

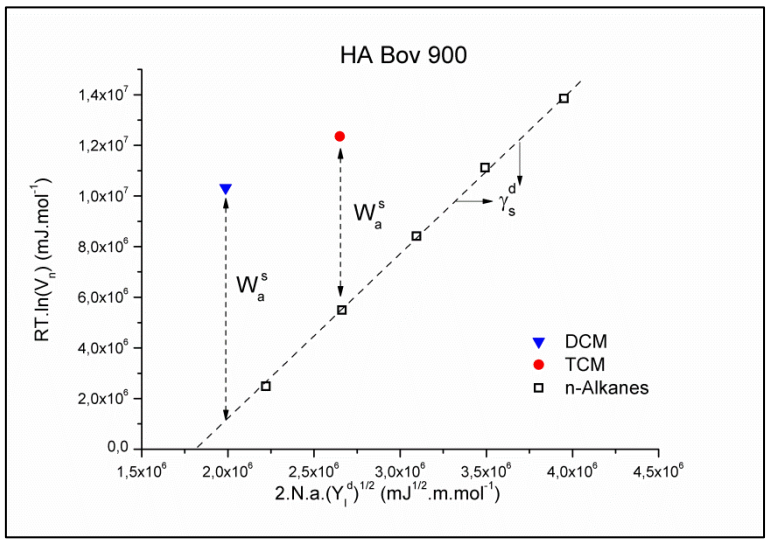

Figure 4.22 - IGC results of natural non-carbonated hydroxyapatite (HA Bov 900) using gaseous *n-alkanes* and and two acidic probes (DCM and TCM). Determination of the dispersive component of the surface energy (γ_s^d) using the Schultz and Lavielle approach, and the specific component of the adhesion work (W_a^s) of both DCM and TCM.

The determination of the dispersive component of the surface free energy of HA Bov 900 by the DG method is represented in Figure 4.23. The results concerning the alkene probes are also included, as well as the graphic method to calculate the separation factor for the C6, C7 and C8 species.

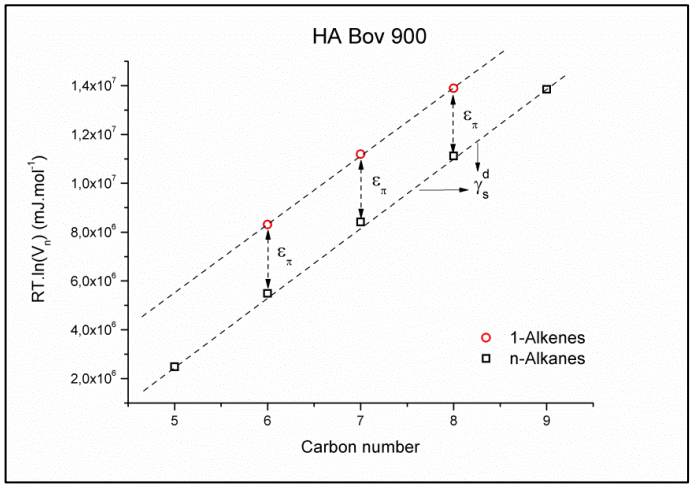

Figure 4.23 - IGC results of natural carbonated hydroxyapatite (HA Bov 600) with *n-alkanes* and 1-alkenes gaseous probes, showing the separation factor (ε_π) for C6, C7 and C8. Determination of the dispersive component of the surface energy (γ_s^d) using the Dorris and Gray methodology.

The comparison between the surface free energy involved in the adsorption of *n-alkanes* and 1-alkenes into both samples of hydroxyapatite vs. the carbon number of the gas probes is presented in Figure 4.24. As observed previously, both samples exhibit linearity on each plot, as well as almost identical slopes.

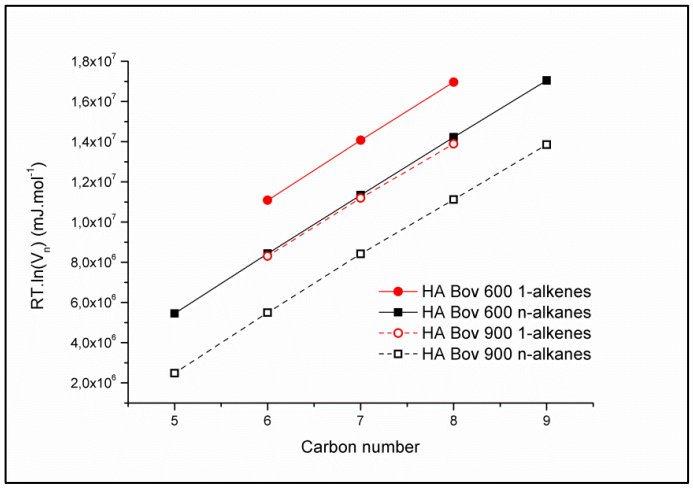

Figure 4.24 - Comparison between IGC results of the carbonated (HA Bov 600) and non-carbonated (HA Bov 900) hydroxyapatite samples.

The overall results of IGC analysis (Table 4.6) show very close values for the surface parameters of carbonated and non-carbonated hydroxyapatite samples. The dispersive component of the surface energy, derived from the interaction with the *n-*

alkanes, is around 45-46 mJ/m^2 for HA Bov 600 and HA Bov 900, regardless the applied method in the calculations. This indicates that the potential of the two materials surfaces to undergo London interactions is similar. On the other hand, the interactions with polar probes can reveal some differences between these samples. The specific component of the adhesion work of the acid probes (DCM and TCM) is around 49 and 28 mJ/m^2, respectively, for HA Bov 600 and around 46 and 25 mJ/mol for HA Bov 900. As for the weak Lewis bases probes, the separation factor is similar for the carbonated and the non-carbonated hydroxyapatite (around 3.0 kJ/mol) .

In general, it can be stated that the highest-energy sites of hydroxyapatite assessed by IGC are predominantly electron acceptors (strong bases were extensively retained in the columns of both samples). However, the Lewis basic character, as measured by the specific interaction with acidic probes, is higher for HA Bov 600, as consequence of the presence of carbonate ions in the mineral structure [176,177]. This suggests that, at body temperature, carbonated hydroxyapatite may be more appropriate to apply in bone substitute materials since, compared to non-carbonated apatite, the former may facilitate protein adsorption and cell adhesion into its surface, promoting essential events for osteointegration of this biomaterial.

Moreover, the higher specific interaction parameters of HA Bov 600 with polar probes also correlate well with physical properties such as lower crystallinity, lower density and higher specific surface area, relative to HA Bov 900. These factors, which have been reported to influence the osteoblastic activity, validate the selection of carbonated hydroxyapatite to apply in the synthesis of the composite of the present study.

Table 4.6- Surface energetic parameters obtained for the hydroxyapatite samples: γ_s^d using SL and DG approaches, W_a^s for DCM and TCM, and ε_π for C6-C8 series of *n-alkanes* and 1-alkenes.

	γ_s^d (mJ/m^2)		W_a^s (mJ/mol)		ε_π (1-alkene-alkane) (kJ/mol)		
	SL	DG	DCM	TCM	C6	C7	C8
HA Bov600	44.5	45.3	49.0	27.8	2.9	3.0	3.0
HA Bov900	45.2	46.1	46.1	24.9	2.9	2.9	2.8

It should be mentioned that the results obtained with this IGC analysis cannot be directly compared with the literature. So far, the published studies that used IGC to characterize hydroxyapatite are very scarce and the mineral samples used in those studies were not identical to those of the present work, nor were well characterized

relative to their chemical composition and applied sample treatments. Moreover, the analyses were performed at very different temperatures, affecting most of the surface energy parameters.

XPS

X-ray photoelectron spectroscopy (XPS), a surface-sensitive quantitative spectroscopic technique, was used to measure the elemental composition of the HA Bov 600 sample. This technique was used to obtain complementary information to that obtained with IGC analysis.

The typical XPS survey spectrum of the bone derived carbonated hydroxyapatite sample is shown in Figure 4.25. Besides the expected Ca, O and P peaks, other elements (C, Mg, Na, Fe) are also detected, corresponding to the atomic percentages presented in Table 4.7. The C 1s signal is of particular interest, since its high-resolution spectrum (Figure 4.26) shows two separate peaks. Whereas the peak at 285.0 eV is attributed to the adventitious carbon from atmospheric contamination, the peak at 289.7 eV is originated from the carbonate content of the sample.

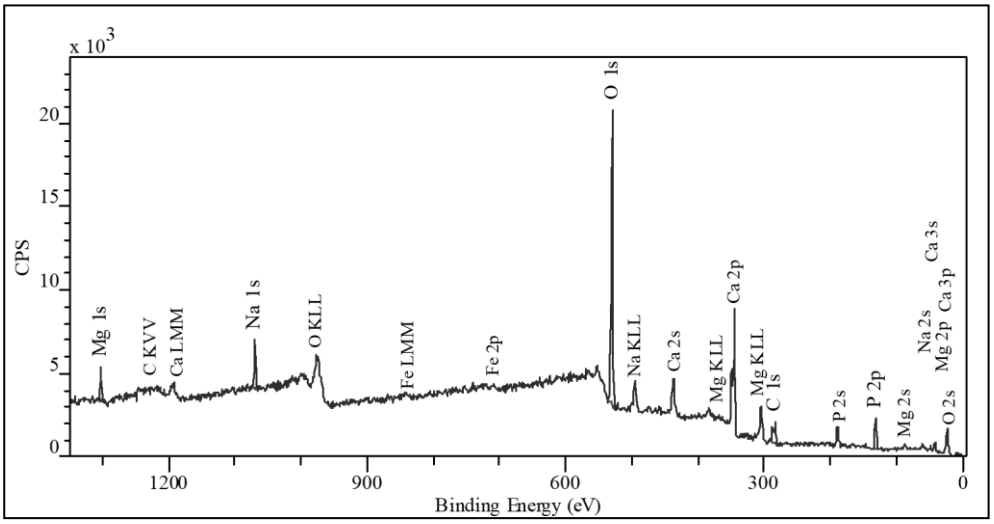

Figure 4.25 – XPS survey spectrum of HA Bov 600, a bone derived carbonated hydroxyapatite.

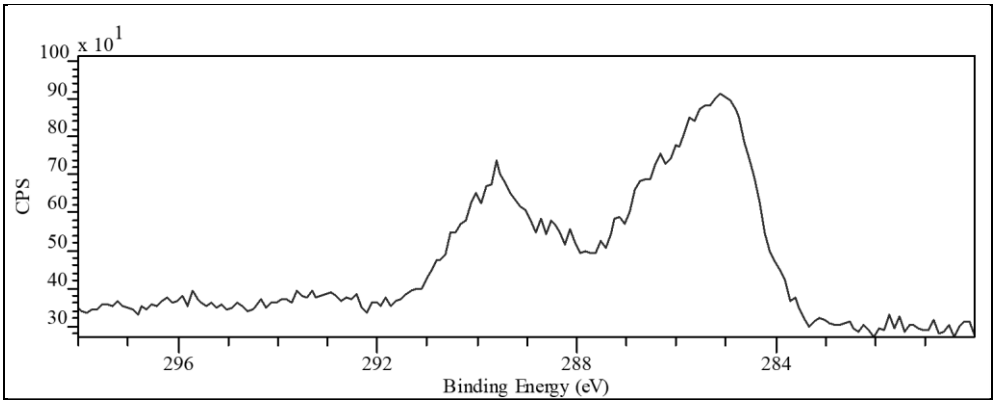

Figure 4.26 High resolution XPS spectrum of the C 1s signal.

The atomic percentages of the detected elements must be evaluated carefully because the IGC technique is a highly sensitive analytical tool and the depth of the surface under analysis is only around 2 nm. The contamination from atmosphere may explain the relative high values of O and C. But, as for the Ca and P content, the obtained Ca/P ratio (1.37) agrees well with a calcium deficient hydroxyapatite, as expected from a bone-derived sample. The presence of minor amounts of Na, Mg and Fe is also expected in these natural minerals, well known to include diverse ionic substitutions. This is also the case of carbonate, as detected in this analysis [131,165,178,179].

Table 4.7– Elements detected in the surface of HA Bov 600 by XPS.

Element	Peak range (eV)	Atomic %
C 1s	292.7 - 278.7	19.7
O 1s	537.5 - 523.8	51.7
Na 1s	1075.2 - 1063.9	4.6
Mg 1s	1306.1 - 1298.1	1.7
P $2p^1$+$2p^3$	136.5 - 126.7	9.3
Ca $2p^1$+$2p^3$	355.0 - 340.9	12.8
Fe $2p^1$+$2p^3$	727.4 - 700.9	0.1

The XPS analysis was not applied to HA Bov 900 because this sample was obtained from the thermal treatment of HA Bov 600 to eliminate its carbonate content, thus keeping the same Ca/P ratio. Since the respective FTIR spectra confirmed the expected chemical compositions regarding the absence of carbonate and XPS analysis, as explained, could not quantify the sample´s C and O accurately, that analysis was not performed.

4.2.2 Synthetic hydroxyapatite

Synthetic hydroxyapatite is frequently preferred to the bone-derived mineral in biomedical applications, mostly because of the risks of disease transmission. Despite the various methods commonly applied in the sterilization of the natural minerals, some pathogenic agents were reported to resist to the standard treatments. Another frequent reason to select synthetic products is the predictable composition and behavior, presuming that the produced substances are more homogeneous than the natural ones. Finally, the economical factor may also have some influence because synthetic products are often less expensive.

Despite the initial intention to only apply natural (bone derived) hydroxyapatite in the composite, it became clear that this study would be more complete if alternative synthetic minerals were also considered. It would be important to know if the composite can be synthesized with synthetic minerals and conclude about its advantages, or disadvantages.

Two kinds of synthetic minerals have been considered: a carbonated hydroxyapatite (Calcibon) and a non-carbonated hydroxyapatite (Inbone). These minerals were used as received. The chemical composition of these commercial products was accessed by FTIR spectroscopy and particle size distribution, by Laser Diffraction Spectroscopy (LDS). The relevance of this technique will be understood in latter stages of this work.

4.2.2.1 Characterization

FTIR

The vibrational spectra of Calcibon (carbonated hydroxyapatite) and Inbone (non-carbonated hydroxyapatite) are presented in Figure 4.27 and the respective assignments are listed in Table 4.8.

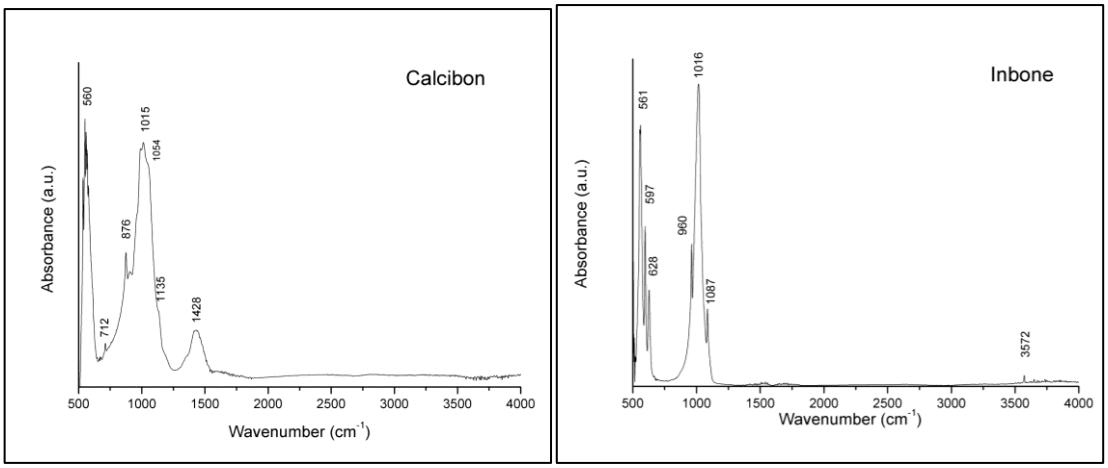

Figure 4.27 - FTIR spectra of Calcibon (left), a synthetic carbonated hydroxyapatite and Inbone (right), a synthetic non-carbonated hydroxyapatite.

In both spectra, the ν_4 phosphate bending vibrations are attributed to the bands around 600 cm^{-1}, being better resolved in that from Inbone. The ν_3 phosphate stretching vibrations originate the most intense peaks in both spectra, at 1015 cm^{-1}. In addition, the spectrum of Calcibon shows some bands (876 and 1428 cm^{-1}) originated by carbonate vibrations. The presence of HPO_4 is also detected, mostly in the spectrum of Calcibon, contributing to broader peaks than those of Inbone. On the other hand, the OH stretching vibration (3572 cm^{-1}) is only detected in the non-carbonated sample.

Table 4.8– Assignments of the FTIR absorption bands of Calcibon and Inbone.

Vibrational Mode	Wavenumber (cm^{-1})	
	Calcibon	Inbone
ν_4 PO_4^{3-} bending	560	561
ν_4 PO_4^{3-} bending	595	597
ν_4 PO_4^{3-} bending	630(sh)	628
ν_2 CO_3^{2-} bending	876	-
$\nu_1 PO_4^{3-}$ sym stretching	-	960
$\nu_3 PO_4^{3-}$ asym stretching	1015	1016
ν_1 HPO_4^{2-} sym stretching	1054	1087
ν_3 HPO_4^{2-} asym stretching	1135	-
ν_3 CO_3^{2-} asym stretching	1428	-
ν OH	-	3572

LDS

The graphics obtained using LDS shown in Figure 4.28 reveal that the particles´ size of Calcibon range from 0.2 to 200 μm, whereas Inbone is mostly composed of particles between 1 and 10 μm. Curiously, the volumetric percentage of particles inferior to 3.6-5.0 μm is approximately the same for both samples (Table 4.9).

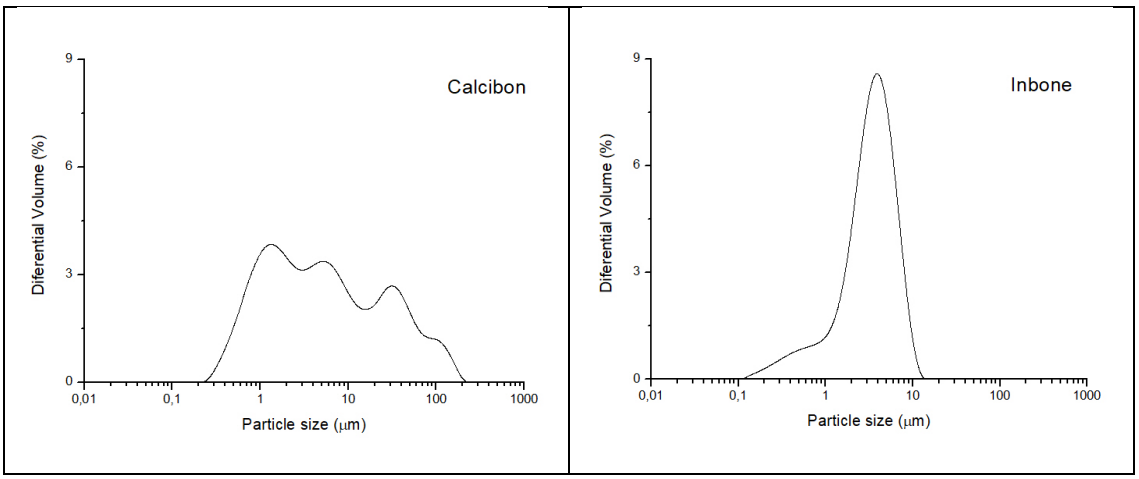

Figure 4.28 - Particle size distribution of Calcibon (left) and Inbone (right).

Table 4.9 - Particle size distribution of Calcibon and Inbone.

	D10	D50	D90
Calcibon	0.9	5.0	53.1
Inbone	1.0	3.6	7.1

4.3 **Contrast agent**

In clinical practice, barium sulphate is the most frequently used contrast agent for x-ray radiology. It is most often used in x-ray imaging of the grastro-intestinal tract, being administered orally or by enema, as a suspension of fine particles on water. For x-ray guidance in vertebroplasty or kyphoplasty procedures, barium sulphate is usually mixed with acrylic cement compositions, accounting up to 30% of the mixture weight. The addition of this mineral is fundamental in order to perform the procedure safely.

Barium sulphate is an odorless white crystalline solid that is highly insoluble in water. This non-resorbable mineral is the least toxic salt of Barium due to its insolubility, which protects the patients from absorbing harmful amounts of that heavy metal. The high atomic number of Ba (Z=56) enables its compounds to absorb more x-ray radiation than compounds derived from lighter nuclei, being thus a reference contrast agent for radiology.

Given that barium sulphate can be considered as a safe conventional contrast agent, the option for using this mineral to achieve an adequate opacification of the composite under study was readily made.

Barium sulphate was characterized as-received (in particle form) using FTIR, XRD, SEM, LDS and radiology (section 4.3).

4.3.1 Characterization

FTIR

The vibrational spectrum of barium sulphate (Figure 4.29) is characterized by two intense bands ant 603 and 1058 cm^{-1}, and less intense bands at 635, 982, 1100 (shoulder) and 1182 cm^{-1}. While the bands in the 600-650 cm^{-1} region are attributed to sulphate bending vibrations, those around 950-1200 cm^{-1} are originated by stretching vibrations of the sulphate bonds, as expected due to its tetrahedral geometry. These assignments are presented in Table 4.10.

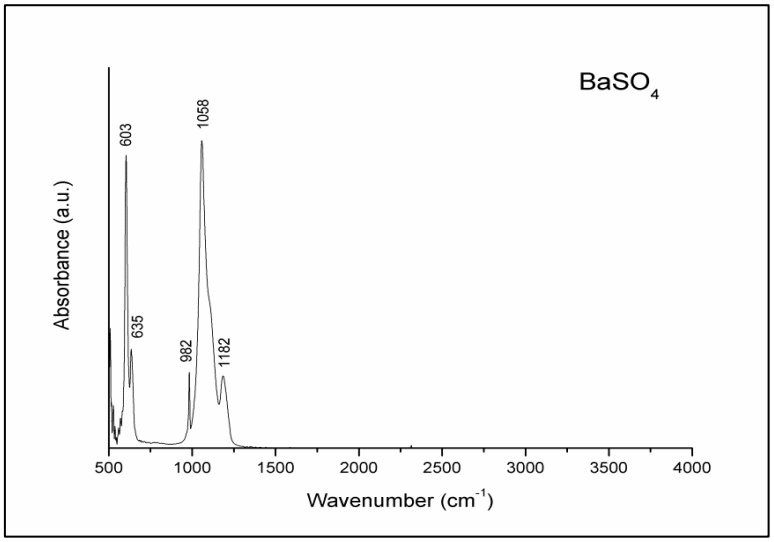

Figure 4.29 - FTIR spectrum of $BaSO_4$.

Table 4.10 – Assignment of the vibrational bands of barium sulphate.

Vibrational Mode	Wavenumber (cm^{-1})
ν_4 SO_4^{2-} bending	603
ν_4 SO_4^{2-} bending	635
ν_1 SO_4^{2-} sym stretching	982
ν_3 SO_4^{2-} asym stretching	1058
ν_3 SO_4^{2-} asym stretching	1100 (sh)
ν_3 SO_4^{2-} asym stretching	1182

XRD

The diffractogram of the barium sulphate used in this study is presented in Figure 4.30. In the measured 2θ range, the obtained profile matches the ICDD data file nº 80-0512, providing confirmation about the qualitative composition of the mineral. All peaks are originated from $BaSO_4$ reflections, being the most intense observed at 30.1, 31.3, 33.5, 49.9 and 50.3 attributed, respectively, to the (021), (210), (121), (311) and (212) Miller plans.

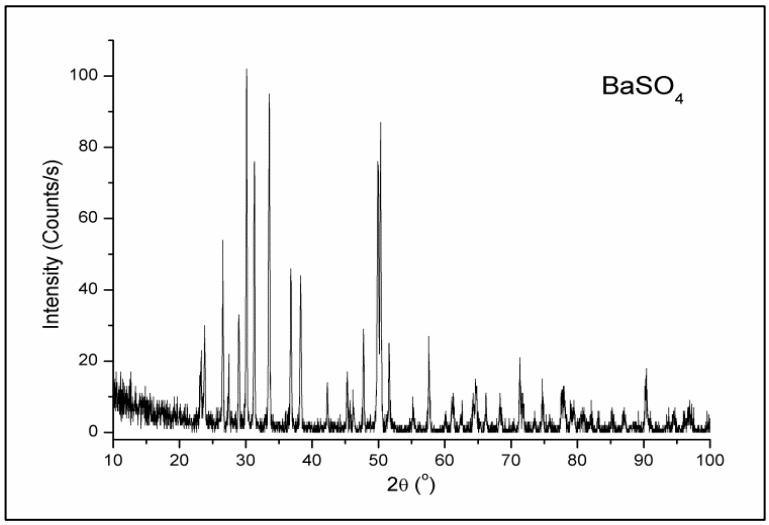

Figure 4.30 - Diffractogram of $BaSO_4$.

LDS and SEM

The physical characterization of barium sulphate regarding particle size distribution and morphology, resulting from LDS and SEM analyses, is presented in Figure 4.31. This mineral is composed of particles characterized by D10=1.04 μm, D50=3.28 μm and D90=7.47 μm, corresponding to a relatively narrow size distribution. The SEM images enable to confirm the size range measured by LDS and to observe the shapes of the particles, many of them with smoothed edges.

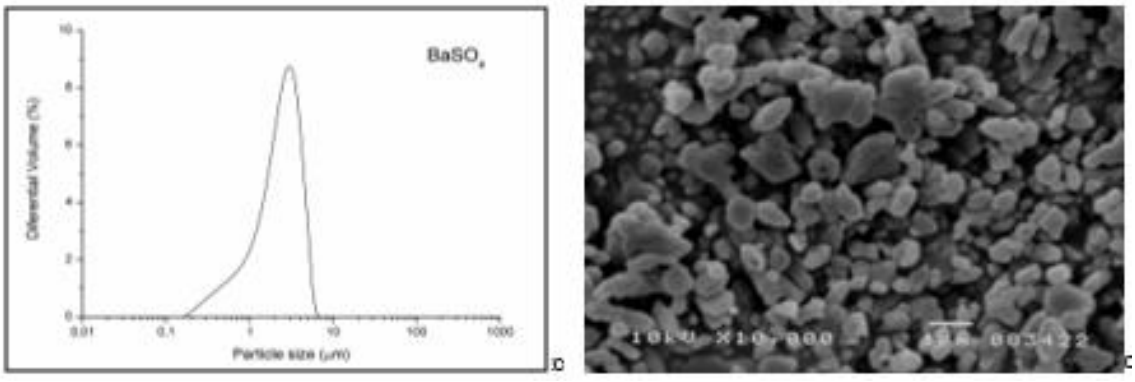

Figure 4.31 - Particle size distribution (left) and morphology and size of the $BaSO_4$ particles (right).

4.4 **Proportion of hydroxyapatite and contrast agent**

One of the features of Kyphoplasthy is that it must be performed under real-time radiologic guidance. The injected material must be more radio-opaque than bone to allow monitoring its insertion into the target vertebral body defect. In case of undesired leakage, the opacity of the material should also enable to track its dispersion.

As it is well known, bone is a very dense material that originates light images in radiographs. Less dense materials (such as soft tissues) originate dark images. These effects reflect the lower or higher ability, respectively, of x-rays passing through materials with different densities and absorption coefficients of this radiation. Whereas conventional radiographs used to capture the radiation that stroked an undeveloped film which required posterior chemical treatment to obtain an image, nowadays digital detectors, often connected to a computer screen, have replaced most ancient systems. Radiographs can now be displayed almost instantaneously.

Most commercial materials used in kyphoplasthy include barium sulphate in their composition since it is a very efficient contrast agent. Concentrations usually range up to 30wt%.

In this study, besides the intentional addition of $BaSO_4$ to cause x-ray contrast, the effect of hydroxyapatite (the mineral dense component of bone) on the radiographs was also considered since, as mentioned, bone itself is already opaque to x-rays.

In order to determine the range of concentrations of minerals in the injectable composition that would provide a good contrast in radiographs, several proportions of hydroxyapatite and $BaSO_4$ were suspended in an aqueous solution of 30wt% PVA80 and injected inside artificially created cavities of numerous vertebrae from an Ovis aries animal model. Given that after injection the suspension becomes surrounded by the bone tissue of the vertebra (which, as mentioned, is opaque to x-ray radiation), the radiologic images of the filled vertebrae allow simulating, *in vitro,* the contrast of the studied materials under the conditions that most influence the quality of the x-ray images *in vivo*.

4.4.1 Procedure

Materials

The studied ceramic materials were used in particle form. Bovine hydroxyapatite was previously prepared by thermal treatment at 600 ºC (HA Bov 600 from BP-II and BC-II methods, as described in section 4.1.1.1) and barium sulphate was used as supplied by the manufacturer.

Diverse ratios of HA Bov 600 and $BaSO_4$ particles were suspended in a viscous aqueous solution of 30 wt% PVA 80 [poly(vinyl alcohol), hydrolysis degree of 80%], wherein each mineral component ranged up to 50 wt% relative to the polymer solution (not to the total weight of the mixture). The composition of the suspensions is described in Table 4.11.

Vertebrae preparation

A complete spine from the animal species Ovis aries was submitted to the same rinsing and preservation procedures as natural bone femur samples (method BP-II described in section 4.1.1.1).

Being the vertebral spine composed of many different vertebrae, some of the most irregular elements were used as a source of complementary information. These vertebrae were cut in the longitudinal and axial directions to intentionally expose the interior of the vertebral body, thus enabling the direct observation and handling of an environment with particular interest for this work.

The most similar and regular elements (shape and size) were selected for the radiologic study. Whereas most of the vertebrae were drilled to introduce structural defects into the middle of their vertebral bodies, some were left intact to provide references (vertebra #0, Table 4.11) for these assays. Each drilled vertebra was x-ray imaged before and after filling the created cavity with a suspension containing known amounts of minerals.

Radiology

In order to evaluate the reference contrast of the materials, preliminary x-ray images of the suspensions inside glass vials were obtained and compared with those from empty vials. This enabled to determine, for various x-ray intensities, the expected contrast from HA Bov 600 and $BaSO_4$. Additionally, these tests allowed estimating the range of intensities that could be used to observe the filled vertebrae, since their thickness can influence the obtained images. The x-ray intensity adjustment was performed in the range 0.10-0.28 rad, being the best contrast obtained with 0.28 rad.

Radiographs of the intact vertebrae, representing the reference for healthy bone samples, were compared with those from the empty drilled ones that simulate bone defects in the vertebral bodies. Each drilled vertebra was filled with a predetermined composition and the respective x-ray image was obtained. The same vertebra could not be used to test different concentrations of minerals because these became partially entrapped in the cancellous structure.

The experimental conditions concerning the kind of system (vial, vertebra), its status (empty, filled) and the concentration of minerals (HA Bov 600, $BaSO_4$) used in the radiologic study are presented in Table 4.11, where vertebra #0 corresponds to an intact (non-drilled) reference system. The range of concentrations of minerals tested inside the glass vials and vertebrae was more extensive, being selected only some of the data since the corresponding results are telling examples.

Table 4.11 – Empty and filled systems (vials and vertebrae) containing different concentrations of HA Bov 600 and $BaSO_4$, tested by radiology.

System	Empty	Filled	
		HA Bov 600 (wt%)	$BaSO_4$ (wt%)
Vial #1	+	50	0
Vial #2	+	20	30
Vertebra #0 [a]	-	-	-
Vertebra #1	+	0	10
Vertebra #2	+	0	20
Vertebra #3	+	0	30
Vertebra #4	+	20	20
Vertebra #5	+	20	30
Vertebra #6	+	50	0

.[a] Intact (non-drilled) vertebra.

4.4.2 Characterization

After the initial preparation method, the physical appearance of the vertebrae is illustrated in Figure 4.32, being the interior of the vertebral body exposed under two perpendicular directions. Although the exposed surfaces have been slightly damaged by the cutting tool, these sections reveal the typical structure of the main anatomic parts of the vertebra: the vertebral body, possessing a large volume of cancellous bone embedded with bone marrow, and a very thin layer of compact bone surrounding the whole structure, as well as the spinous processes with an identical structure, but much less volume.

The manipulation procedure enabled the qualitative evaluation of the mechanical strength of the vertebrae, being the role of the external compact structure clearly recognized. On the other hand, the cancellous part is relatively soft and can be easily punctured or crashed, when its cortical protection is crossed or removed. The crashed cancellous structure, naturally mixed with bone marrow, acquires a paste consistency with a greasy texture. This observation is obviously pertinent in the context of bone substitute materials to apply, in particular, inside bone defects of damaged vertebral bodies.

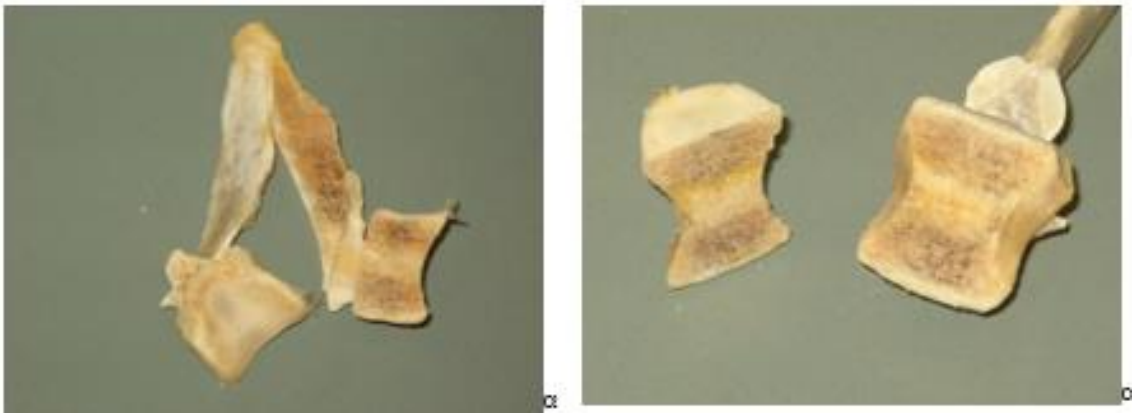

Figure 4.32 - Longitudinal (left) and axial (right) cross-sections of some of the most irregular Ovis aries vertebrae.

The radiographs of the systems described in Table 4.11 are presented in Figures 4.33 and 4.34. The former corresponds to images from the reference systems and the latter, to the x-ray exposure of six test vertebrae before and after filling the respective bone defects with known ratios of minerals. All images are presented in grayscale, synthesized from full color images, as generated by the equipment.

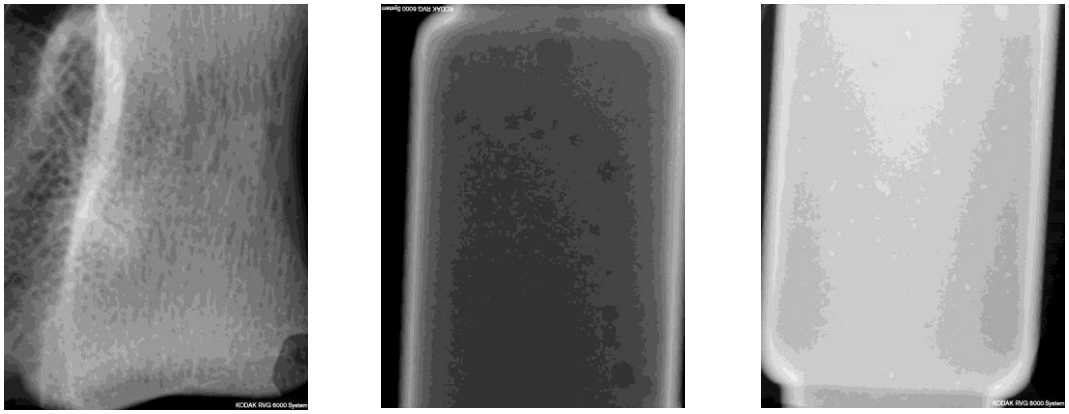

Figure 4.33 - X-ray images of some reference systems. From left to right: intact vertebra #0, glass vial #1 filled with a suspension containing 50% HA Bov 600, and glass vial #2, a mixture of 20% HA Bov 600 and 30% $BaSO_4$, both in aqueous solutions of 30% PVA80.

The reference systems in Figure 4.33 illustrate the typical radiograph of an intact vertebra (#0), where the lighter regions correspond to the densest parts of the observed bone. It also displays the x-ray images of two glass vials (vial#1 and vial#2) possessing different mineral contents. It should be mentioned that the empty vials, as well as the PVA solution, are both transparent to x-rays (data not shown). Vial #1, containing a suspension of 50 wt% hydroxyapatite in PVA solution, originates a dark image but yet discernible from its environment. In vial #2, the contrast obtained with the mixture of 20 wt% hydroxyapatite and 30 wt% $BaSO_4$ suspended in PVA is much stronger.

The radiographic images of the empty drilled vertebrae (Figure 4.34, #1-a to #6-a) enable to observe, in addition to the general appearance of each vertebra, the size and shape of the mechanically introduced bone defects. These come as darker regions due to the lower density across the respective vertebral bodies. Conversely, the mineral suspensions inserted into the bone defects can be easily detected, provided that the material gives stronger contrast than bone itself. Within the studied cases (Figure 4.34, #1-b to #6-b), the only exception is vertebra #6-b whose content is similar to that of vial #1. Although the contrast of the 50 wt% hydroxyapatite suspension is not very high, when this composition is inserted into the vertebral bone defect, both the defect and the material can no longer be detected, and the x-ray image is similar to that of a sound vertebra. This result indicates that the density of the inserted material is similar to the density of the vertebral body. It agrees well with the mineral content (around 65-70 wt%) of the bone matrix, associated to the cancellous bone porosity (it can reach 90%) and bone marrow content (that also contributes to the vertebral density).

The concentration effect of the isolate contrast agent was tested in vertebrae #1, #2 and #3, which were filled with 10, 20 and 30 wt% $BaSO_4$ suspensions,

respectively. As expected, the contrast of the inserted materials increased remarkably and the lower concentration was considered as less adequate.

The intermediate and the higher concentrations of $BaSO_4$ were subsequently selected for testing mixtures containing, in addition, 20 wt% HA Bov 600 (vertebrae #4 and #5, respectively). The material contrast observed in vertebra #4-b is similar to that of vertebra #2-b, suggesting that the added amount of hydroxyapatite is not enough to influence the x-ray absorption intensity of $BaSO_4$. A similar conclusion can be inferred from vertebra #5-b, which contrast is increased relatively to #4-b due to the higher $BaSO_4$ content, with little effect from the hydroxyapatite contribution. Comparing vertebrae #5-b with #3-b, both containing 30 wt% $BaSO_4$, although similar contrasts could be expected, the image of the inserted material in #3-b is brighter. This may be due to thickness differences between the vertebrae. Moreover, the material mixture content in vertebra #5-b is the same than in glass vial #2, being expected to originate similar contrast images. However, the brightness of the radiograph of vial #2 is also stronger than that of vertebra #5-b, probably because whereas glass is transparent to x-rays, bone shows a degree of opacity to this radiation. These results bring the attention to the influence of composition, thickness and density of the systems around the material under observation. Even small variations between the used vertebrae caused some differences in the x-ray absorption.

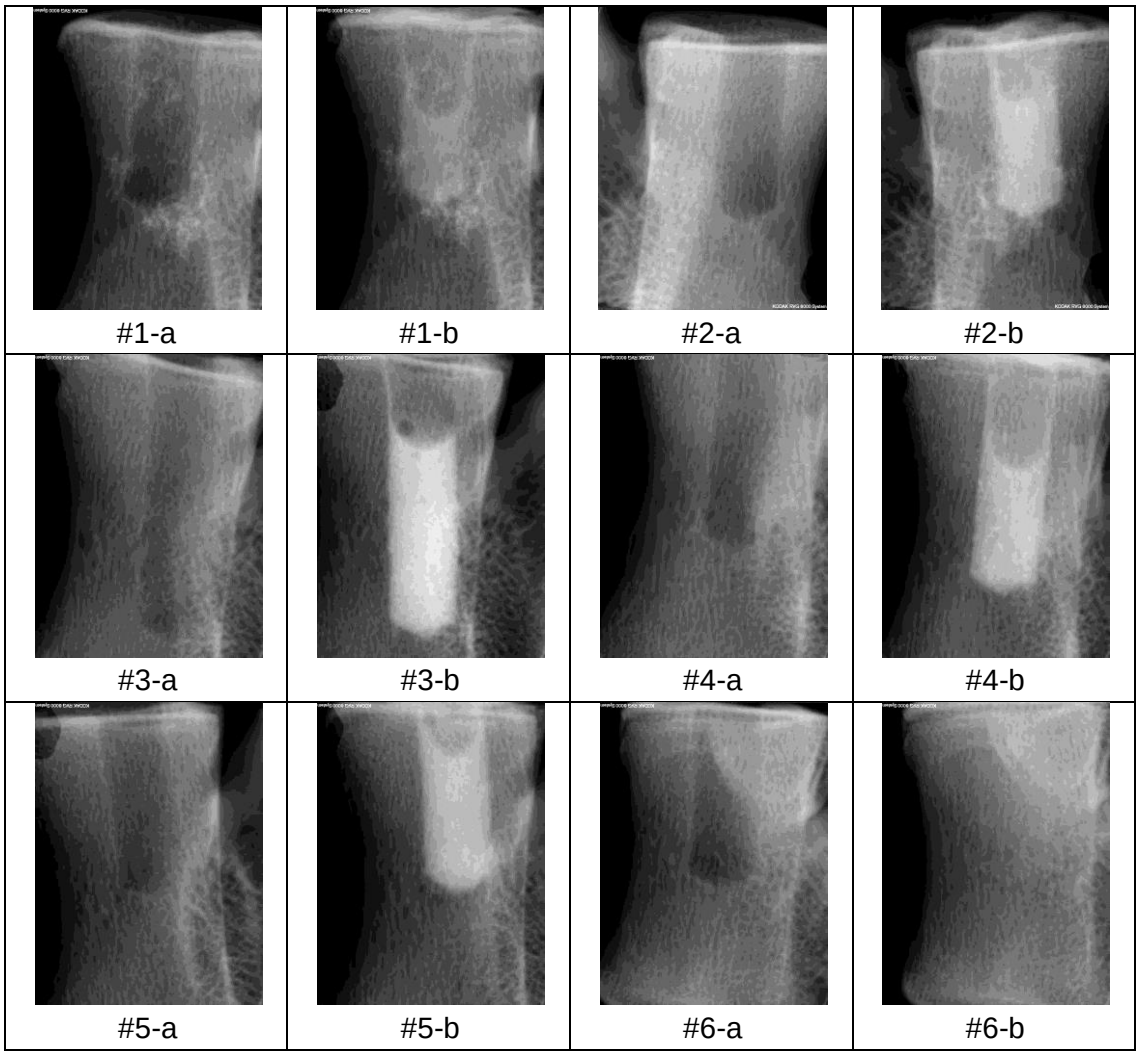

Figure 4.34 - X-ray images of the tested vertebrae (#1 to #6) before (a) and after (b) filling the created cavity with different ratios of hydroxyapatite (HA Bov 600) and $BaSO_4$, as described in Table 4.11.

The results obtained in this radiologic study confirm the high and medium potential contrast of barium sulphate and hydroxyapatite, respectively, being the absorption intensity dependent on the absorption coefficient and the concentration of the minerals. In a mixture containing both minerals, $BaSO_4$ should constitute 20 to 30 wt% of the composition to enable a good contrast. As for hydroxyapatite, given that the concentrations around 50 wt% match the density of the vertebral body, higher amounts may enable higher contrast and consequently contribute to the x-ray detection of the material.

FTIR

The vibrational spectrum of the mixture of equal weight fractions of HA Bov 600 and $BaSO_4$ is presented in Figure 4.35, together with the spectra from each mineral. The spectral assignments have been presented previously in Tables 4.3 and 4.10, respectively. The profile of the resulting spectrum is very similar to that of barium sulphate, being the additional peaks from hydroxyapatite clearly identified.

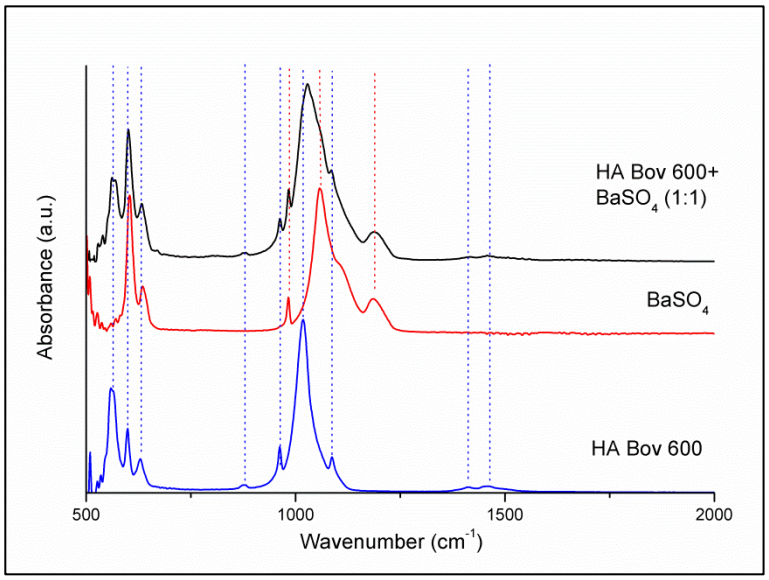

Figure 4.35 – FTIR spectra of the 1:1 mixture of HA Bov 600 and $BaSO_4$, and of the respective control samples.

XRD

The diffractogram of the 1:1 mixture of HA Bov 600 and $BaSO_4$ is shown in Figure 4.36, together with those from the reference samples. Although the weight fraction of each mineral is the same, the peaks in the diffractogram of the mixture are predominantly coincident with those from $BaSO_4$. The single clearly detected peak from hydroxyapatite is observed at 37º, partially overlapped with a peak from barium sulphate. Given that the mole ratio (n $BaSO_4$./n HA Bov 600) of these minerals is approximately 0.2, the higher intensity of the barium sulphate diffractogram indicates that its absorption coefficient of x-ray radiation is much superior to that of hydroxyapatite. Thus, these XRD results agree well with the radiology tests.

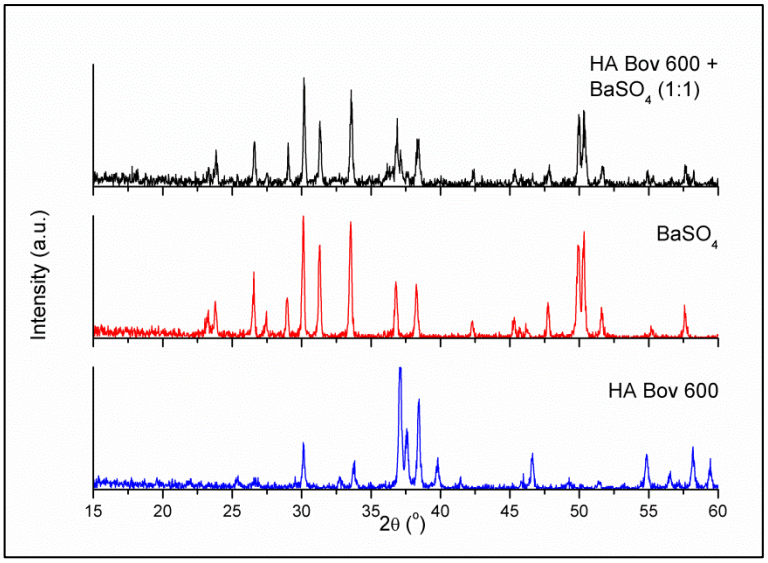

Figure 4.36 - Diffractograms of the 1:1 mixture of HA Bov 600 and $BaSO_4$, and of the respective control samples.

4.5 **Conclusions**

In order to induce a biological response similar to the one generated during bone remodeling, the selection of mineral components for the synthesis of a bioactive bone substitute material is supported by many requirements in addition to the fundamental biocompatibility, biodegradability and non-toxicity. Whether the minerals are applied in particle form, as cements or as solid scaffolds, the resulting material must combine diverse properties that depend not only on the chemical composition, solubility and reactivity, but also on physical properties as density, size, porosity, crystallinity and surface characteristics, namely topography and free energy.

Hydroxyapatite and other calcium phosphate ceramics are widely used in the field of bone tissue engineering because these minerals, especially the former one, have superior properties for the stimulation of bone formation. Bone-derived hydroxyapatite, in particular, naturally presents a set of most promising properties that synthetic minerals are not able to duplicate.

The well-known characteristics of natural hydroxyapatite motivated the selection of this type of mineral to apply in the synthesis of the projected composite. This option implied the detailed characterization of natural human bone since it constitutes the host for the grafting material. To investigate an alternative source to obtain hydroxyapatite, the comparative study of bones of different origins (human, bovine and porcine) was essential, as well as the preparation process of the minerals and their subsequent characterization. In addition, two synthetic apatites (Calcibon and Inbone)

were also briefly characterized, as alternatives to the natural minerals in the synthesis of composites.

The results presented in this chapter allow learning about efficient procedures to prepare bone samples, about the bone matrix composition and structure, the thermal treatments required to obtain bone-derived hydroxyapatite and the effect of the calcination temperature on the chemical composition and structure of the resulting minerals. The great similarities between bones of different origins, before and after calcination at each selected temperature (600, 900 or 1200 ºC), validate the different procedures applied in the preparation and in the calcination of bone. More importantly, these similarities justify the use of non-human samples to obtain the apatite mineral component for the aimed composite.

Regarding bone-derived hydroxyapatite, the study of the calcination process shows that the temperature highly conditions the properties of the bone samples. As expected, higher temperatures lead to more pure forms of hydroxyapatite, with higher crystallinity degrees and larger crystallite sizes, and a less porous structure. Since samples heated to the same temperature exhibit similar characteristics, regardless their origin, those of bovine origin were selected for this work. The larger dimensions of bovine bones provide greater amounts of materials with homogeneous properties.

FTIR spectra indicate that the organic constituents are no longer present in the samples calcined at 600 ºC, suggesting that this temperature is adequate to obtain protein-free samples. Moreover, these spectra also reveal that, at this temperature, a carbonated apatite is obtained, being the carbonate removed from the mineral at higher temperatures. Furthermore, no new mineral phases are evident at higher temperatures, in good agreement with the results of thermal analysis and XRD. Nonetheless, traces of CaO (0.1-0.2 wt%) can be detected in samples heated at 1200 ºC, as revealed by chemical analysis.

Regarding porosity, it is clear that samples calcined at 600 ºC exhibit the highest porosity, around 50 %, which, for a compact bone, is quite relevant. However, as the heating temperature increases, the porous structure condenses, sintering at very high temperatures (1200 ºC) and originating porosity values comparable to those of the non-calcined samples. Pore size distribution curves show that the most relevant contribution to the total sample porosity is in the region 0.1 - 1 µm (i.e., microporosity). Given that this microporosity may be essential for inductive bone formation, samples calcined at 600 ºC may be advantageous for the wanted composite, particularly if reduced to

particulate form. This strategy enables to obtain, simultaneously, macro and microporosity: inter-particle porosity, with pores around 100 μm, which is most convenient for bone remodeling, and microporosity from the isolate particles. Moreover, not surprisingly, as porosity decreases, the density values increase with the calcination temperature.

The IGC analyses of carbonated and non-carbonated bovine-derived hydroxyapatite reduced to particle form show that the high energy surface sites of both minerals have strong affinity towards strong Lewis base molecules. Furthermore, carbonated hydroxyapatite shows stronger interactions with Lewis acid molecules than non-carbonated apatite, suggesting that the former mineral may enhance protein adsorption and cell adhesion into the implanted biomaterial. The slight differences on the surface energetic parameters may be related to the carbonate content (confirmed by XPS), crystallinity and density of the analyzed particles. The hydroxyapatite surface characterization may be important regarding its reactivity in the synthesis of composites and in the context of the interactions with the biological environment, after *in vivo* implantation. The primary interactions between a material and its environment (reagent or biological host) occur on a molecular level and in a very narrow interfacial zone. Thus, surface properties may play a crucial role in ionic exchange dynamics and reactivity, in protein adsorption and in directing the biological properties of the material. Although the influence of the surface properties is clearly recognized, this complex matter is still insufficiently understood.

The outline regarding the selection of bone-derived hydroxyapatite points to bovine bone calcined at 600 ºC because it exhibits most promising properties regarding chemical composition and structure, as well as surface properties, combined with an economical practical implementation. As described, this mineral constitutes the most similar ceramic to the inorganic phase of the bone matrix. Bone calcination at 600 ºC originates a calcium-deficient carbonated hydroxyapatite that, in addition to carbonate, maintains trace amounts of other ions incorporated in the crystal structure. Its surface presents very strong affinity towards electron donors and moderate affinity towards electron acceptors and non-polar molecules, providing more favorable conditions for biological interactions than non-carbonated hydroxyapatite. Other characteristics as lower density, lower crystallinity and higher microporosity also contribute to the advantages of natural carbonated hydroxyapatite regarding its application in bone substitute materials.

Although it is expected that bone-derived hydroxyapatite is a better alternative to synthetic apatites regarding not only physical and chemical properties, but also protein adhesion and cellular events associated to bone metabolism, two synthetic apatite samples were also characterized. The obtained results regarding FTIR enable to confirm that Calcibon is a carbonated hydroxyapatite and Inbone, a non-carbonated apatite, as described by the supplier. The particle size distribution of each of these samples, accessed by LDS, shows that the former is broader and less homogeneous. The applied characterization techniques enabled to acquire some reference data for subsequent studies.

Barium sulphate was the second selected mineral component in this study, being necessary for providing radio-contrast to the composite. Since the use of a contrast agent for X-ray guidance in kyphoplasty is mandatory and this ceramic is widely used in medical practice due to its high contrast and low toxicity properties, the option for $BaSO_4$ finds good support for this specific application. The FTIR, XRD, LDS and SEM analysis of $BaSO_4$ enabled to obtain reference data for posterior comparison with other samples, namely with composites containing both hydroxyapatite and barium sulphate.

The procedure applied to dose the proportion of the selected minerals, bone-derived carbonated hydroxyapatite and barium sulphate, was based on the *in vitro* simulation of the X-ray guidance during kyphoplasty. The strategy consisted of using radiology to observe different ratios of hydroxyapatite and $BaSO_4$, inserted as mineral suspensions in PVA solutions, inside bone defects of animal vertebrae. The results show, as expected, that bone itself originates images with high contrast, bringing the attention for the necessity of using higher contrast materials to monitor the vertebral repair procedure. The radio-contrast properties of barium sulphate are evident, even when applied in concentrations as low as 10 wt% in PVA, being clearly detected inside the used vertebrae. However, higher concentrations are recommended (around 30 wt%) in order to obtain higher contrast. The contrast effect of hydroxyapatite can also be demonstrated by radiology. Although it is much less intense than that of $BaSO_4$, it has an additive effect in compositions containing both minerals. In fact, using different proportions of the selected minerals, the radiographs with higher contrast correspond to PVA suspensions containing 20 to 30wt% $BaSO_4$. As for the hydroxyapatite content, the best images combine the latter suspensions with at least 50 wt% bone mineral relative to the polymer solution.

The characterization of 1:1 mixtures of $BaSO_4$ and hydroxyapatite by FTIR and XRD enable to observe that the relative intensity of bone mineral peaks is, in both types

of spectra, rather inferior to those of barium sulphate. The obtained diffractograms are of particular interest, since they enable confirmation of the higher absorption coefficient of X-ray radiation of $BaSO_4$, compared to hydroxyapatite. This fact also justifies the greater radiologic contrast of $BaSO_4$ relative to the bone mineral and to the bone matrix, as observed in the radiology tests of filled and unfilled vertebrae.

5 Selection and characterization of organic components for the composite

5.1 Introduction

The selection of an organic matrix for the projected injectable composite containing bone-derived carbonated hydroxyapatite and barium sulphate was based on the search for alternatives to acrylic bone cements, such as those based on PMMA. This particular type of *in situ* forming hydrogel is the most currently applied in kyphoplasty despite several drawbacks associated with monomers toxicity, incomplete polymerization, temperature raise and excessive stiffness after the curing process. Moreover, since PMMA hydrogels are not biodegradable, they act merely as inert repair materials.

In this study, the search for an adequate polymer (or polymeric system) followed the standard requirements for biomaterials, previously described in Chapter 2. However, the specific applications for the final composite product implied the fulfillment of many additional conditions, as material questions related to the compatibility between the organic and inorganic phases of the composite and the rheological properties of the composition, which should harden *in situ* (inside a vertebral body, at body temperature) in an appropriate time-window. The chemical and structural properties of the solid composite should be tailored to enable, ideally, not only bone repair, but also bone regeneration. The composition should involve as least as possible manipulation at the operating room and should not oblige to significant changes in the methodology currently used in the vertebral surgery. With the purpose of avoiding the typical problems associated to PMMA and other analogous systems and, above all, aiming to obtain an innovative biomaterial, the acrylic-based systems were initially discarded from the range of possible options for the composite organic components.

In situ forming hydrogels, involving chemical or physical crosslinking reactions, have been widely used in biomedical applications being adequate for diverse minimally invasive procedures. In fact, this type of hydrogels can form in the body, near physiological conditions, from fluid precursors that, in order to be safe, should be non-toxic and preferably water soluble. In addition, the gelation reaction, which may be originated by different mechanisms, should not cause any toxicity or substantial temperature rise, too. Typically, gelation may derive from chemical or physical crosslinking between the hydrogel precursors, or from polymerization reactions initiated chemically or photo-chemically. However, for surgical procedures as kyphoplasty, photo-initiated mechanisms are not recommended because they present diverse technical and practical limitations. For vertebroplasty of kyphoplasty, the instrument used as source of radiation would have to be inserted inside the vertebral body, together with the injected

material. This option has been totally rejected not only because of the difficult control of the kinetics of the chemical reaction, but also because of contamination risks.

With the exception of acrylic-based systems, the general characteristics of *in situ* forming hydrogels were considered as most advantageous for this study. The precursors´ solutions could contain the selected ceramic particles (hydroxyapatite and barium sulphate) being initially supposed that these could be transported into the injection site (the vertebral body defect) without significant interactions with the crosslinking reactions between the hydrogel precursors. However, after testing numerous water-soluble polymers, both natural and synthetic, diverse constraints showed that the selection of an appropriate polymeric system was a serious challenge. The limitations were mostly caused from the mandatory inclusion of minerals to obtain a bioactive and radio-opaque composite. The need for a high mineral content derived from the objective to mimic the natural bone composition and to obtain an adequate contrast for x-ray imaging. Even when the crosslinking reaction between the precursors could occur in isolate polymeric systems, the addition of ceramic particles strongly affected the crosslinking reactions and gelation did not occur. In addition, many of the tested crosslinking reactions needed acid environments, but these caused the degradation of hydroxyapatite and the mutual interference inhibited the gelation process. Furthermore, the rheological properties of the suspensions of mineral particles in polymer solutions were also a limitation, particularly due to phase separation of those components.

Polyvinyl alcohol (PVA; Figure 5.1)) was considered as most promising for this study, being selected polymers (PVA80, PVA96 and PVA98) with different degrees of hydrolysis (80, 96 and 98%, respectively) and diverse molecular weight distributions (9000-10000 mol/g for PVA80, 85000-146000 g/mol for PVA96 and 13000-23000 g/mol for PVA98).

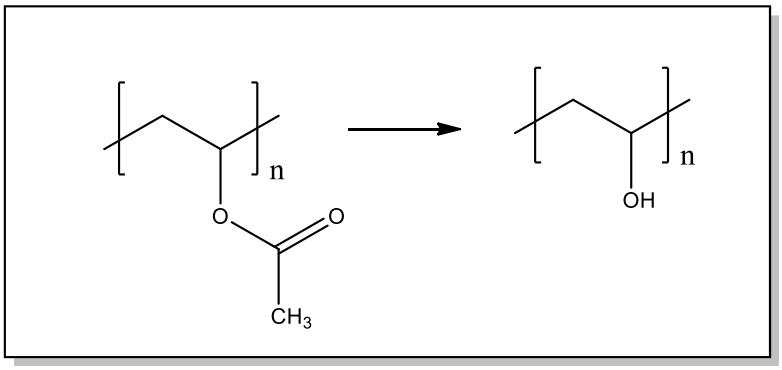

Figure 5.1 - Chemical structure of Poly (Vinyl Alcohol) (PVA; $[C_2H_4O]_n$), derived from the hydrolysis of Poly (Vinyl Acetate) (PVAc; $[C_4H_6O_2]_n$).

This chapter presents a general characterization of PVA, the main polymeric component for the composites of this study. It also describes two methods which were used to crosslink this polymer, in acidic and alkaline environments. The latter method motivated the encapsulation of the crosslinking agent, as a strategy to control the reaction rate. Thus, the synthesis of microcapsules is also described, being analyzed the effects of altering the ratios of their chemical composition on the morphostructural properties of these particles.

The techniques used to characterize PVA and PVA-based materials include rheology, FTIR, NMR (^{1}H and ^{13}C), DSC-TGA, DMTA, XRD, SEC and volumetric titration. On the other hand, the microcapsules characterization required the use of TGA, optical microscopy, SEM, LDS and Hg porosimetry. The experimental details about samples preparation for each instrumental technique are described in Chapter 9 unless those conditions are relevant to understand the respective results. The polymer samples were analyzed in powder form, as supplied, and all PVA solutions were prepared with distilled water or deuterated water (for NMR spectroscopy) at 80-90 ºC.

5.2 PVA characterization

Rheology

In order to evaluate the stability of mineral suspensions in PVA solutions, flow curve measurements were used to examine the rheological properties of PVA-based compositions, under changing shear stress and shear rate conditions, at 25 ºC.

The rheological study was conducted using a 10 wt% PVA96 aqueous solution, bone derived hydroxyapatite (HA Bov 600 from BC-2, sieved to 0.077-0.088 mm) and barium sulphate. Sodium Borate (also known as borax), a PVA crosslinker, was also tested in PVA solutions containing a mixture of minerals (hydroxyapatite and barium sulphate). The suspensions were previously prepared under magnetic stirring.

The used compositions are described in Table 5.1. Each mineral concentration is relative to the polymer solution weight and the crosslinked sample resulted from the addition of 2 ml of an aqueous solution of 3 wt% Borax to 10 ml of the described mineral mixture dispersed in PVA96 solution. The obtained results are presented in Figure 5.2 (shear stress *vs* shear rate) and in Figure 5.3 (viscosity *vs* shear rate). The viscosity values of each sample were determined from the slopes of the respective shear stress-shear rate curves.

Table 5.1 – PVA-based compositions used in the rheological tests.

	PVA96 (wt%)	HA Bov 600 (wt%)	$BaSO_4$ (wt%)
PVA	10	-	-
PVA+HA	10	20	-
PVA+$BaSO_4$	10	-	30
PVA+(HA+$BaSO_4$)	10	20	30
PVA+(HA+$BaSO_4$)+Borax	10	20	30

The shear stress-shear rate curves (Figure 5.2), obtained in the range 0-500 1/s, show that all the tested compositions except the PVA+(HA+$BaSO_4$)+Borax sample indicate a Newtonian behavior at the studied shear rate or shear stress. Moreover, the curves show the stress of the reference sample (PVA) is the lowest, but almost equal to that of PVA+HA. The samples composed of PVA+$BaSO_4$ and PVA+(HA+$BaSO_4$) originate similar curves, with intermediate stress values and finally, the crosslinked sample (PVA+(HA+$BaSO_4$)+Borax is that with higher stress values.

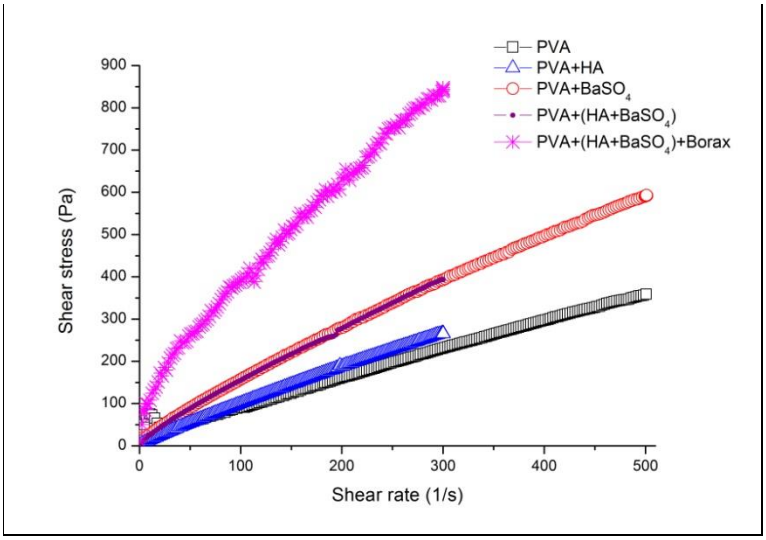

Figure 5.2 – Dependence of shear rate on shear stress for diverse suspensions of minerals (HA Bov 600 and $BaSO_4$,) in an aqueous solution of PVA96 (control sample). The addition of borax (PVA crosslinker) to a suspension containing both minerals was also monitored.

The viscosity curves presented in Figure 5.3 show that after a period of stabilization, all borax-free samples show an independence of the viscosity with shear rate. Measuring the obtained values at 300 1/s, the results show that the addition of 20% HA to PVA increases the polymer viscosity from 0.8 to 1.0 Pa.s and the addition of 30% $BaSO_4$, to 1.2 Pa.s. However, the viscosity of the mixture containing a similar ratio of these minerals is also 1.2 Pa.s. In this case, the increased amount of minerals does not affect the viscosity relative to the latter sample. As for the crosslinked PVA sample, also

containing a mixture of minerals, the viscosity is less stable and much higher (around 3.0 Pa.s) than that of the other samples.

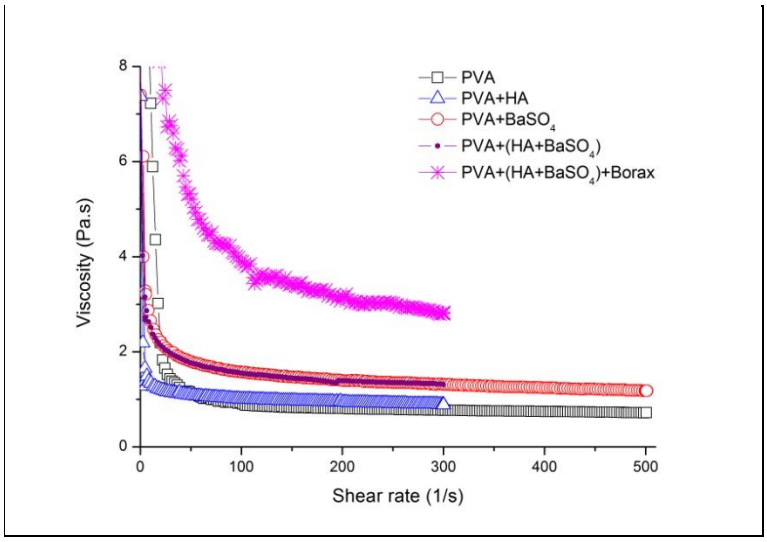

Figure 5.3 - Viscosity as a function of shear rate of diverse suspensions of minerals (HA Bov 600 and $BaSO_4$) in an aqueous solution of PVA96 (control sample). The addition of borax (PVA crosslinker) to a suspension containing both minerals was also monitored.

Similar tests using other concentrations of PVA80 (10, 20 and 30 wt%), and of PVA98 (10 and 20%), combined with equivalent amounts of minerals, showed that these compositions enable to obtain viscous homogeneous suspensions with Newtonian behavior at room temperature. The influence of the particle size of the minerals on the viscosity was not analyzed in this study.

FTIR

The vibrational spectra of PVA80, PVA96 and PVA98 are presented in Figure 5.4. The respective degrees of hydrolysis, 80, 96 and 98%, corresponding to different acetate contents, enable to make the distinction between the analyzed polymers.

All spectra show a similar profile regarding bands originated from the backbone structure of PVA but present some differences in the relative intensity of the bands from acetate vibrations. Thus, the spectral analysis may be divided into a group of skeletal vibrations and another relative to substituent vibrations. The assignments are summarized in Table 5.2.

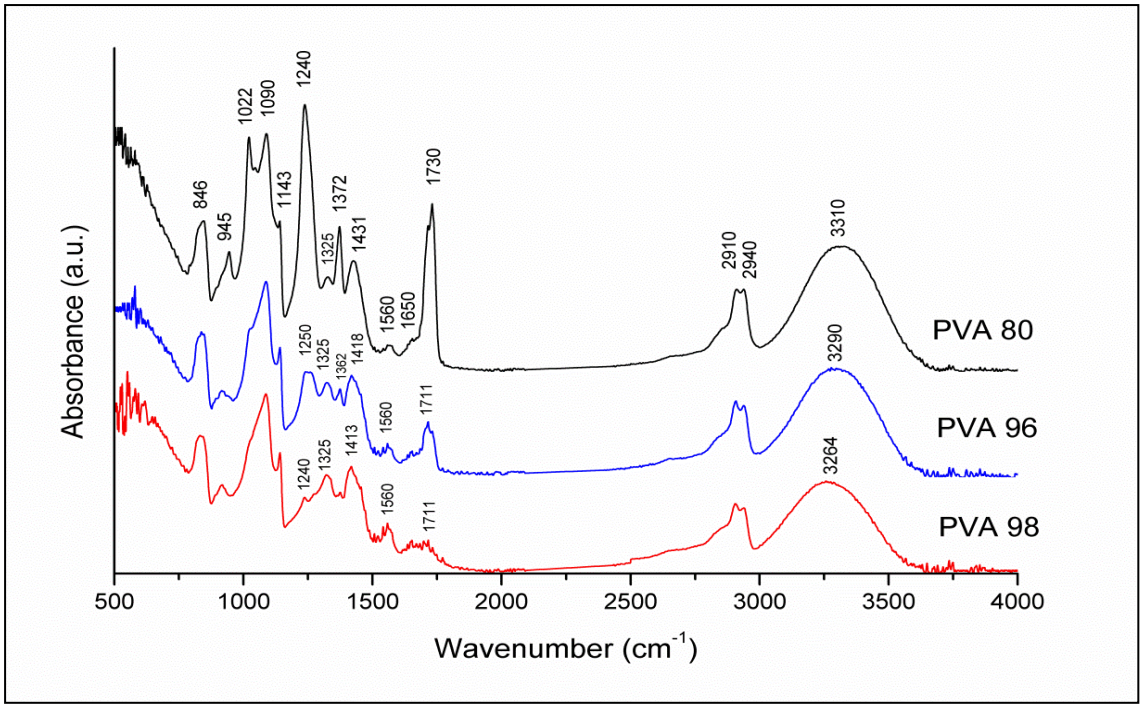

Figure 5.4 – FTIR spectra of PVA 80, PVA 96 and PVA 98.

The most significant bands from the backbone PVA structure, with various bands of medium (m) to very strong (vs) intensities occur in the 500-2000 cm^{-1} region, at 846 (ms), 945 (m), 1022 (s), 1090 (vs), 1143 (ms), 1325 (m), 1431 cm^{-1} (m). These bands are attributed to combined modes of C-C stretching +C-O-C in plane bending (at 846 cm^{-1}), CH_2 wagging (945 cm^{-1}), CH_2 twisting (1022 cm^{-1}), C-O stretching (1090 cm^{-1}), PVA crystallinity (1143 cm^{-1}), CH_2 symmetric deformation (1325 cm^{-1}) and CH_2 asymmetric deformation (1431 cm^{-1}) [135,154,180–182]. According to the literature, the band at 1143 cm^{-1} is influenced by the crystalline portion of the polymeric chains. This peak is related to the symmetric C–C stretching mode or stretching of the C–O of a portion of the chain where an intramolecular hydrogen bond is formed between two neighboring OH groups that are on the same side of the plane of the carbon chain. The ratio of band intensities at 1143 cm^{-1} and 1090 cm^{-1} band was found to be constant in all cases, leading to the conclusion that the different PVA samples have similar degree of crystallinity [135,138,154,180].

As for the substituent vibrations, these are clearly recognized in the spectrum of PVA80, since it contains the higher acetate content, and the respective bands have decreased intensities in the spectrum of PVA96 and even lower in that of PVA98. The intense peaks observed at 1240 (vs), 1372 (ms) and 1730 cm^{-1} (s) are characteristic of acetate C-O stretching vibrations, CH_3 asymmetric deformations and C=O stretching vibrations, respectively. As mentioned, these bands are more intense in the spectrum of PVA80 and less intense in that of PVA98, showing a variation proportional to the

concentration of acetate groups in the molecular structure. Interestingly, the peak at 1022 cm^{-1}, which is attributed to a characteristic backbone vibration (CH_2 twisting), is also more intense in the PVA80 spectrum than in the two other spectra wherein the respective bands are similar [135,138,154,180–182].

In the 2000-4000 cm^{-1} region, all PVA spectra present similar profiles with bands from C-H asymmetric stretching vibrations from CH_2 at 2910 cm^{-1}, and from CH_3 at 2940 cm^{-1}, as well as a broad band ranging from 3000 to 3500 cm^{-1} characteristic of OH stretching [135,138,154,180–182].

Table 5.2 – Vibrational modes associated to PVA80, PVA96 and PVA98.

Vibrational Mode	Wavenumber (cm^{-1})		
	PVA 80	PVA 96	PVA 98
C-C stretching+C-O-C bending	846	846	846
CH_2 wagging	945	945	945
CH_2 twisting	1022	1022	1022
C-O stretching	1090	1090	1090
crystalinity	1143	1143	1143
C-O stretching (acetate)	1240	1250	1240
CH_2 sym deformation	1325	1325	1325
CH_3 asym deformation (acetate)	1372	1372	-
CH_2 asym deformation	1431	1418	1413
C=O stretching (acetate)	1730	1711	1711
CH_2 asym stretching	2910	2910	2910
CH_3 asym stretching	2940	2940	2940
ν OH	3310	3290	3264

NMR

Proton and ^{13}C NMR spectroscopy was used to characterize PVA80 and PVA98, both dissolved in D_20 at adequate concentrations (around 20 mg/ml for ^{1}H spectra and 60 mg/ml for ^{13}C spectra). The spectra were registered at 25 ºC.

Figure 5.5 shows the ^{1}H spectra of PVA80 and PVA98, together with the general structural formula of PVA and assignments of the spectral signals (to proton groups represented as a, b and c). Both spectra have un identical broad peak around 3.8-4.0 ppm, and a group of peaks with similar profile at 1.4-1.9 ppm. The most evident difference between both spectra is the intense peak at 2.0 ppm in the spectrum of PVA80.

The peaks from methylene protons (-CH_2-; a) are observed in both spectra as a broad set in the range 1.4-1.7 ppm, with on intense peak at 1.7 ppm, and a separated sharp peak at 1.8 ppm. At 2.0 ppm, the intense signal observed in the spectrum of

PVA80 is attributed mostly to the methyl protons (-CH_3; c) of acetate. The terminal methyl groups of the backbone structure also contribute to this peak, as observed in the spectrum of PVA98 which peak at 2.0 ppm is much less intense. Finally, the methine protons (-CH-; b) originate an intense peak at 3.8-4.0 ppm in the spectra of both PVA samples [180] [183].

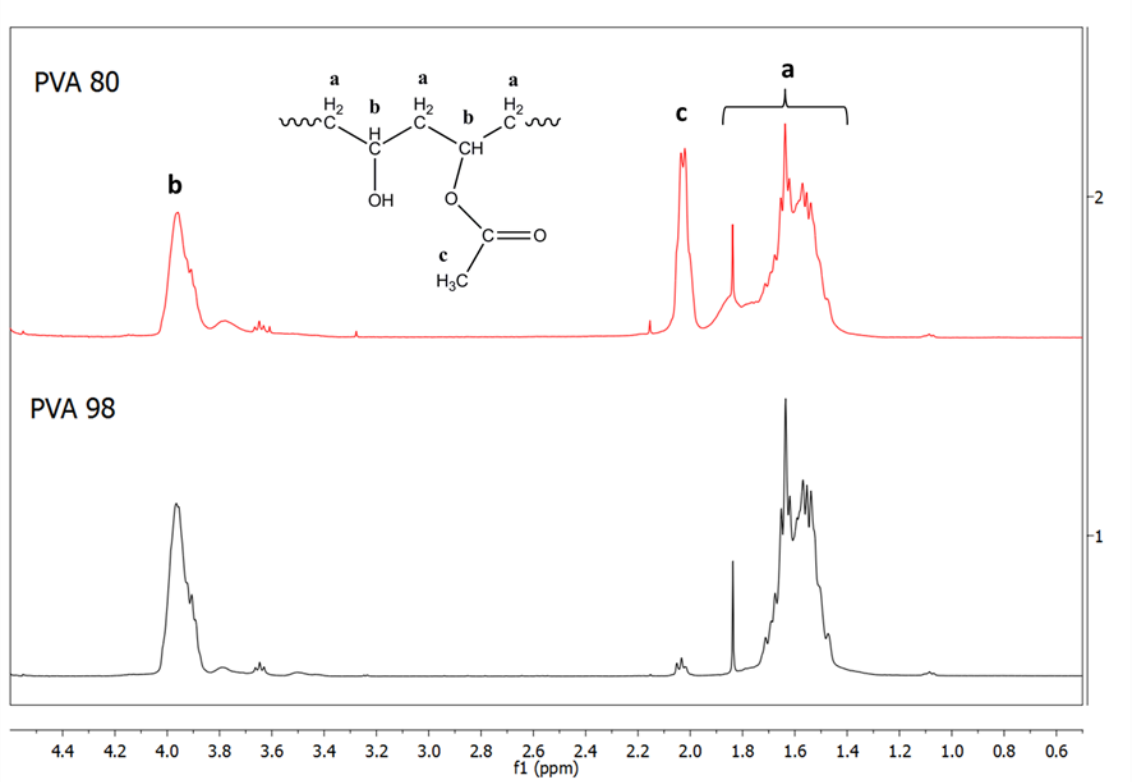

Figure 5.5 – Proton NMR spectra of PVA80 and PVA98.

The ^{13}C spectra of PVA80 and PVA98 illustrated in Figure 5.6 present similar peaks in three separate regions, being the carbon atoms represented as a-d. A singlet around 21 ppm assigned to methyl carbon (CH_3; d), a multiplet around 44 ppm assigned to methylene carbon (-CH_2-; a) and a triplet around 66 ppm assigned to methine carbon (-CH-; b). In addition, some characteristic peaks of acetate are observed in the PVA80 spectrum but are absent, or have extremely low intensity, in the PVA98 spectrum. These peaks occur at 38, 42 and 175 ppm, being the latter attributed to carbonyl (C=O; c) groups [183,184].

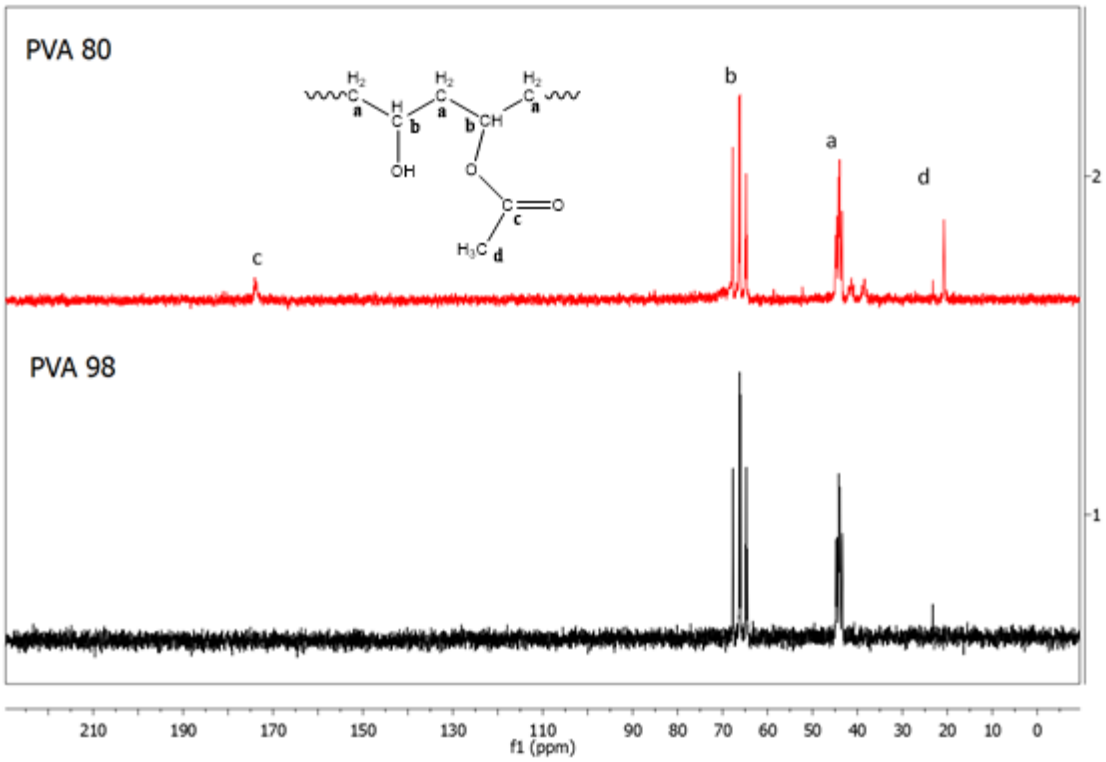

Figure 5.6 – Carbon-13 NMR spectra of PVA80 and PVA98.

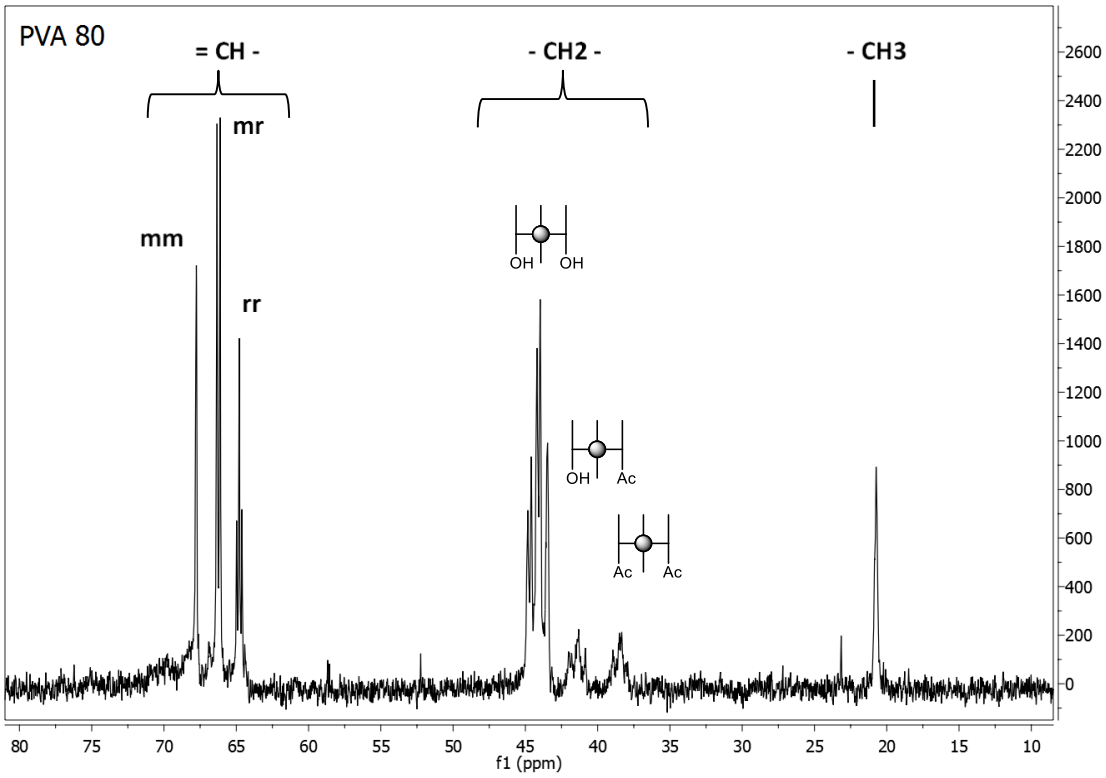

Figure 5.7 - – Detailed assignment of the methyl, methylene and methine peaks in the Carbon-13 NMR spectrum of PVA 80.

Since high resolution ^{13}C NMR spectroscopy can be used in the characterization of the tacticity of PVA, its copolymer composition, branching and co-monomer sequence distribution, the obtained ^{13}C spectra, although less sophisticated, were used to obtain additional information about the PVA samples. The spectra presented in Figure 5.6 were observed with greater detail, expanding the scale in the range 10-80 ppm. Given the similarities between diverse common peaks in both ^{13}C NMR spectra, only that of PVA80, which presents additional signals due to the higher acetate content, is presented in Figure 5.7. The common peaks to both samples show small differences in the relative intensity of some signals.

The detailed assignment of the ^{13}C spectrum of PVA80, based in the literature, is represented in Figure 5.7 where methine signals include the contribution of mm (67 ppm), mr (66 ppm) and rr (65 ppm) triads. The peaks in this triplet, each with a different intensity, show that PVA80 has an atatic structure composed of different proportions of isotatic (mm), heterotactic (mr) and syndiotactic (rr) triads. That proportion is different in PVA98, since its mm and rr signals have identical intensity. In both spectra the central triplet mr signal has the higher intensity [184][185][186].

On the other hand, the methylene signals of PVA80 are splitted according to the relative position of OH and acetate (Ac) groups. Whereas the multiplet around 44 ppm is originated by methylene carbons linked to two H-C-OH groups, the peak around 42 is originated by methylene linkages to H-C-OH and H-C-Ac groups and at 38 ppm, to two H-C-Ac groups. The relative intensity of these peaks shows the prevalence of the former type in PVA80. The absence of the 38 and 42 peaks in the spectrum of PVA98 is in good agreement with this interpretation [184][185][186].

Finally, the detailed assignment of the peaks in the 20-25 ppm region of the PVA80 spectrum may be discussed because in addition to the singlet peak at 21 ppm (which is not present in the PVA98 spectrum), another less intense singlet is observed at 24 ppm in the spectra of both PVA samples. Given that this spectral region is typical of methyl carbon signals, the peaks at 21 and 24 ppm may be respectively attributed to methyl groups in acetate fragments and terminal methyl groups in PVA backbone [184][185][186]. However, the intensity of the latter may be very low or undetectable, particularly in molecular chains with high molecular weight, as polymers. In that case, the signal at 24 ppm may be attributed to impurities in solution.

DSC-TGA

The thermal behavior of PVA80, PVA96 and PVA98 was accessed by simultaneous DSC and TG analysis in the 25-600 ºC range of temperatures (Figure 5.8). Samples were heated at a rate of 10ºC/min, under inert atmosphere. The DSC curve from PVA96 is not displayed to facilitate the graph reading.

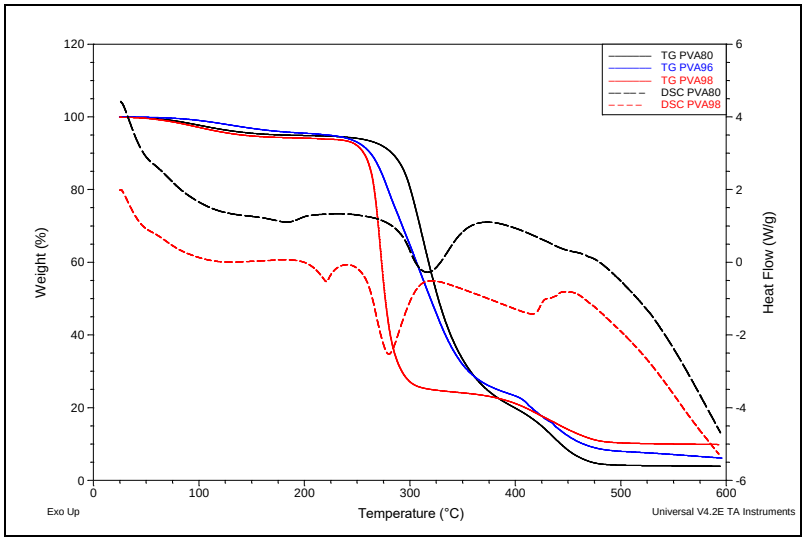

Figure 5.8 – Thermal analysis of PVA80, PVA 96 and PVA 98.

The mass variation with temperature evidences that after a small loss (2-5 wt%, at around 100 ºC) due to water entrapment, all polymer samples show a degradation process that occurs in two main steps. Most of the mass loss (around 70 wt%) occurs between 250 and 380 ºC, followed by an additional smaller loss (inferior to 20 wt%) between 380 and 480 ºC.

As indicated by the DSC profiles, all the samples follow an endothermic process and the rate of the first degradation process reaches the maximum at different temperatures for each polymer: 280 ºC for PVA98, 300 ºC for PVA80 and 320 ºC for PVA96. The mass loss, however, is similar for the different samples, reaching 70-80% of the initial weight. The second degradation step occurs at approximately 420 ºC for all the samples, originating non-volatile residues weighting 5 to 10% of the initial mass of PVA80 and PVA98, respectively. The residue of PVA96 has an intermediate value. According to the literature, the degradation starts with the elimination of polymer side-chains at lower temperatures, followed by the breakdown of the polymer backbone at higher temperatures [59][187][188]. This interpretation agrees with the fact that PVA98, which has the lowest content of acetate side-chains, is the sample that starts degrading at the lowest temperature. PVA 80, with the larger acetate content starts degrading at the higher temperature and PVA 96 has an intermediate behavior.

In addition to the temperatures of degradation, the heat flow profiles of PVA80 and PVA98 enable to determine the temperature of physical processes, namely the glass transition (T_g) and melting (T_m) of these polymers. The direct reading of the DSC profile enabled to determine T_m but T_g required the derivative of the curve to determine this parameter. Whereas both samples have T_g around 50 ºC, T_m is around 190 ºC for PVA80 and 220 ºC for PVA98 [59][187][188]. This derives from increased inter-molecular attraction forces in PVA98. The area of the respective melting peaks shows that PVA80 is less crystalline than PVA98, agreeing well with the theoretical prediction of lower structural organization for the most substituted carbon chains [59][187][188].

DMTA

Dynamic Mechanical and Thermal Analysis (DMTA) was essentially used to determine the glass transition temperature (T_g) of PVA98, tested in single cantilever mode. This technique enables to measure the storage modulus (E´; absorbed energy) and the loss modulus (E´´; dissipated energy) which represent the elastic and viscous portions of the energy involved in the samples mechanical testing at different temperatures. Typically, at the glass transition, the storage modulus decreases dramatically, and the loss modulus reaches a maximum. Thus, tan δ, calculated from the E´´/E´ ratio, enables to determine T_g with high accuracy. This technique is known to possess higher sensitivity than the DSC method.

An aqueous solution of 20 wt% PVA98 was casted into the sample holder (a cantilever) and dried at 37 ºC until constant weight. The resulting film was subsequently analyzed at a heating rate of 5 ºC/min in the -250 to 250 ºC range of temperatures, at constant frequencies of 1 and 10 Hz.

The DMTA graphics presented in Figure 5.9 correspond to results obtained at 1 Hz. The curve relative to tan δ enables to determine that the glass transition temperature of PVA98 is precisely 39.9 ºC. Moreover, the transition detected at around 223 ºC corresponds to the thermal degradation of this polymer, as expected from the respective DSC-TGA results.

The fact that the value of T_g is not equal to that from DSC may be because of the preparation of the sample as a dried film for the DMTA analysis. The polymer, in the as supplied powder form, could not be analyzed with this technique. The preparation of the PVA film requires the use of hot water to dissolve the polymer, followed by a drying process, and both may affect the molecular structure of the polymer (particularly its crystalline degree). Thus, the rearrangement of the polymer chains may alter the

amorphous domains of the polymer and influence the glass transition temperature. The comparison with the literature shows that the obtained values are meaningful [103][123][189].

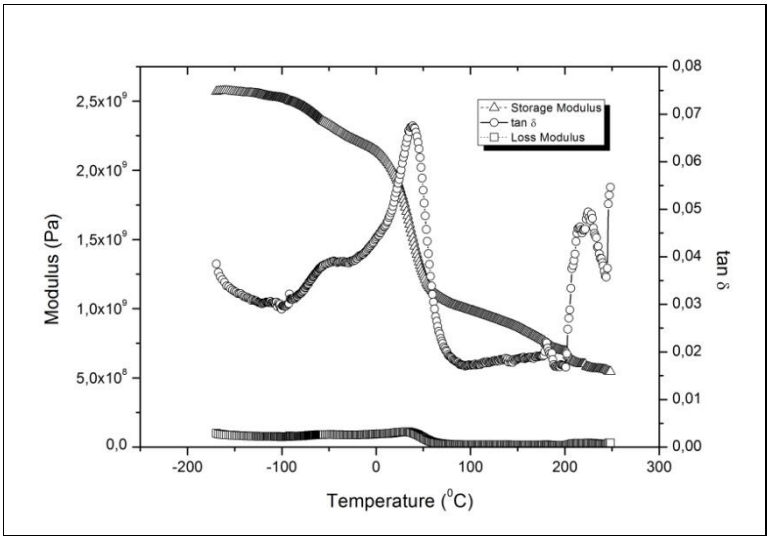

Figure 5.9 – DMTA graphics of PVA 98, representing the storage modulus, the loss modulus and tan δ, obtained at the frequency of 1 Hz.

The results corresponding to 10 Hz are not presented since the obtained curves are only slightly deviated from those obtained at 1 Hz, as typically occurs in these tests.

XRD

X-ray diffraction spectroscopy was used to obtain the characteristic diffractogram of PVA98, a reference sample for other phases of this study. The sample was analyzed in powder form, as received. The diffractogram is presented in Figure 5.10.

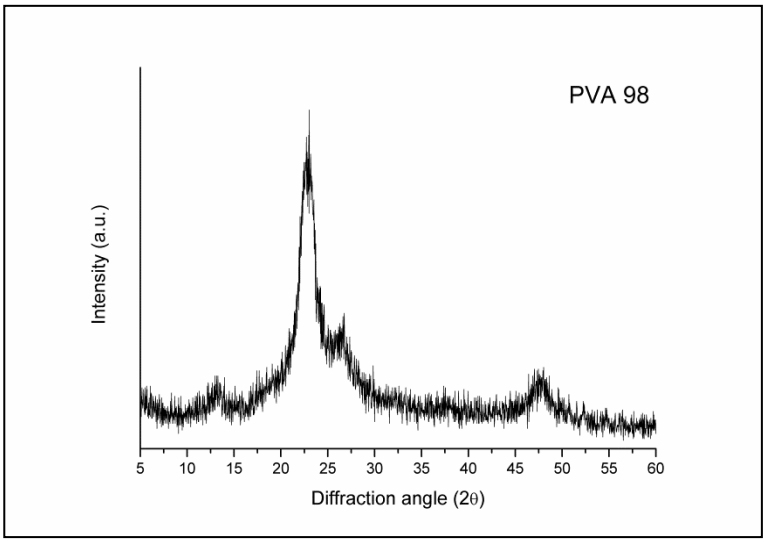

Figure 5.10 - Diffractogram of as-received (powder form) PVA98.

The broad peaks observed in the x-ray diffraction pattern (Figure 5.10) of as-received PVA98 shows that this polymer is, as expected, semi-crystalline. It exhibits an intense peak at 2θ=22.7º and less intense peaks at 2θ=13.0, 26.3 and 47.6º, being all four peaks attributed to the crystalline regions of the polymer structure. The obtained profile is similar to those found in the literature, relative to PVA samples with similar degree of hydrolysis and molecular weight [190][191].

The semi-crystalline structure justifies the thermal transitions detected using DSC. The amorphous part is associated with the glass transition and the crystalline fraction, with the melting of the polymer.

5.2.1 Crosslinking PVA in acidic medium

One of the most described methods to crosslink PVA and other water-soluble polymers containing OH groups is based on the use of dialdehydes such as glyoxal or glutaraldehyde [39,136,151,180,192–194]. However, in order to establish the crosslinking reaction, rather drastic conditions must be applied, such as high temperature (around 80 ºC) and low pH (around pH=4). In addition, these conventional crosslinkers are highly toxic even at low concentrations, motivating the use of alternative molecules to enable safer *in vivo* applications.

5.2.1.1 Procedure - PVA and telechelic PVA

In this study, the strategy applied to crosslink PVA was based on the same mechanism of glutaraldehyde, but this crosslinker molecule was replaced by telechelic-PVA, which is also a dialdehyde. It can be synthesized from the selective oxidation of adjacent diol groups of PVA with sodium periodate. Then, the crosslinking reaction can occur between PVA and telechelic-PVA, thus eliminating the use of a toxic crosslinker.

As previously described, PVA presents scarce (but detectable) 1,2-glycol units randomly distributed along the molecular structure, mostly composed of 1,3-glycol units. The amount of head-to-head sequences which is normally few percent relative to largely predominant head-to-tail sequences, may be determined by acidimetric titration, [140,195,196]. The presence of structural “errors” in the atatic structure of PVA enables the molecular splitting of the polymer chains through oxidation with sodium periodate, in correspondence to the diol goups of PVA (Figure 5.11). The resulting telechelic-PVA

segments bear, at each end, aldehyde groups that may be employed to form acetals (after reaction with –OH groups) or Schiff bases (after reaction with primary amines) [135,136,140,154,195]. In the reaction of PVA with telechelic-PVA, the crosslinking occurs through acetal bridges, as illustrated in Figure 5.12.

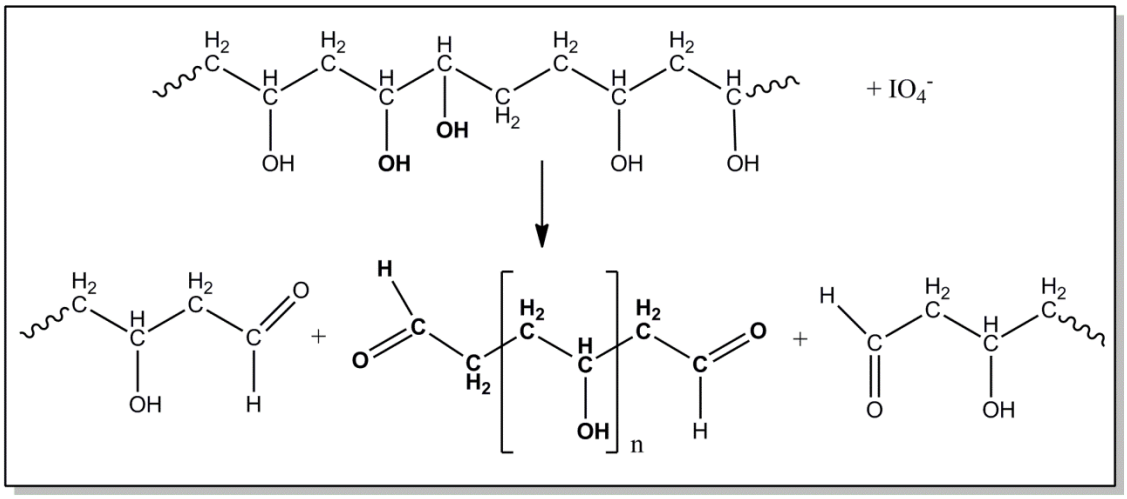

Figure 5.11 - Oxidation of PVA with sodium periodate, leading to the formation of telechelic-PVA.

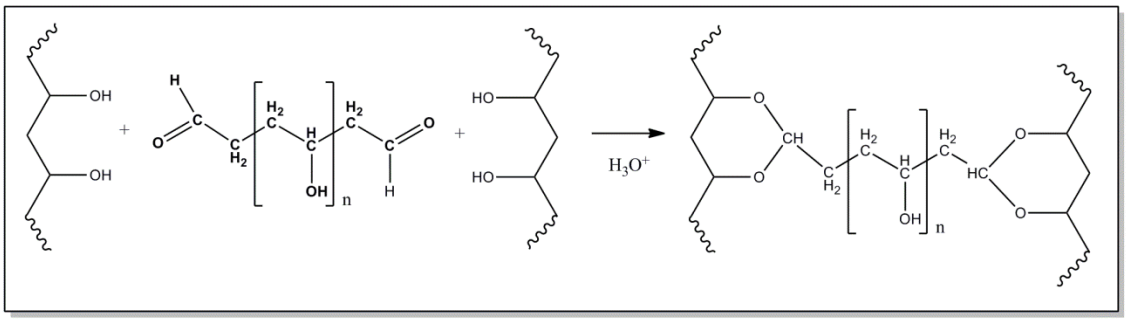

Figure 5.12 - Crosslinking reaction between PVA and telechelic-PVA with formation of acetal bridges.

In order to obtain PVA crosslinked with telechelic-PVA, the selected polymers have been PVA80 and PVA98. Each sample was oxidized to obtain tel-PVA80 and tel-PVA98, to apply in the reaction with the respective starting polymer. The oxidation reaction involved the use of sodium metaperiodate ($NaIO_4$). Its aqueous solutions were freshly prepared and protected from light due to the photosensitivity of iodine. The 1,2-glycol (or adjacent diol) groups content of PVA was determined to estimate the necessary amount of $NaIO_4$ for the oxidation reaction.

5.2.1.2 Characterization – PVA and telechelic-PVA

Acidimetric determination of 1,2-glycol units of PVA

Following a method described in the literature [196], the adjacent diol groups of PVA were determined by volumetric titration with NaOH after hydrolysis with $NaIO_4$. The experimental conditions were similar for both polymers, regardless the different hydrolysis degree from PVA80 and PVA98. The respective molecular weight was taken as approximately 10.000 and 20.000 g/mol, respectively. The values from the technical report of the suppliers is 9.000-10.000 g/mol for PVA80 and 13.000-23.000g/mol for PVA98.

Each PVA sample was dissolved in distilled water at 80-90 ºC at a concentration of 10 wt%. This corresponds to 0.01 M for PVA80 and 0.005 M for PVA98. After complete dissolution, 10 ml of 0.1 M $NaIO_4$ were added to aliquots of 10 ml of PVA80 and aliquots of 5 ml of PVA98. This enabled to have 1.0 g of PVA80 and 0.5 g of PVA98 for each test. The oxidation reaction proceeded for 24 hours, after which triplicate analysis by titration with NaOH 0.1 M using thymol blue indicator (0.1 wt% in ethanol solution) was performed. Three blank samples composed of 10 ml distilled water were also prepared and 10 ml of $NaIO_4$ 0.1 M were added to obtain the reference for the titration.

The spent volume of NaOH for the blank solutions has been, in average, equal to 10.0 ml. For the polymer samples, the volume of NaOH has been, in average, equal to 7.1 ml for PVA80 and equal to 8.2 ml for PVA98. The number of mili Equivalents/gram (mEq) can be calculated from Equation 5.1, where a is the volume of NaOH solution for the sample, b is the volume of NaOH solution for the blank, N is the concentration of the NaOH solution and c is the mass of the sample.

$$mEq = \frac{(b-a)*N}{c} \qquad \text{Equation 5.1}$$

The calculations for the analyzed polymers correspond to (10.0-7.1)x0.1/1.0 and (10.0-8.2)x0.1/0.5, resulting in 0.29 mEq/g for PVA80 and 0.36 mEq/g for PVA98.

Converting this information into the most usual units of concentration, the obtained values enable to estimate the molecular weight of the fragments, being the vast majority composed of telechelic PVA. The exception are the head-to-tail fragments.

The results regarding PVA80 mean that it has 0.00029 moles of vicinal OH groups per gram of polymer, or around 3 moles of diol per 10.000 g (1 mole) of polymer. The oxidation of 1 mole of PVA80 may disrupt the structure in 3 sites and produce 5 fragments with an average molecular weight of around 2000 g/mol.

For PVA98, the 0.00036 moles of diol groups per gram of polymer correspond to 3,6 moles of diol per 10.000 g (0.5 mole) of polymer (or around 7 moles of diol per 20.000 g (1 mole) of PVA98). One mole of PVA98 can be divided in 7 sites, originating 9 fragments with an average molecular weight of around 2200 g/mole.

These results evidence that both PVA polymers possess a similar backbone structure regarding the concentration of adjacent hydroxyl groups.

Synthesis of telechelic-PVA

After the determination of the 1,2 glicol content for each PVA polymer, tel-PVA80 and tel-PVA98 were prepared using adequate molar ratios of $NaIO_4$. Both PVA samples were dissolved with hot distilled water. After cooling, $NaIO_4$ was added up to a molar ratio of 1,2-glycol/$NaIO_4$ equal to 1.5, as recommended in the literature [140][195]. The oxidation reaction took 24 hours and the obtained products were submitted to dialysis against water for three days, using a membrane with cut-off of 300 g/mol. Subsequently, the solution was freeze dried to extract the solvent.

Size Exclusion Chromatography (SEC)

This technique is usually applied to evaluate the size and the molecular weight of large molecules, such as proteins or industrial polymers, in solution. The method consists of passing the solution of the sample through a chromatographic column packed with fine and porous beads, leading to the separation of sample fractions according to their size and time to pass through the stationary phase, since smaller molecules become retained in the column for a longer time period than larger molecules. The pore sizes of these beads and the sample volume that is eluted are used to estimate the dimensions of macromolecules. The molecular weight of a sample may be determined from the analysis of standard solutions of molecules with known molecular weight, applied in the plot of a calibration curve.

From the calibration curve of molecules dissolved with an adequate eluent, SEC enables to determine the number-average molecular weight (Mn) and the weight average molecular weight (Mw) of macromolecules. While Mn represents the statistical average weight of all the chains in a sample, Mw considers the molecular weight of a chain in determining contributions to the molecular weight average. The more massive the chain, the more it contributes to Mw. The ratio Mw/Mn is the Polydispersivity Index

(PI), which is a measure of the width of the distribution. Good quality standards for SEC calibration must have PI values close to the unit.

In this study, SEC was used to evaluate the molecular weight distribution of the PVA samples before and after oxidation with $NaIO_4$. This had the objective of comparing the results with the technical data from the suppliers, and also with the values estimated from the acidimetric determination of the diol groups of PVA.

The analyzed samples have been PVA80, PVA98, telechelic-PVA80 and telechelic-PVA98, being these obtained after oxidation, dialysis and freeze drying. The standards for the calibration curve have been polyethyleneglycol (PEG) solutions, prepared from polymers with molecular weight of 2.000, 6.000, 12.000 and 300.000 g/mol. The solvent has been the same liquid that is normally used as eluent and the samples were filtered before injection into the equipment. The PVA samples were prepared in a similar way, using concentrations of 5 mg/ml.

This technique records the retention time of the sample along its passage through the chromatographic column. Samples with lower molecular weight become entrapped first in the column, thus those with higher molecular weight arrive sooner to the detector of the equipment. The calibration curve drawn from the retention time of PEG standard solutions of sharp molecular weight distribution has been used to establish the comparison with the samples under analysis. The obtained results are summarized in Table 5.3.

Table 5.3 – Molecular weight parameters of PVA80 and PVA98 obtained by SEC, before and after oxidation (telechelic fragments: tel-PVA80 and tel-PVA98).)

	Mw (mol/g)	Mn (mol/g)	PI
PVA80	16000	4200	3.8
PVA98	18000	6900	2.6
tel-PVA80	2800	1200	2.3
tel-PVA98	2900	1400	2.1

The results from PVA80 and tel-PVA80 are represented in Figure 5.13, together with the calibration curve from PEG standards. The retention time of PVA80 was 8.1 s and from tel-PVA80 was 9.2 s, corresponding respectively to Mw=16000 and 2800 g/mol. The values of Mn were 4200 and 1200 g/mol, resulting in PI= 3.8 for PVA80 and PI= 2.3 for tel-PVA80.

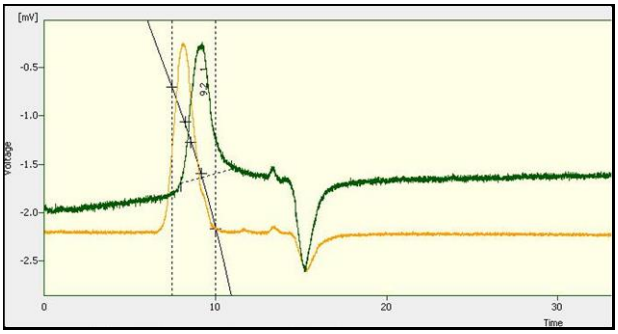

Figure 5.13 – SEC analysis of PVA80 as received (orange) and oxidized with $NaIO_4$ (green).

As for PVA98 and tel-PVA98, the results are displayed in Figure 5.14. The retention time of PVA98 was 7.9 s and from tel-PVA98 was 9.1 s, corresponding to Mw=18000 and 2900 g/mol, respectively. The values of Mn were 6900 and 1400 g/mol, resulting in PI= 2.6 for PVA98 and PI= 2.1 for tel-PVA98.

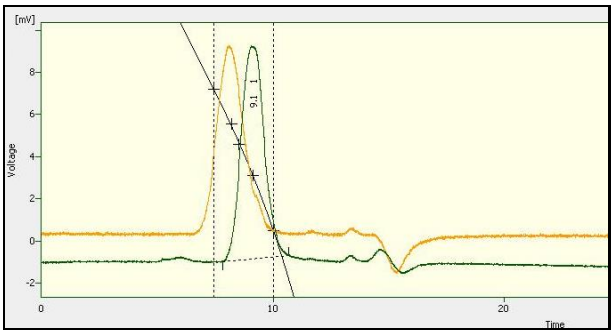

Figure 5.14 - SEC analysis of PVA98 as received (orange) and oxidized with $NaIO_4$ (green).

Despite the values of the molecular weight of the polymers before oxidation were not coincident with those from the technical data, they corresponded to the expected range. The experimental value for PVA80 (16.000 g/mol) was higher, and that for PVA98 (18.000 g/mol) was lower, than the respective described values of 9.000-10.000 g/mol and 18.000-23.000 g/mol. The value obtained for the oxidized sample of PVA80, tel-PVA80 with 2800 g/mol, was very close to the estimated from the titration (2000 g/mol). For tel-PVA98, the obtained value (2900 g/mol) was also close to that previously estimated (2200 g/mol).

The polydispersivity index of the samples indicates that the width of the molecular weight distribution of PVA80 is broader than that of PVA98, but not as significant as could be expected from the technical sheet from the suppliers. The oxidized samples, on the other hand, present sharper distributions that are similar for both polymers. This

shows that the telechelic fragments had identical structures whether they were obtained from PVA80 or PVA98.

Carbon-13 NMR

In order to confirm the chemical composition of telechelic PVA, samples of tel-PVA80 and tel-PVA98 were analyzed by NMR spectroscopy. The Carbon-13 spectrum of tel-PVA80 (Figure 5.15) is representative of the obtained results.

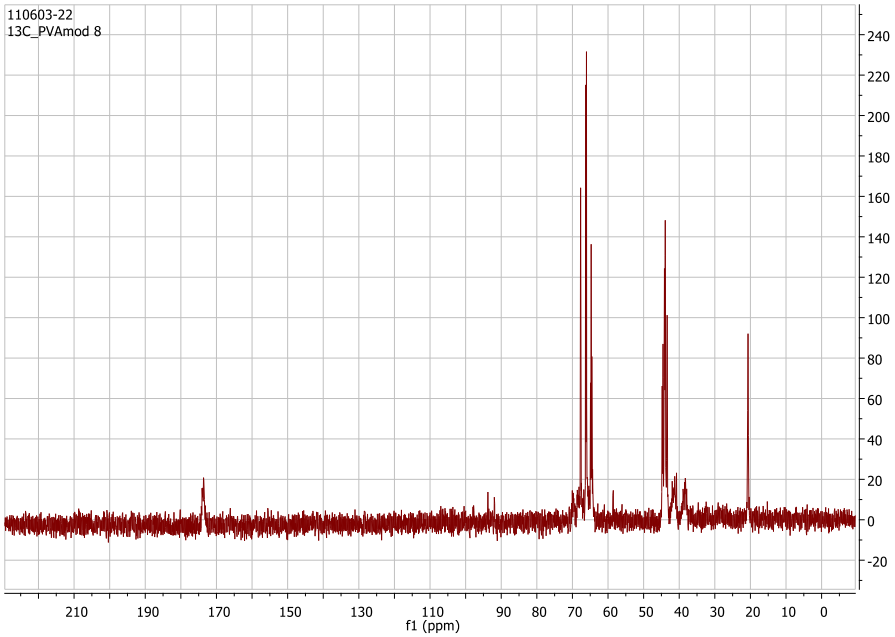

Figure 5.15 – Carbon-13 NMR spectrum of telechelic PVA80.

Although NMR spectroscopy is usually adequate to determine small differences in the chemical composition or structure of the molecules, in this case the spectrum is coincident with that from the non-oxidized sample (Figures 5.6 and 5.7). The same happened with the spectrum of tel-PVA98 (not shown). The expected difference between the spectrum of PVA before and after oxidation would be in the relative intensity of the carbonyl (C=O) chemical shift (around 175 ppm) because the telechelic form of PVA contains additional carbonyl groups relative to the original polymers.

Crosslinking reaction between PVA and telechelic PVA

As described previously, the crosslinking reaction was projected to be made with two combined forms of PVA: PVA80 crosslinked with tel-PVA80 and PVA98 crosslinked

with tel-PVA98. The general procedure was similar to that of glyoxal (or glutaraldeyde), being this crosslinker replaced by tel-PVA. The reagents were prepared as solutions of appropriate concentrations and the reactions were made at temperatures from 25 to 60 ºC, at pH 4-6.

Although diverse experimental conditions were tested, the results did not correspond to the objectives. The only way to obtain a crosslinked material, insoluble in water, has been after solvent extraction (by drying or freeze-drying). It was never possible to obtain a hydrogel with adequate characteristics for this study. Moreover, with the addition of ceramic particles, hydroxyapatite and barium sulphate, the blended materials did not show any evolution towards the solidification of the organic components. The crosslinking reaction may have been stopped by the steric hindrance, along with the alkaline environment caused by those minerals.

Since these crosslinking experiments were unsuccessful to comply with a composite able to harden in situ, inside a vertebral body, the results concerning the chemical characterization of the diverse obtained products are not presented. Despite all, the described set experiments were useful to learn more about the properties of PVA, the polymer that has been selected to constitute the main organic component of the composite matrix.

5.2.2 Crosslinking PVA in alkaline medium

5.2.2.1 Procedure

The use of sodium borate, or borax ($Na_2B_4O_7.10H_2O$), to crosslink PVA is probably the most well-known process to obtain a hydrogel from this polymer [193,197–200]. Borax is the salt of a strong base and a weak acid. In water, it hydrolyzes to form a boric acid-borate buffer with pKa=9.2, the equilibrium of which is expressed by Equation 5.3.

$$B(OH)_3 + 2H_2O \rightarrow B(OH)_4^- + H_3O^+ \qquad \text{Equation 5.3}$$

The chemical reaction with PVA is normally represented as shown in Figure 5.16, but the mechanism and chemical structure of the crosslinked material depends of many factors, as the tacticity PVA, the concentration of the reagents in solution, the temperature and the reaction time [193,197–201].

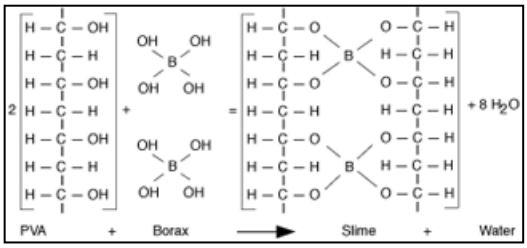

Figure 5.16 – Simplified representation of the crosslinking reaction of PVA with Borax.

In this study, PVA of different hydrolysis degrees (80, 96 and 98%) were prepared with concentrations ranging from 10 to 20 wt% with distilled water at 80 ºC using magnetic stirring. The selection of this range of concentrations is related to the need of having a polymer solution with high viscosity, able to support a high content of minerals.

The polymer powder was slowly added to the hot water to dissolve it gradually and prevent clumping. The dissolution took up to 4 hours to get a homogeneous viscous solution. Independently, borax was dissolved to obtain a stock solution with concentration of 0.1M.

For each PVA solution, the crosslinking reactions were performed using a matrix of diverse combinations of concentrations of reagents. For instance, 1 ml of borax 0.01 M -0.1 M solution was added to 10 ml solution of PVA98 at 10 wt%, being the reagents mixed mechanically because of the dramatic increase in viscosity as borax was impregnated into the PVA structure. Soon after mixing the reagents, a strong gel was always obtained. After diverse experiments, it became perceptible that the interaction between borax and the polymer provoked the instantaneous gelation of the contact site, even with a slow dropwise addition and very low borax concentrations. It was also evident that crosslinking was reversible because the hydrogel could be easily disrupted by the addition of water. This observation agrees with the interpretation that this crosslinking reaction is mostly a physical interaction involving hydrogen bridges with the water molecules in solution (Figure 5.17) [141,198–200,202]. Moreover, after drying the hydrogel, the subsequent addition of water caused the dissolution of the polymer instead of its swelling due to rehydration, as could be expected if the initial tridimensional derived from strong covalent bonds [127,141,198–200,202].

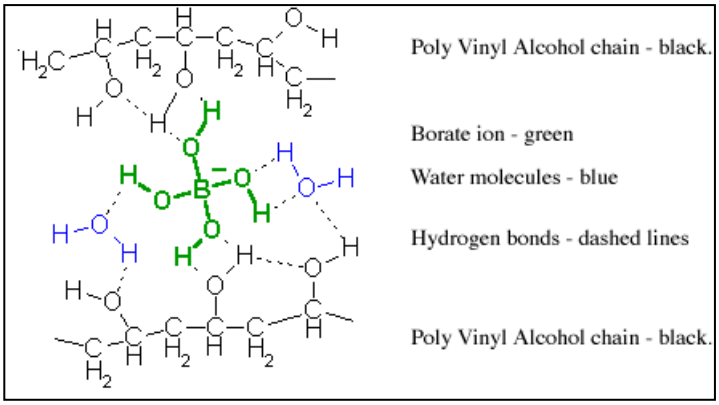

Figure 5.17 – Hydrogen bonding in the complex PVA-Borax in aqueous solution.

5.2.2.2 Characterization

FTIR

In order to investigate the chemical composition of the material obtained from crosslinking between PVA and borax, some of the obtained hydrogels were analyzed using FTIR spectroscopy. The samples were dried before analysis or else the spectra would only detect water. Figure 5.18 displays the spectra of PVA96, borax and a dried PVA96-borax hydrogel.

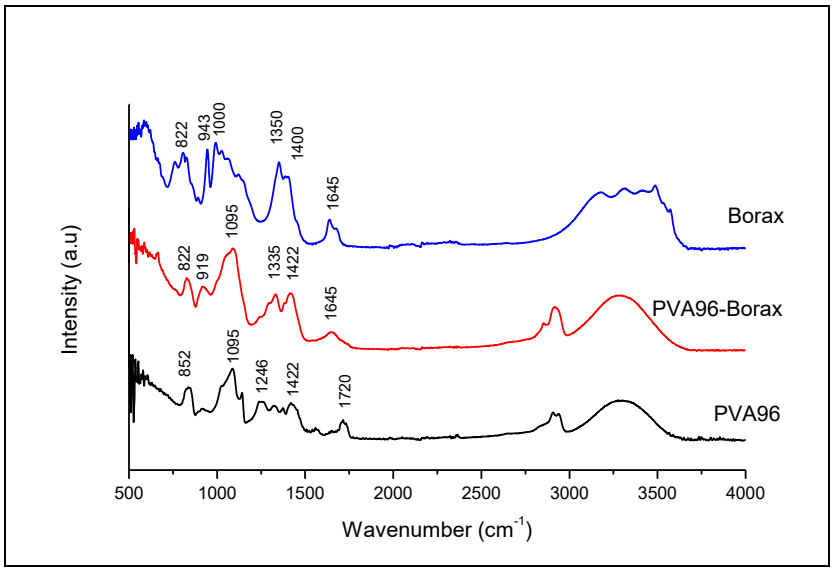

Figure 5.18 – FTIR spectra of PVA96, Borax and a PVA-Borax hydrogel.

The absorption bands in this spectrum of PVA96 (Figure 5.18) present some shifts relative to the spectrum of Figure 5.4, probably because of the sample preparation

method associated with instrumental variations. These shifts do not affect, however, the general profile of the spectrum nor the assignments of the vibrational modes. Thus, only the most intense peaks will be described in this analysis. The band at 846 cm^{-1} is originated by the combination of C-C stretching with C-O-C bending and the most intense band that occurs at 1095 cm^{-1} is due to C-O stretching, being both from the backbone of PVA. The C-O stretching mode from the pending acetate groups band gives rise to the band at 1246 cm^{-1}. The asymmetric deformation of the alkyl CH_2 groups is attributed to the band at 1446 cm^{-1}. The typical C=O stretching vibration from acetate originates the band at 1720 cm^{-1}. In the range 2000-4000 cm^{-1}, the spectrum presents a characteristic profile with bands at 2910 and 2940 cm^{-1} from CH_2 and CH_3 asymmetric stretching, and a broad band centered around 3300 cm^{-1} from OH stretching vibrations.

The Borax spectrum presents strong absorption bands with peaks at 822, 943, 1000 cm^{-1}, and in the region of 1300 to 1400 cm^{-1}. It also contains a weak intensity band at 1645 cm^{-1} and a broad band in the hydroxyl region 3000-4000 cm^{-1}, being both due to the water molecules in the mineral structure. These bands are attributed to H-O-H bending and OH stretching, respectively.

The assignment of the Borax spectrum is probably more complex than it could be expected. Boron may exist in its tetrahedral or triangular planar configuration, originating different B-O vibrations. These are also influenced by the water molecules that hydrate the mineral. Borax loses water in dry air and that can change the spectrum slightly. In addition, the coordination of hydrated borates with different atoms (Na, K, Ca, Mg, Sr,…) originates a wide range of minerals with corresponding spectral variations. All these variables explain why the spectral assignment of hydrated borates must be done with caution. The hydration of the borate anions can produce spectra which cannot be interpreted readily from a knowledge of the spectra of the corresponding anhydrous anion [203].

Comparing with the literature, the spectrum of the Borax sample of this study is similar to that of pinnoite $Mg[B_2O(OH)_6]$ where the bands at 800-1000 cm^{-1} are ascribed to asymmetrical vibrations from the BO_4 tetrahedral units and above 1100 cm^{-1}, from distortion modes originated by triangular BO_3 units [198,203].

As for the crosslinked material, PVA96-Borax, the obtained spectrum reveals some differences relative to the starting polymeric sample of PVA96. There is a new

band at 919 cm^{-1}, the band at 1246 cm^{-1} has lower relative intensity and that at 1720 cm^{-1} is no longer observed. Some bands clearly from Borax contribution originate an increase in the relative intensity of the bands at 1335 and 1442 cm^{-1} and a new band at 1645 cm^{-1} in the PVA96-Borax sample.

The absence (or low intensity) of the C=O and C-O stretching bands (1720 and 1246 cm^{-1}) from acetate indicates that these groups are not present in the crosslinked sample. On the other hand, the presence of bands from Borax that are overlapped with bands from PVA96 does not provide new information regarding the chemistry of the obtained hydrogel. The new vibrational band at 919 cm^{-1} may be due to the formation of a new bond or may be just a shift from the band at 943 cm^{-1} from Borax because the mineral was dissolved with water, and subsequently dried after forming the hydrogel. In solution, Borax totally dissociates into equal quantities of boric acid [$B(OH)_3$], borate ion [$B(OH)_4^-$] and Na^+, and it is well known that the hydration state and the geometry of the molecules have strong influence in their vibrational spectra [193,198,199,203]. Finally, the band at 1645 cm^{-1} is originated by H-O-H bending vibrations from the water molecules of the hydration sphere of the mineral.

TGA

To proceed with the investigation about the hydrogel PVA96-Borax, this sample was submitted to thermogravimetric analysis and the results were compared with that of the isolated polymer PVA96. The analysis was performed in the range 25-600 ºC and the obtained curves are shown in Figure 5.19.

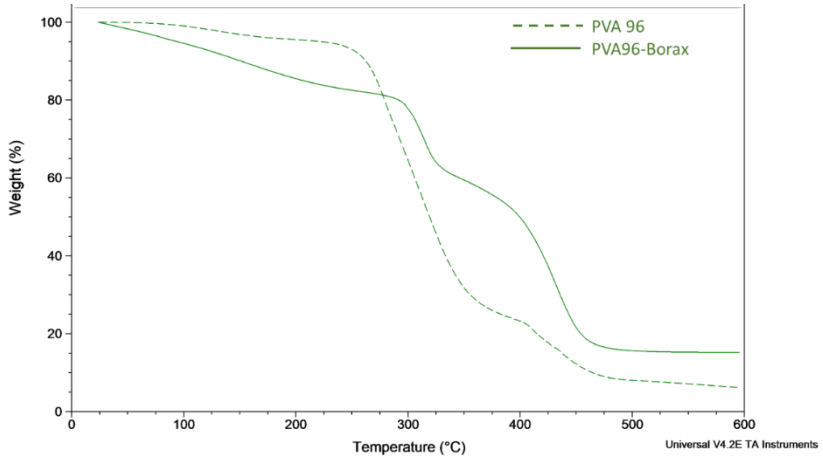

Figure 5.19 - Thermogravimetry of PVA96 before (----) and after (—) crosslinking with Borax.

As discussed previously, following a small mass loss (5 wt%) due to dehydration of the polymer sample around 100 ºC, PVA96 degrades in two main steps. Between 250 and 380 ºC, the mass loss is approximately 75 wt% and between 380 and 480 ºC, around 15 wt%, with a final residue of 5 wt%. The first process corresponds to the stripping of the lateral groups and the second, to the hydrocarbon backbone degradation [188,189,204].

For PVA96-Borax, there is progressive mass loss of around 20 wt% from 25 ºC to 310 ºC, a rapid loss of another 20 wt% at 310-340 ºC and a greater loss of 50 wt% at 340-480 ºC. The residue at 600 ºC corresponds to 10 wt% of the initial mass. The initial mass loss is probably mostly originated by residual water molecules and from organic fragments of low molecular weight (eventually acetate-based) entrapped in the hydrogel. Above 300 ºC, the obtained curve shows that the composition is more resistant to thermal degradation than the polymer alone. The equivalent to its first step of degradation corresponds to a much lower mass, being typically assigned to the stripping of lateral -H, -OH and -acetate groups. According to FTIR results, the latter occur in lower amount in the crosslinked polymer and the structural model implies that part of the lateral groups are linked to borate, hence more resistant to degradation Thus, the lower mass loss may be due to less free lateral groups than in the original polymer. Conversely, the second step corresponds to a greater mass loss because the backbone of the polymer is linked to Borax. This may also explain the higher degradation temperature.

Crosslinking suspensions of minerals in PVA with Borax

The preparation of minerals (hydroxyapatite and barium sulphate) suspensions in PVA solutions, in diverse proportions as reported in the radiology tests (Chapter 4), enabled to obtain viscous fluids adequate for injection. The rheological tests previously described clearly indicate that those mixtures were homogeneous, stable and injectable with a syringe of appropriate dimensions (needle diameter, in particular). Borax was tested to act as a crosslinker of the mineral suspensions in PVA of different hydrolysis degrees. These tests were performed being aware that the crosslinking could be less effective than it should. However, the crosslinked material could constitute an initial transient form to combine with additional reagents. The approach would be the formation of an interpenetrating network (IPN) with other compatible and stronger hydrogels.

The crosslinking tests are not described because the results have been qualitatively similar in all experimental conditions, and inappropriate for the designed

application. The addition of any Borax solution (different volumes and concentrations) to the suspensions of minerals in PVA provoked always the immediate gelation of the mixture. This behavior showed that the injectability was compromised and that this system required another technical solution. The use of a controlled delivery device that could delay the contact between Borax and PVA has been the next step in this research.

5.3 Microcapsules

As described, crosslinking PVA with Borax using the direct contact between the respective aqueous solutions is almost an instantaneous process that is not significantly affected by the presence of hydroxyapatite and barium sulphate. Thus, encapsulating Borax could be a way to delay that contact, enabling a slower and eventually rate controlled crosslinking reaction.

The strategy has been to synthesize microcapsules with poly (lactic acid) (PLA), a well-known biodegradable polymer, adding Borax as a filler. The microcapsules would be dispersed in the PVA suspension with minerals, being this mixture able to be injected with a syringe. Then, after the injection, the encapsulated Borax would be released through the PLA shell to start the crosslinking of the composition around the microcapsules. Because of its biodegradation properties, PLA would gradually be hydrolyzed into innocuous lactic acid and disappear from the crosslinked hydrogel [161]. At latter stages of this study, it became important to test another filler for the PLA microcapsules. In addition to Borax, this section also describes the use of an acrylic monomer (2-hydroxyethyl methacrylate (HEMA)) as a filler.

One classical way of forming microcapsules based on emulsification/solvent evaporation method is the water-in oil-in water (w/o/w) approach [161,164]. This process involves four steps, the first of which consists on mixing an aqueous solution containing the filler component with an organic solution containing the dissolved polymer intended for the shell material. This leads to the formation of the primary water-in oil (w/o) emulsion. In the second step, this emulsion is dispersed under continuous agitation in an aqueous solution medium, usually containing an appropriate stabilizer agent (a surfactant), forming the secondary oil-in water (o/w) emulsion. The third step involves the evaporation of the organic solvent, allowing the microdroplets to turn into microcapsules. Finally, the microcapsules are harvested by centrifugation or filtration of the solution, followed by being washed and dried.

5.3.1 Synthesis of PLA microcapsules

The microcapsules were produced by the w/o/w double emulsion method using PLA for the shell and PVA80 as surfactant, to obtain three types of particles: unfilled, filled with Borax, and filled with Borax and HEMA. The methodology applied to obtain the unfilled species has been adjusted for the other microcapsules, using the amounts described in Table 5.4. The samples are named as mC from microCapsules, followed by S (Standard), B (Borax) and H (HEMA). The synthesis involved the variation of components to obtain microcapsules of different sizes and different porosity. To monitor the properties of the obtained products, these were analyzed using Thermogravimetric Analysis (TGA), Laser Diffraction Spectrometry (LDS), porosimetry by Hg Intrusion, Optic Microscopy (OM) and Scanning Electron Microscopy (SEM).

The standard microcapsules (mC-S) were obtained from the addition of 5 ml of water to 0.9 g of PLA dissolved in 30 ml of chloroform. This emulsion was added to a solution of 1.6 g of PVA80 in 80 ml of water. Both emulsions were made under magnetic stirring. The second one was prepared at 1500 rpm and was left overnight at 300 rpm to evaporate the organic solvent. Afterwards, the microcapsules were separated by centrifugation (3000 rpm), with three intermediate washing procedures with distilled water. Finally, the microcapsules were dried at 50 ºC. The geometric representation of these capsules (Figure 5.21) corresponds to a hollow PLA shell, surface-coated with PVA, being the interior filled with water. The volume of the sphere, the thickness of the shell and the concentration of surfactant have been taken as references to represent the expected differences in the other microcapsules.

The inclusion of Borax in the microcapsules was tested under different conditions. First, it was added to the standard composition using 0.5 g of Borax dissolved in 5 ml of water, keeping the other components. This originated the mC-BS (microCapsules - Borax Standard) species, represented in Figure 5.21 by the same shell and the same surfactant than in mC-S, but with a Borax solution as the filler instead of water.

A series of four other Borax-containing microcapsules (mC-B1 to mC-B4) was prepared altering a single variable at each case for mC-B1 to mC-B3, and two variables for mC-B4, relative to mC-BS. For mC-B1, the volume of water has been the double; for mC-B2, the mass of PVA has been one half; for mC-B3, the mass of PLA has been the double and for mC-B4, both the mass of PLA and the mass of PVA have been the double than the standard sample. The geometry of the respective samples (Figure 5.20) corresponds to capsules with the double volume in mC-B1, with half of the surfactant in

mC-B2, with the double thickness in mC-B3 and in mC-B4, with the double thickness and double surfactant at the surface.

Following the same basic procedure (w/o/w), some microcapsules containing Borax and HEMA were also prepared. In mC-BH1, 2 ml of HEMA were added to the PLA solution on chloroform, which means that the acrylic monomer will be impregnated in the shell of the microcapsule. For mC-BH2, 2 ml of HEMA were added to the Borax solution. This corresponds to the inclusion of the monomer inside the shell. Finally, in mC-BH3, 1 ml of HEMA was added to the PLA and the volume of the Borax solution was augmented to 7 ml. This corresponds to a microcapsule with half of the HEMA in the shell, but with 50% higher core volume than the reference sample. These geometries are represented in Figure 5.20.

Table 5.4 – Reagents applied in the synthesis of microcapsules.

Microcapsules	Borax m (g)	Water V(ml)	PLA m (g)	PVA m (g)	HEMA V (ml)
mC-S	**0.0**	5	0.9	1.6	
mC-BS	0.5	5	0.9	1.6	
mC-B1	0.5	**10**	0.9	1.6	
mC-B2	0.5	5	0.9	**0.8**	
mC-B3	0.5	5	**1.8**	1.6	
mC-B4	0.5	5	**1.8**	**3.2**	
mC-BH1	0.5	5	0.9	1.6	**2.0** (a)
mC-BH2	0.5	5	0.9	1.6	**2.0** (b)
mC-BH3	0.5	**7**	0.9	1.6	**1.0** (a)

(a) Added to PLA/$CHCl_3$ solution.

(b) Added to Borax/H_2O solution.

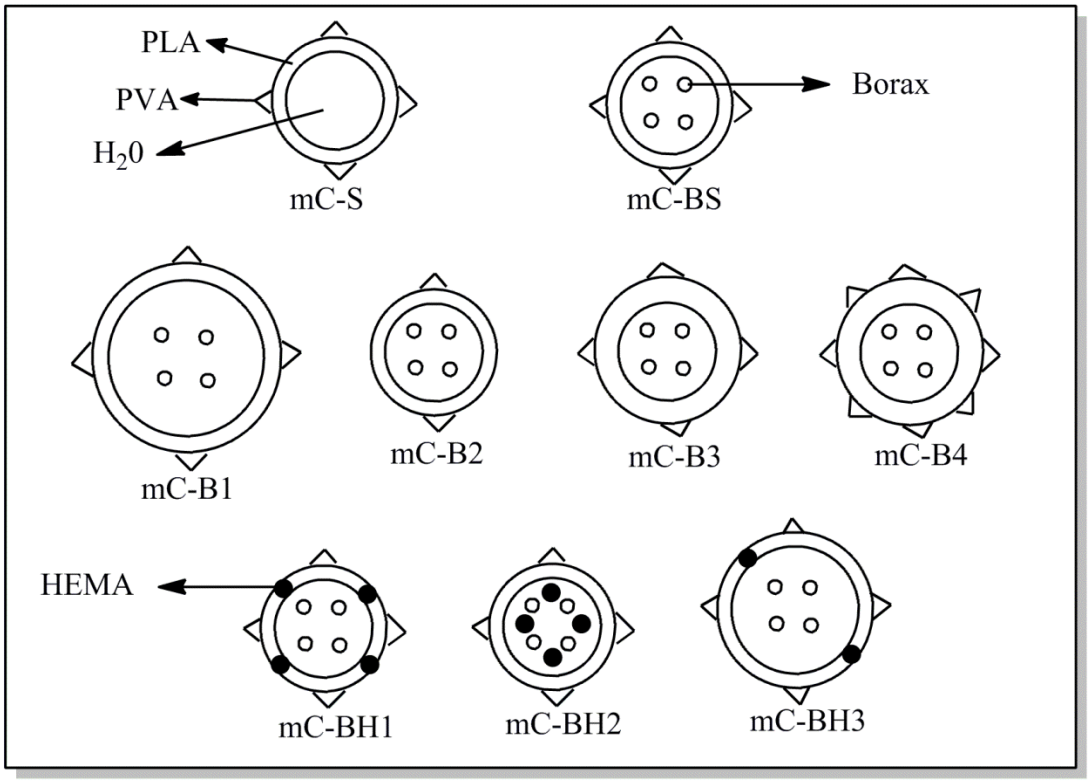

Figure 5.20 - Schematic representation of various types of microcapsules (mC) produced with different amounts of PLA, PVA, H_2O, Borax and HEMA, as quantified in Table 5.4. In the top row, the mC-S and mC-BS types represent the standard (S) composition of unfilled and Borax (B) containing capsules, respectively. The mC-B1 to mC-B4 types (middle row) represent variations to mC-BS: mC-B1 were produced using the double water volume, mC-B2, using half of the PVA, mC-B3, the double PLA and mC-B4, both double PLA and double PVA. The bottom row represents microcapsules containing Borax and HEMA in the PLA shell (mC-BH1 and mC-BH3) or as the fillers in the core solution (mC-BH2). The production of mC-BH3 involved more water volume and less HEMA than the other mC-BH types.

5.3.2 Characterization

TGA

The thermal behavior of the mC-S microcapsules was compared with that of PLA, the polymer that forms the shell, using TGA from 25 ºC to 600 ºC. The results are shown in Figure 5.21.

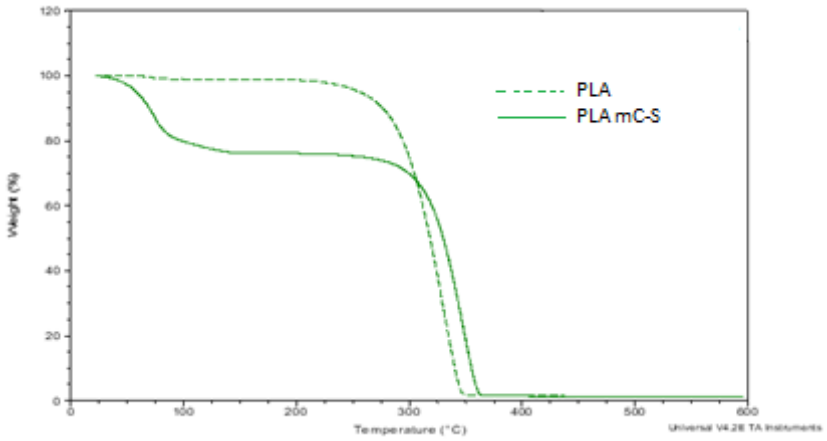

Figure 5.21 - Thermogravimetry of PLA (---) and of mC-S PLA microcapsules (—).

The mass loss profile of PLA is characterized by a plateau from room temperature until 260 ºC, followed by a total mass loss in the range 260-350 ºC. This result agrees with the literature [205]. On the other hand, the standard PLA microcapsules present a mass loss of 25 wt% around 100 ºC, a plateau from 100 ºC to 280 ºC and a loss of 75 wt% in the range 280-370 ºC. According to the components used in the synthesis of the microcapsules, the first process corresponds to the loss of water. This indicates that despite being previously dried, the microcapsules still contain a significant amount (25 wt%) of water molecules entrapped in its structure. The second mass loss corresponds to the degradation of the polymer. The fact that it occurs at slightly higher temperatures than the original polymer may be due to the presence of a small amount of PVA which was used as surfactant to stabilize the surface of the microcapsules.

Optic Microscopy

This technique was used to monitor the microcapsules at the final step of the synthesis method, after the washing and centrifugation procedures. The microcapsules were observed in an aqueous medium at diverse magnifications. The observation enabled a convenient quality control before the drying process.

The images displayed in Figure 5.22, relative to standard microcapsules mC-S and mC-BS, show that these particles have round shapes of very distinct size ranges. The unfilled mC-S microcapsules have much lower sizes than the Borax-filled mC-BS ones. The largest particles of mC-S reach around 20 μm and those of mC-BS, around 100 μm. Another distinctive feature is the surface appearance of these microcapsules,

Whereas the mC-S type has a smooth and homogeneous shell, mC-BS has a irregular surface that seems to contain air bubbles.

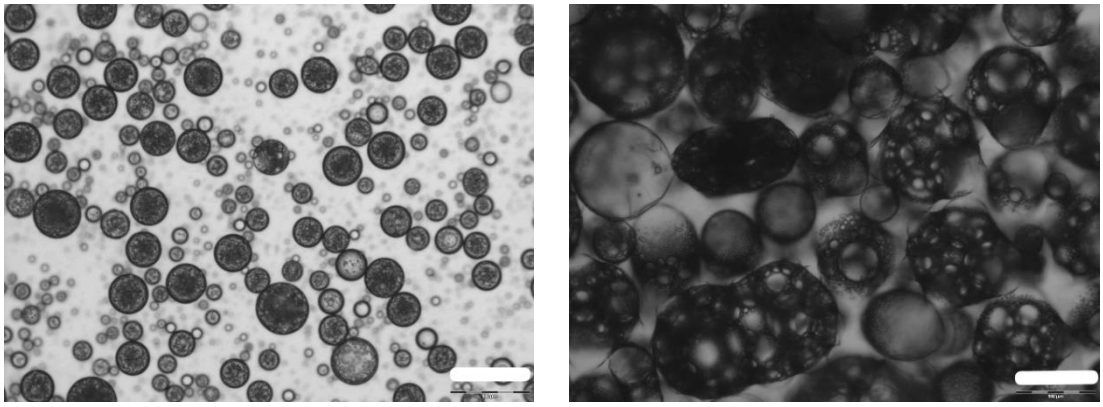

Figure 5.22 – Standard PLA microcapsules dispersed in water, observed by optic microscopy (bar=100 μm). Effect of the addition of borax into the filler solution: unfilled mC-S (left) and filled mC-BS (right) microcapsules.

SEM, LDS and Hg Porosimetry

The physical characterization of the dry microcapsules was made using SEM, LDS and Hg Porosimetry to obtain complementary information from these techniques. The obtained parameters (D10, D50 and D90 from LDS and porosity percentage) are displayed in Table 5.5.

mC-S microcapsules

The standard microcapsules observed using SEM (Figure 5.23) present a homogeneous spherical shape with different particle sizes, most having diameters around 50 μm. There are also many microcapsules inferior to 10 μm. The images also show that the surface of these particles is continuous and homogeneous. Although it is expected to have hollow particles because of the w/o/w production process, the images don´t show any broken microcapsule that would allow to observe if they are hollow or compact.

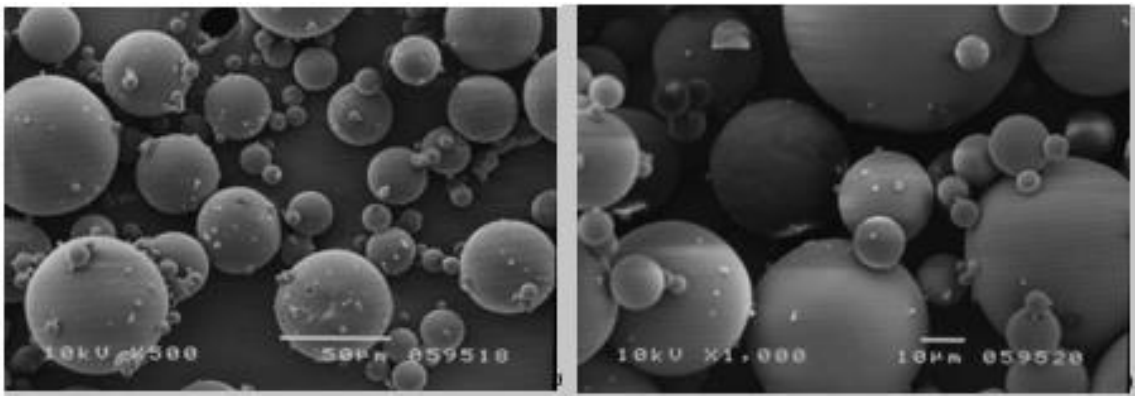

Figure 5.23 – SEM images of standard PLA microcapsules (mC-S).

The particle size observed in SEM images is corroborated by LDS, as shown in Figure 5.24-left and quantified by the respective D_{10}, D_{50} and D_{90} parameters (Table 5.5). The particle size distribution is sharp around 56 μm and there is a small fraction of microcapsules with diameters around 8 μm. The porosity measurements presented in Figure 5.24-right show the differential curve of the intruded mercury has an intense sharp peak at 16 μm. Since the surface of the microcapsules has no pores, and that value is of the same order of the particle size, that peak is originated by inter-particle porosity.

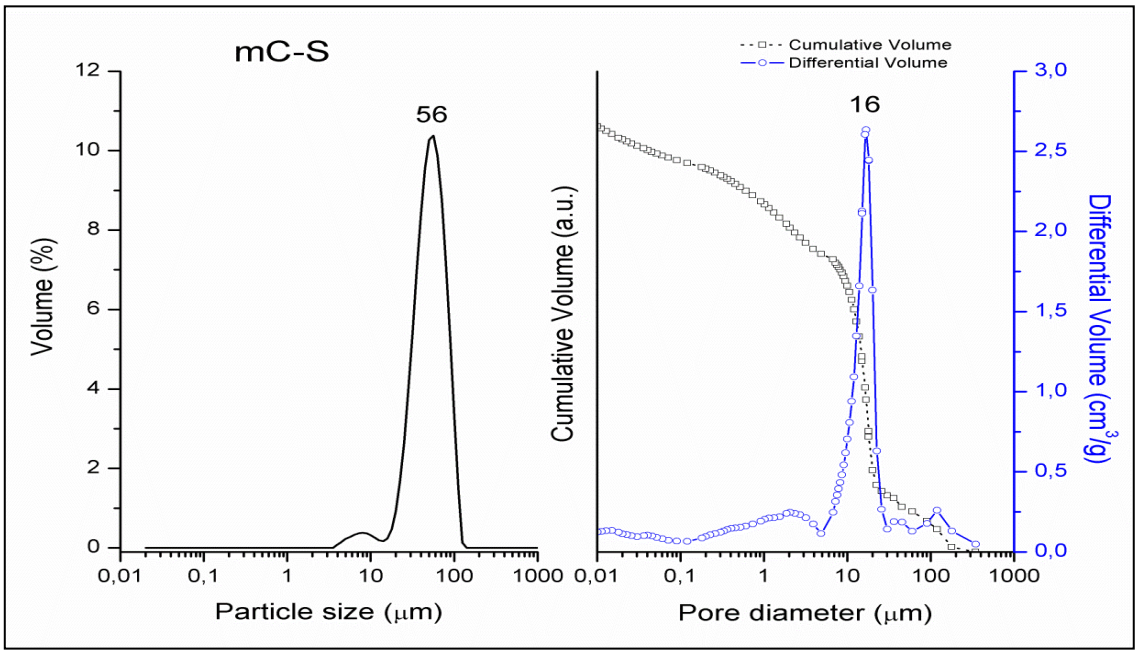

Figure 5.24 - Particle size distribution and Hg intrusion curves of microcapsules mC-S.

mC-BS microcapsules

According to the SEM images (Figure 5.25), the standard microcapsules containing Borax have a spherical but irregular appearance, being the average particle size around 20 μm. The surface of these microcapsules is smooth but presents many circular impressions, probably caused by collisions while the shells were being formed. The lack of uniformity of the surface may result from the action of Borax over the surfactant, PVA. Some capsules seem to be incompletely formed because their shells have some parts that are not totally closed. This allows to observe that these particles are hollow, being assumed the same for all the others.

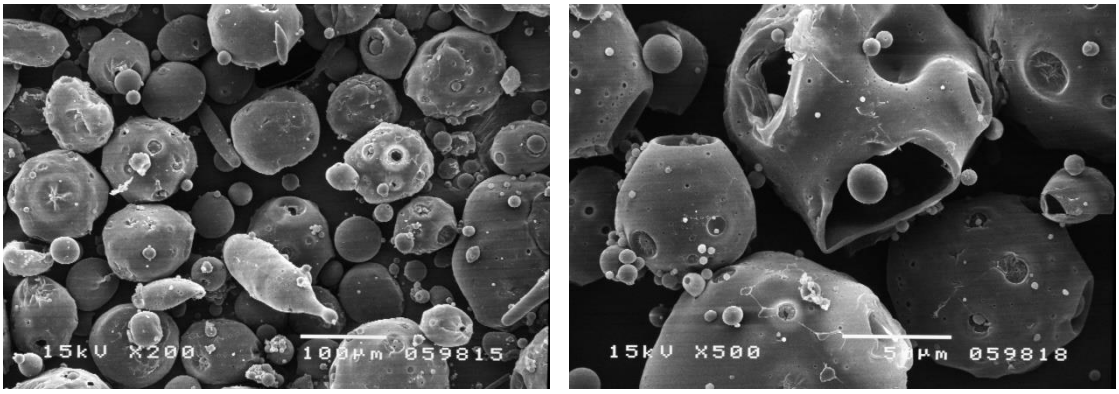

Figure 5.25 - SEM images of standard PLA Borax-containing microcapsules (mC-BS).

At higher magnifications (Figure 5.26), the thickness of the shell may be observed with greater detail. The images show that it may be very thin (inferior to 1 μm), or it can be thicker (around 4 μm) in the larger microcapsules.

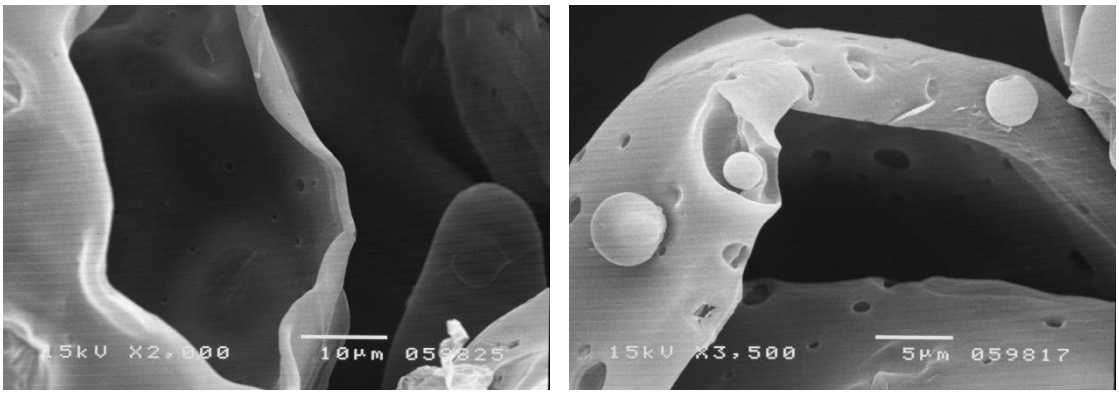

Figure 5.26 - SEM images of standard PLA Borax-containing microcapsules (mC-BS). Details from the thickness of the shell.

mC-B1 microcapsules

The mC-B1 microcapsules were produced with twice the volume of water in the Borax solution than the standard particles. As observed in the SEM images of Figure 5.27, this difference originated much larger particles, in a high proportion, with irregular spherical shape and ruffled surface. The smaller particles, with diameters of few micrometers, are much less frequent. Some microcapsules present pores of circular shape with diameters inferior to 10 μm.

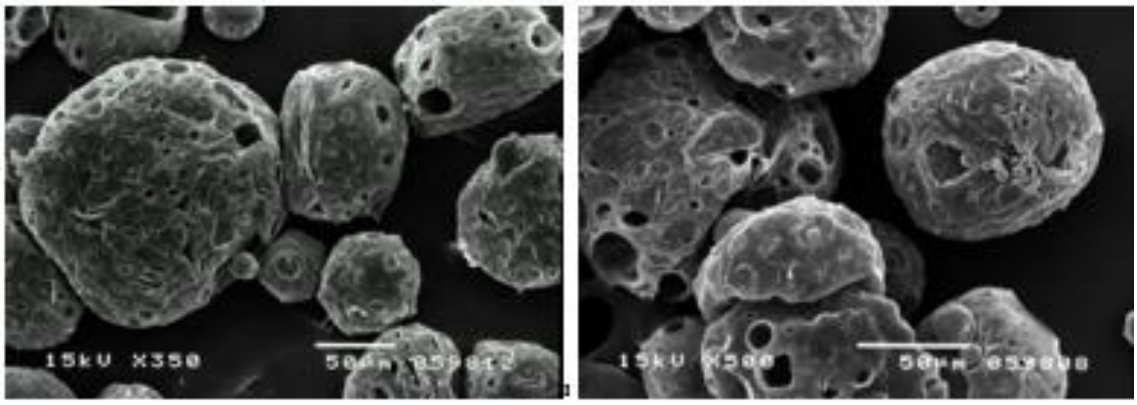

Figure 5.27 - SEM images of microcapsules mC-B1.

The measurements by LDS (Figure 2.28-left; Table 5.5) show that the particle size of mC-B1 ranges from around 50 to 500 μm, being D_{10}=88 μm and D_{90}=369 μm. The median (D_{50}) of the distribution is 202 μm. As for the porosity, from the peaks of the differential curve (Figure 5.28-right) at 5 μm and at 90 μm, the former corresponds mostly to the pores in the shells of the capsules and the latter, to inter-particle spaces.

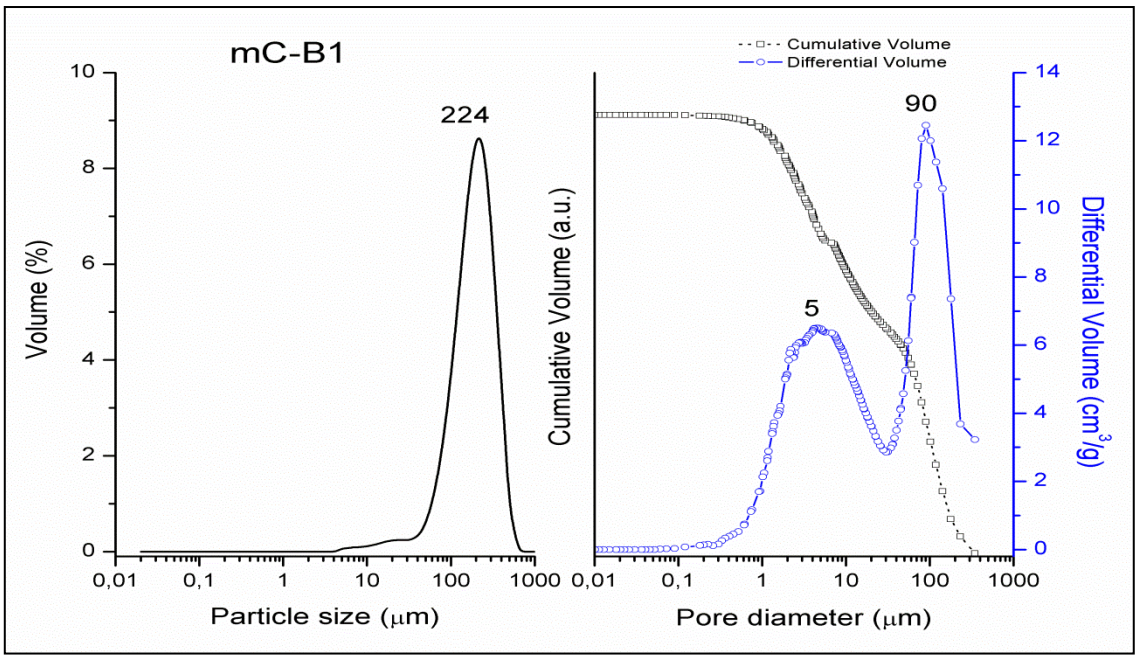

Figure 5.28 - Particle size and pore diameter distribution of microcapsules mC-B1.

mC-B2 microcapsules

The mC-B2 microcapsules were produced with half of the surfactant relative to the standard mC-BS particles. The SEM images from mC-B2 (Figure 5.29) show that most microcapsules have sizes around 50-100 μm. Smaller particles, inferior to 10 μm, are also observed. The most frequent shape is spherical but there are also diverse flattened particles. Another feature that occurs is the incomplete closure of the capsules originating pores of assorted dimensions. This enables to confirm that these particles are hollow and gives access to the observation of the shell thickness and of the interior side of the microcapsules. The surface is relatively smooth, having some signals from collisions during the synthesis.

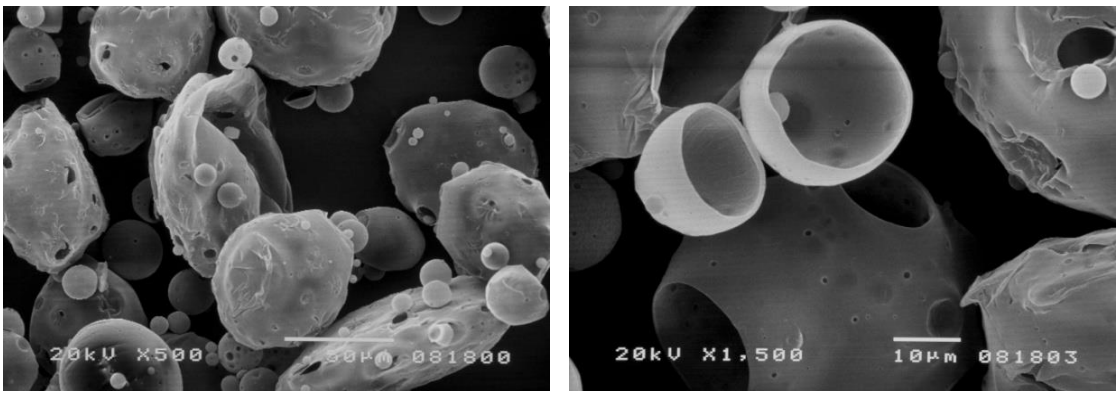

Figure 5.29 . SEM images of microcapsules mC-B2.

mC-B3 microcapsules

The mC-B3 type of microcapsules were produced with twice the PLA of the standard mC-BS particles. Figure 5.30 shows that the mC-B3 capsules have a more compact appearance and a more regular spherical shape. The average particle size accessed by SEM points to the presence of a high proportion of large particles, around 200-300 μm. These capsules are also hollow, and the large thickness of the shell is clearly derived from the higher amount of PLA in the synthesis. The surface is not very regular since it presents some ruffles.

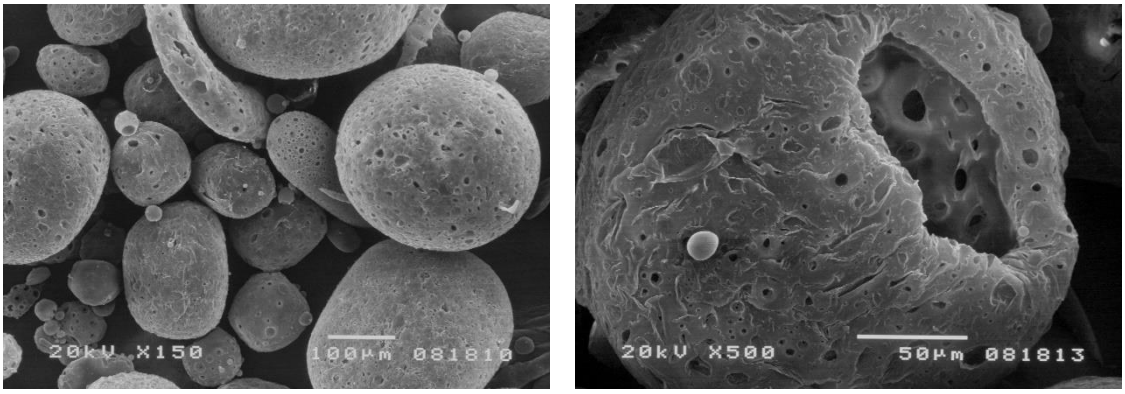

Figure 5.30 - SEM image of microcapsules mC-B3.

The results from LDS (Figure 5.31-left; Table 5.5) indicate that the particle size distribution of mC-B3 is bi-modal, with maxima at 60 μm and 400 μm. Most microcapsules have large sizes, as reflected by the parameters D_{10}=60 μm, D_{50}=348 μm and D_{90}=500 μm. The porosity of the sample is reflected in graphs of Figure 5.31-right, being the broad peak at 13 μm relative to pore diameter in the shells and the peak at 120 μm, relative to inter-particle porosity.

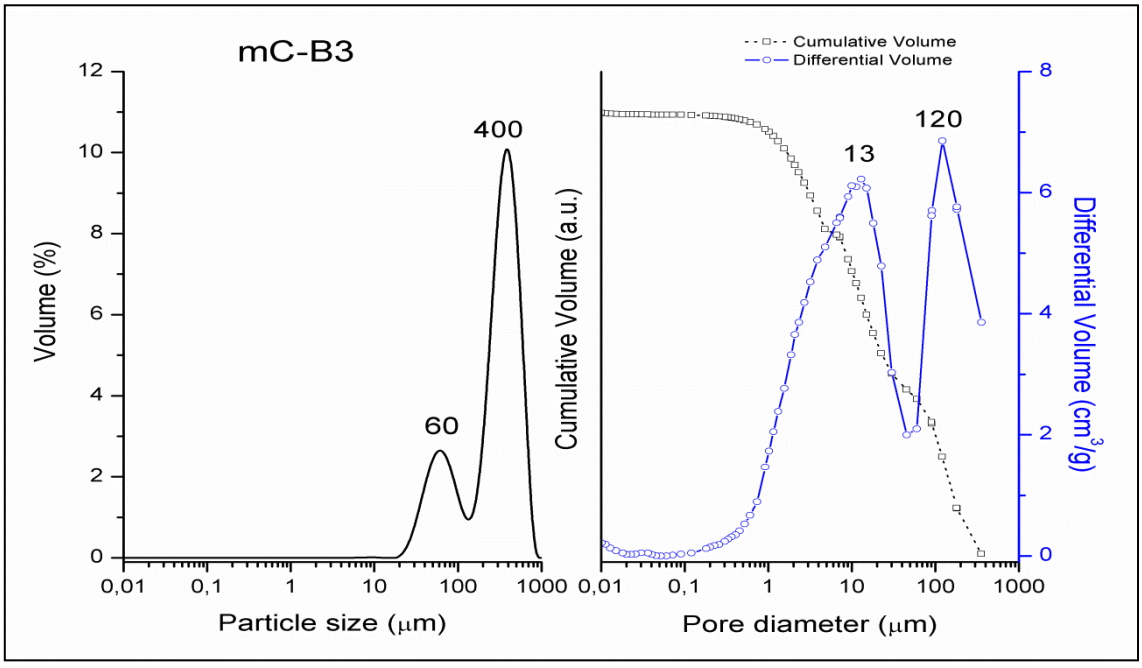

Figure 5.31 – Particle size and pore diameter distribution of microcapsules mC-B3.

mC-B4 microcapsules

The microcapsules mC-B4 were produced using twice the PLA and twice the PVA relative to the standard mC-BS particles. The size and shape of the mC-B4 capsules is shown in Figure 5.32. These have the typical spherical shape, but slightly

irregular, and an average size superior to 300 μm. The surface is full of circular cavities that don´t pass across the shell and give a spongy appearance to the particles.

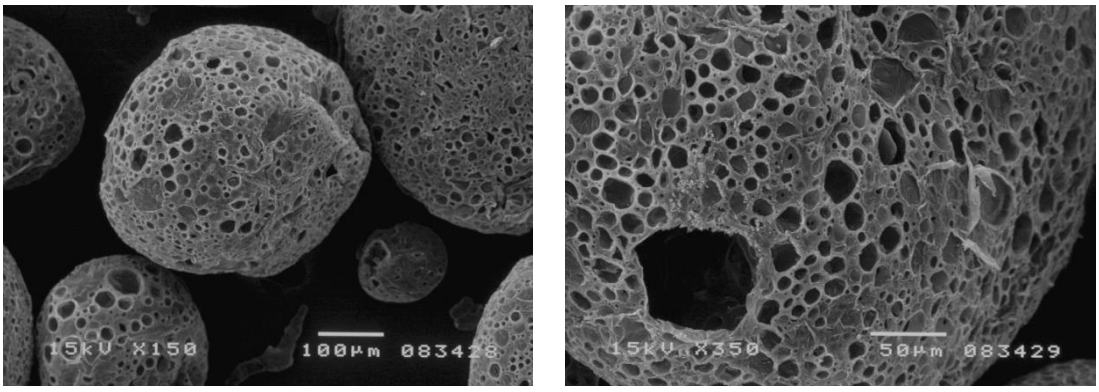

Figure 5.32 - SEM image of microcapsules mC-B4.

mC-BH1 microcapsules

The microcapsules mC-BH1 were produced using HEMA in the shell composition, keeping all the other components used in the standard mC-BH particles. The morphology, the dimensions and the surface characteristics of the mC-BH1 type is displayed in the SEM images of Figure 5.33. These particles size is, in average, inferior to 100 μm and their shape consists of regular hollow spheres. In general, the surface is smooth, but has multiple minor punctures dispersed around the structure.

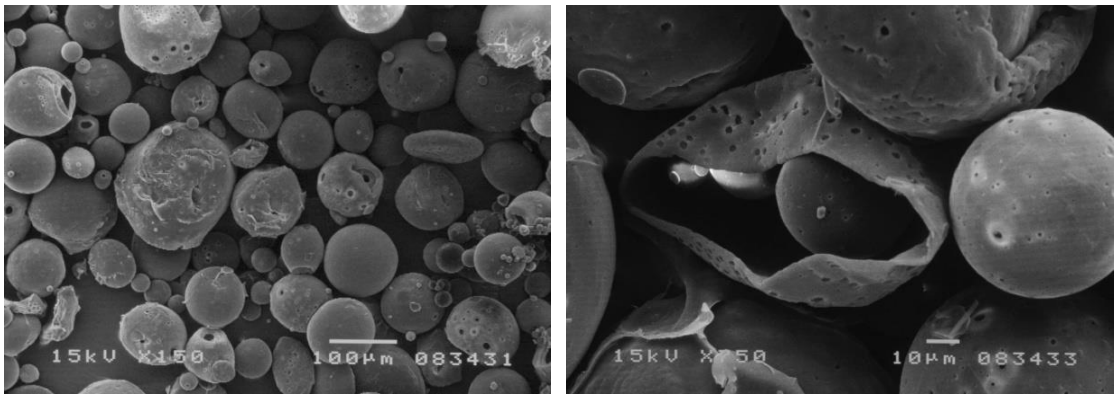

Figure 5.33 - SEM images of microcapsules mC-BH1.

The particle size distribution, according to the data from LDS, matches the values estimated from microscopy imaging. The curve in Figure 5.34-left shows that most of the microcapsules follows a unimodal distribution centered at 67 μm. A residual percentage has sizes from 5 to 20 μm. The pores sizes, deduced from the differential curve of the Hg intrusion (Figure 5.34-right), range from 0.1 to 1.0 μm. The inter-particle porosity originates the peak at 30 μm.

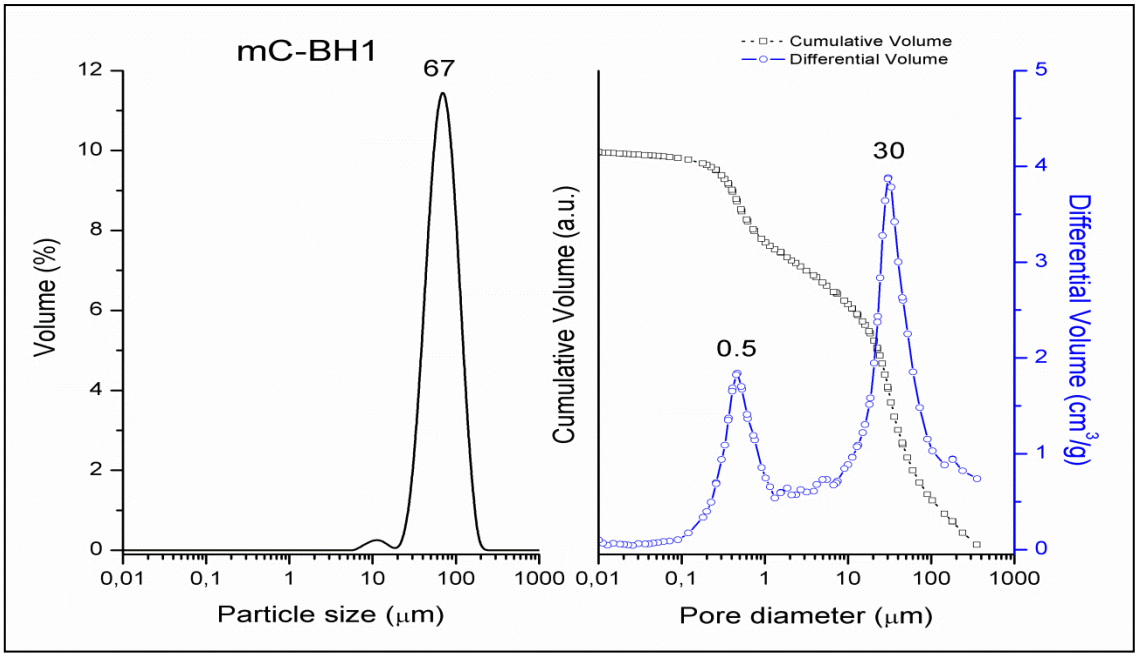

Figure 5.34 - Particle size distribution and pore diameter of microcapsules mC-BH1.

mC-BH2 microcapsules

The microcapsules mC-BH2 were synthesized using HEMA together with the Borax solution standardly applied as a filler in the mC-BS particles. The SEM images of the mC-BH2 microcapsules are presented in Figure 5.35. They show spherical particles with regular shapes and smooth surfaces, with less punctures than in mC-BH1 type. The average size is also inferior to 100 μm and the images suggest that these capsules have inferior sizes to those of mC-BH1.

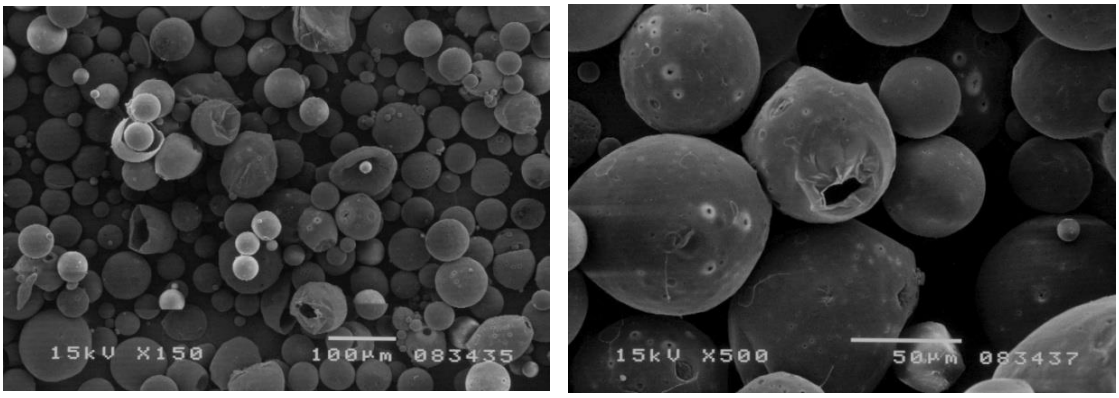

Figure 5.35 - SEM images of microcapsules mC-BH2.

The parameters from mC-BH2 obtained using LDS (Table 5.5) point to a particle size distribution similar to mC-BH1, except for D_{90} which occurs at higher values. The curve displayed in Figure 5.36-left, with its maximum peak at 76 μm, represents the obtained volumetric distribution. In Figure 5.36-right, the graph from Hg intrusion has a

sharp peak at 0.6 μm due to intra-particle porosity and a broad band ranging 10-400 μm that corresponds to inter-particle porosity.

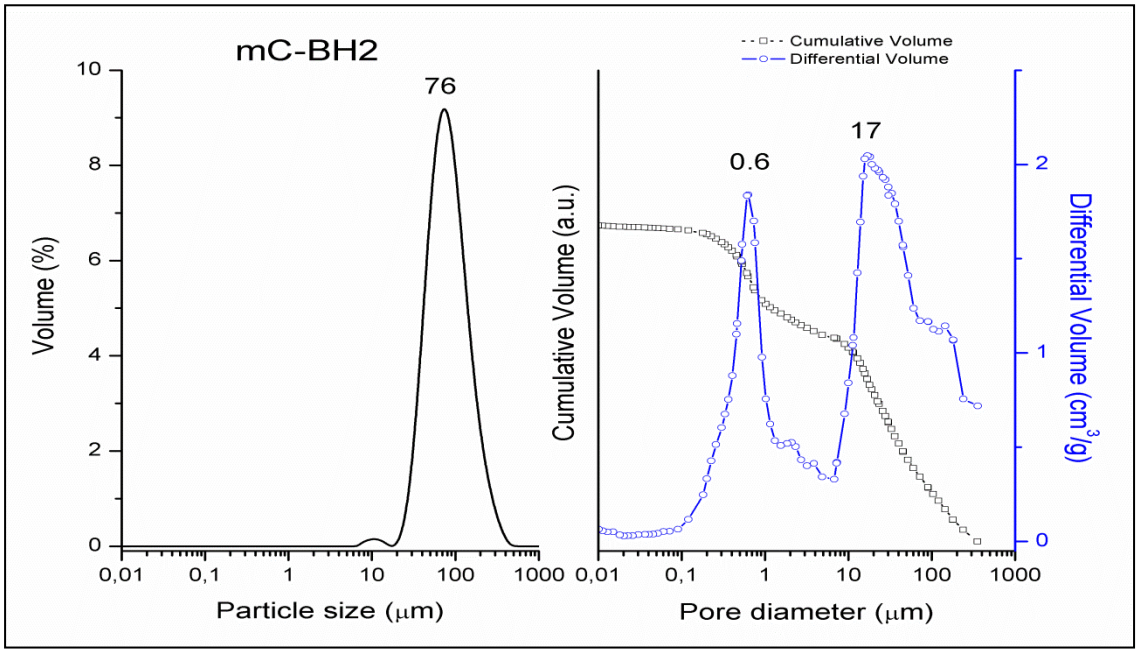

Figure 5.36 - Particle size distribution and Hg intrusion curves of microcapsules mC-BH2.

mC-BH3 microcapsules

The mC-BH3 microcapsules were produced with 40% more volume of water in the filler solution of Borax and half of the volume of HEMA in the shell, relative to the other mC-BH particles. The resulting capsules were observed using SEM (Figure 5.37), being characterized by heterogeneous size and shape. There is a large volume of particles with sizes superior to 200 μm and the shape is not a perfect sphere. In addition, the spongy appearance of the surface makes the mC-BH3 microcapsules resemble the mC-B4 type.

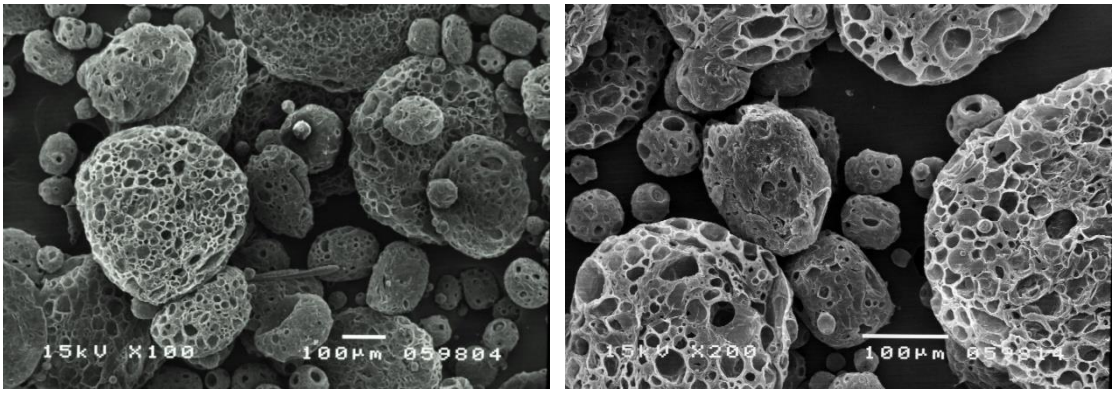

Figure 5.37 - SEM images of microcapsules mC-BH3

The curve obtained by LDS shows that the size distribution is almost unimodal with a maximum at 186 μm. There is, however, a small proportion of smaller particles (Figure 5.38-left). The size parameters of mC-BH3 are presented in Table 5.5. The intra-particle pores have diameters around 2 μm and the inter-particle spaces measure 20-400 μm (Figure 5.38-right).

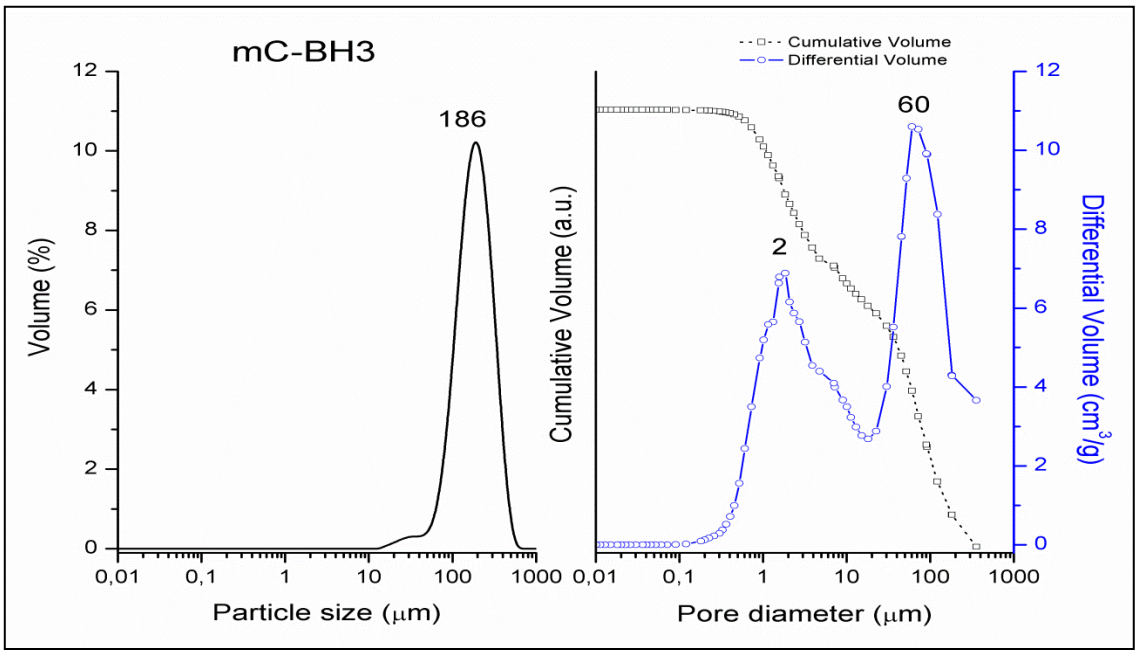

Figure 5.38 - Particle size distribution and pore diameter of microcapsules mC-BH3.

The comparison between the particle size distribution curves of microcapsules mC-S, mC-B1, mC-B3, mC-BH1, mC-BH2 and mC-BH3 is expressed in Figure 5.39, in the 10-1000 μm scale range. Table 5.5 gathers the particle size parameters (in volume percentages) of these microcapsules in terms of median diameter (D_{50}), as well as the particle size range expressed by the 10 % and 90 % percentiles (D_{10} and D_{90}).

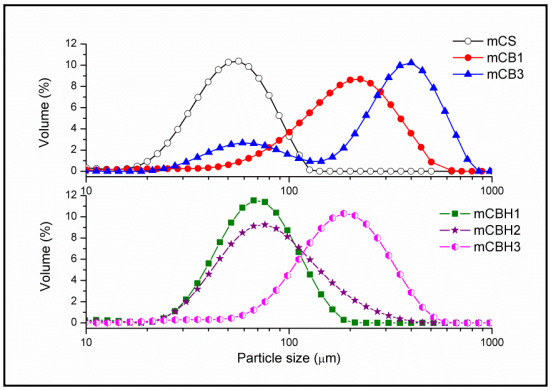

Figure 5.39 - Particle size distribution of various microcapsules. Top: mC-S (standard), mC-B1 (with borax and additional water in the filler) and mC-B3 (with borax filler and additional PLA in the shell). Bottom: mC-BH1 (with borax filler and HEMA in the shell), mC-BH2 (with borax and HEMA in the filler) and mC-BH3 (with borax and additional water in the filler and HEMA in the shell).

As described earlier, the mC-S standard particles have the smallest sizes but those types with Borax and HEMA which were produced with the standard filler volume (mC-BH1 and mC-BH2) are both only slightly larger than mC-S. These three types have also in common the smooth appearance of the surface. The effect of the water volume of the filler solution is evidenced in the increasing size from mC-BH3 to mC-B1. However, the factor with the highest influence in the particle size is the amount of PLA that forms the shell, as occurs with mC-B3 (and mC-B4) that has the double than the others and corresponds to the largest particle size.

Table 5.5 - Particle size parameters (in volume percentages) of the microcapsules: median diameter (D_{50}) and size range expressed in percentiles (D_{10} and D_{90}).

Microcapsules	D_{10} (μm)	D_{50} (μm)	D_{90} (μm)
mC-S	29	54	90
mC-B1	88	202	369
mC-B3	60	348	588
mC-BH1	41	73	124
mC-BH2	43	83	179
mC-BH3	87	171	306

Other properties, namely the shell thickness or the surface roughness are also distinctive. The addition of Borax into the filler has some effect on the disruption of the surface, probably because of the use of PVA as surfactant. The crosslinking reaction certainly occurs during the synthesis process, altering the distribution of PVA across the surface of the microcapsules. The Borax-containing particles mC-B1, mC-B3 and mC-B4, unlike mC-B2 that has half of the Borax, have very ruffled surfaces. The mC-B4 has even greater effect (spongy surface) that derives from the additional surfactant. The addition of HEMA to the shell (mC-BH1) or to the filler (mC-BH2) of Borax-containing capsules blocks the disruption of the surface except when the filler volume is augmented (mC-BH3). On the other hand, the thickness of the shells is clearly proportional to the amount of PLA applied in the synthesis process.

The porosity measurements enabled to conclude that the standard microcapsules are the only type made of closed particles, as obtained by other authors [161]. The shells of the other types of capsules possess pores of diameters generally inferior to 10 μm.

The relevance of all these characteristics of the microcapsules is notorious when they are applied as delivery systems.

5.3.3 Controlled delivery of Borax

Some of the obtained microcapsules were tested for the controlled delivery of Borax into PVA solutions and into mineral suspensions of hydroxyapatite and barium sulphate in PVA. The selected capsules were mC-B1 and mC-B3, both with the same Borax content and large particle size compared to the other particles. The former type was produced with the double amount of water, thus the concentration of Borax in the filler was half of the others during the synthesis. However, after the final step of drying the particles, the only factor that matters is the amount of solute which was the same for mC-B3. The most relevant difference between the samples was the thickness of the shell and the roughness of the surface. mC-B1 was thinner and smoother, mC-B3 was thicker and ruffled. These differences were expected to influence the release of Borax from the capsules to the surrounding environment, causing a faster gelation with the mC-B1 type.

The applied procedure was very simple. An equal amount of each type of microcapsules was added to similar volumes of the different PVA solutions and suspensions. In all the cases, the PVA became crosslinked after a few seconds. This result was not expected, and it motivated a different test to verify what had happened.

Atomic Absorption Spectroscopy

Microcapsules mC-B1 and mC-B3 were added to a volume of water and left without stirring for one hour. After this period, the water was collected for analysis using Atomic Absorption Spectroscopy to detect the sodium from Borax. This time, the results matched the expectations. From the calibration curve with standard solutions and adequate dilution of the obtained samples, the concentration of sodium from mC-B1 was 16 mg/l and from mC-B3 it was 4 mg/l. The amount of Borax that passed through the thinner shell was significantly superior to the other which shell was not only thicker, but also irregular. These structural factors showed a great influence in the diffusion kinetics in aqueous environment.

To justify the results of the Borax-containing capsules with the PVA systems, it should be remembered that in previous experiments, the crosslinking between the polymer and Borax solutions occurred always very suddenly, even using very low

concentrations of this molecule. This indicates that the Borax in the capsules is probably not only inside the shell, but also at the surface, and the contact of even small amounts of Borax with the surrounding PVA leads immediately to the gelation of the polymer.

Porosity of the PVA-Borax hydrogel with microcapsules

The properties of the microcapsules inspired the idea for a different application for these particles. In addition to the delivery of molecules as anti-inflammatory drugs, antibiotics, proteins (BMPs) or other active substances (including cells), the PLA microcapsules may be used to create porosity inside a biomaterial. Since PLA is biodegradable, the microcapsules would gradually create voids corresponding to their original particle size. For bone graft applications, the obtained particle size distribution (10-400 μm) would be adequate for colonization by osteogenic cells. The interconnected porosity would be another objective to achieve in order to enhance the transport of nutrients and facilitate angiogenesis. The intra-particle pores of the microcapsules would also be useful to increase the exchanges between the core and the surrounding environment.

In order to evaluate the initial porosity due to microcapsules dispersed in a PVA hydrogel, samples from the tests of Borax release from the particles to the polymer solution were submitted to Hg intrusion. For instance, a 20 wt% aqueous solution of PVA98 was mixed with a proportion of mC-B1 microcapsules around 10 % V/V. The polymer was crosslinked with Borax which was delivered from these microcapsules. After gelation, the obtained material was dried at 50 ºC to allow the use of the Hg technique. The final shape of the material was cylindrical. Considering that the drying process of the sample caused total water loss, the obtained material had a significant dimensional contraction and the microcapsules might have eventually collapsed. Freeze drying was not an option because it would leave pores in the hydrogel structure that would mask the effect of the microcapsules. The result of this test is presented in Figure 5.41.

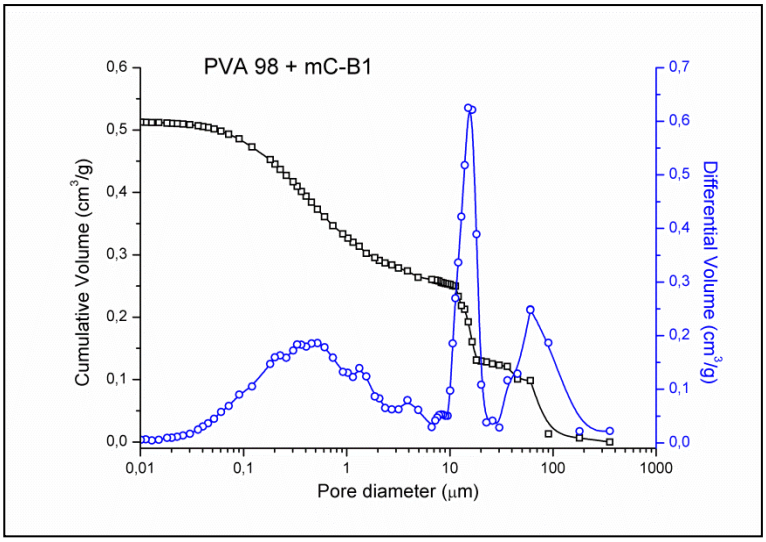

Figure 5.40 - Pore size distribution of PVA crosslinked with microcapsules mC-B1.

The pores diameters from the PVA98-mC-B1 sample have a wide range of values. The differential volume curve presents a broad distribution between 0.01 and 10 μm, a sharp intense peak at 20 μm and another peak around 100 μm. The presence of pores inside the sample indicates that although there was a dimensional contraction, the microcapsules did not collapse entirely. The larger diameter in the graph is inferior to the average particle size of the particles, but of the same magnitude. On the other hand, the intrusion of mercury into the core of the particles may be explained by the pores in their shells. These pores of few micrometers contribute to part of the curve corresponding to the smaller diameters. The other contributions may be from collapsed capsules or correspond to the space formerly occupied by the water molecules. The peak at around 20 μm remains to explain because it corresponds to a discontinuity in the pores´ distribution. This value is relatively high and there is no reason to attribute it to collapsed capsules because the initial particle size was unimodal and the procedure applied to prepare the sample should affect all components evenly.

5.4 Tests with biopolymers

Dextran, starch and carboxymethyl cellulose were some of the biopolymers that were studied as potential components for the projected composite material. However, they were discarded after testing the respective crosslinking reactions in the presence of hydroxyapatite, one of the main components for the mineral phase of the composite.

Among diverse procedures to crosslink this class of biopolymers and obtain an injectable hydrogel that hardens in situ, the following method is often described in the literature [39,61,121,125,126,129,137,206]. It was tested with the three mentioned

polysaccharides, using adipic acid dihidrazide as crosslinker. First, these water-soluble polymers were oxidized with sodium periodate solution, originating gel precursors with diverse degrees of functionalized groups consisting of aldehyde moieties. The oxidized polymers were separated using a dialysis membrane and freeze dried to preserve them from degradation. Then, appropriate amounts of solutions of adipic acid dihidrazide were added to the dissolved oxidized polymers. These reactions were also made with minerals suspensions in the polymeric solutions. The gelation was only observed in the former cases. Although crosslinking between each of the functionalized biopolymers and dihydrazide could occur in isolate polymeric systems, the same was not observed in the presence of minerals. The oxidized polysaccharides were also applied in tests using collagen and Borax as crosslinkers. The crosslinking should occur between the aldehyde moieties from the former polymers and the amine groups from collagen, with a synergistic effect from Borax [126]. The obtained results were equivalent to those with adipic acid dihidrazide. As soon as hydroxyapatite was added to the system, gelation did not occur. The addition of mineral particles was performed under diverse conditions, but none resulted on crosslinked composites and the obtained products did not produce solid materials.

Chitosan, another polysaccharide, was also tested using a different crosslinking method. After dissolving chitosan in dilute acetic acid solution and neutralizing the resulting solution, chitosan could be easily crosslinked with genipin to originate a hydrogel [39,194,207–209]. However, in the presence of natural hydroxyapatite, the polymer precipitated immediately originating a flocculated mixture, and the crosslinking reaction with genipin could not occur. Anyway, since the rapid flocculating effect could not be avoided, even using low mineral concentrations, the obtained mixture was not injectable. Being the precipitation of chitosan known to occur at pH superior to 6.2, the addition of hydroxyapatite particles (of alkaline character) must be very restricted to obtain a stable suspension. This limitation was not compatible with the projected composite that requires high mineral content to fill vertebral bone defects.

The intention to prepare interpenetrating networks (IPN) from blending PVA with the mentioned biopolymers was also unsuccessful in the presence of minerals. The crosslinking of one, or two polymers, in a binary blend only occurred in systems without the addition of hydroxyapatite.

5.5 Conclusions

The selection of a polymer to apply as the organic matrix of a composite reinforced with hydroxyapatite and barium sulphate was focused in poly(vinyl alcohol) (PVA) based on its chemical composition and physical properties. Polymers with different hydrolysis degrees and diverse molecular weight distributions (9000-10000 mol/g for PVA80, 85000-146000 g/mol for PVA96 and 13000-23000 g/mol for PVA98) were characterized using different techniques.

The preliminary evaluation of the rheologic properties of PVA96 showed that the aqueous solutions of this polymer have a Newtonian behavior, as well as the respective suspensions of minerals, hydroxyapatite and barium sulphate, at concentrations of 20 and 30 wt% relative to the polymer solution at 10 wt%. The suspensions are stable, without phase separation with time, which indicates that there is a high affinity between the minerals and the polymer.

The FTIR spectra of the different PVA samples enables their identification based on the intensity of the characteristic acetate vibrational modes. The bands from the backbone structure are identical for the three samples, but those from the substituent groups are more intense in the PVA80 spectrum than in that of PVA98, having intermediate values in the bands of PVA96. The bands at 1240 and 1730 cm^{-1}, respectively assigned to C-O and C=O stretching from pending acetate groups, are those with greater variation.

The NMR spectra of PVA80 and PVA98 reflect the composition of these polymers and allows to distinguish them based on the chemical shifts from the acetate groups. These peaks are intense in the spectrum of PVA80 and are not observed in that of PVA98. In the proton spectra, the peak at 2.0 ppm is attributed to the methyl hydrogens of acetate and in the carbon-13 spectra, the peaks at 21 ppm and at 180 ppm are due to the carbon atoms from methyl and carbonyl, respectively. The carbon-13 spectra give also information about the tacticity of both polymers. The triplet centered at 66 ppm indicates slightly different proportions of isotatic (mm), heterotactic (mr) and syndiotactic (rr) triads for each polymer. The peaks in the 38-45 ppm region reflect the abundance of acetate groups and their distribution along the backbone.

The DSC-TGA analysis of PVA shows that the glass transition occurs around 50 ºC and the melting temperature is approximately 190 ºC for PVA80 and 220 ºC for PVA98. This shows that the inter-molecular forces in PVA98 are stronger than in PVA80, as expected from the better structural packing of the former. The degradation profile of

PVA occurs in two consecutive steps, starting with the stripping of the side chains (280-320 ºC) and the carbon backbone for higher values (380-480 ºC). Regardless the proportion of acetate groups, the first process causes a mass loss of 70-80 wt% and the second is inferior to 20 wt%.

The glass transition temperature of PVA98 was determined with higher accuracy using DMTA. The obtained value, 39.9 ºC is inferior to that obtained by DSC. This difference alerts for the fact that not only the instrumental conditions may influence the measurement of thermal properties, but also the previous manipulation of the samples, particularly of polymeric nature. For very accurate results, polymers are usually submitted to standardized thermal cycles in order to erase the largest effect caused by temperature variations. After those cycles, the thermal properties converge to more stable parameters. This kind of treatment was not performed with any of the PVA samples. Thus, the thermal history of PVA98 certainly reflects the structural rearrangements associated with sample preparation for DMTA. It was dissolved with distilled water at 90 ºC, then cooled to room temperature and next, it was dried at 50 ºC. XRD may be used to evaluate the influence of these conditions on the structure of polymers. The diffractogram of PVA98 was obtained using the sample as received, in powder form, like in DSC-TGA characterization. The diffraction profile corresponds to a semi-crystalline material, hence the amorphous fraction originates the glass transition and the crystalline fraction, the melting process revealed in the heat flow curve by DSC.

Other structural details relative to PVA80 and PVA 98 were obtained from the objective of crosslinking the polymer in acidic medium, using telechelic-PVA as alternative to conventional di-aldeydes (as glyoxal or glutaraldeyde). The synthesis of telechelic-PVA starts from the oxidation of vicinal OH groups in the polymer structure. In order to find the right stoichiometry for the reaction, the number of diol groups in PVA80 and PVA98 were determined by volumetric titration. The estimated number, converted to molecular weight of each oxidized PVA fragment, tel-PVA80 and tel-PVA98, was compared with measurements using SEC. This technique was also used to analyze the as-received polymers and to compare with data from the suppliers.

Despite the SEC values of the molecular weight of the polymers before oxidation were not coincident with those from the technical data, they corresponded to the expected range. The experimental value for PVA80 (16.000 g/mol) was higher, and that for PVA98 (18.000 g/mol) was lower, than the respective described values of 9.000-10.000 g/mol and 18.000-23.000 g/mol. The value obtained for the oxidized sample of PVA80, tel-PVA80 with 2800 g/mol, was very close to the estimated from the titration

(2000 g/mol). For tel-PVA98, the obtained value (2900 g/mol) was also close to that previously estimated (2200 g/mol). These results indicate that, in average, PVA80 and PVA98 have a similar distribution of vicinal diol groups along the backbone structure.

The crosslinking reaction at acidic pH of PVA80 with tel-PVA80, and PVA98 with tel-PVA98, was tested under diverse experimental conditions but, the results did not correspond to the objectives. The only way to obtain a crosslinked material, insoluble in water, has been after solvent extraction (by drying or freeze-drying). It was never possible to obtain a hydrogel with adequate characteristics for this study. Moreover, with the addition of ceramic particles, hydroxyapatite and barium sulphate, the blended materials did not show any evolution towards the solidification of the organic components. The crosslinking reaction may have been stopped by the steric hindrance, along with the alkaline environment caused by those minerals.

The crosslinking of PVA was also tested in alkaline environment using Borax as crosslinker. The characterization using FTIR and TGA confirmed the formation of a crosslinked material. The thermal profile presents significant differences relative to the original polymer. The degradation of the crosslinked PVA96-Borax occurs in three steps. After dehydration and pyrolysis of small organic fragments released from the reaction, the fraction relative to the stripping of lateral groups is around 20 wt%, much inferior to the 70-80 wt% from the non-crosslinked polymer. The last step leads to a greater mass loss, around 50 wt% compared with 15 wt%, at higher temperatures than the original polymer, which may be justified by the backbone structure having its lateral groups linked to borate. The problem with this method to crosslink PVA with Borax is that the reaction occurs too fast, even in the presence of mineral particles of hydroxyapatite suspended in the polymer solution.

The use of microcapsules produced with poly(lactic acid) (PLA) filled with an aqueous solution of Borax was tested as a strategy to control the kinetics of the crosslinking reaction between PLA and borate. A series of microcapsules were produced using the w/o/w methodology with different proportions of reagents. The capsules were characterized regarding particle size distribution, microstructure and porosity. The obtained standard PLA microcapsules (mC-S), unfilled, have perfect spherical shape with size distribution around 56 μm, and a smooth continuous surface without pores across the shell. Similar capsules containing a reference amount of Borax were taken as the standard for the filled ones (mC-BS). These present slightly larger sizes, spherical bur irregular shape, pores across the shell and smooth surface with collision marks. Four variations from these were obtained (mC-B1, mC-B2, mC-B3 and mC-B4), whether by using, respectively, the double volume of water of the Borax solution, half of the

surfactant (PVA), the double PLA, or the double PLA and double PVA simultaneously. All these particles are hollow and possess pores across the shell. The porosity and the irregularities at the surface may derive from the disruption caused by the reaction between Borax and PVA, the surfactant. The particle size distribution, as well as the surface roughness, are dependent of the water volume, as observed in capsules mC-B1 that measure around 224 μm and have a ruffled appearance. This increase of the water volume probably expands the pores for diameters around 5 μm, but maintains the thickness of the shell relative to mC-BS. The decrease of the surfactant, while the other components are constant, has little effect on the mC-B2 particles. On the other hand, the increase in the amount of PLA, both in mC-B3 and mC-B4, cause a significant augment in the particle size (reaching 400 μm) with is more notorious in the latter case due to the additional surfactant of the surface. The thickness of the shell is also increased, and the surface becomes even rougher, with a spongy appearance.

An identical procedure was applied in the synthesis of microcapsules filled with Borax and HEMA. The addition of HEMA to the shell (mC-BH1) or to the filler (mC-BH2) of Borax-containing capsules originates capsules of particle size distributions close to the standard mC-BS. The appearance of the surface is smooth, suggesting that HEMA blocks the effect of Borax over the surfactant PVA, except when the filler volume is augmented (mC-BH3), giving a spongy appearance to the particles. The pores of this series of mC-BH microcapsules have smaller dimensions than those without HEMA.

The role of the structural properties of some of the Borax-containing microcapsules was tested in crosslinking tests of PVA suspensions with hydroxyapatite. Since the gelation occurred too fast, the kinetics of delivery was tested with the simplest possible method. It showed, as expected, that capsules with the double thickness and irregular surface can deliver one fourth of Borax to the surrounding environment.

The acquired experience in the synthesis of microcapsules enables to manipulate features as size, porosity, thickness and roughness to obtain tailored materials with a predictable behavior. Although the results retrieved from the application of microcapsules did not match the objectives relative to the crosslinking of PVA with Borax, these capsules may be used to deliver other molecules in a controlled way. That is the case of HEMA, a reagent of interest in this study. The application of Borax-containing capsules that possess HEMA in the core, or in the shell, may be used mostly because of the HEMA content and structural properties, not because of Borax.

The microcapsules may also serve the purpose of creating porosity inside a material, for instance, inside the bone graft composite of this work. Being composed of

a biodegradable polymer that decomposes into non-toxic components and having appropriate dimensions to cell colonization, the obtained microcapsules have potential to enhance some of the conditions that influence osteogenesis.

To conclude, the polymeric components which were selected to proceed have been PVA80 and PVA98, being PVA96 removed from the experimental plans. Since the selected polymers have approximate molecular weights, the hydrolysis degree is the main variable that may influence the properties of the composite matrix. The PLA microcapsules (with or without Borax and HEMA) were also selected to create porosity and eventually to deliver specific molecules to the composite matrix.

6 Synthesis and characterization of an injectable *in situ* solidifying composite for bone repair

6.1 Introduction

The present chapter describes the experimental research work leading to the synthesis of an injectable material able to solidify *in situ*, for vertebral repair through the surgical procedure of kyphoplasty. The research included the objective to obtain a new material possessing many properties of natural bone after solidification.

The multiple requirements for such material determined the preliminary selection of bone-derived hydroxyapatite (HA) and barium sulphate to constitute the mineral phase of the composite. The former was selected to mimic the composition of natural bone and the latter, to provide radiocontrast during surgery. Carbonated hydroxyapatite obtained from bovine bone calcined at 600 ºC (HABov 600), was considered as the most adequate for bone grafting. However, this study also included non-carbonated hydroxyapatite from bovine bone calcined at 900 ºC (HABov 900) and equivalent minerals of synthetic origin (Calcibon and Inbone, respectively). These other minerals were included to evaluate alternatives for HABov 600, if needed.

The main organic component selected for the composite matrix, which compares with collagen in natural bone, has been poly (vinyl alcohol) (PVA). The selection of polymers with different hydrolysis degrees (80% in PVA80 and 98% in PVA98) enabled to evaluate the effect of acetate content in the properties of studied materials. One of the reasons for the choice of PVA was related to its affinity with the minerals that were mandatory in this study. The aqueous solutions of PVA provided appropriate support to high concentrations of the minerals in particle form, being obtained homogeneous suspensions able to be injected without phase separation.

The other type of organic component that was decided to test has been the microcapsules made of poly (acid lactic) (PLA). These could be used not only as conventional drugs delivery devices for antibiotics or many other products, but as a source of porosity as well. The PLA microcapsules could be synthesized to meet adequate structural properties for the different purposes. However, the microcapsules should only be included in the composite after finding an effective formulation.

The most concerning issue with the chosen starting materials has been the difficulty to find a way to crosslink the polymer suspension, or solidify it by other means, under diverse specific conditions that could not be altered. These conditions include chemical and physical properties of the reagents, but also to conditions related to the method and site of application.

The strategy to solve this problem required extensive investigation that was much more based in new practical experiments than in replicating procedures from the literature. Naturally, previous works from different fields provided important guidelines to follow. More frequently, however, the literature was more useful in assisting the

interpretation of the results than to inspire what to do. Overall, most of the advances in this research resulted from trial and error sequences that acted as a matrix of decisions. The results reported hereafter reflect the studies that allowed to reach the objectives of this research. The sequence of chemical reactions with new reagents that were successively introduced originated a series of intermediate products difficult to characterize despite the use of diverse techniques. This was because the chemical alterations were masked by the major components involved in the synthesis of the composites. The interpretation of many of intermediate results required the comparative analysis of the final products (at the end of the synthesis path), to look backwards for explanations.

After many different attempts to find suitable reagents to obtain an injectable composite with all the properties already described, a new idea turned this investigation to a new direction. The new approach was based on the synthesis of an interpenetrating network (IPN) by addition of gelatin (from hydrolysis of collagen) to the PVA suspension with minerals, and crosslink the protein using a carbodiimide (CDI). The use of carbodiimides as crosslinkers between the carboxylic and the amine groups of adjacent molecules, with formation of new amide bonds, is a conventional method widely applied in biochemistry [126,192,210–212]. Although the most logical procedure would be to add the CDI crosslinker to all the other mixed reagents, the applied procedure has been different. The carbodiimide was added to the polymer solution, before the hydroxyapatite and the hydrolyzed collagen. Surprisingly, the addition of the HA minerals to the PVA solution with CDI evidenced the existence of a chemical reaction because there were gas bubbles emerging from the suspension. This observation, combined with subsequent achievements (described latter in this document), motivated a new starting point for this research.

The main steps of the new synthesis method involved the following procedures:

1- Reaction of PVA with a carbodiimide (CDI) to obtain PVA-CDI
2- Reaction of PVA-CDI with hydroxyapatite (HA) to obtain PVA-CDI-HA
3- Reaction of PVA-CDI-HA mixed with $BaSO_4$, $K_2S_8O_2$, HEMA and hydrolyzed collagen

These procedures were performed under different experimental conditions regarding preliminary reagents preparation, order of addition and environment, since the intermediate materials must be combined to originate a solid material at body temperature, inside a closed space. To monitor the whole process, the applied techniques have been NMR (solution and solid-state CP-MAS; proton and carbon-13), FTIR, LDS, XRD, DSC.TGA, DMTA, SEM and optic microscopy. The most promising samples were tested regarding swelling, degradation in PBS; biocompatibility and

hemocompatibility. As mentioned, there are many experimental results that do not provide evidences of the applied procedures in virtue of the masking effect mostly from the minerals. Thus, the inclusion of all that information is not needed nor would be important to analyze in detail. The most significant results that enable the detection of chemical or physical alterations are presented in this chapter.

6.2 PVA reaction with CDI

6.2.1 Procedure

The synthesis procedure of the composite started from the chemical reaction between PVA (PVA80 and PVA98) and a biocompatible water-soluble carbodiimide (N-cyclohexyl-N´-(2-morpholinoethyl) carbodiimide methyl-p-toluenesulfonate; CDI).

Stock solutions of PVA-CDI

The stock solutions of PVA-CDI were prepared as follows: aqueous solutions of PVA80 and PVA98 were prepared with a concentration of 20 wt% (around 0.01 M and 0.005 M, respectively) and CDI with a concentration of 0.05 M. To each volume of 20 ml of PVA, the amount of added CDI solution was 3 ml. The mixed solutions (PVA and CDI) were stirred at room temperature during 48 to 96 hours. The obtained samples are named as 20PVA80-3CDI and 20PVA98-3CDI to describe the composition (20 wt% PVA and 0.05 M CDI) and volume proportion (20:3) of the reagents.

The diverse PVA-CDI samples and the respective reagents were analyzed using FTIR (Figure 6.1 and 6.2) and NMR (Figures 6.3 – 6.6) spectroscopies. These techniques required the previous drying of aliquots from both solutions, not only to enable the solutes detection by FTIR, but also replace the ordinary distilled water by deuterated water for NMR.

6.2.2 Characterization

FTIR

The vibrational spectrum of 20PVA80-3CDI is compared with the spectrum of PVA80, the starting polymer, and with the spectrum of water (Figure 6.1). The spectra from both polymeric samples are almost coincident, being the relative intensity of the PVA-CDI bands systematically more intense than those from PVA, except in the 3000-4000 cm^{-1} region where the relative intensity is inverse. The main differences between the spectra are observed at the typical wavenumbers for H-O-H bending (1642 cm^{-1}) and OH stretching (broad band at 3000-4000 cm^{-1}) modes of the water molecules. In the

spectrum of PVA-CDI, the band at 1642 cm^{-1} is clearly originated from remaining water molecules entrapped in the sample that was dried before analysis. It should be expected to find the same tendency at 3000-4000 cm^{-1}. However, the broad band from OH stretching has lower intensity than the PVA spectrum. This indicates that there are less OH groups linked to the backbone of the polymer in PVA-CDI, as a result from the reaction between PVA and CDI.

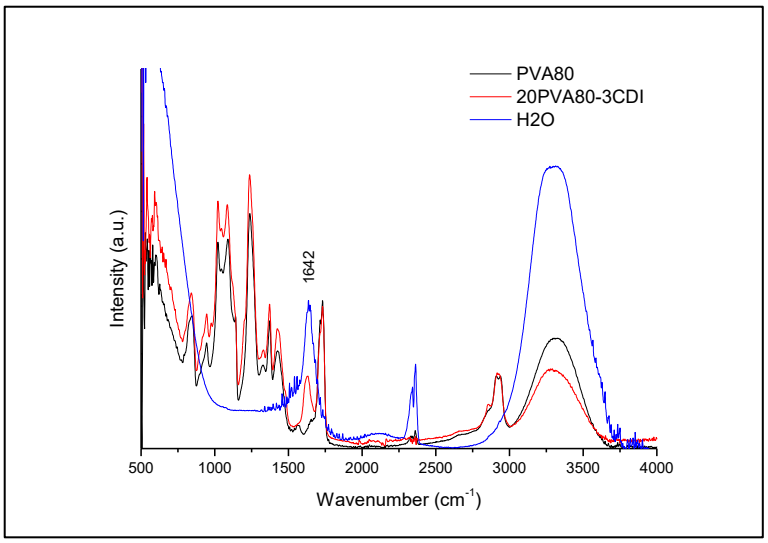

Figure 6.1 – FTIR spectra of PVA80, 20PVA80-3CDI and water.

The spectra of 20PVA98-3CDI and of PVA98 presented in Figure 6.2 provide less information. The ratio between the intensity of all bands of PVA-CDI/PVA is 3 and there is only a single new band in the PVA-CDI spectrum. That is the band at 1642 cm^{-1} from the water molecules that remained in the dried sample. Thus, in this case, the results do not evidence molecular changes in PVA98 due to the reaction with CDI.

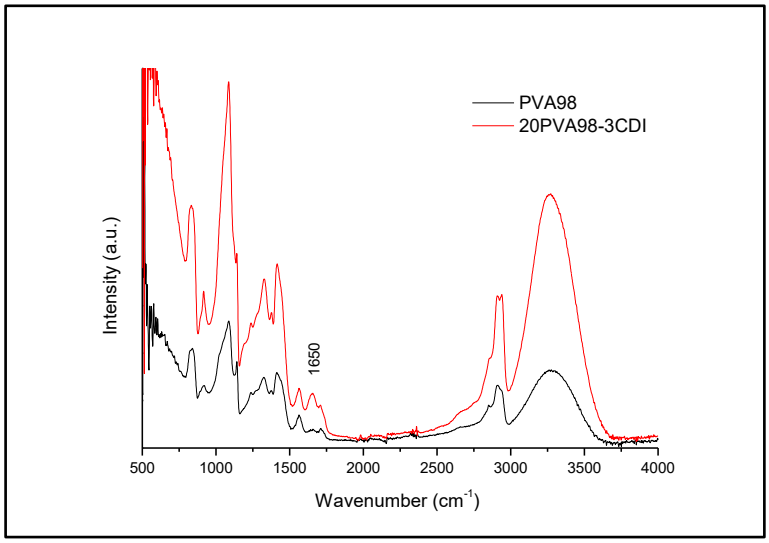

Figure 6.2 – FTIR spectra of PVA98 and 20PVA98-3CDI.

NMR

Proton and ^{13}C NMR spectroscopy was used to characterize the carbodiimide CDI, 20PVA80-3CDI and 20PVA98-3CDI, all dissolved in D_20 at adequate concentrations (around 20 mg/ml for ^{1}H spectra and 60 mg/ml for ^{13}C spectra). The spectra were registered at 25 ºC and are presented in Figures 6.3-6.4 (proton-NMR) and in Figures 6.5-6.7 (carbon13-NMR). Both spectra from CDI are not attributed because they are not relevant for the discussion of the other spectra, except for observation of the presence or absence of peaks.

The proton-NMR spectrum of the PVA-CDI samples are compared in Figure 6.3. Both the spectrum of 20PVA80-3CDI and that of 20PVA98-3CDI are coincident with the spectra of the starting polymers PVA80 and PVA98 (Figure 5.5; Chapter 5), except regarding the appearance of a new intense peak at 2.15 ppm. This peak is not from the carbodiimide (Figure 6.4) because there are no signals from the free reagent in the PVA-CDI spectra. As described in Chapter 5, in both spectra, the peaks at 2.0 ppm are attributed to methyl groups mostly from the acetate substituents. The terminal methyl groups of the polymer also contribute to this peak. The chemical shift at 2.15 ppm, the only new peak, may derive from the formation of a new bond, with hydrogen atoms less shielded than those from methyl groups of the pending acetates.

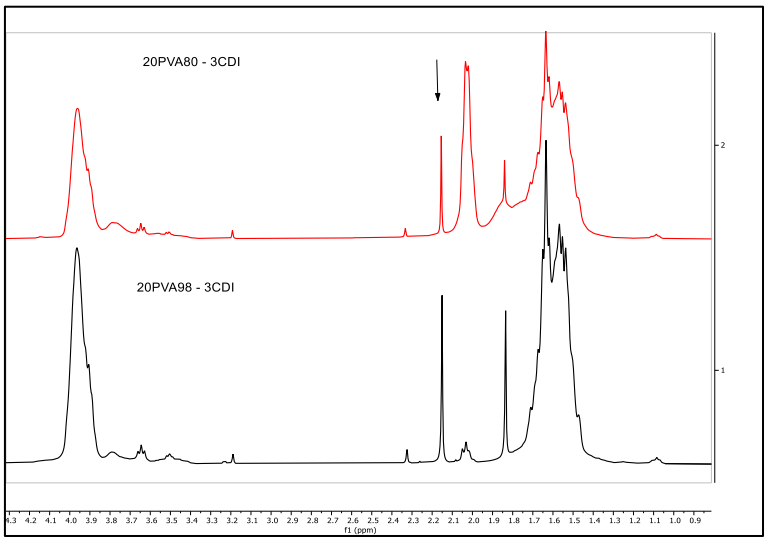

Figure 6.3 – Proton-NMR spectra of 20PVA80-3CDI and 20PVA98-3CDI. The arrow points to a new peak relative to the spectra of PVA80 and PVA98 before reaction with CDI.

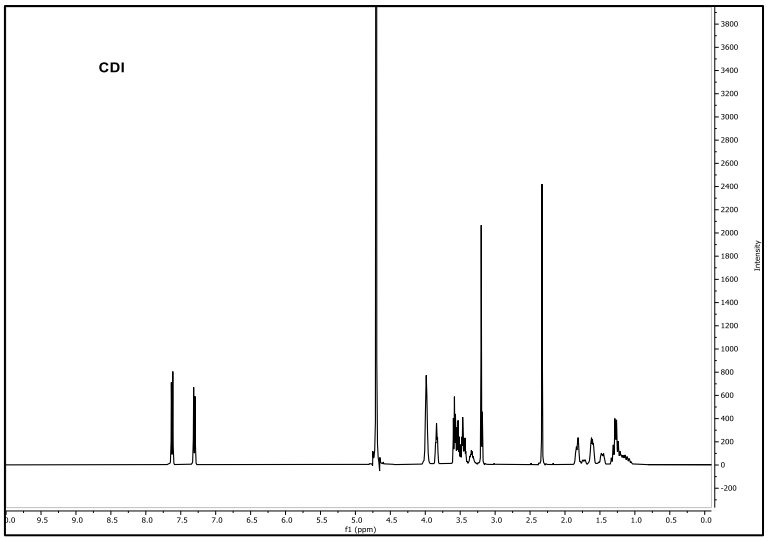

Figure 6.4 - Proton-NMR spectrum of CDI.

As for the carbon-13 NMR results, the spectra from 20PVA80-3CDI and 20PVA98-3CDI are displayed in Figures 6.5 (full scale) and 6.6 (22-70 ppm). In these spectra, the peak from carbonyl (typically around 180 ppm) is not observed and both present peaks at four different regions in the range 0-70 ppm.

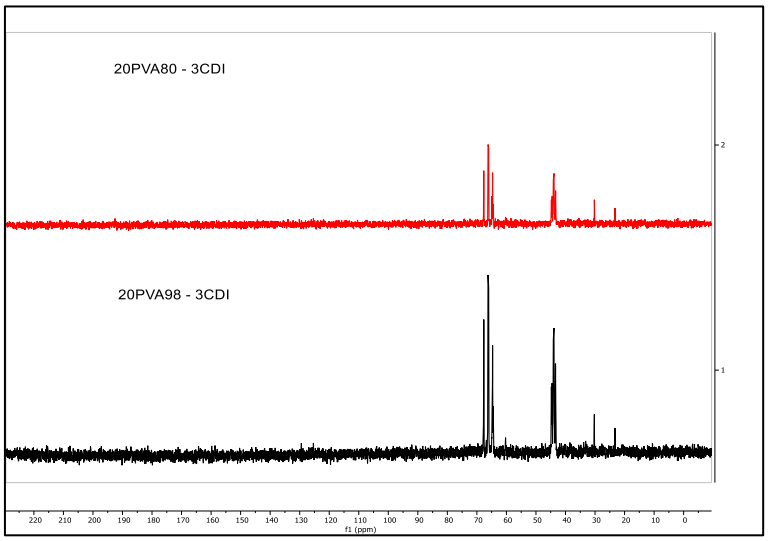

Figure 6.5– Carbon13-NMR spectra of 20PVA80-3CDI and 20PVA98-3CDI.

Compared to the ^{13}C spectra of PVA80 and PVA98 (Figures 5.6 and 5.7; Chapter 5), the triplet around 66 ppm assigned to methine (-CH-) carbon and the multiplet around 44 ppm assigned to methylene carbon (-CH_2-) also occur in both spectra of PVA-CDI, with some differences in the relative intensity of the peaks that may be related to the tacticity of the polymers. Moreover, there is a new peak around 30 ppm in both spectra of PVA-CDI, and the peak at 23 ppm seems shifted from that at 21 ppm (assigned to methyl carbon) in the spectra of the original polymers. Finally, the low

intensity peaks associated to acetate groups of PVA80 (at 38 and 42 ppm) are no longer observed in the spectrum of 20PVA80-3CDI. The peaks from the CDI spectrum (Figure 6.7) are also absent in the spectra of both PVA-CDI samples, indicating that the concentration of free carbodiimide is not enough to be detected.

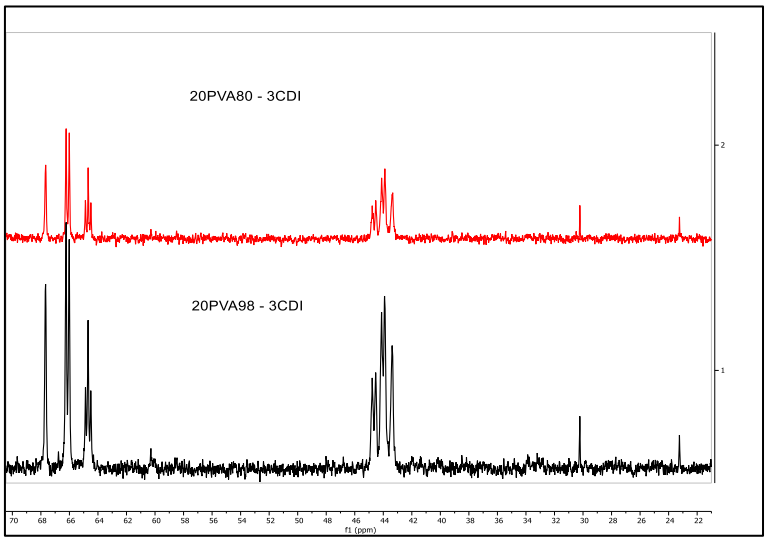

Figure 6.6 - Carbon13-NMR spectra of 20PVA80-3CDI and 20PVA98-3CDI.

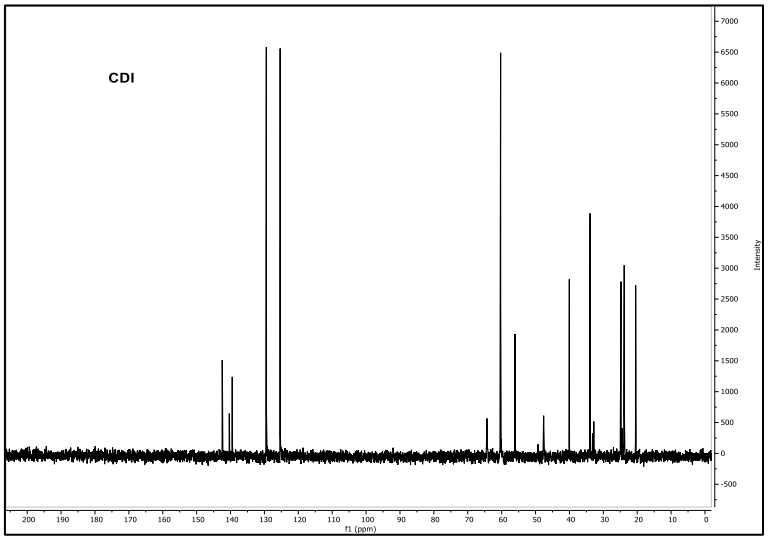

Figure 6.7 – Carbon13-NMR spectrum of CDI.

The results obtained with carbon13-NMR suggest that the reaction of PVA with CDI originates the loss of the acetate groups in both polymers because the respective typical peaks (at 180, 42 and 38 ppm) are not observed. On the other hand, the new peak at 30 ppm may derive from a new bond with carbon atoms in a chemical environment that provides a shieling effect intermediate between those of CH_3 and CH_2.

Combining ^{1}H and ^{13}C spectra, the hypothesis that the reaction between PVA and CDI lead to the loss of acetate is not confirmed. The results are contradictory. The proton peaks from methyl groups of acetate remain in the spectra, whereas the

respective peaks from carbon disappear after the reaction. Nonetheless, both techniques agree regarding the formation of a new chemical bond because of new peaks in all the NMR spectra, that are not from free carbodiimide. The hypothesis of a chemical reaction can be explained by the effect of activation of the hydroxide groups of PVA through the carbodiimide [211][, but the mechanism can not be deduced from the obtained results.

Since the spectral results could not elucidate about the interaction between PVA and CDI, further investigations were preformed to confirm if there was a chemical reaction between PVA and CDI. This research focused the next stage of the synthetic pathway by analyzing the effect of the complex PVA-CDI over hydroxyapatite.

6.3 PVA-CDI reaction with hydroxyapatite

The following stage in the synthesis procedure involves the addition of hydroxyapatite to the solution of PVA, after its reaction with CDI for 48-96 hours.

The variables which were studied in this reaction have been the hydrolysis degree of PVA and the chemical composition of the apatite minerals. The selected polymers were PVA80 and PVA98. The minerals of natural origin were HABov600 and HABov900, and those of synthetic origin were Calcibon and Inbone, providing carbonated and non-carbonated hydroxyapatite for the reaction with 20PVA80-3CDI and 20PVA98-3CDI, previously prepared.

From this point forward, all the samples of PVA-CDI type are aliquots weighting 3.0 g from stock solutions composed of 20 ml aqueous solutions of PVA80 or PVA98 with a concentration of 20 wt%, mixed with 3 ml CDI with a 0.05 M concentration.

6.3.1 Bone-derived carbonated and non-carbonated hydroxyapatite

6.3.1.1 Procedure

The preliminary tests involved the addition of 0.6 g of bone-derived hydroxyapatite to the PVA solutions, and to the PVA-CDI solutions. Each polymeric sample composition was composed of 3.0 g of aqueous solutions of PVA80 or PVA98 with a concentration of 20 wt%, or 3.0 g of 20PVA80-3CDI and 20PVA98-3CDI previously prepared.

The reaction between PVA-CDI and bone-derived hydroxyapatite (with and without carbonate content) is evidenced by some gas release from the samples, as shown in Figure 6.8. The mineral suspensions in PVA80 and PVA98 aqueous solutions (Figure 6.8-left) are homogeneous viscous fluids with no signs of chemical reactions,

whereas the appearance of hydroxyapatite suspensions in 20PVA80-3CDI and 20PVA98-3CDI (Figure 6.8-right) suggests the reactivity of the components involved.

Figure 6.8 – Suspensions of HABov600 and HABov900 in aqueous solutions of PVA80 and PVA98 (left), and in aqueous solutions of 20PVA80-3CDI and 20PVA98-3CDI (right). In both cases, the top row corresponds to carbonated hydroxyapatite, and the bottom row, to non-carbonated hydroxyapatite.

In order to investigate if PVA had reacted with CDI and the resulting complex (PVA-CDI) was needed to originate a reaction with hydroxyapatite, a series of comparative tests schematically represented in Figure 6.9 were performed.

Hydrolyzed collagen was used is some of those experiments to test if CDI carbodiimide would react with PVA in the presence of the protein. Since collagen is insoluble in water, it required a hydrolysis process to obtain soluble collagen-derived proteins (gelatin) [213–215], enabling its addition to the solutions of PVA.

Stock solutions of hydrolyzed collagen

The applied procedure was replicated at latter stages of this work, being obtained stock solutions to be consumed in diverse experiments. The hydrolysis of 100 mg of collagen was made in 10 ml HCl 0.1 M and in 10 ml NaOH 0.1 M environment, originating gelatin type A (acid hydrolysis) or gelatin type B (alkaline hydrolysis), respectively. Then, the ionized gelatin samples were neutralized with the opposite reagents.

Diagram of Figure 6.9 represents a series of experiments involving PVA (PVA80 and PVA98), CDI, hydrolyzed collagen (type A and type B) and hydroxyapatite (HABov600 and HABov900). From left to right, it displays the sequence of reagents that were added to PVA solutions, and the time period of each process. The symbols for collagen and for hydroxyapatite represent two variables each.

In all cases, the used quantities were 3.0 ml of PVA80 solution 20 wt% in water, 3.0 ml of PVA98 solution 20 wt% in water, 450 μl of CDI 0.05 M, 500 μl of hydrolyzed collagen type A, 500 μl of hydrolyzed collagen type B, 0.6 g HABov600 and 0.6 g

HABov900. The outcome of each trial is marked as positive with a V, and negative with a X, relative to the observation of gas release.

The first three rows of the diagram are related to the use of PVA80, and the next three to PVA98. The explanations for the second group case are equivalent to the first one.

First row – This row represents two sequences of tests because hydroxyapatite corresponds to two variables. Two solutions of PVA80 were mixed with CDI for 48-96 hours. Next, the addition of HABov600 and HABov900 to each previous solution led both to gas release, the visible sign of a chemical reaction. The gas release started a few hours after the addition of the minerals and continued to be observed for around 48 hours.

Second row – This row represents four experiments because hydrolyzed collagen corresponds to two variables and hydroxyapatite also corresponds to two variables. Thus, the starting samples were four solutions of PVA80. Each PVA80 solution was mixed with CDI and with hydrolyzed collagen (type A and type B), being these compositions mixed for 48-96 hours. Next, HABov600 was added to the two different solutions, as well as HABov900 which was also added to the other two solutions. The addition of hydroxyapatite led to gas release in all four samples, the visible sign of a chemical reaction.

Third row – This row represents two experiments. In one of the tests, PVA80 was blended with HABov600 and in another test, with HABov900. Both were mixed for 48-96 hours. Next, the addition of CDI to each solution did not originate any gas release. This indicates that no chemical reaction occurred.

In the next rows, the observations were equivalent using PVA98 as the starting polymer.

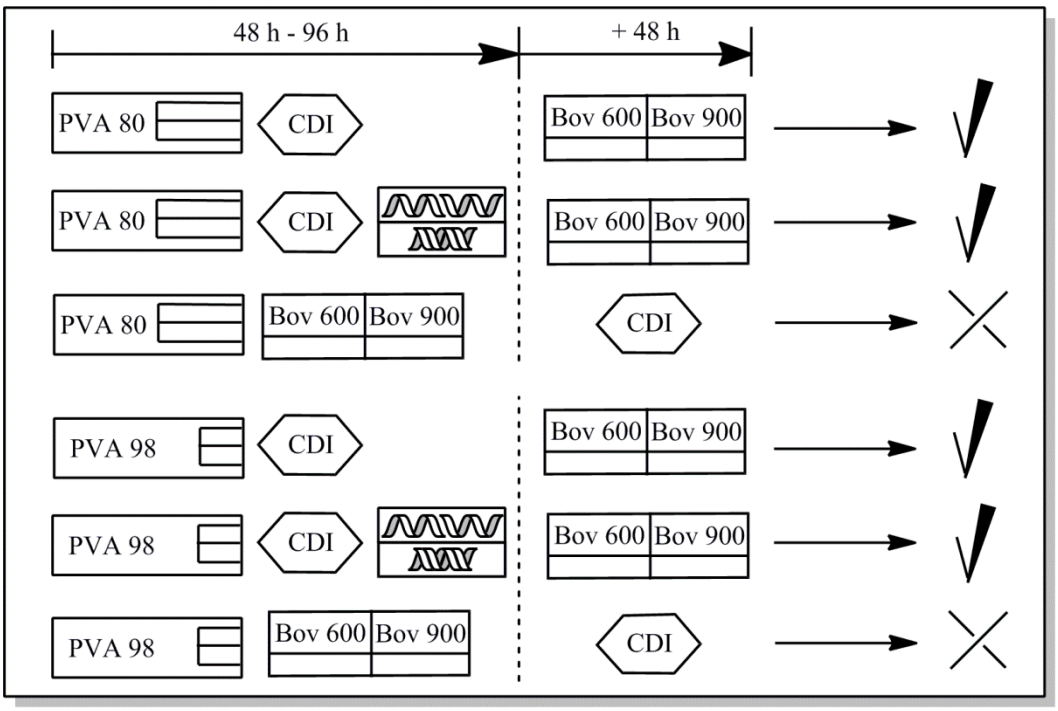

Figure 6.9 – Diagram representing sequences of addition of reagents (CDI, hydrolyzed collagen type A and type B, and natural hydroxyapatite HABov600 and HABov900) to PVA80 and PVA98. The outcome is gas release (V) or no reaction (X).

The obtained results show that the gas release only occurs when hydroxyapatite is added to a solution of PVA mixed with CDI for a certain time period. The presence of a small volume of hydrolyzed collagen in the solutions of PVA with CDI does not interfere. These tests also show that the addition of CDI to the suspensions of HA in PVA solutions has a different effect. In this case, the gas release does not occur. This may be explained by the large proportion of mineral particles in the suspension (0.6 g HA: 3.0 g PVA) that prevent the contact between PVA and CDI.

These observations suggest that PVA effectively reacts with CDI, and the PVA-CDI complex is necessary to originate a chemical reaction with bone-derived hydroxyapatite, whether containing carbonate or not. The source of the released gas is a question of debate because it has happened with the two types of mineral (carbonated and non-carbonated), as well as with PVA polymers having different acetate content.

The result of that chemical reaction would be a material of type PVA-CDI-HA, corresponding to a hybrid organo-ceramic new product.

6.3.1.2 Characterization

Bone-derived carbonated hydroxyapatite

SEM

The samples showed in Figure 6.8 were dried and observed using SEM microscopy. The images displayed in Figure 6.10 correspond to the HABov600 suspensions in PVA98, and the images in Figure 6.11 correspond to suspensions of the same HABov600 minerals in 20PVA98-3CDI.

The suspension of HABov600 in PVA98 (Figure 6.10) has a heterogeneous appearance since the mineral particles present a broad particle size distribution. At a magnification of 350x, there are many particles with large dimensions (some particles reach around 50 μm) surrounded with smaller ones. Increasing the magnification to 7500x, the smaller particles sizes are inferior to 1 μm and their distribution in the material is not continuous. These particles are surrounded by the polymeric matrix which can be observed separately from the minerals.

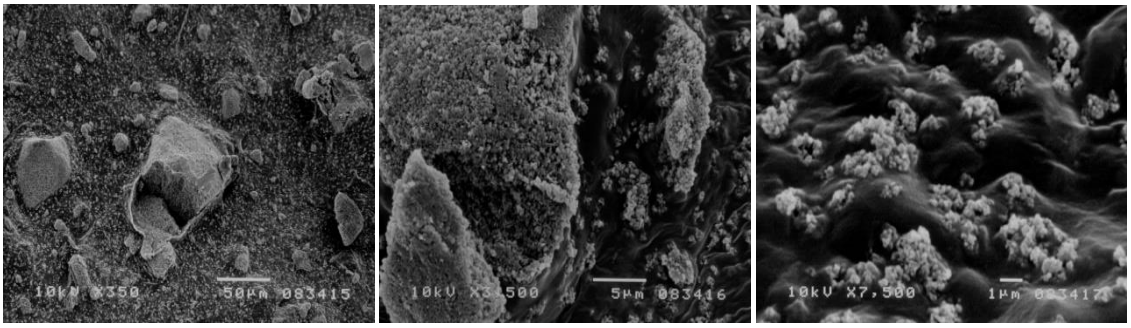

Figure 6.10 – Suspension of HABov600 in PVA98.

The suspension of HABov600 in 20PVA98-3CDI (Figure 6.11) has a homogeneous appearance, with the mineral particles having similar sizes and being evenly distributed in the polymeric matrix. At a magnification of 500x, the particles have similar dimensions, being necessary to apply higher magnifications (7500x) to measure their approximate size, inferior to 1 μm. In this sample, the polymer matrix is not observed alone, separated from the particles. The polymer surrounds each particle, as a coating material.

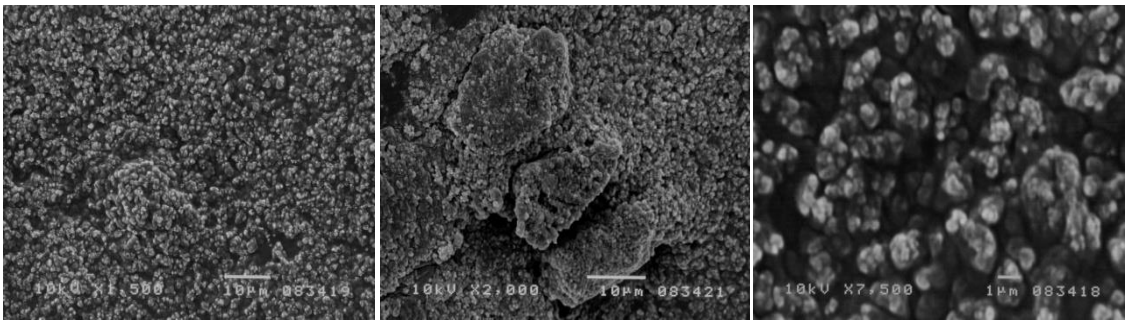

Figure 6.11 - Suspension of HABov600 in 20PVA98-3CDI.

The differences observed in SEM images show that the polymeric matrix composition influences the particle size distribution of the hydroxyapatite particles. The mineral suspensions in PVA-CDI type of matrix present systematically sharper distributions of particles sizes, with smaller particles than in PVA matrix.

LDS

The particle size distribution of hydroxyapatite suspensions in diverse solutions of potential reagents (Figure 6.12) was examined to investigate the results obtained so far, to understand the observations at macro and micro scales of the effect of PVA-CDI in the size of the mineral particles.

Starting with natural carbonated hydroxyapatite (HABov600), 0.6 g of hydroxyapatite was dispersed in 3.0 g of water (reference sample) and it was mixed with 3.0 g aqueous solutions of PVA80 (20 wt%), 20PVA80-3CDI, PVA98 (20 wt%), 20PVA98-3CDI, CDI (450 µl 0.05 M in 3 ml of water) and urea (450 µl 0.05 M in 3 ml of water). These compositions were selected to compare, in equivalent conditions, the influence of the PVA polymers (before and after the possible reaction with CDI). The introduction of urea, in this study, was motivated by its known effect on tailoring the particle size of some minerals and also as a linker between hydroxyapatite and organic molecules [33,216–218]. The period of mixture was 48 hours.

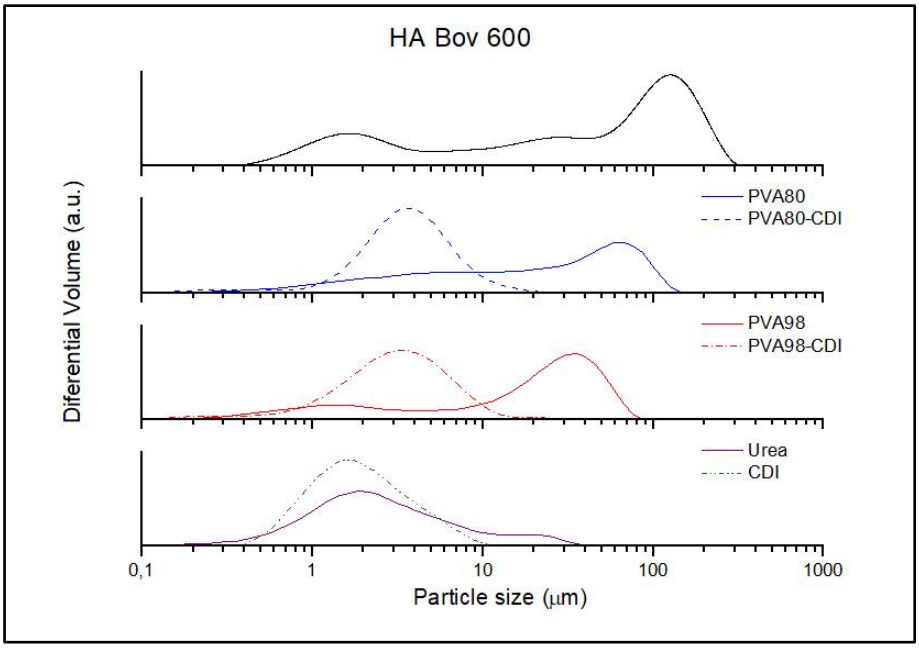

Figure 6.12 – Particle size distribution of natural carbonated hydroxyapatite (HABov600) after 48 hours in water and in aqueous solutions of PVA80, 20PVA80-3CDI, PVA98, 20PVA98-3CDI, CDI and urea.

The graphs of Figure 6.12 represent the particle size distribution of the HABov600 sample in diverse media.

The reference sample (first row) presents a near bi-modal distribution, with particles in the whole range from 0.4 μm to 300 μm. The distribution curve presents its maximum in the 60-200 μm range, indicating that most particles measure around 130 μm. Lower sizes around 0.2-0.2 μm and around 20-30 μm constitute also a significant part of the sample.

The second row represents the mineral particles suspended in PVA80 and in 20PVA80-3CDI. Using the original PVA80 polymer, the shape of the distribution curve is very similar to that obtained with just water. However, the range of particle sizes is narrower, from 0.3 μm to 200 μm, with maximum at 60-80 μm. The profile obtained with the PVA-CDI solution is a gaussian curve ranging from 0.1 μm to 20 μm, with maximum at 4 μm. These results show the influence of PVA-CDI on the significant decrease of HABov600 particles size relative to the PVA, suggesting that it derives from the action of CDI.

The third row displays the distribution curves of HABov600 suspended in PVA98 and in 20PVA98-3CDI. The global shape of the distribution curve relative to PVA98 is also similar to the reference sample, but the values are shifted to the range from 0.3 μm to 100 μm, with maximum at around 40 μm. Using the PVA-CDI solution, the size distribution of the mineral particles is represented by a gaussian centered at 3 μm, in the 0.3 μm to 200 μm range. The average particle size of the mineral decreases in the

presence of PVA-CDI, relative to PVA alone. The shift to lower sizes observed in the distribution curve of the hydroxyapatite particles is probably related to the CDI component.

The fourth row presents the results obtained with HABov600 suspensions in CDI and in urea solutions. Both distribution curves range from 0.3 μm to 10 μm, although that relative to urea medium also denotes a small proportion of minerals with 10-30 μm. These two resembling distribution curves, with maxima at 2 μm, demonstrate that CDI and urea originate a significant particle size decrease of HABov600 relative to the reference sample.

This set of results obtained with LDS enables to corroborate the size values of HABov600 particles that were estimated using SEM. Moreover, these results evidence that carbodiimide CDI is effectively involved in the decrease of particle size of bone-derived carbonated hydroxyapatite.

The conjunction of the analyzed data from spectroscopic techniques (FTIR, ^{1}H-NMR, ^{13}C-NMR and LDS) and SEM imaging confirm that there are chemical reactions involved in the two first steps of the composite synthesis. Thus, the materials obtained at this stage were submitted to further analysis to try to characterize them chemically. These materials, generically of type PVA-CDI-HA, were analyzed with DSC-TGA, DMTA, FTIR and XRD. These techniques did not provide helpful results because the high content of hydroxyapatite (0.6 g HA in 3.0 g of PVA-CDI) in the materials superimposes its signals over the others, and the chemical changes from the reactions are barely detected. Nevertheless, some results from FTIR and XRD are presented to exemplify the situation.

As for the physical characterization regarding particle size, the materials containing HABov600 correspond to results already presented. The other types of hydroxyapatite will be discussed after concluding the analysis of FTIR and XRD results concerning that bone-derived carbonated mineral.

FTIR

Infrared vibrational spectroscopy was applied to investigate the chemical composition of materials type PVA-CDI-HA, namely the composition represented by 20PVA80-3CDI-HA. Figure 6.13 illustrates its spectrum, together with those from CDI, 20PVA80-3CDI and HA-Bov600, the components involved in the synthesis of PVA-CDI-HA. The detailed analysis of HABov600 and PVA-CDI spectra have been presented before and that of CDI could be analyzed here to discuss the result of the resulting

material. However, the features of the PVA-CDI-HA spectrum only reveal an additive effect of the polymeric component with the mineral phase which bands have higher relative intensity. In the range 500-2000 cm^{-1}, the most intense bands are coincident with those from HABov600 (phosphate bending in 500-650 cm^{-1}; phosphate stretching around 1090 cm^{-1}) and the less intense bands are coincident with those from PVA-CDI (as C=O stretching band around 1700 cm^{-1}). In a qualitative way, it can be stated that PVA-CDI-HA is less crystalline than the mineral HA alone, as deduced from the larger width of the bands, particularly those assigned to phosphate stretching modes. In the 2000-4000 cm^{-1}, the bands in PVA-CDI-HA result from the contribution of PVA-CDI. The bands from CDI are not detected in the spectra of both materials that contain this reagent.

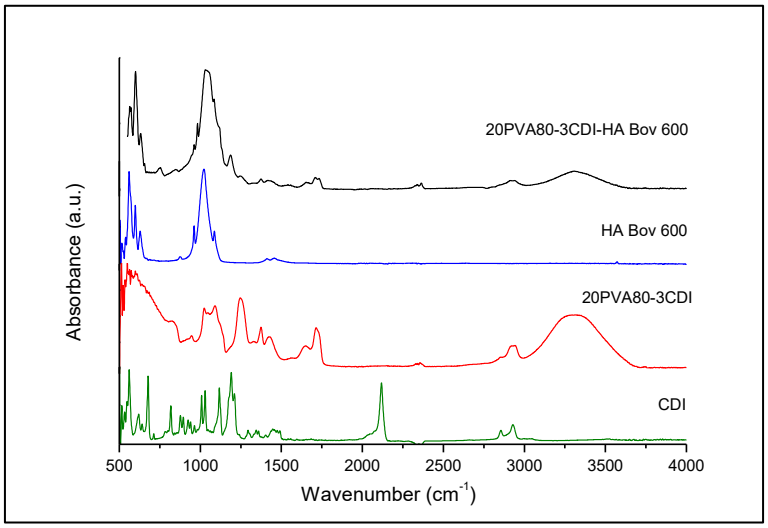

Figure 6.13 - FTIR spectra of 20PVA80-3CDI-HA, HA-Bov600, 20PVA80-3CDI and CDI.

An equivalent analysis regarding other combinations of variables resulting in 20PVA98-3CDI-HABov600, 20PVA80-3CDI-HA900, 20PVA98-3CDI-HA9OO was also made, with a similar outcome. FTIR spectra were parallel to those of Figure 6.13. Additional tests replacing bone-derived hydroxyapatite with synthetic minerals (carbonated and non-carbonated) originated materials equivalent to the former ones. The obtained spectra, as expected, revealed high intensity of the bands from the minerals, overlapping the contribution of the organic components. Due to this fact, the FTIR analysis of type PVA-CDI-HA materials is inconclusive and the respective spectra are excluded from this report.

XRD

X-ray diffraction spectroscopy was used with the purpose of investigating the changes in the mineral components of samples of type PVA-CDI-HA. The use of this technique could be promising because of the high mineral content of these compositions.

Diverse samples of type PVA-CDI-HA, using polymer hydrolysis degree and mineral composition as variables, were analyzed.

The diffractograms of the suspensions in PVA-CDI were coincident with those of the individual minerals without polymers attached, except for the broader width of the peaks, lower signal-to-noise ratio and irregular baseline. Since the diffractograms did not contain new relevant information, they were excluded from this report. Despite this setback, this technique was still applied to investigate the effect of CDI and of urea on the hydroxyapatite composition. The selected samples were those from the LDS experiments.

The HABov600 samples mixed with CDI and with urea from the LDS tests were dried and submitted to XRD spectroscopy. The purpose of using XRD is to ascertain if there was a chemical reaction with formation of different molecules, or a physical interaction leading to the progressive dissolution of the mineral samples. The reference samples are the original mineral particles.

The diffractograms relative to the addition of CDI to HABov600 are presented in Figure 6.14 and those concerning the addition of urea, in Figure 6.15. In both cases, the peaks of the diffractograms of HABov600 are assigned to hydroxyapatite minerals according to the reference ICDD data file nº 84-1998. This has been discussed in Chapter 4, about XRD of diverse bone-derived samples (Figure 4.13).

The diffraction pattern of HA-CDI is almost coincident with that of the reference HA, but two differences occur in the 28º-42º range (Figure 6.14) where the peaks at 30.1, 32.8, 33.7, 37.0, 37.5, 38.4 and 39.7º are respectively assigned to the (002), (102), (210), (211), (112), (300) and (202) Miller plans of hydroxyapatite. After interaction with CDI, the peak from to the (002) Miller plan occurs at 2θ=30.0º, slightly shifted from that at 30.1º, and there is a new diffraction peak at 39.2º relative to the reference. Whereas the shift of the former peak suggests a difference in the crystal lattice of HABov600, the latter peak is more difficult to interpret. Since the carbodiimide that was used does not have a standard ICDD data file to compare to, the doubt about the new peak remains. It can be caused by free CDI, or from a crystal change in the apatite sample.

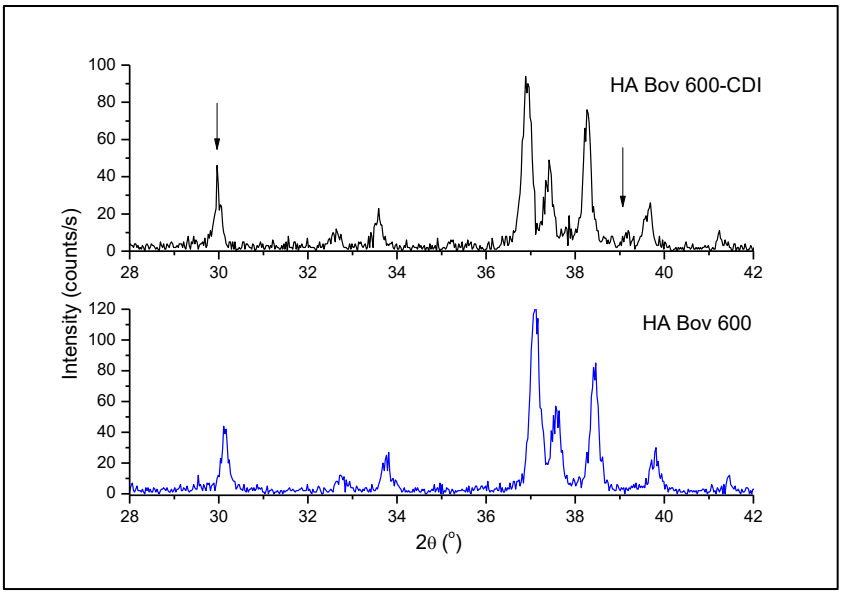

Figure 6.14 – Diffractograms of HABov600 and HABov600-CDI. The arrow points to the differences between the samples.

The diffractograms relative to the interaction between HABov600 and urea are displayed in Figure 6.15, in the range 24º-64º. Compared to the reference sample, the pattern of HA-urea has three additional peaks. According to the ICDD 83-1436 data file of urea, these peaks at 25.9, 28.7 and 34.2 derive from the (1 1 0), (1 0 1) and (1 1 1) miller plans of urea, respectively. The position of the peaks and the relative intensity match the most relevant diffraction peaks of urea. The fact that no other difference is observed in the diffractogram of HABov600 suggests that the mineral structure was not affected by the addition of urea, being the additional peaks originated by free urea in the sample HA-urea.

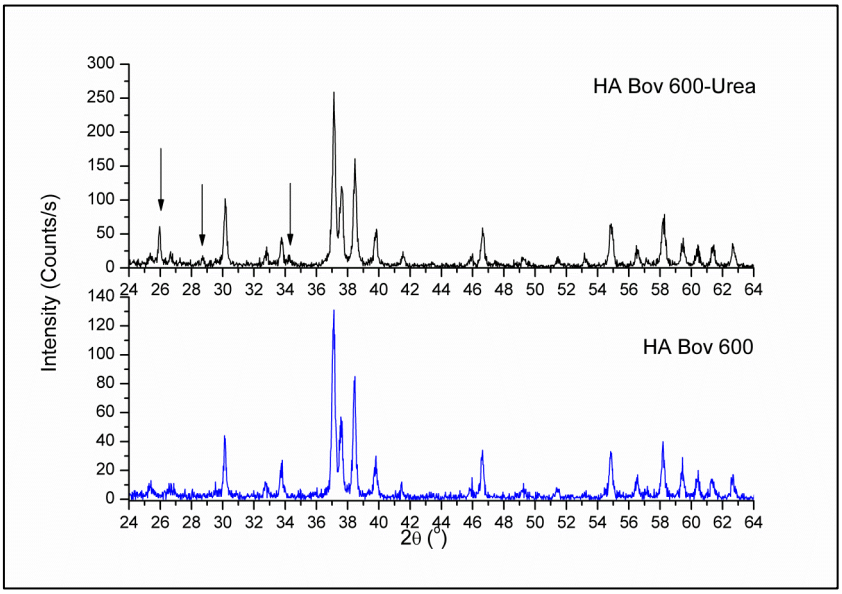

Figure 6.15- Diffractograms of HABov600 and HABov600-Urea. The arrow points to the differences between the samples.

Bone-derived non-carbonated hydroxyapatite

The research made with HABov600 was replicated with non-carbonated hydroxyapatite, HABov900. The most relevant results are those concerning particle size measurements using the same experimental conditions as described before.

LDS

The particle size distribution curves obtained with HABov900 dispersed in water, in solutions of PVA80, 20PVA80-3CDI, PVA98 and CDI are shown in Figure 6.16.

The bi-modal profile of the distribution curve relative to HABov900 in water is identical to its analogous carbonated sample, but the largest particle sizes are shifted to smaller values (from around 130 μm in HABov600 to 20 μm in HABov900). This may derive from the preliminary procedure to obtain hydroxyapatite from bone. The calcination at 900 ºC increases the brittleness of the mineral, originating smaller particles for the same milling conditions. The sieving mesh was the same for both samples. The total range of sizes for the HABov900 particles is from 0.1 μm to 50 μm. The maximum of the corresponding curve occurs around 20 μm and the other intense region is around 3 μm.

The suspensions of HABov900 in the diverse polymer solutions, according to the obtained LDS profiles, generally maintain the dimensions of the mineral particles and the total range observed with the reference sample. There are few differences to report. Some agglomeration may explain the detection the larger particles in PVA98 and in CDI solutions. The only different curve is relative to PVA80 that presents inverted relative intensities at 20 μm and at 1 μm. This profile is unexpected, but it can derive from the analysis of an aliquot that did not represent the whole sample.

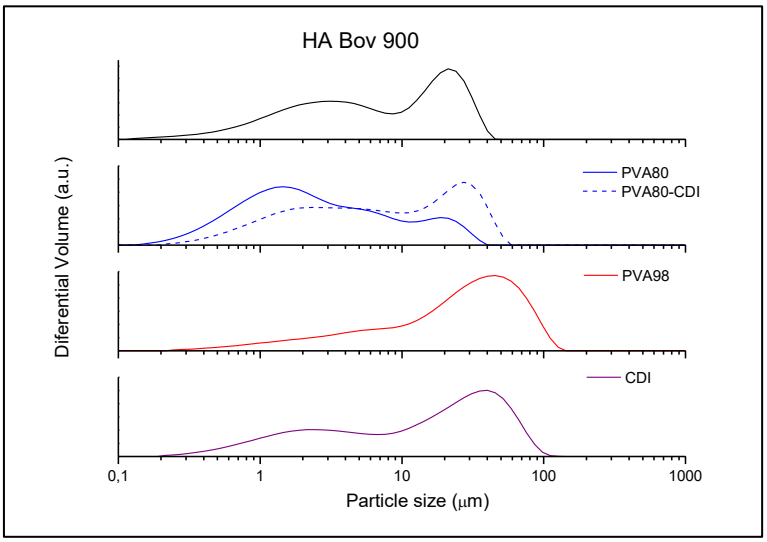

Figure 6.16 - Particle size distribution of natural non-carbonated hydroxyapatite (HABov 900) after 48 hours in water and in aqueous solutions of PVA80, 20PVA80-3CDI, PVA98 and CDI.

Globally, these LDS results show that particle sizes of non-carbonated bone-derived hydroxyapatite is not affected by the presence of CDI in the dispersive medium.

6.3.2 Synthetic carbonated and non-carbonated hydroxyapatite

6.3.2.1 Procedure

Calcibon and Inbone, both commercial synthetic hydroxyapatite samples, were also studied following the same methodology applied to the natural minerals. Calcibon is composed of carbonated hydroxyapatite and Inbone, non-carbonated hydroxyapatite. These minerals were also applied to react with PVA-CDI, namely with 20PVA80-3CDI and 20PVA98-3CDI. The visual appearance of the respective suspensions corresponds to a stable viscous fluid, without any gas release at the surface. So, these suspensions with synthetic minerals do not evidence a chemical reaction with PVA-CDI

The characterization of the chemical compositions of these synthetic PVA-CDI-HA samples is limited by the high mineral content, as mentioned about the analogous previously described. The interest of this characterization is not so important because the reactivity of the components was not evidenced. Even so, LDS analysis was conducted to investigate other possible effects from the use of PVA-CDI. The applied procedure was the same as with the natural apatite samples.

6.3.2.2 Characterization

Synthetic carbonated hydroxyapatite

LDS

The particle size distribution curves relative to Calcibon are displayed in Figure 6.17. The starting mineral presents a broad and continuous distribution in the range 0.2-200 μm, with a significant fraction around 2 μm. The smaller particles may be aggregated in the PVA80 and PVA98-CDI solutions because the respective curves have lower intensity at 0.2-3 μm and maxima shifted to around 5 μm and 8 μm, respectively, relative to the mineral suspension in water. Using the solution of PVA98 as dispersive medium, the size distribution curve of Calcibon is approximately equal to the original one. With urea solution, the particle size is described by a gaussian in the 0.3-10 μm range, centered around 3 μm, followed by a flat curve of low intensity for larger sizes. Comparing this set of results indicates that Calcibon particles are only responsive to the added urea. The differences in the other curves may be explained by sampling variations.

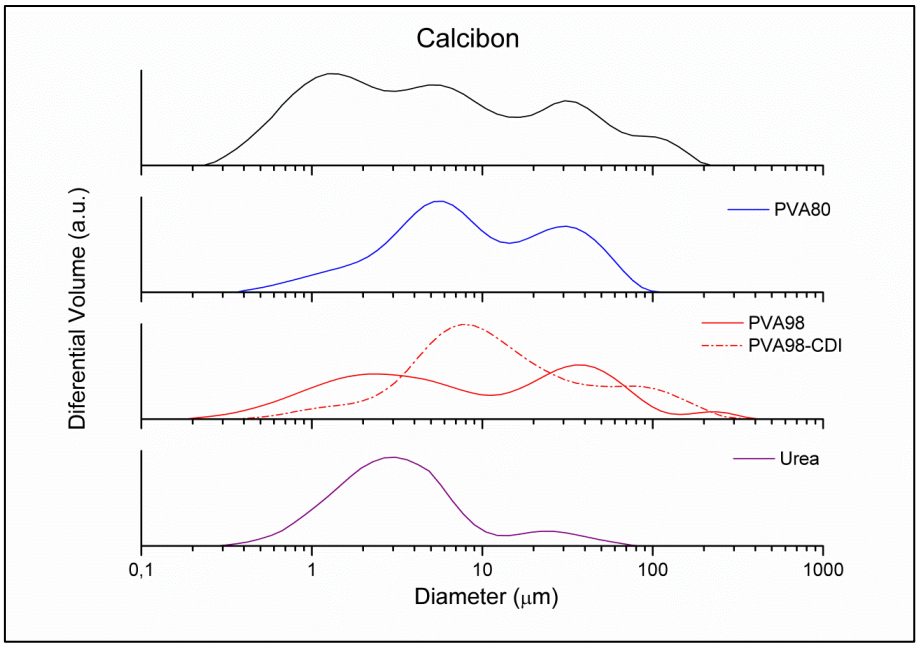

Figure 6.17 - Particle size distribution of synthetic carbonated hydroxyapatite (Calcibon) after 48 hours in water and in aqueous solutions of PVA80, PVA98, 20PVA98-3CDI and urea.

Synthetic non-carbonated hydroxyapatite

LDS

The particle size distribution results concerning Inbone are presented in Figure 6.18. This mineral has a near gaussian profile in the range 1-10 μm, with most particles around 5 μm. Using PVA80 solution as dispersive medium, the particle size distribution keeps the same profile only slightly shifted to higher values. With 20PVA80-3CDI, a fraction of the mineral particles may be aggregated, hence the curve reaches 30 μm, while most of the sample keeps the original dimensions. This trend is also observed in the distribution curve relative to PVA98. As for the use of urea, no change is detected and the LDS curve of Inbone is coincident with the as-received mineral.

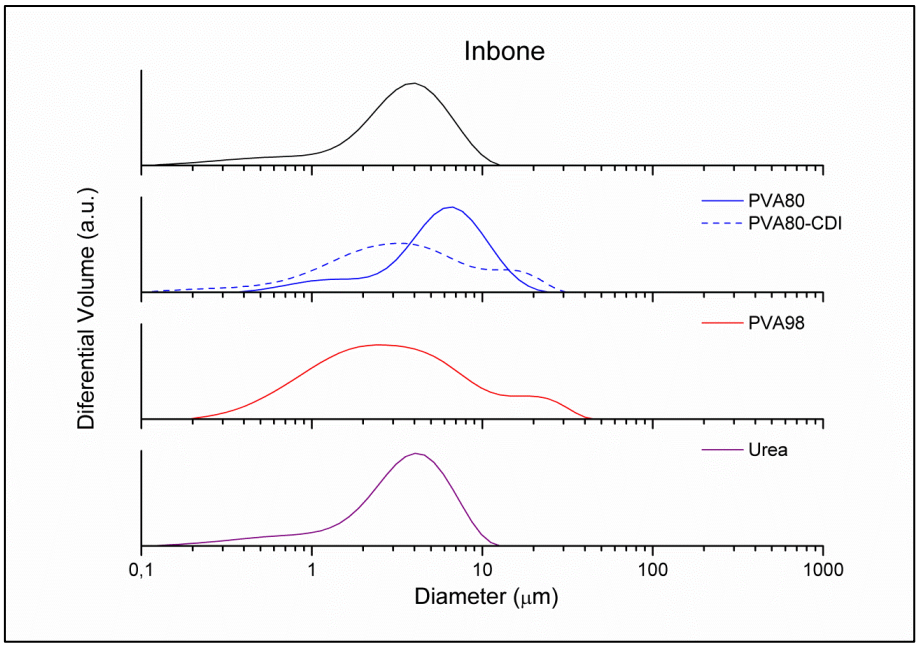

Figure 6.18 - Particle size distribution of synthetic non-carbonated hydroxyapatite (Inbone) after 48 hours in water and in aqueous solutions of PVA80 and PVA80-CDI, PVA98, and Urea.

6.4 Contrast agent addition

6.4.1.1 Procedure

The contrast agent selected for this study was Barium sulphate. Its addition to the reaction medium was made after obtaining a homogeneous hybrid composition of type PVA-CDI-HA. At the end of this stage, after the addition of $BaSO_4$, the composition which is generically named as PVA-CDI-HA-$BaSO_4$, can be referred to as a pre-composite material because it is still a suspension, and classified as composite after being dried. This composite has an innovative character, according to the obtained results. Instead of having a conventional organic matrix phase reinforced with two different minerals, it is based on a hybrid organo-ceramic matrix, reinforced with one additional mineral. The difference can be represented by [(PVA-CDI)+(HA-$BaSO_4$)] *versus* [(PVA-CDI-HA)+$BaSO_4$].

In order to help to identify the Barium sulphate mineral particles in compositions also containing hydroxyapatite dispersed in a polymeric matrix, a sample formed by the suspension of 30 wt% $BaSO_4$ in a PVA98 solution at 20 wt% in water was observed, after being dried, using electronic microscopy.

6.4.1.2 Characterization

SEM

The SEM image displayed in Figure 6.19, obtained at 7500x magnification, enables to observe that the mineral particles are homogeneously dispersed in the polymer matrix, without forming aggregated blocks. It also illustrates the size and shape of the particles, being characterized by uniform dimensions inferior to1 μm. These particles present smooth edges and spherical shapes, as previously observed in Figure 4.31 (Chapter 4).

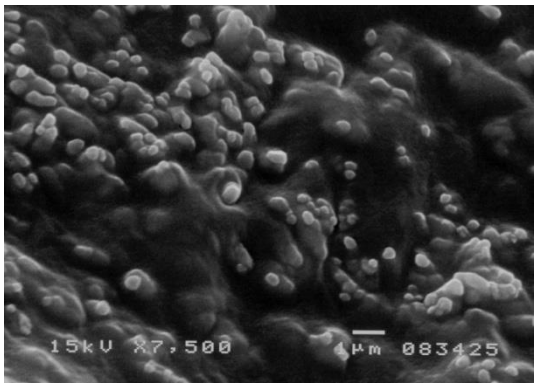

Figure 6.19 – SEM image of the dried suspension of $BaSO_4$ particles (30 wt% in PVA98).

XRD

Barium sulfate was added to diverse combinations of the obtained hybrid organo-ceramics of type PVA-CDI-HA, as mentioned.

X-ray diffraction spectroscopy was used to characterize the composite PVA-CDI-HA-$BaSO_4$ type of samples, being one of these spectra illustrated in Figure 6.20, together with those of the corresponding references. The sample under analysis is composed of 20PVA98-3CDI-HABov600-$BaSO_4$, with each mineral content corresponding to 20 wt% of the polymer matrix. The reference samples are PVA98 and a 1:1 (weight proportion) blend of HABov600 with $BaSO_4$. The respective diffraction patterns were previously discussed in Chapter 5 (Figure 5.10) and in Chapter 4 (Figures 4.30 and 4.36).

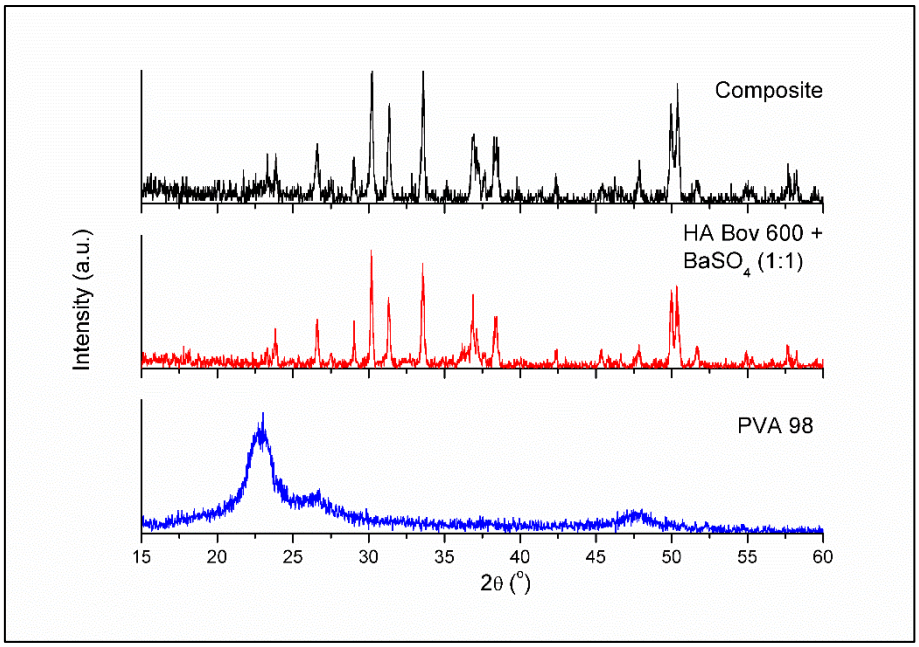

Figure 6.20 – Diffractograms of PVA98, HABov600 blended with BaSO4 (1:1) and of a composite based on the combination of this polymer with these minerals.

The diffraction pattern of the composite is identical to that of the blended minerals, being the contribution of the polymeric phase mainly manifested on the lower signal-to-noise ratio and on the lower definition of the base line. The width of the peaks is also affected but, anyway, all diffraction signals can be identified. Almost all the composite peaks are assigned to Barium sulphate, as discussed in Chapter 4. Most peaks from hydroxyapatite are overlapped by $BaSO_4$. This is due to its greater absorption coefficient of x-ray radiation, derived from the atomic number of Barium (Z=56). Nonetheless, the most intense peaks of hydroxyapatite (2θ=35º-40º) are also present in the diffractogram of the composite.

FTIR

FTIR was applied to obtain an equivalent characterization of the composite analyzed by XRD. Its vibrational spectrum reflected the major contribution of the mineral components and some low intensity bands from the matrix. The most intense bands derived from Barium sulphate vibrational modes, overlapping those of hydroxyapatite. Since the spectrum was identical to that described in Chapter 4 (Figure 4.35), it is not presented in this section.

6.5 Crosslinking of the composite

The search for adequate crosslinker reagents for the PVA-CDI-HA-$BaSO_4$ pre-composite has been the greatest challenge of the present study. Without an appropriate crosslinking system, this composite would not comply with the specific requirements for solidifying *in situ* and become insoluble in water.

After testing numerous potential solutions, the investigation focused the use of an acrylic substance despite the initial intention to avoid this type of reagents.

The acrylic substance or, more exactly, the acrylic system selected for this study was the monomer 2-hydroxyethylmethacrylate (HEMA) together with potassium persulfate ($K_2S_2O_8$) and tetramethylethylenediamine (TEMED), conventional molecules that act as initiator and catalyst, respectively, in radical-initiated polymerization reactions [145,219–222]. N,N´-Methylenebisacrylamide (MbisA) was also part of this system, to act as a crosslinker of polymerized HEMA, thus creating a network of poly(HEMA) rather than unconnected linear chains of this polymer.

The monomer HEMA is a biocompatible water-soluble molecule which becomes insoluble after polymerization and acquires a swelling potential that depends of its chemical composition and structure. It can absorb water from 10 to 600 wt% relative to its dry weight, being one of the reasons why it finds many applications in biomedical fields [219,222–226].

The concept of interpenetrating network (IPN) was subjacent to the idea of adding HEMA and co-adjuvant reagents to the pre-composite suspension [146,148,226–228]. The IPN would result from the interaction between PVA-CDI-HA-$BaSO_4$ and poly(HEMA). In advance, it is already revealed that collagen was also a fundamental reagent in the formulation of the new biomaterial. Collagen had to be hydrolyzed into gelatin to become soluble and miscible with all the other components. It was prepared as previously described (stock solutions of hydrolyzed collagen; section 6.2.1.1).

In order to obtain a product that could be easily prepared at the operating table, the suspension of the pre-composite formulation would have to contain the initiator, the catalyst and the crosslinker, whereas the monomer would have to be in a separate vial. The monomer would be added to the other mixed components just before placing the final blend inside the injection device. Then, this final mixture would be injected into the vertebral body and the crosslinking reaction would occur *in situ* to enable vertebral repair.

To simulate the general conditions expected to occur in real life, during vertebral surgery, with the new biomaterial, its preparation procedure was made at room temperature because it had to be composed of two parts, both stable at room temperature. After blending the two components, the mixture was put inside a closed vessel at 37 ºC, to simulate the interior of a vertebra, at body temperature. Each

experiment was performed in duplicates to encompass both environmental conditions. At open air and room temperature, the reactions could be monitored by direct observation. In a closed container at 37 ºC, the reactions proceeded as *in vivo* conditions. Moreover, each procedure involved triplicate samples, as recommended in any controlled laboratorial work. Doing the math, each synthesis experiment involved six starting PVA solutions.

This section starts with the description of a series of experiments that guided the selection of reagents to crosslink the pre-composite. These assays are termed as Preliminary Tests (PT-1, PT-2 and PT-3) and their schematic representation is explained along the text. It is worth mentioning that the quantification of the reagents is not necessary, at this point, to understand the sequence of results. Thus, these PT procedures will be described in a qualitative way.

After reaching some promising results, an additional set of experiments was necessary to improve the obtained properties. A quantitative analysis was required to understand the correlations between composition and physical properties. The chemical characterization of compositions even more complex (than those which were analyzed from the first step of the synthesis procedure until the addition of the contrast agent) did not provide much helpful results. Conversely, physical properties as swelling or mechanical resistance to compression were important to evaluate the effect of chemical variations of the reagents.

From the physical behavior of some crosslinked composites, the following filter was the compatibility of the materials with osteoblasts and with blood. From this evaluation, one single sample was selected for *in vivo* implantation in an animal model.

The total sequence of this research is presented hereafter.

6.5.1 Preliminary tests – Procedure and Results

In the preliminary tests, the question of adding the monomer as the last component of the formulation was not a primary matter of concern. The objective was to obtain a crosslinked material inside the reaction vessel, by gradual solidification without extracting the water by drying or any other means. The procedure was made always in triplicate numbers

In order to have a reference for the polymerization of the HEMA added to the pre-composites suspensions, all the tests were compared with side vessels where the conventional reactions were made, with and without the addition of TEMED and MbisA. This allowed to observe the progressive formation of poly(HEMA) that occurred at room temperature. Usually, the persulfate initiator is dissolved at 70 ºC to originate the radicals

that start the polymerization reactions [138,139,146,158,229]. However, the experience showed that the reaction could occur, even without warming the initiator solution.

6.5.1.1 Preliminary Test - 1

The first test is represented in Figure 6.21. All the procedures were made with PVA80 following the methodology described before, from the reaction with CDI until the addition of the contrast agent and formation of the complex PVA-CDI-HA-$BaSO_4$. The following reagents and the outcome of each procedure are briefly described to explain the diagram from the first to the fourth row.

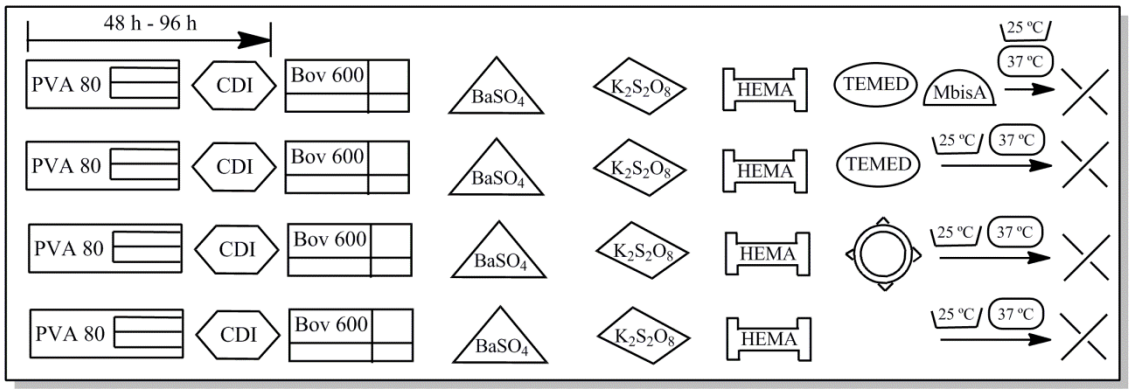

Figure 6.21 – Preliminary Test PT-1 : The complex PVA-CDI-HA-$BaSO_4$ does not solidify, even containing all the reagents to produce poly(HEMA) and a IPN.

First row – A solution of PVA80 reacted with CDI for 48-96 hours. Then, HABov600 was added to obtain a hybrid PVA80-CDI-HA type material. Next, $BaSO_4$ was dispersed in that suspension, followed by $K_2S_2O_8$, another solid reagent in powder form. After, the liquid monomer HEMA was added, then the catalyst TEMED and finally the crosslinker MbisA. This complex mixture was left at room temperature. Another equal mixture was placed in a closed vial, at 37 ºC. The result was that both did not solidify.

Second row – Everything was made like in the first row but excluding MbisA. In both conditions, open air at room temperature and closed environment at 37 ºC originated similar results. None of the systems became solid.

Third row - Everything like in first row, except the addition of TEMED and MbisA. The last components added to the suspension were PLA microcapsules of type mC-S (Standard microcapsules as described in Chapter 5, Section 5.2). Both environmental conditions did not result in solidified materials.

Fourth row – Everything like in first row, until the addition of HEMA. Once more, the solidification did not occur at either experimental conditions.

The described procedures were also made with PVA98 with the same results.

The main conclusion from PT-1 is that the addition of HEMA and potassium persulfate to the PVA-CDI-HABov600-$BaSO_4$ did not lead to the formation of an IPN nor the solidification of the resulting material. Even with the addition of the catalyst (TEMED), and the catalyst together with the crosslinker (MbisA), all the reagents necessary to obtain poly(HEMA), the polymerization was not observed. The inclusion of standard microcapsules (mC-S) had the purpose of testing its compatibility with the suspension components. No visible interaction was detected, which indicates that the PLA microcapsules may be added to the formulations without causing unexpected problems.

6.5.1.2 Preliminary Test - 2

The second test is represented in Figure 6.22. The difference in the procedures relative to PT-1 is that hydrolyzed collagen (in acid medium; Type A gelatin) was added to the PVA-CDI-HABov600-$BaSO_4$ suspension, before the set of HEMA reagents.

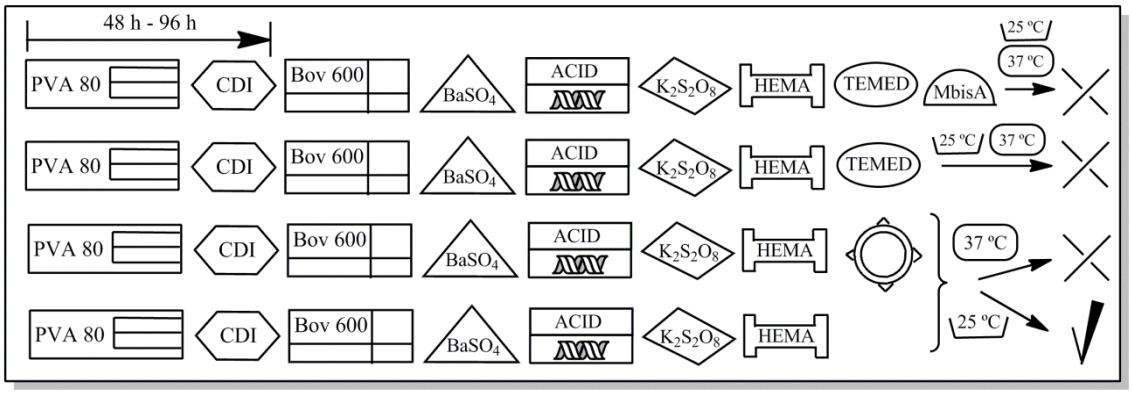

Figure 6.22 – Preliminary Test PT-2 : Using acid-hydrolyzed-collagen, persulfate and HEMA, the complex PVA-CDI-HA-$BaSO_4$ becomes crosslinked only when TEMED and MbisA are not added. Moreover, the composition degrades after 48 hours at 37 ºC in a closed environment but maintains its integrity at 25 ºC and exposed to air atmosphere, whether it contains PLA microcapsules or not.

The only procedures that resulted in the stable solidification of the collagen containing material correspond to the third and fourth rows, were the reaction with HEMA occurred because TEMED and MbisA were not present. However, solidification was only observed to be sustainable in the vessels at open air and room temperature. Using closed conditions, at 37 ºC, there was a gradual solidification but, after 48 hours, the composite lost its integrity and started degrading into a paste consistency. Furthermore, the PLA microcapsules confirmed to be inert in this medium since the results were the same, with and without mC-S particles.

The described procedures were also made with PVA98 with the same results.

Briefly, PT-2 showed that hydrolyzed collagen is required to obtain a solid composite from the hybrid mineral suspension in PVA, using radical initiated HEMA

polymerization. It also showed that this result could not be obtained at living conditions. This raised the hypothesis that acid-hydrolyzed collagen, despite being neutralized, could still contain ionized fragments that would react with the alkaline minerals. Hydroxyapatite solutions in water have pH around 8. Thus, a typical acid-base reaction could have occurred after the initial solidification of the material and interfere in this process.

Since collagen showed that it is was essential to crosslink the biomaterial, the new question was how to prevent the degradation of the obtained composite. The next series of experiments were based on the substitution of the hydrolysis method in acid medium to alkaline.

6.5.1.3 Preliminary Test - 3

The third series of tests, represented in Figure 6.23, were made with PVA98 mixed with hydrolyzed collagen (both in acid and in alkaline media) and CDI in the first step of the reaction. As described before (Figure 6.9), collagen can be mixed with PVA and CDI simultaneously, origination a gas release reaction. Subsequently, the other reagents were HABov600, $BaSO_4$ and $K_2S_2O_8$. After obtaining a homogeneous suspension, HEMA was added to two vessels: one containing type A gelatin and another with type B gelatin. The two remaining vessels took both HEMA and TEMED.

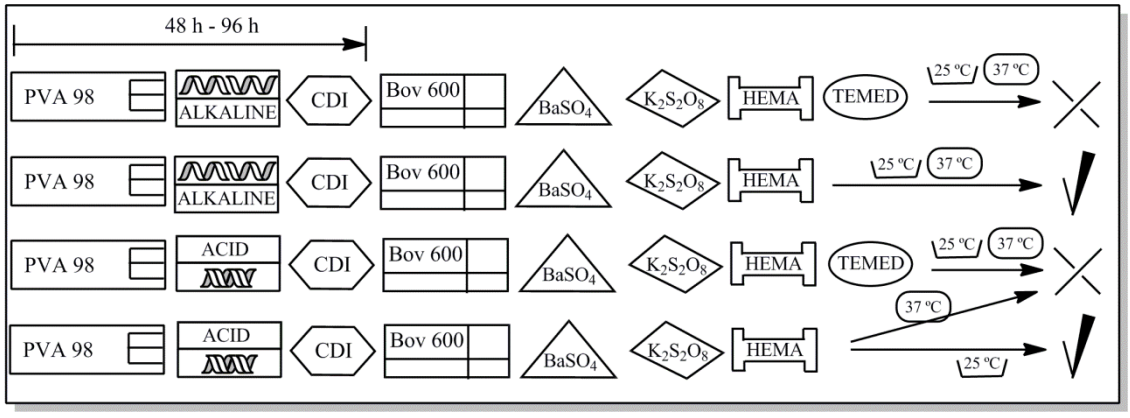

Figure 6.23 – Using TEMED, the suspensions never crosslink, no matter the hydrolysis method applied to collagen. The solidification of the biomaterial occurs at 37 ºC in a closed environment only in samples containing collagen previously hydrolyzed in alkaline medium.

Just like happened in PT-1 and PT-2, the reaction vessels containing TEMED did not solidify in any environmental condition. The vessels without TEMED, containing different types of hydrolyzed collagen, both gave positive results using open air and room temperature conditions. However, the only sample that resulted in a solid composite, in a closed vessel at 37 ºC, was the one containing collagen hydrolyzed in alkaline medium.

The fourth row of PT-2 and PT-3 are equivalent, being the starting polymer (PVA80 versus PVA98) and the composition of the suspension to which hydrolyzed collagen is added, the differences between the respective procedures. Since the result regarding solidification was the same in both tests, this comparison confirms that both PVA80 and PVA98 are adequate for the desired application. It also shows that collagen can be added to the reaction at different moments of the synthetic pathway, before HEMA. The same applies to BaSO4 and the microcapsules. These two components could be added at different moments since they behaved as inert materials.

At the end of PT-3, the chemical composition that was selected to explore further in this study was the last one. This formulation is taken as reference for subsequent studies. PVA 98 was considered more adequate because the viscosity of the initial solution was higher than PVA80, at the same concentration. Carbonated hydroxyapatite (HABov600) was preferred over non-carbonated because of two main reasons: its greater similarity with natural bone and higher affinity with PVA (which is an electron donor substance), as shown by IGC results (Chapter 4; Section 4.1.1.3). The other mandatory reagents were collagen hydrolyzed in alkaline medium, potassium persulfate and HEMA to crosslink the pre-composite, and $BaSO_4$ to provide x-ray contrast to the composition. The microcapsules were optional.

Combining all the results, the explanation for the observed solidification of the pre-composite material is that HEMA did not polymerize into a homopolymer, but it was grafted to the hydrolyzed collagen structure through a radical initiated mechanism. Persulfate supplied the radicals that activated the C=C double bonds from HEMA and from collagen [219,221,230]. The propagation of the reaction resulted in a grafted collagen-HEMA polymer capable of holding the other components by physical crosslinking.

This theory could end here. However, there were other tests that change this interpretation. After optimization of the procedure that gave the best results, new tests involved the single difference of using PVA without the reaction with CDI. The obtained materials were not able to solidify. These results show that the synthesis of the hybrid PVA-CDI-HA is necessary to proceed the reaction until the whole material becomes solid. This means that the graft polymerization of collagen and HEMA also involves the former hybrid component. However, the nature of this interaction is not clearly understood because of limitations intrinsic to the materials compositions.

Solid-state CP-MAS NMR

Solid-state NMR spectroscopy was used to analyze a composite equivalent to the last biomaterial of PT-3, except for the presence of the contrast agent. The ^{1}H-NMR and ^{13}C-NMR spectra are presented in Figures 6.24 and 6.25, respectively, together with those of reference materials involved in the synthesis. Some of these spectra may be compared to those obtained in deuterated water solutions (Chapter 5, Section 5.1, Figures 5.5-5.7 and Chapter 6, Section 6.2, Figures. 6.3-6.7).

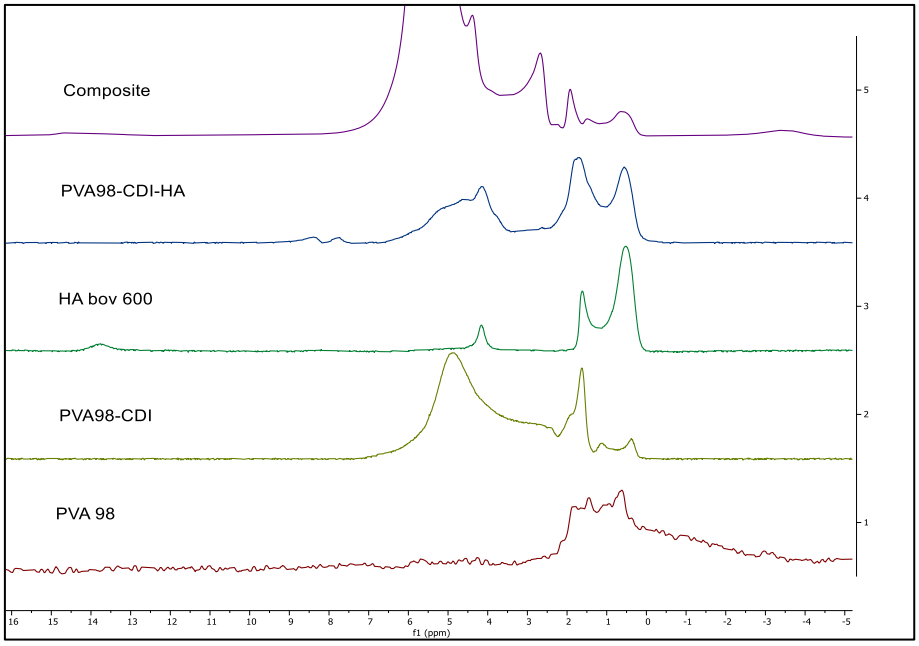

Figure 6.24 – Proton CP-MAS NMR spectra of a composite and respective components.

In Figure 6.24, the spectrum of the polymer, PVA98, presents a broad band with peaks discernable at 0.7, 1.6 and 1.9 ppm that are also observed in all the other spectra. These peaks derive from methylene H-C-H groups. No peak is observed around 4.0 ppm, as expected from the solution spectrum and from the literature, due to methyne protons (H-C-OH bonds) from the backbone of the polymer [153,186,231–233].

The spectrum of PVA98-CDI presents broad peaks of low intensity from 0.0 ppm to 2.2 ppm, with an intense peak at 1.6 ppm. The broad band in the range 2.2-6.5 ppm may contain contributions of methyne protons from the polymer, and contributions of hydroxyl groups from water molecules adsorbed to the sample. The respective peaks typically occur around 4.0 and 5.0 ppm respectively. Compared to PVA98, the spectrum of PVA98-CDI has a better signal-to-noise ratio and the methylene peaks are shifted to lower field. The eventual presence of a new peak around 2.1 ppm is not confirmed. It would correspond to the single new peak detected in the PVA-CDI solution [153,186,231–233].

As for the hydroxyapatite sample, the NMR profile is characterized by two broad peaks at 0.0-2.0 ppm partially overlapped. The maximum intensity occurs at 0.5 ppm and the other peak, at 1.6 ppm. The former is attributed to hydroxyl groups of the mineral and the latter to protons from H bonds to phosphate groups. The low intensity peak at around 4.2 ppm derives from adsorbed water molecules [174,234–237].

The spectrum relative to the PVA-CDI-HA sample denotes the two intense peaks from the mineral phase in the range 0.0-2.0 ppm, with inverse relative intensity. This may be due to the additive effect from the intense peak of PVA98-CDI at 1.6 ppm. The low intensity peaks at 7-8 ppm result from resonance forms of hydrogenphosphate protons. Since these peaks are absent in the HA spectrum, this shows that the chemical environment around phosphate is different in the PVA-CDI-HA hybrid material. Moreover, the broad peak in the range 3.5-6.0 is originated by the polymeric component and adsorbed water [153,174,186,231–237].

Finally, the ^{1}H-NMR spectrum of the composite has an identical profile to that of PVA-CDI in the range 0.0-2.0 ppm, and to that of PVA98-CDI in the range 4.0-7.0. However, the peaks in the first range are slightly shifted to higher field. A new broad peak is observed at 2.4-3.2 ppm, being attributed to the collagen-HEMA because the composite is the only sample that contains these components [153,174,186,231–237].

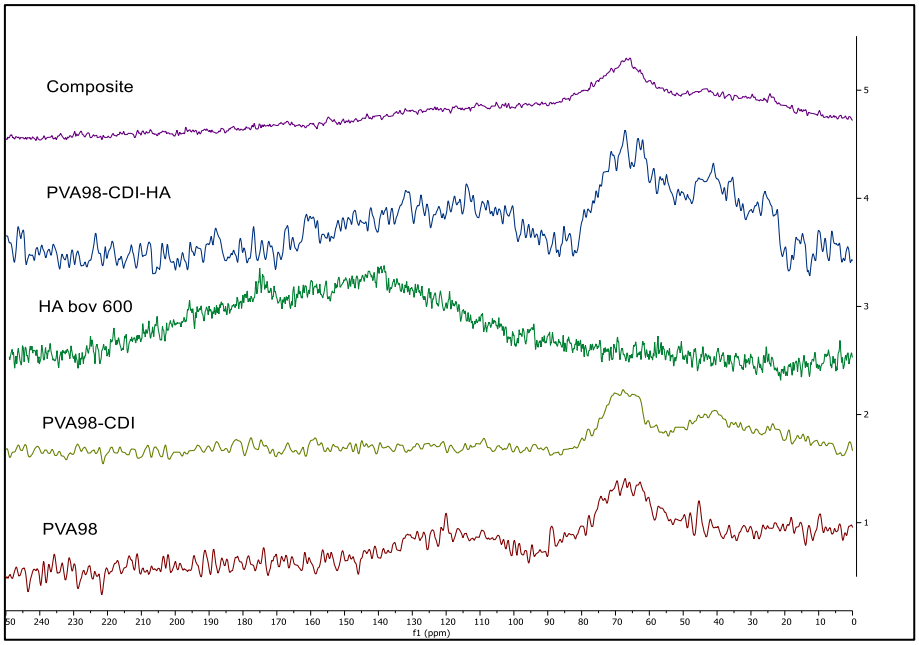

Figure 6.25 – Carbon-13 CP-MAS NMR spectra of a composite and respective components.

The carbon-13 NMR spectra relative to the same samples are displayed in Figure 6.25. Globally, all except that of the composite have very low resolution. The profile relative to the samples that contain PVA are nearly identical, with peaks at 40 and 65 ppm assigned to methylene and methyne carbons from the backbone of the polymer.

The most different spectrum is that of hydroxyapatite, being the broad absorption peak from carbonate substituents in the crystal lattice [153,186,231–233].

SEM

The microstructure of the last composite of PT-3, containing all the reagents described before, was examined using SEM imaging.

Figure 6.26-left shows the global appearance of the solid composite. At low magnification (50x), this biomaterial looks homogeneous and with some porosity that probably results from entrapped air bubbles during the mixture of the reagents. Then, the subsequent solidification process occurred in a closed environment and the gas did not leave, or else the material would have collapsed. Using high magnification (15000x), the mineral particles are clearly observed, both regarding shape and size details. Most particles are inferior to 1 μm and the different shapes enable to confirm a uniform distribution of HABov600 and $BaSO_4$. The polymer matrix, containing PVA-CDI, hydrolyzed collagen and HEMA, is not observed. This may be due to its relative concentration. The minerals are involved by the polymeric components as a thin coating material that is not detected in this sample.

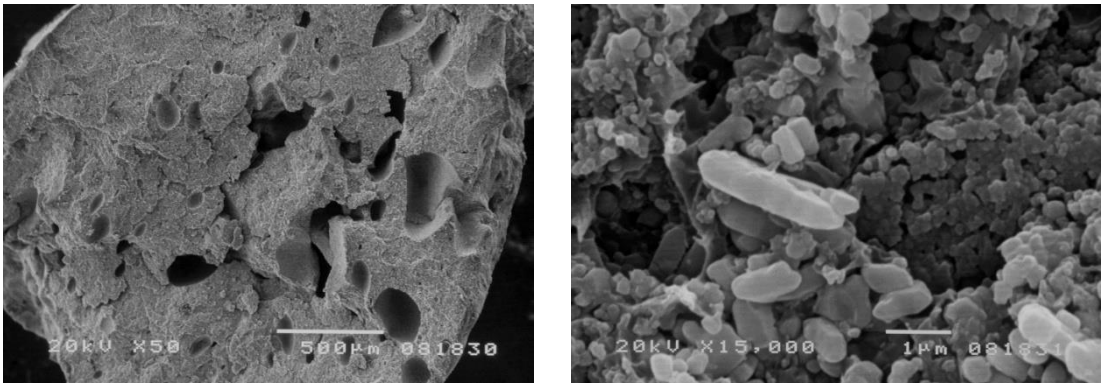

Figure 6.26 – Global appearance and microstructure of the composite from PT-3. The polymeric matrix is not observed due to its concentration.

In order to observe the matrix of the composite, a sample containing an additional proportion of organic components was also observed through SEM. Figures 6.27-left and -right, obtained at 20000x magnification, allow the detailed analysis of the composite microstructure. The images show that the mineral particles are homogeneously surrounded by thin layers of materials with smooth texture, the polymeric matrix.

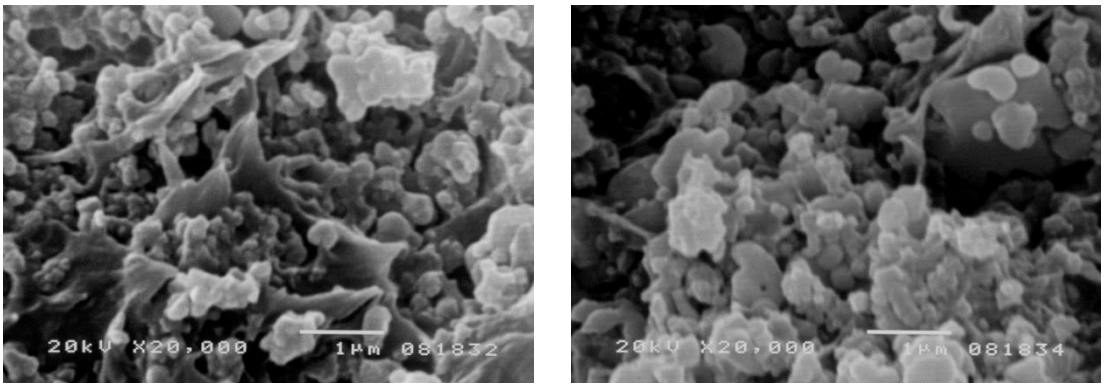

Figure 6.27 - Microstructure of a composite with higher polymeric concentration than samples from PT-3. The polymeric matrix is evenly distributed around the mineral particles.

6.5.1.4 **Microcapsules for controlled delivery and porosity**

The use of microcapsules as devices for drug-controlled delivery is a frequent strategy in biomedical applications [161,163,164]. In this study, the purpose on adding microcapsules to the composite has been the transport of substances (medical drugs or others) and the creation of porosity in the biomaterial solidified inside the vertebra. A series of microcapsules based of poly(lactic acid) (PLA) were developed using a double emulsion method, being obtained hollow particles with different properties (size, thickness, porosity, surface properties). These microcapsules are described in Chapter 5 (Section 5.2). The incorporation of microcapsules in the composite does not interfere with the solidification chemistry, as demonstrated in the preliminary tests.

Microcapsules were used in this study to take advantage of their potential for drug release and investigate the chance of delivering the monomer HEMA inside a microcapsule to the pre-composite suspension. Using this method, it would not be necessary to have a flask with this liquid reagent at the operation table, to withdraw a strict volume, and mix it with the suspension containing all the other required components. This procedure would be much easier and non-toxic if HEMA was incapsulated in solid particles. After the blending procedure, HEMA would be gradually released to the suspension and initiate the polymerization leading to the solidification of the biomaterial. The kinetics of delivery could be predictable by preliminary studies with microcapsules with different properties (as microcapsules mC-BH1, mC-BH2 and mC-BH3).

The other potential function of the microcapsules is creating porosity inside the composite. The use of capsules made with borax, that have surface pores, enhances the porosity effect. There is a faster biodegradation of PLA due to easier exchanges with the environment and the hollow space of the core becomes available for cell invasion.

The size of the microcapsules was tailored to appropriate dimensions for cell colonization. This approach may increase the biological mechanisms for bone repair.

In order to investigate some of these assumptions, three different composites were prepared using the reference composition from the last PT-3 sample. One without microcapsules, a second one containing Standard mC-S microcapsules and a third one with mC-BH1 (with HEMA in the shell). These composites were observed using SEM. The first corresponds to Figure 6.26 and the others to Figures 6.28 and 6.29.

The composite with mC-S microcapsules (Figure 6.28) looks like the reference sample but with the polymeric spheres dispersed in the material. At macro scale, pores with dimensions that reach 400 μm are observed, likely due to air bubbles. Increasing the magnification, the microcapsules demonstrate to have a good adhesion to the composite. The capsules are also mechanically resistant because most keep the integral shape and size. A broken capsule enables to confirm that these particles are hollow, and that the thickness of the shell is around 3 μm.

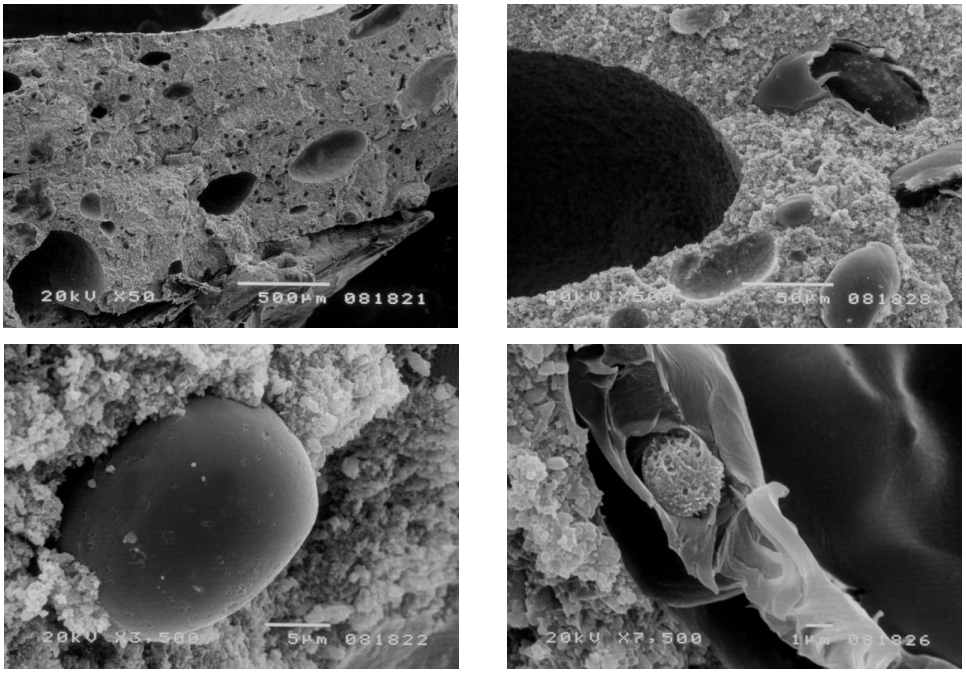

Figure 6.28 - Crosslinked composite with microcapsules mC-S distributed in the matrix.

The composite of Figure 6.29 contains mC-BH1 porous microcapsules spread across the biomaterial. The average size of the capsules is superior to mC-S, as expected. The pores in the shells are other features that were developed intentionally. Although the interfacial adhesion is inferior to the Standard type, these mC-BH1 show another means to become attached to the composite. There are polymeric filaments coming out of the microcapsules to the matrix around, linking both materials through a

thin network. These filaments must derive from the release of HEMA to the suspension of reagents and subsequent polymerization.

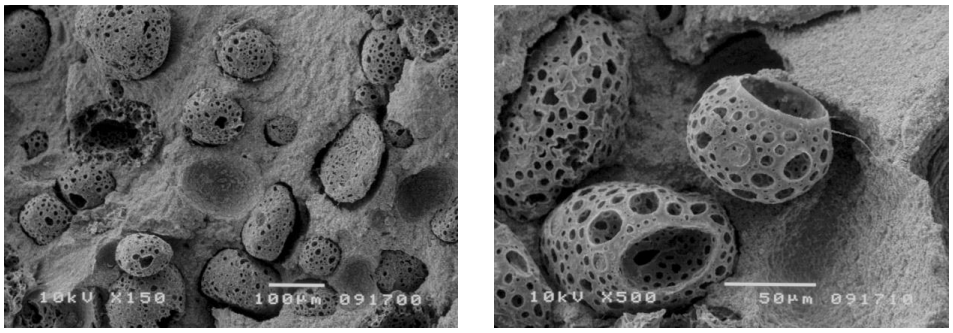

Figure 6.29 – Crosslinked composite with microcapsules mC-BH1 linked to the matrix through filaments of poly(HEMA).

After passing the microstructural analysis, the last capsules were put aside for specific tests to evaluate the compatibility with osteoblasts (bone forming cells).

6.5.2 *In vitro* evaluation

Having decided about the qualitative composition of the new biomaterial, the definition of quantitative ratios derived from additional tests, mostly based in physical properties.

Diverse techniques were used to try to characterize the composite regarding its chemical composition. Because of its complexity and high proportion of mineral components, the obtained results were not conclusive regarding the variation of small amounts of reagents. Thus, the physical behavior as swelling and degradation in PBS were tested. PBS is usually applied to simulated in vivo environments, being adequate to predict bone bioactivity [238]. Furthermore, some of the samples were tested for biocompatibility with osteoblasts and hemocompatibility.

6.5.2.1 Tested compositions

In order to illustrate the methodology followed to test the variables in each synthesis procedure, two sets of compositions are described in Tables 6.1 and 6.2. In these tables, 20PVA98-3CDI stands for 30 wt% solution of 20PVA98-3CDI, COL 200 for a collagen stock solution prepared from the alkaline hydrolysis of 200 mg of protein. The microcapsules of mC-BH-1 were prepared with 1 ml of HEMA. All the samples were polymerized in a closed environment at 37 ºC.

Table 6.1 - Test T1 – Quantification of the reagents involved in the synthesis of the composite. For each triplicate with the same amount of collagen, the variable is the volume of HEMA.

Sample	20PVA-3CDI (g)	COL 200 (μl)	HA (g)	$BaSO_4$ (g)	$K_2S_2O_8$ (mg)	HEMA (μl)
1	3.00	500	0.60	0.60	200	150
2	3.00	500	0.60	0.60	200	200
3	3.00	500	0.60	0.60	200	300
4	3.00	300	0.60	0.60	200	150
5	3.00	300	0.60	0.60	200	200
6	3.00	300	0.60	0.60	200	300
7	3.00	600	0.60	0.60	200	150
8	3.00	600	0.60	0.60	200	200
9	3.00	600	0.60	0.60	200	300

Table 6.2 - Test T2 – Quantification of the reagents involved in the synthesis of the composite. The variables are the amount collagen and HEMA (in solution, or incapsulated in mC-BH1 particles). Sample #5 corresponds to the composition applied in bio-related assays.

Sample	20PVA-3CDI (g)	HA (g)	COL 200 (μl)	BaSO4 (g)	$K_2S_2O_8$ (mg)	HEMA (μl)	Microcapsules mC-BH1 (g)
1	3.00	0.60	500	0.60	200	300	-
2	3.00	0.60	600	0.60	200	400	-
3	3.00	0.60	300	0.60	200	200	-
4	3.00	0.60	500	0.60	200	300	-
5	**3.00**	**0.60**	**600**	**0.60**	**200**	**400**	-
6	3.00	0.60	300	0.60	200	200	-
7	3.00	0.60	500	0.60	200	-	0.3
8	3.00	0.60	600	0.60	200	-	0.3
9	3.00	0.60	300	0.60	200	-	0.3

Equivalent tests were also performed with Calcibon and Inbone, the synthetic minerals selected to compare with HABov600 and HABov900, respectively. At the end of each procedure, both pre-composites solidified with the addition of HEMA. This showed that the developed formulation may be applied to obtain totally synthetic composites or biomaterials of dual character.

6.5.2.3 Swelling and Degradation in PBS

The composites obtained using the diverse formulations described in section 6.4.2.1 were put in PBS solution, as illustrated in Figure 6.30. The original shape of the samples was a disk of around 3.5 cm diameter and 2.0-3.0 mm thickness.

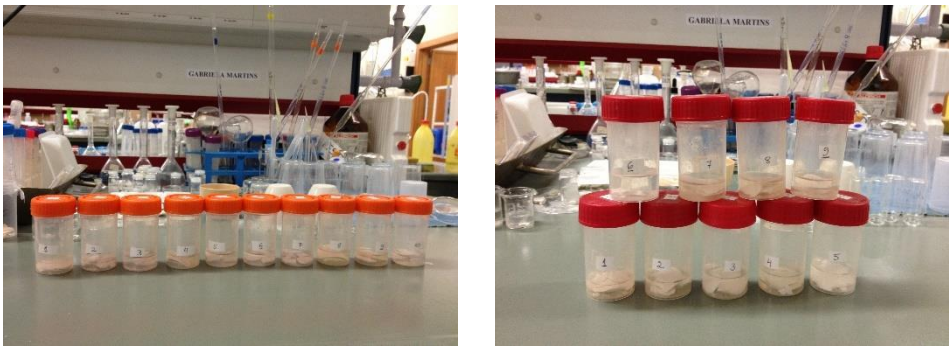

Figure 6.30 – Composite samples immersed in PBS solutions.

The swelling and degradation in PBS were monitored simultaneously, in the same experiments, for a period of several weeks (reaching 50 days). The samples were blotted using an absorbent paper. Then, they were analyzed relative to weight and dimensional variations, being the results expressed as percentages relative to the initial mass and initial diameter.

Figure 6.31 shows that after 24-48 hours immersion in PBS, the mass of samples from Test-1 increased to around 140 wt% of the initial weight in compositions containing 150 and 300 μl HEMA, whereas those containing 200 μl HEMA increased to 160 wt%. An identical effect occurred in samples containing 500 μl hydrolyzed collagen, with higher weight increase to 170 wt%. Following the swelling due to water absorption, the graphs draw a plateau showing that all samples maintained their weight. However, some were broken into fragments after 1 month in PBS. The variations in the plateau are certainly due to the experimental errors associated to the blotting procedure.

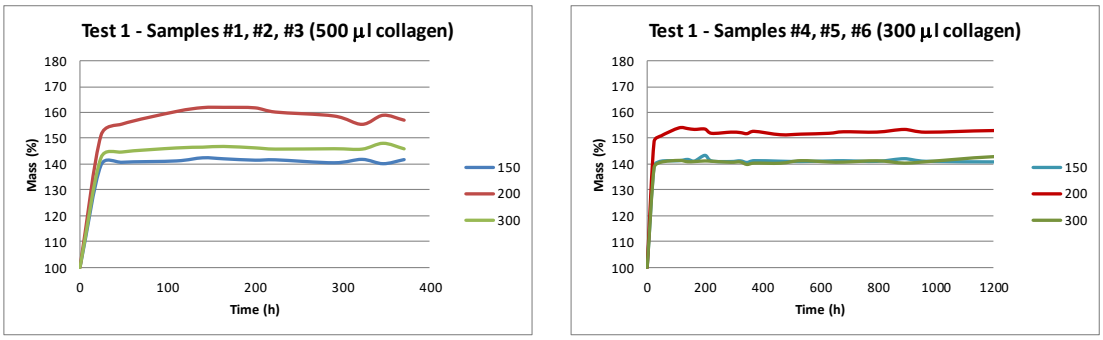

Figure 6.31 – Test 1 - Mass variation of composite samples containing 500 μl (left) or 300 μl (right) collagen solution, and variable amounts of HEMA (150, 200, 300 μl).

The results obtained in Test 2 showed a similar trend, with weight variations between 140 and 180 wt% at the first hours of the assays.

In general, the collagen:HEMA ratio that originated the greatest swelling corresponded to 500:200 (V/V), or 600:400 (V/) using the stock solutions previously described.

As for the dimensional variations, the diameter increase associated to the absorption of water reached around 15 % of the initial value. This constitutes an advantage for the bone repair procedure. The composite can occupy the total volume of the bone defect and adapt to its irregular shape. This way, the interfacial adhesion between the solidified composite and bone tissue may be enhanced, leading to better mechanical properties.

6.5.2.4 Mechanical strength under compression (creep tests)

Under physiological conditions, bone is constantly submitted to compressive and tensile forces [75,96,239] One of the requirements that bone grafts should obey to, is to possess mechanical strength under compression similar to that of natural bone. Although the mechanical properties depend of the specific place in the skeleton, the differentiation between cortical and cancellous is bone is determinant. The intrinsic porosity of cancellous bone is detrimental to its resistance, but much more factors affect it throughout life [111,119,239,240]. The reference values of compressive strength for human cortical bone is around 90-230 MPa (tensile strengths ranging from 90-190 MPa), whereas the compressive strength of cancellous bone ranges between 2-45 MPa.

The following results (Figure 6.32) illustrate the mechanical behavior of four samples under a compressive force of 5 N for a period of 3 hours. The samples were selected from a series containing 500 μl hydrolyzed collagen stock solution and 150, 200 and 300 μl HEMA (Test 1; samples #1, #2, #3). A sample containing only 10 μl HEMA was used as reference. All the samples were previously immersed in a PBS solution, for a week, to mimic in vivo conditions. The reference sample needed a minimum volume of HEMA, otherwise it would dissolve in the PBS medium. Each sample had a diameter of approximately 10 mm and 3 mm thickness. The graphs report the decrease on this last dimension during compression.

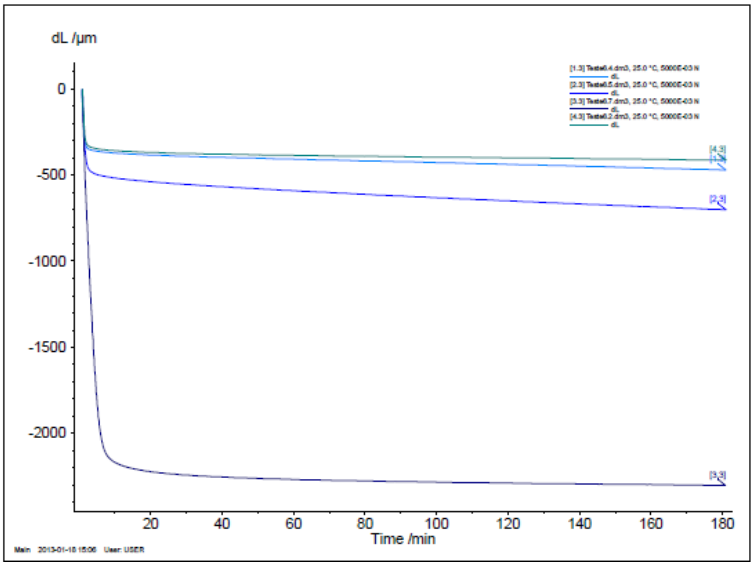

Figure 6.32 – Deformation of composite samples submitted to 5N compressive force for 3 hours.

The results from these tests show that the effect of the applied stress (50 MPa-60 MPa) occurs in the first 10 minutes of the assays, with a high rate of deformation that stops after a contraction of 13, 15 and 17% for the samples containing, 150, 200 and 300 µl HEMA, and 85% for the reference sample. The sample with more HEMA content experienced higher swelling before the test, and this caused a greater contraction with the applied compression force.

6.5.2.5 Biocompatibility

Procedure

The composite materials selected for tests of biocompatibility with human osteoblasts (bone forming cells) were prepared according to the diagram of Figure 6.33. The optimized compositions correspond to sample #5 of Test-2 (Table 6.2). Two different samples were prepared to test the cells interaction not only with the material itself (Figure 6.34; sample T2-5a), but also the microcapsules mC-S dispersed in the composite (Figure 6.34; sample T2-5b).

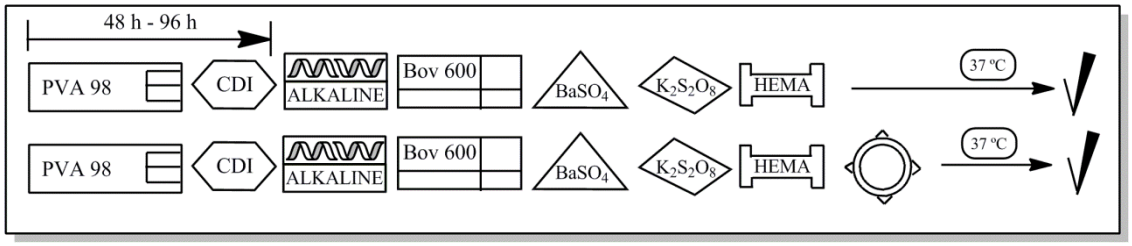

Figure 6.33 – Diagram of the synthesis path of two samples tested for biocompatibility. The composition is described in Table 6.2 (Test2-sample #5) and microcapsules are mC-S type.

The biocompatibility of each selected composite with osteoblasts was accessed by applying a standard protocol for citotoxicity assays. This method involves the preparation of osteoblasts cell cultures, and comparison of the cell viability and proliferation in the absence (controls), or in the presence of a test material. Furthermore, the morphology of the sample material without osteoblasts, or in the presence of these cells, is also part of the methodology.

In order to perform a cell proliferation study, a culture of human osteoblasts was previously prepared as described in Section 9.2. To evaluate cell behaviour in the presence of the composite samples, osteoblast cells were seeded with the test materials in 96-well plates at a density of $10x10^3$ cells per well, during a week. The materials were sterilized by UV irradiation for 30 minutes, before being placed in contact with cells. Cell growth was monitored using an inverted light microscope.

The characterization of the cytotoxicity profile of the composites involved seeding the human osteoblast cells in the presence of the materials in a 96-well plate with 100 µl of DMEM-F12 and subsequent incubation at 37°C, in a 5% CO_2 humidified atmosphere. After an incubation period (1, 2, 3, 4, 5, 6, and 7 days), cell viability was assessed through the reduction of the MTS into a water-soluble formazan product. Briefly, the medium of each well was removed and replaced with a mixture of 100 µL of fresh culture medium and 20 µL of MTS/PMS reagent solution. Then, cells were incubated for 4 hours at 37°C, under a 5% CO_2 humidified atmosphere. The absorbance was measured at 492 nm using a microplate reader. Wells containing cells in the culture medium without materials were used as negative controls (K-). Ethanol (96%) was added to wells that contained cells, as a positive control (K+).

Finally, the sample materials morphology with and without cells was analyzed by SEM. To evaluate cell adhesion and proliferation, human osteoblast cells were seeded over the materials. After 1 day of culture, the samples were fixed overnight with 2.5% glutaraldehyde in PBS at 4 °C. Hereafter, samples were rinsed three times with distilled water for 2 minutes and dehydrated in graded ethanol of 70, 80, 90, and 100% for 10 min in each solution. After this procedure, samples were gold sputtered for SEM observation.

Results

In order to characterize the physiological response of the osteoblast in the presence of the composite materials (samples T2-5a and T2-5b), MTS assays were performed. The MTS assay results (Figure 6.34) showed that none of the materials

affected cell integrity or viability, which is fundamental for the biomedical applications proposed for these materials. These tests validate also the use of mC-S microcapsules.

In vitro studies were performed seeding human osteoblast cells with the same initial density in the 96-well plates, with or without the composite materials to assess their cytotoxicity. Cell adhesion and proliferation in the presence of the materials was characterized through an inverted light microscope (Figure 6.35) and SEM analysis (Figure 6.36).

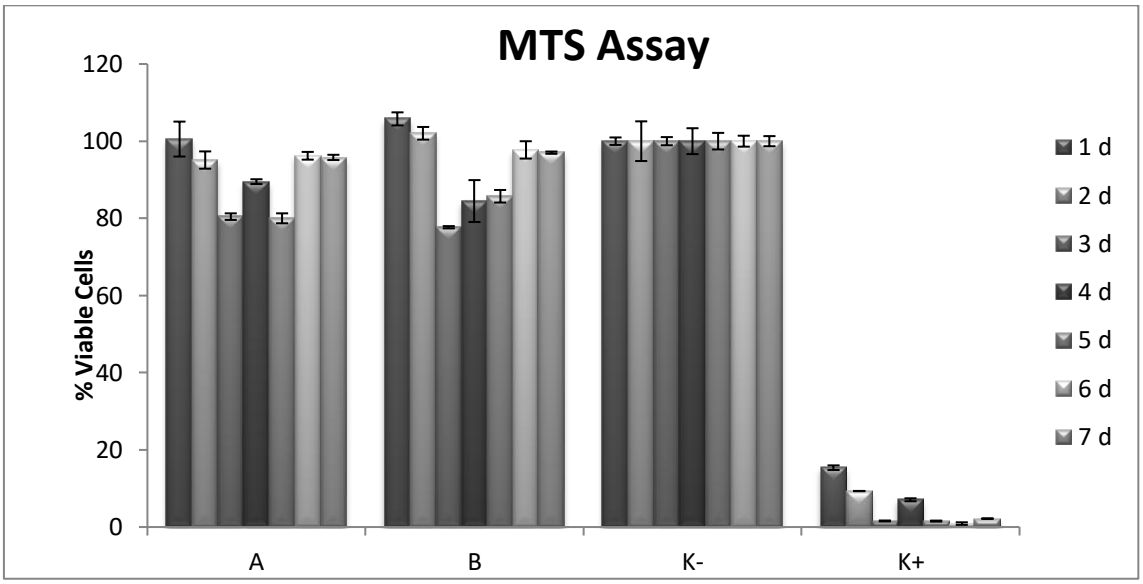

Figure 6.34 – Results from the MTS assay. The cell viability of both test samples (A= T2-5a and B= T2-5b) is identical to the negative control (K-).

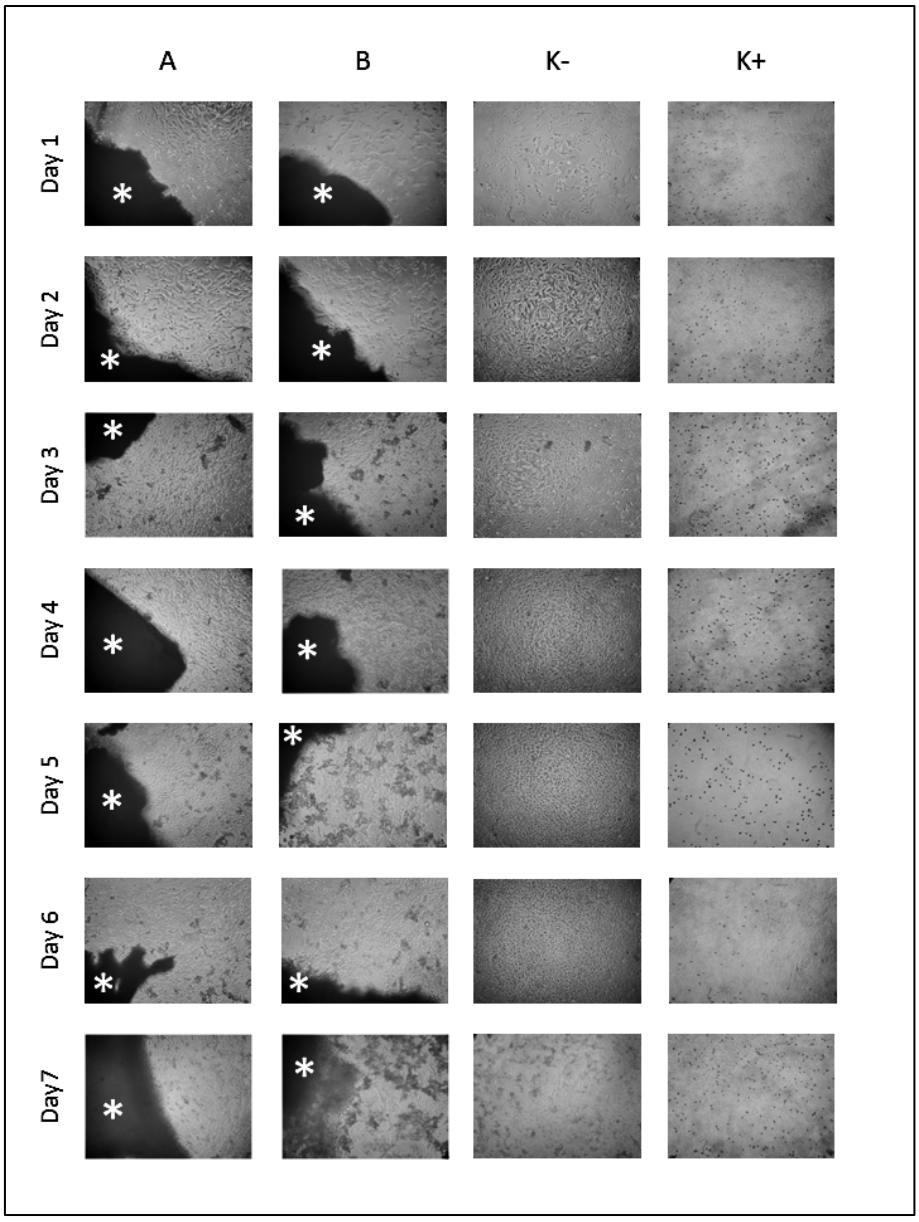

Figure 6.35 - Images from inverted light microscopy of the composite materials ((A= T2-5a and B= T2-5b) and control samples (K-=negative; K+=positive). Osteoblasts adhered and proliferated in contact with both test materials and in the negative control.

Both Figures 6.35 and 6.36 show that cells adhered and proliferated in contact with all the materials and in the negative control (Figure 6.35). The SEM images (Figure 6.36) show that both materials are homogeneous, with uniform particle sizes. In the images of composites with cells, both present osteoblasts with increased Cell *filopodium*, indicating that human osteoblast cells were attached and spread on the materials after 24 h, showing that they have suitable morphological and chemical properties.

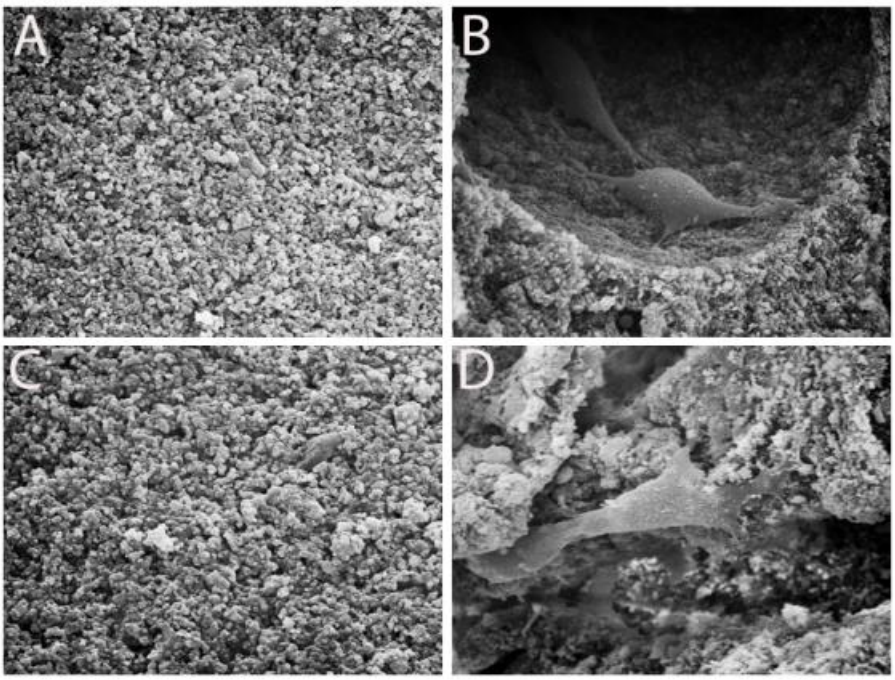

Figure 6.36 - SEM images of the tested composites with osteoblasts (right column; B and D) or without osteoblasts (left column; A and C). Top row: Sample T2-5a - composite without microcapsules. Bottom row: sample T2-5b - composite with microcapsules.

6.5.2.6 Hemocompatibility

The T2-5 composite samples were selected not only for biocompatibility assays with osteoblasts, but also to evaluate hemocompatibility *in vitro* by hemolysis tests, in particular.

Procedure

The hemocompatibility was evaluated *in vitro* according to the International Standard Organization (ISO) 10993-4 [22] by hemolysis tests. These were performed as described in the F756-00 standard of American Society for Testing and Materials (ASTM) [24]. Rabbit venous blood used in these studies was colleted in polypropylene tubes with a 9:1 blood/ACD (acid citrate dextrose) solution [17] ratio and was used immediately after collection.

Rabbit venous blood used in these studies was colleted in polypropylene tubes to which an appropriate volume of acid citrate dextrose (ACD) solution was added. The recommended ratio was 9:1 blood/ACD and the prepared solution was used immediately after collection. Tests were run in triplicate.

For each test material, six samples were placed in polypropylene test tubes and 7 mL of PBS were added to three of them. After 72 h of incubation at 37 ºC, the PBS was removed and reserved. Then, 1 mL of diluted blood/ACD (9.02 mg/mL) was added to each incubated sample and also both to the PBS extraction solution and to three samples of composites with no previous treatment with PBS, being all samples maintained at 37 ºC for 3 h. Positive and negative controls were prepared by adding the same amount of blood/ACD to 7 mL of water and PBS, respectively.

All tubes were gently inverted twice each 30 min to maintain contact of the blood with the material. After incubation, each fluid was transferred to a suitable tube and centrifuged at 2000 rpm for 15 min. The hemoglobin released by hemolysis was evaluated measuring the optic density (OD) of the supernatants at 540 nm using a spectrophotometer. The percentage of hemolysis was calculated as described in the following equation:

$$Hemolysis\ (\%) = 100 \times \left(\frac{OD_{test} - OD_{negative\ control}}{OD_{positive\ control} - OD_{negative\ control}}\right)$$

Results

After the complete procedure, the composite samples T2-5a and T2-5b showed an identical behavior to the negative control, indicating that they do not cause hemolysis in contact with blood (Figure 6.37).

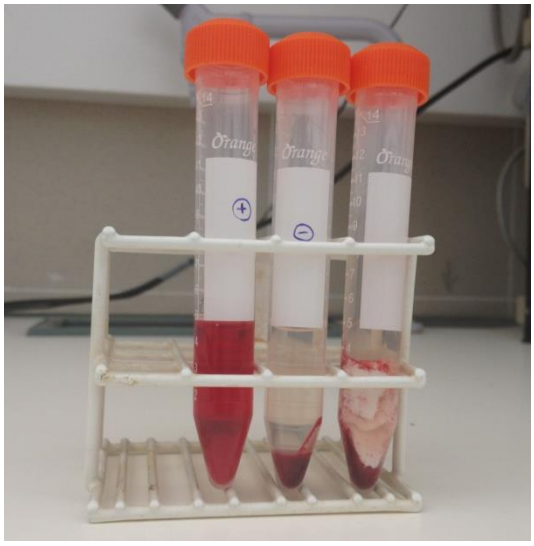

Figure 6.37 – Comparison between the test tubes containing (from left to right) the positive control, the negative control and the T2-5b sample (composite containing mC-S microcapsules) after testing its hemolysis potential.

The optical density of the analyzed samples was determined from the calibration curve presented in Figure 6.39. The calculations returned the following hemolysis

percentages: 90 % for the positive control, 2% for the negative control; 3% for composite T2-5a and 4% for composite T2-5b.

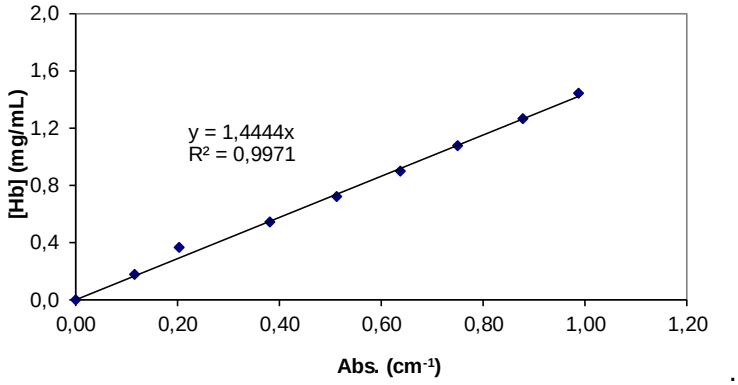

Figure 6.38 – Calibration curve of the hemolysis test.

The results from the hemolysis test enabled to reinforce the indications from the cytocompatibility assays in that the studied composites are adequate for in vivo applications, particularly for interaction with bone tissue.

6.6 **Conclusions**

This chapter reports the experimental work in the search for an adequate system of reagents to solidify a composition based in a PVA suspension of hydroxyapatite and Barium sulphate.

A series of tests involving different reagents and variables were successively introduced in the initial suspension.

The main steps of the new synthesis method involved the following procedures:

1- Reaction of PVA with a carbodiimide (CDI) to obtain PVA-CDI
2- Reaction of PVA-CDI with hydroxyapatite (HA) to obtain PVA-CDI-HA
3- Reaction of PVA-CDI-HA mixed with $BaSO_4$, $K_2S_2O_8$, HEMA and hydrolyzed collagen

These procedures were performed under different experimental conditions regarding preliminary reagents preparation, order of addition and environment, since the intermediate materials had to be combined to originate a solid material at body temperature, inside a closed space. To monitor the whole process, the applied techniques have been NMR (solution and solid-state CP-MAS; proton and carbon-13), FTIR, LDS, XRD, DSC-TGA, DMTA, SEM and optic microscopy. Many experimental results were not conclusive since they did not provide evidences of the applied

procedures in virtue of the masking effect mostly from the minerals. The most significant results that enabled the detection of chemical or physical alterations have been presented along this chapter. At final stages of the synthesis path, the most promising samples were tested regarding swelling, degradation in PBS; biocompatibility and hemocompatibility.

The first step of the synthesis procedure, the interaction between PVA and CDI is difficult to justify. After mixing PVA and CDI for at least 48 hours, the subsequent addition of hydroxyapatite releases gas bubbles from the suspension. The gas release shows that a chemical reaction is undergoing but the FTIR and NMR spectra do not provide unequivocal results. The only clue in the literature points to an activation of the polymer bonds through the carbodiimide moiety [211]. Regardless the theoretical explanation, in addition to the gas release, other evidences show that there was, effectively, a chemical reaction. If this step was not done, the final composition of the pre-composite would not solidify with HEMA.

In the second step of the procedure, the influence of PVA-CDI in the particle size distribution of hydroxyapatite minerals was monitored by LDS, being studied bone-derived and synthetic samples, carbonated and non-carbonated. These samples were also dispersed in CDI and urea solutions. The sample that presented the larger variation was HABov600. The PVA-CDI complex acts in an equivalent manner to urea with that sample. At the end of this stage, the composition was termed PVA-CDI-HA.

The addition of the contrast agent could be done at any point of the reaction from this stage. It showed an inert behavior. The resulting complex PVA-CDI-HA $BaSO_4$ was then submitted to further tests to search for a solidifying mechanism.

In the third step, the only system that worked under physiological conditions involved hydrolyzed collagen in alkaline medium and the binary potassium persulfate associated to HEMA. The conventional TEMED catalyst and MbisA crosslinker could not be used.

The proposed mechanism for the solidification process of the pre-composite is based on a graft polymerization initiated by the persulfate radicals [219,221,230]. These activate not only the C=C double bonds of HEMA and of collagen, but also the PVA-CDI-HA hybrid composition, resulting in crosslinked network that hardens gradually becoming insoluble in water.

The manipulation of different ratios of components enabled to obtain a composition with appropriate swelling properties and mechanical strength adequate for bone substitution inside vertebral bodies.

The use of microcapsules was also tested, being demonstrated that they are inert chemically and do not cause any detrimental biological effect. These can be used to contain HEMA and create porosity inside the composite, increasing the potential for bone repair.

The optimized composition that retrieved the most adequate properties and that presented biocompatibility with osteoblasts and insignificant hemolysis potential has the following formulation: 3.0 g of 20PVA98-3CDI at a concentration of 20 wt%, 0.6 g HABov600, 0.6 g BaSO4, 0.5 ml alkaline-hydrolyzed collagen, 200 mg $K_2S_2O_8$ and 0.4 ml HEMA

Looking at the results reported in this chapter with increased detail, the starting point was, as mentioned, the interaction between PVA and CDI. The purpose of adding CDI to the polymer solution was to use it with together with collagen, that would be added posteriorly to a well dissolved polymer with CDI. The purpose was to use a conventional, well described process to crosslink collagen and try to make un interpenetrating network between crosslinked collagen and PVA. In the meanwhile, HABov600 was added to the PVA-CDI solution and there was a visible reaction since a gas release was observed. The same happened with HABov900. This means that the carbonate content of hydroxyapatite was not the cause of that effect.

This event could be forgotten, except for the fact that only the HA suspensions in PVA that had been prepared with CDI first could become crosslinked at the final of the synthesis procedure. If CDI was added to the reaction vessel at any other moment, the mixture would never solidify.

In order to investigate the chemical reaction between PVA and CDI, FTIR and NMR spectroscopies were used, and the variables were the hydrolysis degree of the polymer (PVA80 and PVA98). The FTIR spectrum of PVA80-CDI showed a decrease in the relative intensity of the broad OH stretching band in the range 3000-4000 cm^{-1}, indicating that this polymer had less free hydroxide groups. However, the spectrum of PVA98-CDI had no change. As for the proton-NMR spectra, both solutions of PVA-CDI presented a new peak at 2.15 ppm that derives from a new chemical bond. This peak is

not observed in the spectrum of CDI; thus, it derives from the reaction that forms PVA-CDI molecules, or just modified PVA (not linked to CDI). However, the former term was adopted in the description of the process. The Carbon13-NMR spectra of both polymers confirm that some chemical changes occurred due to CDI. The spectrum of PVA80 loses the C=O peak at 180 ppm and both polymers present two new peaks at lower fields (at 30 and 21 ppm). The problem with these new NMR peaks is that the assignment should be supported by a rational mechanism of reaction and the literature is not helpful in this regard.

The next step of the investigation was focused in the reaction between PVA-CDI and hydroxyapatite. The variables were the hydrolysis degree and the type of hydroxyapatite, natural and synthetic, carbonated, or not. The results by FTIR or XRD showed mostly the mineral contribution and the minor changes in the polymeric component were not detectable.

The decision to characterize the PVA-CDI-HA samples using LDS was made at the end of diverse synthesis procedures, with many more reagents involved. Part of these procedures had negative results and the composites did not solidify. The observation by SEM of samples that solidified, and others that did not, showed that the particle sizes of hydroxyapatite was much smaller in the materials that started with PVA-CDI. The smaller mineral particles were also better distributed in the organic matrix.

The results from LDS showed that the particle size distribution of HABov600 shifts to ranges between 1 and 10 μm when mixed with PVA-CDI, or CDI alone. This effect is identical with urea, which was tested for curiosity. Ionic liquids are often based on this molecule, being used to dissolve diverse solid materials. The sample of HABov900 had a totally different result with LDS. The particle size was not affected by PVA-CDI nor CDI alone. The test of the synthetic minerals showed that Calcibon had small changes with PVA-CDI, but a great shift with urea. Inbone, on the other hand, did not change its particle size significantly but the starting size was already in the range 1-10 μm.

The selection of a crosslinking system for the complex PVA-CDI-HA-$BaSO_4$ was based on the conventional reaction of radical induced polymerization of HEMA. The initiator was potassium persulfate. The usual catalysts and crosslinkers TEMED and MbisA were detrimental for the material at study. In this work, the intention was to avoid acrylic monomers but because many other systems were unsuccessful, it was worth trying HEMA, with the concern of using the least as possible. Curiously, the addition of

HEMA and coadjutants to the suspension did not result in a solid material. Under the conditions applied, the formation of poly(HEMA) was not possible.

The solution to this problem came with the addition of collagen, previously hydrolyzed to become soluble. The hydrolysis with acid was the first option and the pre-composite formulation containing this collagen and potassium persulfate solidified after adding HEMA. This seemed a good result, but this reaction proceeded in a closed environment at 37 ºC (to simulate the vertebra) from a solid to a paste again. This showed that the material was degrading, possibly due to acid-base reactions. Thus, being so close to a solution for the challenge of obtaining a stable solid, the next experiment was made with alkaline hydrolyzed collagen. Finally, the outcome was positive. The chemical characterization was made with solid state NMR.

Having an optimized formulation regarding the solidification of the pre-composite, other tests were made to ascertain the ratios of reagents that would return better properties. The swelling tests and mechanical tests were important to decide the range of concentrations for the components of the composite. In general, the collagen:HEMA ratio that originated the greatest swelling corresponded to 500:200 (V/V), or 600:400 (V/). The experiments regarding biocompatibility and hemolysis showed that the composite may be used in bone graft applications.

These studies also included the use of PLA microcapsules, some of them with sizes around 100 μm and porous structure, known to be favorable for bone regeneration. The purpose of these particles is to use them to deliver the HEMA to the suspension and to create porosity inside the composite to increase the cell invasion *in vivo*.

7 In vivo test

7.1 Introduction

The last chapter dedicated to the experimental work that was developed to obtain a biomaterial adequate for kyphoplasty procedures is a report of a test *in vivo*, with an animal model. The present study has the objective of testing the biocompatibility and the bone substitution capacity of an optimized composite based in a polymeric matrix mainly composed of PVA, reinforced with bone-derived carbonated hydroxyapatite and containing a contrast agent. Other organic and inorganic components are also part of the formulation, including PLA microcapsules combined to enable the injection and posterior in situ solidification of the biomaterial inside a collapsed vertebral body.

The test involved two parts. First, the implantation of the biomaterial in an animal model. This work was performed in Universidade da Beira Interior, at Centro de Investigação em Ciências da Saúde (CICS), under the supervision of Doutor Ilídio Ferreira. Then, the histological sections obtained after five weeks implantation were supplied to be analyzed in this study. This methodology enables the study of the osteocondutive and osteocondutive properties.

Since the material under study is meant for application in large bone defects, the animal model, a rabbit, was selected accordingly [5,54,96,241,242]. The international standard for the biological evaluation of medical devices recommends a maximum of 6 implants (3 test and 3 control implants) per rabbit (International Standard ISO 10993-6, 1994). This is half the maximum number of implants recommended for sheep, dogs, goats and pigs. Also, the size of the implant which may be inserted is limited. Cylindrical implants are no recommended to be larger than 2 mm in diameter and 6 mm in length, again this is half that recommended for the other larger species mentioned (International Standard ISO 10993-6, 1994). Despite this, the rabbit remains a very popular choice of species for the testing of implant materials in bone [5,54,96,241,242].

The selected composite was previously tested for biocompatibility with osteoblasts and for hemocompatibility. Since the outcome was positive, the next step was the evaluation of the bioactivity (osteoconductivity and if possible, osteoinductivity and angiogenesis).

7.2 Procedure

This experiment started with the preliminary preparation of the composite material. As described in Chapter 6 (Table 6.2, Sample #5), this composite is based on a final reaction between PVA98-CDI-HABov600-$BaSO_4$-COL-$K_2S_2O_8$ and HEMA. Additionally, standard microcapsules of type mC-S were also included in the suspension. The polymerization and crosslinking occurred for 48 hours in a closed vessel, at 37 ºC.

After the synthesis, the solid composite was immersed in PBS for 24 hours with the purpose of swelling it to around 140 wt% of the initial mass. Next, according to the usual protocol, a tube with internal diameter of 5 mm was used to cut eight disks from the starting sample. These were put in a well culture plate and sterilized with UV radiation for thirty minutes. Then, the plate was sealed with adhesive tape (Figure 7.1).

Figure 7.1– Composite samples in disk shape (5 mm diameter) after UV sterilization.

The animal model was an adult male rabbit weighting around 2.8 Kg, in good health conditions.

The surgery was performed by a veterinary doctor and the procedure went smoothly. Proper care with pre-operative conditions included the administration of anxiolytic drugs (butorfanol + diazepam) to avoid the release of catecholamines that are potentially fateful in rabbits. After the trichotomy and topic antiseptics with iodopovidona (betadine®), an incision of 3 cm was made at the distal part of the femur, in the lateral region of the joint. Then, the muscle tissues were spread and the appropriate site for implantation was identified. The perforation to create a bone defect was made with successive drills until a depth of 6 mm. The composite material was put inside the defect, and the procedure ended with the suture of the tissues. After the surgery, analgesics and antibiotis were also part of the postoperative treatment. The clinical evolution was monitored in the next 5 weeks using x-ray imaging. After euthanasia, the bone was collected and prepared for histological analysis.

The x-ray images in Figure 7.2 were obtained at days 1, 8 and 35 after the surgery. The enhanced contrast relative to natural bone shows that the proportion of minerals in the composite is adequate for monitoring the position, shape and size of the implanted material.

After extracting the femur and removing the surrounding tissues, the piece containing the composite material was cleaned.

Diverse histologic sections were prepared from the defect area which included the surrounding natural bone. The slices were extracted from three regions across the composite: the middle and two extremities (Figure 7.3). All samples were prepared for hematoxylin and eosin (H&E) staining. First, they were fixed in 10% formalin for 5 days

and then they were decalcified with 10% formic acid for 5 days. During this process, the acid was changed daily, and the degree of decalcification was evaluated manually. After decalcification was complete, the samples were put into lithium carbonate for 5 minutes and then each specimen was divided into two parts at the center and prepared for histologic examination in a routine manner. The samples were put into an automatic autotechnicum machine. In this machine they were put into a series of graded alcohol concentrations for dehydration as well as xylol. After they were mounted in paraffin from the cut side, histologic sections (5 mm) were created and stained with H&E.

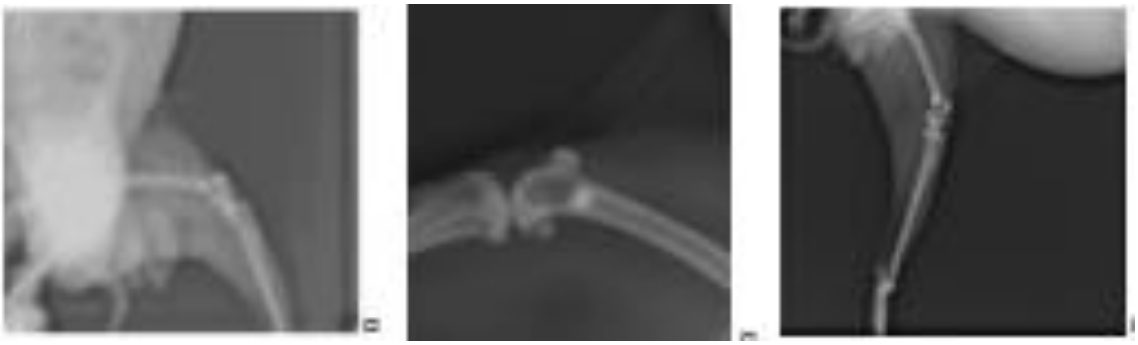

Figure 7.2 – X-ray images of the implanted region at days 1, 8 and 35 after the surgery.

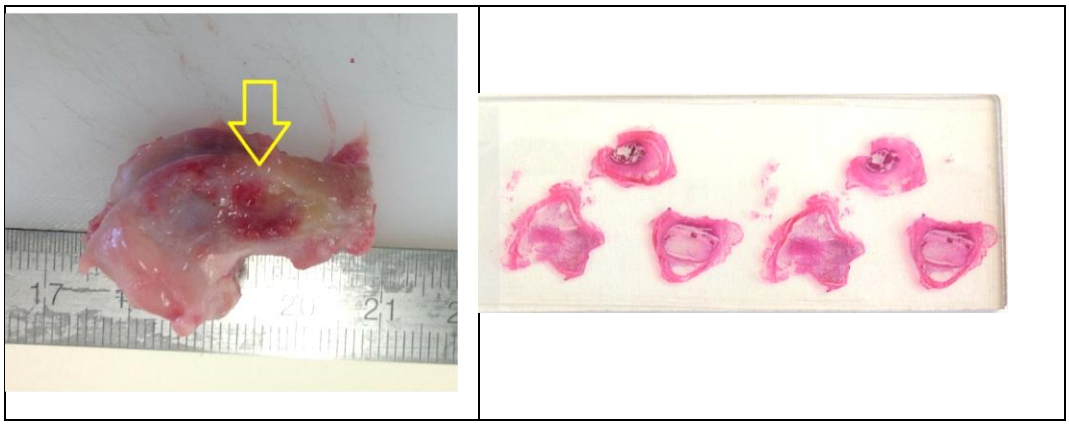

Figure 7.3 – Bone piece containing the bone defect with the implanted composite (left). Histologic sections from different slices across the composite (right).

7.3 Histological analysis

The histologic sections were examined microscopically at diverse magnifications. There were some signs of a foreign-body reaction, an inflammatory response by granulomatous cells, being this effect a frequent event in bone grafting [5,7,13,243].

At 20x magnification (Figure 7.4) half of the middle section of the composite disk is observed next to the surrounding cortical bone. The composite includes multiple microcapsules dispersed in the whole cross section and there are fissures of diverse

dimensions. The structure of cancellous bone, with thin trabeculae immersed in bone marrow is clearly observed in Figure 7.5. This is the biological environment for which this composite has been developed.

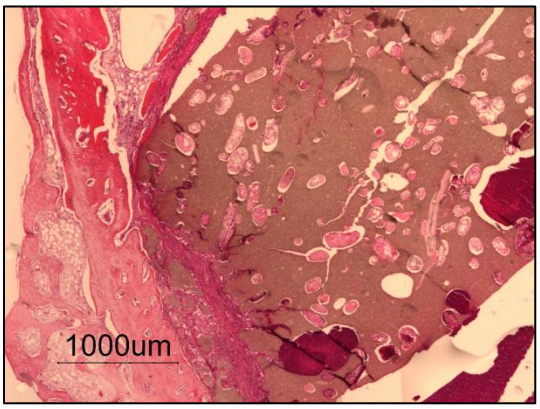

Figure 7.4 – Global appearance of the cross-sectioned composite after 5 weeks implantation.

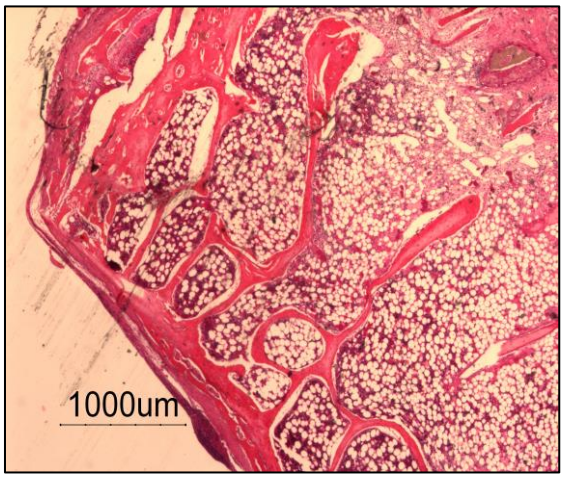

Figure 7.5 - Internal structure of cancellous bone

Increasing the magnification to 400x-1000x, many details can be observed, as depicted in Figures 7.6-7.8.

The field of view in Figure 7.6 is focused on a fragment separated from the periphery of the bulk. At 400x, it shows two different environments. The left side of the image shows adypocites and many other cells around the trabeculae, and the right side presents a different background. More importantly, the top side of the fragment is covered by new bone tissue, as evidenced by its morphology, staining and close adhesion to the surface of the composite [36,96,242,244].

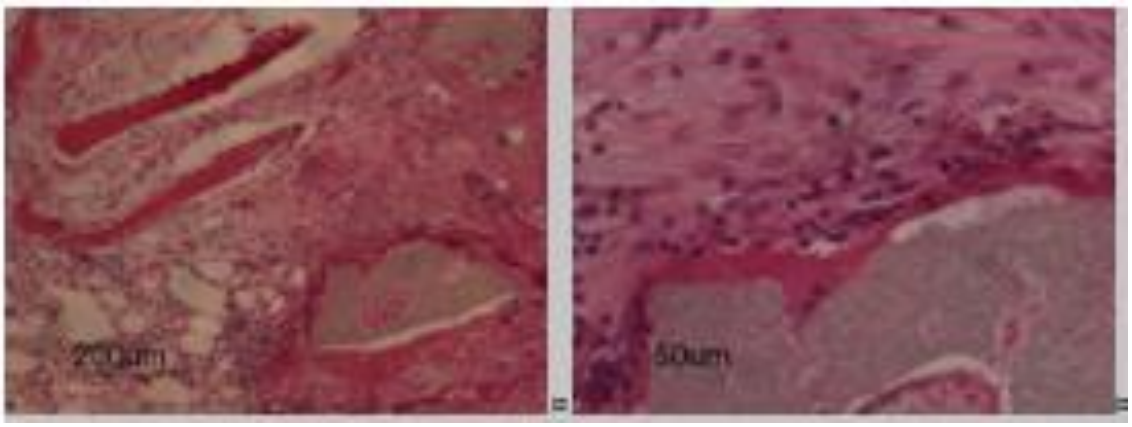

Figure 7.6 – New bone tissue formed on the surface of a composite fragment.

The images of Figure 7.7 depict different cases. On the left, the composite particle is surrounded by fibrous tissue and the material surface has multinucleated cells that may be osteoclasts resorbing it. Numerous other cells with comparable dimensions are also observed. On the right image, the composite is next to a bone trabecula that is full of bone linning cells on the surface. The composite has a fissure and it seems that the bone tissue is invading this passage in the direction of a microcapsule. In that porous space, some bone tissue is also observed.

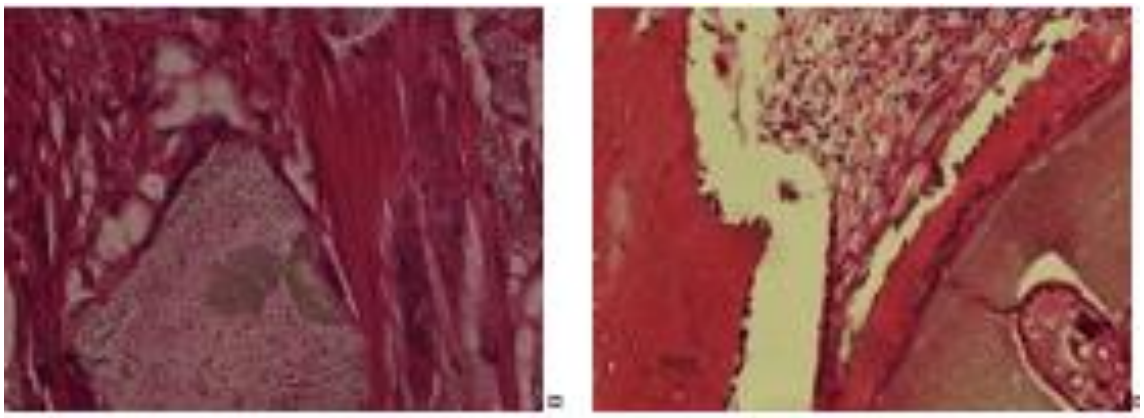

Figure 7.7 – Osteoclasts resorbing the surface of the composite (left). Bone tissue invasion through a fissure in the composite, in the direction of a microcapsule.

To finish this description, it should be remembered the role of vascularization in the integration of bone grafts or other bioactivity events [41,57,245-247]. Figure 7.8 is not focused in the composite. Instead, it shows the cross section of an artery with its walls and erythrocytes inside, and a vein with is numerous erythrocytes. Around them, the large adipocyte cells show their typical morphology.

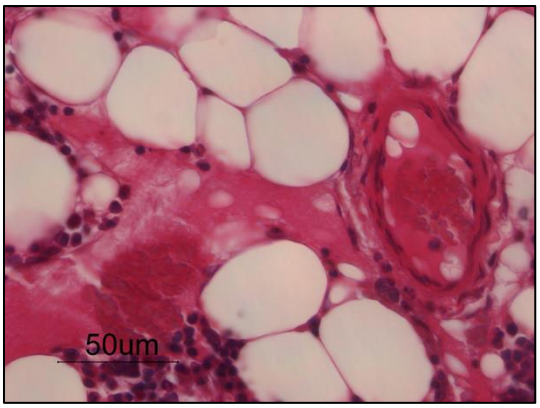

Figure 7.8 – Detail of the bone marrow composition. An artery (with its walls and erythrocytes inside), a vein (with its numerous erythrocytes), adipocytes and other cells.

7.4 Conclusions

The results from the test in vivo showed that the composite material containing standard PLA microcapsules has promising properties for bone grafting.

After five weeks implantation, there are evidences of bone regeneration, although in limited extent. The formation of new bone tissue over some composite fragments by osteoblasts and the observation of osteoclasts resorbing the surface of other fragments point to a dynamic activity involving the composite material.

Moreover, the cell and tissue invasion of the fissures in the material, into the pores of the microcapsules are also positive signs regarding osteocondutive properties. Despite the composite does not possess interconnected porosity after injection, the expected trend is that the microcapsules will contribute to create more porosity, as they degrade into the local environment.

This raises the question about the biodegradation potential of the composite. To reach a conclusion on this subject, further tests are required using the rich and complex medium of the bone marrow. The cellular environment and enzymes may determine the biodegradation profile of the implanted material.

8 Conclusions

8.1 Final remarks

The present study constitutes an opportunity to obtain better knowledge about diverse subjects since it combined chemical engineering, materials science engineering, biology and medicine, reflecting the necessary dialog between such diverse fields. In addition, it enabled to learn about over twenty experimental techniques and multiple procedures that were applied to characterize different materials, namely diverse ceramics and diverse polymers of natural and synthetic origins. The characterization focused multiple chemical and physical properties, such as chemical composition, thermal behavior, microstructure, viscosity, surface energy, porosity, particle size distribution, compression strength, biocompatibility, hemocompatibility and osteogenesis. Most importantly, this study enabled to correlate different properties, driving the research to the achievement of the objectives defined at the beginning of the work.

The motivation for the scientific research developed in the present work has been the development of biomaterials alternative to PMMA and other bone cements to apply in the repair of collapsed vertebrae through kyphoplasty. The main challenge of this work has been the search for an innovative composite material, rather than developing a product from reagents with little differences from those usually applied in the synthesis of bone cements.

With the objective of obtaining a composite that mimics bone, this study focused the mineral phase and the organic phase of a new biomaterial that needed to be injectable and to be able to solidify *in situ*, inside a vertebral body. The test of different formulations and chemical synthesis paths allowed the progress of the research from a wide set of options to a single specific product that passed all the virtual filters.

The results retrieved from this study enabled to obtain a formulation that complies with the initial objectives, although it was necessary to include an acrylic component in the composition. Nevertheless, its concentration is extremely low compared to commercially available acrylic bone cements. In addition to the formulation, the interpretation of the results contributed to develop a theory about the chemical reactions involved in the synthesis procedure. Moreover, the results suggest that the biomaterials that were optimized in this study may be applied in other anatomical sites for bone repair procedures, particularly for cancellous bone defects.

At the end of the research, diverse questions remain unsolved and these can constitute suggestions for future work:

- Can the composite be synthesized with another carbodiimide? That´s the only reagent kept constant in the procedure (besides potassium persulfate, the chemical initiator).

- Are there other techniques to enlighten the reaction mechanism? Some steps could be better characterized. Molecular dynamics computing could provide valuable information to explain some chemical reactions.

- Is the composite biodegradable? A large proportion is bone-derived hydroxyapatite and it also contains collagen. So, it is at least partially biodegradable. But how about the set of polymers from the organic phase? Are there specific enzymes to degrade it inside a bone defect? Additional *in vivo* tests would be necessary.

-Should it be biodegradable? Most bone repair clinical procedures are applied in elderly patients, with limited potential forl new bone formation. For these, is it better to have a non-biodegradable bone graft?

- Can the microcapsules transport and deliver antibiotics, BMPs, growth factors or other substances to the composite? If so, what is their delivery kinetics like? The type and concentration of additives would need to be scaled to the target site.

- Can the obtained formulation be applied in 3D-printing devices? This would enable the synthesis of bone grafts with complex shapes and controlled architecture. Scaffolds with interconnected porosity and adequate pore sized could be manufactured for specific bone defects and specific clinical applications.

All these questions are open to debate and would require further experimental work. And, as usual in science, even the questions that seem closed issues may always be reviewed.

9 Appendix

9.1 **Main reagents**

Table 9.1 - Acquired reagents and respective manufacturers.

Reagent	Manufacturer
Inbone	Agoramat
Calcibon	Biomet
PVA 80% hydrolized, Mw 9000-10000	Sigma Aldrich
PVA 96% hydrolized, Mw 85000-146000	Sigma Aldrich
PVA 98% hydrolized, Mw 13000-230000	Sigma Aldrich
Sodium Metaperiodate	Sigma Aldrich
Urea	Sigma Aldrich
N-cyclohexyl-N´-(2-morpholinoethyl) carbodiimide methyl-p-toluenesulfonate	Sigma Aldrich
Amino methyl propanol	Sigma Aldrich
Sodium borate	Sigma Aldrich
Boric acid	Sigma Aldrich
Potassium persulphate	Sigma Aldrich
PLA	Sigma Aldrich
HEMA	Sigma Aldrich
Collagen Type I from bovine Achilles tendon	Sigma Aldrich
PBS	Sigma Aldrich
ACD acid citrate dextrose	Sigma Aldrich
Rabbit venous blood	

9.2 **- Instrumental**

TGA-DSC

Simultaneous thermogravimetric analysis (TGA) and Differential Scanning Calorimetry (DSC) measurements were carried out using a SDT Q600 equipment (TA Instruments, New Castle, DE, USA). Samples weighting 10-20 mg were heated in an alumina crucible at a rate of 10ºC/min from 25ºC-1500ºC (bone samples) or from 25-600 ºC (polymers, intermediate compositions and composites) under an oxidizing atmosphere using 55 cm^3/min flux of air.

FTIR

Fourier Transform Infrared Spectroscopy (FTIR) was used to investigate the chemical composition of almost all samples. The FTIR spectra were obtained using a Nicolet Magna IR-750 spectrometer (Nicolet, Madison, WI, USA) in the attenuated total reflection (ATR) mode. The spectra were registered in the 500-4000 cm^{-1} region using 64 scans and a spectral resolution of 4 cm^{-1}.

XRD

The samples spectra were collected using a Philips X-PERT diffractometer (Philips, Amsterdam, Netherlands) operating in the Bragg-Brentano configuration with Co-k□ (λ=1.78897 Å) radiation at a current of 35 mA and an accelerating voltage of 40 kV. Intensity data were collected by the step counting method (step 0.02º and time 0.5 s) in the range 2θ = 10-100º. Phase identification was performed with reference to the database supplied by the International Centre for Diffraction Data, namely using the Powder Diffraction Files nº 84-1998 (hydroxyapatite), 80-0512 (barium sulphate) and 83-1436 (urea).

Mercury intrusion porosimetry

Porosity and pore size distribution were determined using the AutoPore IV 9500 (Micromeritics Instrument Corp., Norcross, GA, USA). The pressure range varied between 0.5 psi and 30000 psi, which enabled the measurement of pore diameters between 400 µm and 0.006 µm, respectively.

SEM

SEM observations were carried out in a Philips XL30 microscope (Philips, Amsterdam, Netherlands) operating at 20 kV. The test samples were mounted on a double-coated carbon conductive tape and sputter coated with gold.

SEM (UBI)

Samples were sputter coated with gold using an Emitech K550 equipment (London, UK). The SEM images were acquired with a scanning electron microscope Hitachi S-2700 (Tokyo, Japan) with an acceleration voltage of 20 kV at different magnifications.

Light microscopy

The washing and separation stage of the synthesis process of microcapsules was monitored by light microscopy (LM). Samples consisted on aqueous suspensions of those particles.

Light microscopy was performed using a Nikon Optiphot equipment (Nikon Inc., Melville, NY, USA).

These samples were further analysed by image analysis (*BH-2* microscope from *Olympus* coupled with morphometry software *CUE-2* also from *Olympus*).

LDS

Particle size measurements were made by laser diffraction spectrometry using a *Coulter LS 130* equipment.

IGC

The analysis was carried out on a DANI Instruments (Milan,Italy) GC1000 digital pressure control gas chromatography instrument equipped with a H_2 FID at a column temperature of 37 °C, injector temperature of 180 °C and detector temperature of 200 °C. He was the carrier gas, and methane was the reference.

XPS

The XP spectra were obtained by an ESCALAB 200A (VG Scientific, East Sussex, UK) instrument in combination with PISCES software (Data Systems, Bristol, UK). An achromatic Al (Kα) X-ray source operating at 15 kV (300 W) was used. The spectrometer, calibrated with reference to Ag 3d 5/2 (368.27 eV), was operated in constant analyzer energy mode with 20 eV pass energy. Samples were analyzed at least in duplicate with pellets of approximately 1 cm diameter.

NMR

NMR spectroscopy was used to characterize the PVA80 and PVA98 polymer samples before and after reaction with AMP and CDI.

^{1}H and ^{13}C NMR spectra were obtained at 25 ºC on a Bruker Avance III 400 MHz spectrometer. Samples (20-30 mg) were allowed to dissolve in 600 □l D_2O for at least 24 hours and spectra were recorded using a total of 64 scans for proton and around 3000 scans for 13-carbon.

Solid state NMR

Solid-state NMR spectra were recorded at room temperature using a Inova 750 MHz spectrometer at proton, ^{31}P and ^{13}C resonance frequencies of 20, 160 and 100 MHz, respectively. Echo and crosspolarization (CP) experiments were performed using proprietary double-bearing MAS (magic angle spin) probes and zirconia rotors, spun by dry air. The ^{31}P and $^{1}H/^{13}C$ chemical shifts were externally referenced to 85% H_3PO_4 and TMS, respectively.

SEC

SEC was performed in a HPLC system composed of a degasser and a WellChrom Maxi-Star k-1000 pump (Knauer), coupled to a RI detector and a single column (PL aquagel-OH Mixed 8 lm) from Polymer Laboratories. The whole system was kept at room temperature and the eluent was composed of a previously filtered solution of 1% (v/v) acetic acid and 0.1 M Na_2SO_4 in mili-Q water. The standards used for conventional calibration were composed of polyethyleneglycol (PEG) ranging from 300 to 40000 g/mol. Both standards and samples were dissolved in the eluent solution (3 mg/ml and 10 mg/ml, respectively) and the injection volume was 50 □l, at a flow rate of 1 ml/min.

Viscosity measurements

The viscosity was determined with a controlled stress rheometer, Haake model RS1, equipped with a refrigerated bath ThermoHaake model C35P. Samples were tested using a cone-plate sensor system C60 with 1º angle and 60 mm diameter, enabling measurements in the 0-600 1/s shear rate range

DMTA

DMTA of the samples was carried out using a Tritec 2000 DMA (Triton Technology Ltd.-Nottinghamshire, UK) under single cantilever mode (pocket). All samples were analyzed over a temperature range from -150°C to 250°C, at frequencies 1 and 10 Hz, using a heating rate of 5 °C/min.

Creep

Creep tests were carried out using a DMA 242 E (Netzsch- Germany) under compression mode. All samples were analyzed at room temperature (25 ºC), using a dynamic force of 2 N and 5 N for 1 and 2-3 hours, respectively.

Cell culture for osteoblasts citotoxic assay

Human osteoblast cells were seeded in T-flasks of 25 cm^2 with 6 ml of DMEM-F12 supplemented with heat-inactivated FBS (10% v/v) and 1% antibiotic/antimycotic solution. After the cells become confluent, they were subcultivated by a 3-5 minutes incubation in 0.18% trypsin (1:250) and 5 mM EDTA. Subsequently, cells were centrifuged, resuspended in culture medium and then seeded in T-flasks of 75 cm^2. Hereafter, cells were kept in culture at 37 °C in a 5% CO_2 humidified atmosphere, inside an incubator.

10 References

[1] H.G. Deen, D.S. Fenton, T.J. Lamer, Minimally Invasive Procedures for Disorders of the Lumbar Spine, Mayo Clin Proc. 78 (2003) 1249–1256.

[2] S. Teyssédou, M. Saget, P. Pries, Kyphoplasty and vertebroplasty, Orthop. Traumatol. Surg. Res. 100 (2014) S169–S179. doi:10.1016/j.otsr.2013.11.005.

[3] J.H. Lee, J.-H. Lee, Y. Jin, Surgical techniques and clinical evidence of vertebroplasty and kyphoplasty for osteoporotic vertebral fractures, Osteoporos. Sarcopenia. 3 (2017) 82–89. doi:10.1016/j.afos.2017.06.002.

[4] Z. He, Q. Zhai, M. Hu, C. Cao, J. Wang, H. Yang, B. Li, Bone cements for percutaneous vertebroplasty and balloon kyphoplasty: Current status and future developments, J. Orthop. Transl. 3 (2015) 1–11. doi:10.1016/j.jot.2014.11.002.

[5] G. Fernandez de Grado, L. Keller, Y. Idoux-Gillet, Q. Wagner, A.M. Musset, N. Benkirane-Jessel, F. Bornert, D. Offner, Bone substitutes: a review of their characteristics, clinical use, and perspectives for large bone defects management, J. Tissue Eng. 9 (2018). doi:10.1177/2041731418776819.

[6] T. Sozen, L. Ozisik, N. Calik Basaran, An overview and management of osteoporosis, Eur. J. Rheumatol. 4 (2017) 46–56. doi:10.5152/eurjrheum.2016.048.

[7] Y.C. Hu, D.J. Hart, Complications of vertebroplasty and kyphoplasty, Tech. Reg. Anesth. Pain Manag. 11 (2007) 164–170. doi:10.1053/j.trap.2007.05.010.

[8] D. Synthes, VBS – Vertebral Body Stenting System., DePuy Synth. - Surg. Tech. (n.d.) 1–50. www.depuysynthes.com/ifu (accessed July 1, 2018).

[9] Y. Yimin, Z. Zhi, R. ZhiWei, M. Wei, R.K. Jha, Applications of memory alloy stent in vertebral fractures, Med. Sci. Monit. Basic Res. 20 (2014) 76–81. doi:10.12659/MSMBR.890835.

[10] M. Advantage, Percutaneous Balloon Kyphoplasty and Mechanical Vertebral Augmentation, Medicare Advant. Rev. Protoc. 10/01/14. (2014) 1–6.

[11] V. Denaro, U.G. Longo, N. Maffulli, L. Denaro, Vertebroplasty and kyphoplasty, Clin. Cases Miner. Bone Metab. 6 (2009) 125–130. doi:10.1007/s00701-006-0762-0.

[12] R. Rotter, H. Martin, S. Fuerderer, M. Gabl, C. Roeder, P. Heini, T. Mittlmeier, Vertebral body stenting: A new method for vertebral augmentation versus kyphoplasty, Eur. Spine J. 19 (2010) 916–923. doi:10.1007/s00586-010-1341-x.

[13] I.H. Lieberman, D. Togawa, M.M. Kayanja, Vertebroplasty and kyphoplasty: Filler materials, Spine J. 5 (2005) S305–S316. doi:10.1016/j.spinee.2005.02.020.

[14] P. Heini, U. Berlemann, Bone substitutes in vertebroplasty, Eur. Spine J. 10 (2001) 205–213. doi:10.1007/s005860100308.

[15] B. Zhang, M. Dai, Filler Materials Used in Kyphoplasty and Vertebroplasty for Osteoporotic Vertebral Compression Fractures, Adv. Mater. Res. 393–395 (2011) 766–771. doi:10.4028/www.scientific.net/AMR.393-395.766.

[16] A.S. Brydone, D. Meek, S. MacLaine, Bone grafting, orthopaedic biomaterials, and the clinical need for bone engineering, in: Proc. Inst. Mech. Eng. Part H J. Eng. Med., 2010: pp. 1329–1343. doi:10.1243/09544119JEIM770.

[17] F. Barrère, C. a. van Blitterswijk, K. de Groot, Bone regeneration: Molecular and cellular interactions with calcium phosphate ceramics, Int. J. Nanomedicine. 1 (2006) 317–332.

[18] M. Bohner, Design of ceramic-based cements and putties for bone graft substitution, Eur. Cells Mater. 20 (2010) 1–12. doi:10.1016/S1369-7021(10)70014-6.

[19] E. Hughes, T. Yanni, P. Jamshidi, L.M. Grover, Inorganic cements for biomedical application: Calcium phosphate, calcium sulphate and calcium silicate, Adv. Appl. Ceram. 114 (2015) 65–76. doi:10.1179/1743676114Y.0000000219.

[20] G. Fuentes, Y. Hernández, Y. Campos, N. López, M.L. Rojas, E. Peón, A. Almirall, J.A. Delgado, Composition influence on properties of acrylic composites loaded with synthetic hydroxyapatite, Lat. Am. Appl. Res. 38 (2008) 105–112.

[21] H. Davis, J. Leach, Hybrid and Composite Biomaterials in Tissue Engineering, in: N. Ashammakhi (Ed.), Top. Multifunct. Biomater. Devices, 2008: pp. 1–26. doi:10.1016/j.injury.2007.02.014.

[22] A. Sionkowska, J. Kozlowska, Characterization of collagen/hydroxyapatite composite sponges as a potential bone substitute, Int. J. Biol. Macromol. 47 (2010) 483–487. doi:10.1016/j.ijbiomac.2010.07.002.

[23] W.R. Moore, S.E. Graves, G.I. Bain, Synthetic bone graft substitutes, ANZ J. Surg. 71 (2001) 354–361. doi:10.1046/j.1440-1622.2001.02128.x.

[24] D. Yang, Y. Jin, G. Ma, X. Chen, F. Lu, J. Nie, Fabrication and characterization of chitosan/PVA with hydroxyapatite biocomposite nanoscaffolds, J. Appl. Polym. Sci. 110 (2008) 3328–3335. doi:10.1002/app.28829.

[25] M. Wang, Composite Scaffolds for Bone Tissue Engineering, Am. J. Biochem. Biotechnol. 2 (2006) 80–84. doi:10.3844/ajbbsp.2006.80.84.

[26] Y. Fillingham, J. Jacobs, Bone grafts and their substitutes, Bone Joint J. 98-B (2016) 6–9. doi:10.1302/0301-620X.98B.36350.

[27] V. Van Thai, Y. Min, B. Lee, Fabrication of Hybrid Composites Consists of Poly Methyl Methacrylate and Polyvinyl Alcohol and Hydroxyapatite, Bioceram. Dev. Appl. 1 (2011) 1–4. doi:10.4303/bda/D110171.

[28] K. Rezwan, Q.Z. Chen, J.J. Blaker, A.R. Boccaccini, Biodegradable and bioactive porous polymer/inorganic composite scaffolds for bone tissue engineering, Biomaterials. 27 (2006) 3413–3431. doi:10.1016/j.biomaterials.2006.01.039.

[29] K.E. Tanner, Bioactive composites for bone tissue engineering, Proc. Inst. Mech. Eng. Part H J. Eng. Med. 224 (2010) 1359–1372. doi:10.1243/09544119JEIM823.

[30] M. Puska, A. J., P. Vallittu, Polymer Composites for Bone Reconstruction, in: D.P. Tesinova (Ed.), Adv. Compos. Mater. - Anal. Nat. Man-Made Mater., InTech Eur, Intechopen, Rijeka, Croatia, 2011: pp. 55–72. doi:10.5772/20657.

[31] C. Duval-Terrié, L. Lebrun, Polymerization and Characterization of PMMA, J. Chem. Educ. 83 (2006) 443–446. doi:10.1021/ed083p443.

[32] S. Simplex, V. Al, H.T. Water, A. This, Experiment 10 : Polymerization of methyl methacrylate (MMA) in bulk to form PMMA ., Bone. (n.d.).

[33] S. Dorozhkin, Calcium orthophosphates, J. Mater. Sci. 42 (2007) 1061–1095. doi:10.1007/s10853-006-1467-8.

[34] B.H. Fellah, P. Weiss, O. Gauthier, T. Rouillon, P. Pilet, G. Daculsi, P. Layrolle, Bone repair using a new injectable self-crosslinkable bone substitute, J. Orthop. Res. 24 (2006) 628–635. doi:10.1002/jor.

[35] M. Vert, Y. Doi, K. Hellwich, M. Hess, P. Hodge, P. Kubisa, M. Rinaudo, F. Schué, Terminology for biorelated polymers and applications (IUPAC Recommendations 2012), Pure Appl. Chem. 84 (2012) 377–410. doi:10.1351/PAC-REC-10-12-04.

[36] A.R. Rokn, M.A. Khodadoostan, A.A. Reza Rasouli Ghahroudi, P. Motahhary, M.J. Kharrazi Fard, H. De Bruyn, R. Afzalifar, E. Soolar, A. Soolari, Bone formation with two types of grafting materials: a histologic and histomorphometric study, Open Dent. J. 5 (2011) 96–104. doi:10.2174/1874210601105010096.

[37] X. Li, C. a. van Blitterswijk, Q. Feng, F. Cui, F. Watari, The effect of calcium phosphate microstructure on bone-related cells in vitro, Biomaterials. 29 (2008) 3306–3316. doi:10.1016/j.biomaterials.2008.04.039.

[38] G. Daculsi, Biphasic calcium phosphate concept applied to artificial bone, implant coating and injectable bone substitute, Biomaterials. 19 (1998) 1473–1478. doi:10.1016/S0142-9612(98)00061-1.

[39] H. Tan, K.G. Marra, Injectable, biodegradable hydrogels for tissue engineering applications, Materials (Basel). 3 (2010) 1746–1767. doi:10.3390/ma3031746.

[40] R.N. Rothon, Particulate-filled polymer composites, Polym. Test. 15 (1996) 397. doi:10.1016/0142-9418(96)00004-9.

[41] M.O. Wang, C.E. Vorwald, M.L. Dreher, E.J. Mott, M.H. Cheng, A. Cinar, H. Mehdizadeh, S. Somo, D. Dean, E.M. Brey, J.P. Fisher, Evaluating 3D-printed biomaterials as scaffolds for vascularized bone tissue engineering, Adv. Mater. 27 (2014) 138–144. doi:10.1002/adma.201403943.

[42] S. Panzavolta, M. Fini, A. Nicoletti, B. Bracci, K. Rubini, R. Giardino, A. Bigi, Porous composite scaffolds based on gelatin and partially hydrolyzed a-tricalcium phosphate, Acta Biomater. 5 (2009) 636–643. doi:10.1016/j.actbio.2008.08.017.

[43] A. La Gatta, A. De Rosa, P. Laurienzo, M. Malinconico, M. De Rosa, C. Schiraldi, A novel injectable poly(epsilon-caprolactone)/calcium sulfate system for bone regeneration: synthesis and characterization, Macromol. Biosci. 5 (2005) 1108–17. doi:10.1002/mabi.200500114.

[44] V. Karageorgiou, D. Kaplan, Porosity of 3D biomaterial scaffolds and osteogenesis, Biomaterials. 26 (2005) 5474–5491. doi:10.1016/j.biomaterials.2005.02.002.

[45] Y. Suetsugu, D. Walsh, J. Tanaka, S. Mann, Hydroxyapatite pattern formation in PVA gels, J. Mater. Sci. 44 (2009) 5806–5814. doi:10.1007/s10853-009-3815-y.

[46] P. Bradna, SLIDES: Polymerization Synthetic polymers used in dentistry, Dent. Mater. (2012) 1–33.

[47] R. Moss, J. Pfister, C. Edmonson, J. Kneedler, D. Reeves, Preparation and safe use of

PMMA bone cement, 2011.

[48] J. Zhang, W. Liu, V. Schnitzler, F. Tancret, J. Bouler, Calcium phosphate cements for bone substitution : Chemistry , handling and mechanical properties, Acta Biomater. 10 (2014) 1035–1049. doi:10.1016/j.actbio.2013.11.001.

[49] C. Rey, C. Combes, C. Drouet, H. Sfihi, A. Barroug, Physico-chemical properties of nanocrystalline apatites: Implications for biominerals and biomaterials, Mater. Sci. Eng. C. 27 (2007) 198–205. doi:10.1016/j.msec.2006.05.015.

[50] E. Rumpel, E. Wolf, E. Kauschke, V. Bienengräber, T. Bayerlein, T. Gedrange, P. Proff, The biodegradation of hydroxyapatite bone graft substitutes in vivo, Folia Morphol. (Warsz). 65 (2006) 43–48.

[51] K. Ishikawa, Bone substitute fabrication based on dissolution-precipitation reactions, Materials (Basel). 3 (2010) 1138–1155. doi:10.3390/ma3021138.

[52] G. Turnbull, J. Clarke, F. Picard, P. Riches, L. Jia, F. Han, B. Li, W. Shu, 3D bioactive composite scaffolds for bone tissue engineering, Bioact. Mater. 3 (2018) 278–314. doi:10.1016/J.BIOACTMAT.2017.10.001.

[53] J.R. Jones, S. Lin, S. Yue, P.D. Lee, J. V Hanna, M.E. Smith, R.J. Newport, Bioactive glass scaffolds for bone regeneration and their hierarchical characterisation, in: Proc. Inst. Mech. Eng. Part H J. Eng. Med., 2010: pp. 1373–1387. doi:10.1243/09544119JEIM836.

[54] A. Hasan, B. Byambaa, M. Morshed, M.I. Cheikh, R.A. Shakoor, T. Mustafy, H.E. Marei, Advances in osteobiologic materials for bone substitutes, J. Tissue Eng. Regen. Med. 12 (2018) 1448–1468. doi:10.1002/term.2677.

[55] W. Wang, K.W.K. Yeung, Bone grafts and biomaterials substitutes for bone defect repair: A review, Bioact. Mater. 2 (2017) 224–247. doi:10.1016/J.BIOACTMAT.2017.05.007.

[56] Q. Hou, P.A. De Bank, K.M. Shakesheff, Injectable scaffolds for tissue regeneration, J. Mater. Chem. 14 (2004) 1915–1923. doi:10.1039/b401791a.

[57] K.S. Griffin, K.M. Davis, T.O. McKinley, J.O. Anglen, T.-M.G. Chu, J.D. Boerckel, M.A. Kacena, Evolution of Bone Grafting: Bone Grafts and Tissue Engineering Strategies for Vascularized Bone Regeneration, Clin. Rev. Bone Miner. Metab. 13 (2015) 232–244. doi:10.1007/s12018-015-9194-9.

[58] M. Scheffler, R. Bordia, N. Travitzky, P. Greil, Development of a rapid crosslinking preceramic polymer system, J. Eur. Ceram. Soc. 25 (2005) 175–180. doi:10.1016/j.jeurceramsoc.2004.07.013.

[59] M.Y. Jen, Z.W. Hung, C.Y. Chun, Modification and characterization of semi-crystalline poly(vinyl alcohol) with interpenetrating poly(acrylic acid) by UV radiation method for alkaline solid polymer electrolytes membrane, J. Memb. Sci. 322 (2008) 74–80. doi:10.1016/j.memsci.2008.05.035.

[60] J.M. Chenal, J.M. Widmaier, Entanglements in interpenetrating polymer networks evidenced by simple physicochemical investigations, Polymer (Guildf). 46 (2005) 671–675. doi:10.1016/j.polymer.2004.11.095.

[61] D. Mawad, R. Odell, L. a Poole-Warren, Network structure and macromolecular drug

release from poly(vinyl alcohol) hydrogels fabricated via two crosslinking strategies, Int. J. Pharm. 366 (2009) 31–7. doi:10.1016/j.ijpharm.2008.08.038.

[62] M.A. Karsdal, A. V. Neutzsky-Wulff, M.H. Dziegiel, C. Christiansen, K. Henriksen, Osteoclasts secrete non-bone derived signals that induce bone formation, Biochem. Biophys. Res. Commun. 366 (2008) 483–488. doi:10.1016/j.bbrc.2007.11.168.

[63] L. Bozec, M. a Horton, Skeletal tissues as nanomaterials, J. Mater. Sci. Mater. Med. 17 (2006) 1043–8. doi:10.1007/s10856-006-0442-x.

[64] B. Clarke, Normal bone anatomy and physiology, Clin. J. Am. Soc. Nephrol. 3 Suppl 3 (2008) 131–139. doi:10.2215/CJN.04151206.

[65] C.H. Lohmann, D. Andreacchio, G. Köster, D.L. Carnes, D.L. Cochran, D.D. Dean, B.D. Boyan, Z. Schwartz, Tissue response and osteoinduction of human bone grafts in vivo, Arch. Orthop. Trauma Surg. 121 (2001) 583–590. doi:10.1007/s004020100291.

[66] R.E. Guldberg, M.E. Oest, A.S.P. Lin, K.M. Dupont, A. Peister, R. V. Bellamkonda, D.J. Mooney, E.M. Schwarz, X. Zhang, R.J. O'Keefe, Strategies for segmental bone repair, in: Eur. Cells Mater., 2007: p. 9.

[67] J.Y. Rho, L. Kuhn-Spearing, P. Zioupos, Mechanical properties and the hierarchical structure of bone, Med. Eng. Phys. 20 (1998) 92–102. doi:10.1016/S1350-4533(98)00007-1.

[68] O.S. Rabotyagova, P. Cebe, D.L. Kaplan, Collagen structural hierarchy and susceptibility to degradation by ultraviolet radiation, Mater. Sci. Eng. C. 28 (2008) 1420–1429. doi:10.1016/j.msec.2008.03.012.

[69] M.J. Olszta, X. Cheng, S.S. Jee, R. Kumar, Y. Kim, M.J. Kaufman, E.P. Douglas, L.B. Gower, Bone structure and formation: A new perspective, Mater. Sci. Eng. R-Reports. 58 (2007) 77–116. doi:10.1016/j.mser.2007.05.001.

[70] S. Viguet-Carrin, H. Follet, E. Gineyts, J.P. Roux, F. Munoz, R. Chapurlat, P.D. Delmas, M.L. Bouxsein, Association between collagen cross-links and trabecular microarchitecture properties of human vertebral bone, Bone. 46 (2010) 342–347. doi:10.1016/j.bone.2009.10.001.

[71] M. Tzaphlidou, The role of collagen in bone structure: an image processing approach, Micron. 36 (2005) 593–601. doi:10.1016/j.micron.2005.05.009.

[72] X. Banse, J.P. Devogelaer, A. Lafosse, T.J. Sims, M. Grynpas, A.J. Bailey, Cross-link profile of bone collagen correlates with structural organization of trabeculae, Bone. 31 (2002) 70–76. doi:10.1016/S8756-3282(02)00800-1.

[73] H.M. Goldman, C.D.L. Thomas, J.G. Clement, T.G. Bromage, Relationships among microstructural properties of bone at the human midshaft femur, J. Anat. 206 (2005) 127–139. doi:10.1111/j.1469-7580.2005.00385.x.

[74] V. Ottani, M. Raspanti, A. Ruggeri, Collagen structure and functional implications, Micron. 32 (2001) 251–260. doi:10.1016/S0968-4328(00)00042-1.

[75] E.H. Burger, J. Klein-Nulend, Mechanotransduction in bone--role of the lacuno-canalicular network., FASEB J. 13 Suppl (1999) S101-12.

http://www.ncbi.nlm.nih.gov/pubmed/10352151.

[76] H.L. Morris, C.I. Reed, J.W. Haycock, G.C. Reilly, Mechanisms of fluid-flow-induced matrix production in bone tissue engineering, in: Proc. Inst. Mech. Eng. Part H J. Eng. Med., 2010: pp. 1509–1521. doi:10.1243/09544119JEIM751.

[77] M. Kikuchi, S. Itoh, S. Ichinose, K. Shinomiya, Self-Organization Mechanism in a Bone-Like Hydroxyapatite / Collagen Nanocomposite Synthesized In Vitro and its Biological Reaction In Vivo, Biomaterials. 22 (2001) 1705–1711. doi:10.1016/S0142-9612(00)00305-7.

[78] M.E. Ruppel, L.M. Miller, D.B. Burr, The effect of the microscopic and nanoscale structure on bone fragility, Osteoporos. Int. 19 (2008) 1251–1265. doi:10.1007/s00198-008-0579-1.

[79] S.E. Etok, E. Valsami-Jones, T.J. Wess, J.C. Hiller, C.A. Maxwell, K.D. Rogers, D. a C. Manning, M.L. White, E. Lopez-Capel, M.J. Collins, M. Buckley, K.E.H. Penkman, S.L. Woodgate, Structural and chemical changes of thermally treated bone apatite, J. Mater. Sci. 42 (2007) 9807–9816. doi:10.1007/s10853-007-1993-z.

[80] K. Haberko, M.M. Bućko, J. Brzezińska-Miecznik, M. Haberko, W. Mozgawa, T. Panz, A. Pyda, J. Zarebski, Natural hydroxyapatite - Its behaviour during heat treatment, J. Eur. Ceram. Soc. 26 (2006) 537–542. doi:10.1016/j.jeurceramsoc.2005.07.033.

[81] J.M. Katz, C. Nataraj, R. Jaw, E. Deigl, P. Bursac, Demineralized bone matrix as an osteoinductive biomaterial and in vitro predictors of its biological potential, J. Biomed. Mater. Res. B. Appl. Biomater. 89 (2009) 127–34. doi:10.1002/jbm.b.31195.

[82] T. Yamada, Bone-demineralized bone-bone graft for ligament reconstruction in rats, J. Med. Dent. Sci. 51 (2004) 45–52.

[83] A.L. Boskey, Assessment of bone mineral and matrix using backscatter electron imaging and FTIR imaging, Curr. Osteoporos. Rep. 4 (2006) 71. doi:10.1007/s11914-006-0005-6.

[84] E. Landi, G. Celotti, G. Logroscino, A. Tampieri, Carbonated hydroxyapatite as bone substitute, J. Eur. Ceram. Soc. 23 (2003) 2931–2937. doi:10.1016/S0955-2219(03)00304-2.

[85] I. Rehman, W. Bonfield, Characterization of hydroxyapatite and carbonated apatite by photo acoustic FTIR spectroscopy, J. Mater. Sci. Mater. Med. 8 (1997) 1–4. doi:10.1023/A:1018570213546.

[86] C. Rey, C. Combes, C. Drouet, M.J. Glimcher, Bone mineral: Update on chemical composition and structure-Erratum, Osteoporos. Int. 20 (2009) 1013–1021. doi:10.1007/s00198-009-0860-y.

[87] K. Verdelis, L. Lukashova, J.T. Wright, R. Mendelsohn, M.G.E. Peterson, S. Doty, a. L. Boskey, Maturational changes in dentin mineral properties, Bone. 40 (2007) 1399–1407. doi:10.1016/j.bone.2006.12.061.

[88] D. Farlay, G. Panczer, C. Rey, P.D. Delmas, G. Boivin, Mineral maturity and crystallinity index are distinct characteristics of bone mineral, J. Bone Miner. Metab. 28 (2010) 433–445. doi:10.1007/s00774-009-0146-7.

[89] D.R. Eyre, J.J. Wu, Collagen cross-links, Top. Curr. Chem. 247 (2005) 207–229. doi:10.1007/b103828.

[90] E.P. Paschalis, R. Recker, E. DiCarlo, S. Doty, E. Atti, A.L. Boskey, Distribution of collagen cross-links in normal human trabecular bone, J. Bone Miner. Res. 18 (2003) 1942–1946. doi:DOI 10.1359/jbmr.2003.18.11.1942.

[91] S. Viguet-Carrin, P. Garnero, P.D. Delmas, The role of collagen in bone strength, Osteoporos. Int. 17 (2006) 319–336. doi:10.1007/s00198-005-2035-9.

[92] E.P. Paschalis, K. Verdelis, S.B. Doty, a L. Boskey, R. Mendelsohn, M. Yamauchi, Spectroscopic characterization of collagen cross-links in bone, J. Bone Miner. Res. 16 (2001) 1821–1828. doi:10.1359/jbmr.2001.16.10.1821.

[93] K. Anselme, A. Ponche, M. Bigerelle, Relative influence of surface topography and surface chemistry on cell response to bone implant materials. Part 2: biological aspects, Proc. Inst. Mech. Eng. H. 224 (2010) 1487–1507. doi:10.1243/09544119JEIM901.

[94] P. Jayakumar, L. Di Silvio, Osteoblasts in bone tissue engineering, Proc. Inst. Mech. Eng. H. 224 (2010) 1415–1440. doi:10.1243/09544119JEIM821.

[95] C. Rey, C. Combes, C. Drouet, M.J. Glimcher, Bone mineral: Update on chemical composition and structure, Osteoporos. Int. 20 (2009) 1013–1021. doi:10.1007/s00198-009-0860-y.

[96] D.R. Epari, G.N. Duda, M.S. Thompson, Mechanobiology of bone healing and regeneration: In vivo models, in: Proc. Inst. Mech. Eng. Part H J. Eng. Med., 2010: pp. 1543–1553. doi:10.1243/09544119JEIM808.

[97] M. Saito, K. Marumo, Collagen cross-links as a determinant of bone quality: A possible explanation for bone fragility in aging, osteoporosis, and diabetes mellitus, Osteoporos. Int. 21 (2010) 195–214. doi:10.1007/s00198-009-1066-z.

[98] B.A.L. Boskey, Using bone quality to assess fracture risk, AAOS Now. (2011). doi:10.1002/humu.21475.

[99] E. Donnelly, Methods for Assessing Bone Quality: A Review, Clin. Orthop. Relat. Res. 469 (2011) 2128–2138. doi:10.1007/s11999-010-1702-0.

[100] M. Saito, K. Marumo, Collagen cross-links as a determinant of bone quality: A possible explanation for bone fragility in aging, osteoporosis, and diabetes mellitus, Osteoporos. Int. 21 (2010) 195–214. doi:10.1007/s00198-009-1066-z.

[101] J. Aerssens, S. Boonen, J. Joly, J. Dequeker, Variations in trabecular bone composition with anatomical site and age: Potential implications for bone quality assessment, J. Endocrinol. 155 (1997) 411–421. doi:10.1677/joe.0.1550411.

[102] S. Hirayama, S. Takagi, M. Markovic, L.C. Chow, Properties of Calcium Phosphate Cements With Different Tetracalcium Phosphate and Dicalcium Phosphate Anhydrous Molar Ratios, J. Res. Natl. Inst. Stand. Technol. 113 (2008) 311–320. http://www.pubmedcentral.nih.gov/articlerender.fcgi?artid=2749267&tool=pmcentrez&rendertype=abstract.

[103] W. Song, D.C. Markel, X. Jin, T. Shi, W. Ren, Poly(vinyl alcohol)/collagen/hydroxyapatite

hydrogel: Properties and in vitro cellular response, J. Biomed. Mater. Res. - Part A. 100 A (2012) 3071–3079. doi:10.1002/jbm.a.34240.

[104] W. Schneiders, A. Reinstorf, W. Pompe, R. Grass, A. Biewener, M. Holch, H. Zwipp, S. Rammelt, Effect of modification of hydroxyapatite/collagen composites with sodium citrate, phosphoserine, phosphoserine/RGD-peptide and calcium carbonate on bone remodelling, Bone. 40 (2007) 1048–1059. doi:10.1016/j.bone.2006.11.019.

[105] D. Offner, G. Fernandez de Grado, I. Meisels, L. Pijnenburg, F. Fioretti, N. Benkirane-Jessel, A.-M. Musset, Bone Grafts, Bone Substitutes and Regenerative Medicine Acceptance for the Management of Bone Defects Among French Population: Issues about Ethics, Religion or Fear?, Cell Med. 11 (2019) 215517901985766. doi:10.1177/2155179019857661.

[106] M. Motomiya, M. Ito, M. Takahata, K. Kadoya, K. Irie, K. Abumi, A. Minami, Effect of Hydroxyapatite porous characteristics on healing outcomes in rabbit posterolateral spinal fusion model, Eur. Spine J. 16 (2007) 2215–2224. doi:10.1007/s00586-007-0501-0.

[107] P. Kasten, I. Beyen, P. Niemeyer, R. Luginbühl, M. Bohner, W. Richter, Porosity and pore size of β-tricalcium phosphate scaffold can influence protein production and osteogenic differentiation of human mesenchymal stem cells: An in vitro and in vivo study, Acta Biomater. 4 (2008) 1904–1915. doi:10.1016/j.actbio.2008.05.017.

[108] K.A. Hing, B. Annaz, S. Saeed, P.A. Revell, T. Buckland, Microporosity enhances bioactivity of synthetic bone graft substitutes, J. Mater. Sci. Mater. Med. 16 (2005) 467–475. doi:10.1007/s10856-005-6988-1.

[109] W.S. Pietrzak, S.N. Ali, D. Chitturi, M. Jacob, J.E. Woodell-May, BMP depletion occurs during prolonged acid demineralization of bone: Characterization and implications for graft preparation, Cell Tissue Bank. 12 (2011) 81–88. doi:10.1007/s10561-009-9168-6.

[110] S. Tanwatana, A. Kiewjurat, S. Suttapreyasri, Chemical and thermal deproteinization of human demineralized tooth matrix: Physicochemical characterization and osteoblast cell biocompatibility, J. Biomater. Appl. (2019) 088532821986603. doi:10.1177/0885328219866039.

[111] A.G. Robling, A.B. Castillo, C.H. Turner, Biomechanical and Molecular Regulation of Bone Remodeling, Annu. Rev. Biomed. Eng. 8 (2006) 455–498. doi:10.1146/annurev.bioeng.8.061505.095721.

[112] A.L. Giraldo-Betancur, D.G. Espinosa-Arbelaez, A. Del Real-López, B.M. Millan-Malo, E.M. Rivera-Muñoz, E. Gutierrez-Cortez, P. Pineda-Gomez, S. Jimenez-Sandoval, M.E. Rodriguez-García, Comparison of physicochemical properties of bio and commercial hydroxyapatite, Curr. Appl. Phys. 13 (2013) 1383–1390. doi:10.1016/j.cap.2013.04.019.

[113] M. Figueiredo, A. Fernando, G. Martins, J. Freitas, F. Judas, H. Figueiredo, Effect of the calcination temperature on the composition and microstructure of hydroxyapatite derived from human and animal bone, Ceram. Int. 36 (2010) 2383–2393. doi:10.1016/j.ceramint.2010.07.016.

[114] J.C. Hiller, T.J.U. Thompson, M.P. Evison, a. T. Chamberlain, T.J. Wess, Bone mineral

change during experimental heating: An X-ray scattering investigation, Biomaterials. 24 (2003) 5091–5097. doi:10.1016/S0142-9612(03)00427-7.

[115] S. Marković, L. Veselinović, M.J. Lukić, L. Karanović, I. Bračko, N. Ignjatović, D. Uskoković, Synthetical bone-like and biological hydroxyapatites: a comparative study of crystal structure and morphology, Biomed. Mater. 6 (2011) 045005. doi:10.1088/1748-6041/6/4/045005.

[116] B. Ben-Nissan, Natural bioceramics: From coral to bone and beyond, Curr. Opin. Solid State Mater. Sci. 7 (2003) 283–288. doi:10.1016/j.cossms.2003.10.001.

[117] S.M. Best, a. E. Porter, E.S. Thian, J. Huang, Bioceramics: Past, present and for the future, J. Eur. Ceram. Soc. 28 (2008) 1319–1327. doi:10.1016/j.jeurceramsoc.2007.12.001.

[118] J.S. Sun, H.C. Liu, W.H.S. Chang, J. Li, F.H. Lin, H.C. Tai, Influence of hydroxyapatite particle size on bone cell activities: An in vitro study, J. Biomed. Mater. Res. 39 (1998) 390–397. doi:10.1002/(SICI)1097-4636(19980305)39:3<390::AID-JBM7>3.0.CO;2-E.

[119] R. Shimogoryo, T. Eguro, E. Kimura, M. Maruta, S. Matsuya, K. Ishikawa, Effects of added mannitol on the setting reaction and mechanical strength of apatite cement, Dent. Mater. J. 28 (2009) 627–33. http://www.ncbi.nlm.nih.gov/pubmed/19822995.

[120] H.N. Chia, B.M. Wu, Recent advances in 3D printing of biomaterials, J. Biol. Eng. 9 (2015) 4. doi:10.1186/s13036-015-0001-4.

[121] X.Z. Shu, Y. Liu, F.S. Palumbo, Y. Luo, G.D. Prestwich, In situ crosslinkable hyaluronan hydrogels for tissue engineering, Biomaterials. 25 (2004) 1339–1348. doi:10.1016/j.biomaterials.2003.08.014.

[122] T.M. Don, C.F. King, W.Y. Chiu, C. a. Peng, Preparation and characterization of chitosan-g-poly(vinyl alcohol)/poly(vinyl alcohol) blends used for the evaluation of blood-contacting compatibility, Carbohydr. Polym. 63 (2006) 331–339. doi:10.1016/j.carbpol.2005.08.023.

[123] A. Sinha, A. Guha, Biomimetic patterning of polymer hydrogels with hydroxyapatite nanoparticles, Mater. Sci. Eng. C. 29 (2009) 1330–1333. doi:10.1016/j.msec.2008.10.024.

[124] J.P. Gong, Y. Katsuyama, T. Kurokawa, Y. Osada, Double-network hydrogels with extremely high mechanical strength, Adv. Mater. 15 (2003) 1155–1158. doi:10.1002/adma.200304907.

[125] R. Jin, C. Hiemstra, Z. Zhong, J. Feijen, Enzyme-mediated fast in situ formation of hydrogels from dextran-tyramine conjugates, Biomaterials. 28 (2007) 2791–2800. doi:10.1016/j.biomaterials.2007.02.032.

[126] B. Balakrishnan, A. Jayakrishnan, Self-cross-linking biopolymers as injectable in situ forming biodegradable scaffolds, Biomaterials. 26 (2005) 3941–3951. doi:10.1016/j.biomaterials.2004.10.005.

[127] E.H. Schacht, Polymer chemistry and hydrogel systems, J. Phys. Conf. Ser. 3 (2004) 22–28. doi:10.1088/1742-6596/3/1/004.

[128] T. Coviello, G. Coluzzi, A. Palleschi, M. Grassi, E. Santucci, F. Alhaique, Structural and rheological characterization of Scleroglucan/borax hydrogel for drug delivery, Int. J. Biol.

Macromol. 32 (2003) 83–92. doi:10.1016/S0141-8130(03)00041-2.

[129] J. Maia, M.P. Ribeiro, C. Ventura, R.A. Carvalho, I.J. Correia, M.H. Gil, Ocular injectable formulation assessment for oxidized dextran-based hydrogels., Acta Biomater. 5 (2009) 1948–55. doi:10.1016/j.actbio.2009.02.008.

[130] G. Balasundaram, T.J. Webster, An overview of nano-polymers for orthopedic applications., Macromol. Biosci. 7 (2007) 635–42. doi:10.1002/mabi.200600270.

[131] A. Ponche, M. Bigerelle, K. Anselme, Relative influence of surface topography and surface chemistry on cell response to bone implant materials. Part 1: Physico-chemical effects, in: Proc. Inst. Mech. Eng. Part H J. Eng. Med., 2010: pp. 1471–1486. doi:10.1243/09544119JEIM900.

[132] A.J. El Haj, S.H. Cartmell, Bioreactors for bone tissue engineering, Proc. Inst. Mech. Eng. Part H J. Eng. Med. 224 (2010) 1523–1532. doi:10.1243/09544119JEIM802.

[133] D.A. Ossipov, S. Piskounova, J. Hilborn, Poly(vinyl alcohol) cross-linkers for in vivo injectable hydrogels, Macromolecules. 41 (2008) 3971–3982. doi:10.1021/ma800332c.

[134] S.J. Segvich, H.C. Smith, D.H. Kohn, The adsorption of preferential binding peptides to apatite-based materials, Biomaterials. 30 (2009) 1287–98. doi:10.1016/j.biomaterials.2008.11.008.

[135] E.F. dos Reis, F.S. Campos, A.P. Lage, R.C. Leite, L.G. Heneine, W.L. Vasconcelos, Z.I.P. Lobato, H.S. Mansur, Synthesis and characterization of poly (vinyl alcohol) hydrogels and hybrids for rMPB70 protein adsorption, Mater. Res. 9 (2006) 185–191. doi:10.1590/S1516-14392006000200014.

[136] B. Bolto, T. Tran, M. Hoang, Z. Xie, Crosslinked poly(vinyl alcohol) membranes, Prog. Polym. Sci. 34 (2009) 969–981. doi:10.1016/j.progpolymsci.2009.05.003.

[137] K. Das, D. Ray, N.R. Bandyopadhyay, A. Gupta, S. Sengupta, S. Sahoo, A. Mohanty, M. Misra, Preparation and characterization of cross-linked starch/poly(vinyl alcohol) green films with low moisture absorption, Ind. Eng. Chem. Res. 49 (2010) 2176–2185. doi:10.1021/ie901092n.

[138] S. Nkhwa, K.F. Lauriaga, E. Kemal, S. Deb, Poly(vinyl alcohol): Physical Approaches to Designing Biomaterials for Biomedical Applications, Conf. Pap. Sci. 2014 (2014) 1–7. doi:10.1155/2014/403472.

[139] N. Tudorachi, R. Lipsa, Copolymers based on poly (vinyl alcohol) and acrylamide, J. Optoelectron. Adv. Mater. 8 (2006) 659–662.

[140] G. Paradossi, R. Lisi, M. Paci, V. Crescenzi, New chemical hydrogels based on poly(vinyl alcohol), J. Polym. Sci. Part A Polym. Chem. 34 (1996) 3417–3425. doi:10.1002/pola.1996.874.

[141] D.C. Bugada, A. Rudin, Characterization of poly(vinyl alcohol), Appl. Polym. Sci. 30 (1985) 4137–4147. doi:https://doi.org/10.1002/app.1985.070301015.

[142] L. V Thomas, U. Arun, S. Remya, P.D. Nair, A biodegradable and biocompatible PVA-citric acid polyester with potential applications as matrix for vascular tissue engineering, J. Mater. Sci. Mater. Med. 20 (2009) S259–S269. doi:10.1007/s10856-008-3599-7.

[143] O. Şanli, N. Ay, N. Işiklan, Release characteristics of diclofenac sodium from poly(vinyl alcohol)/sodium alginate and poly(vinyl alcohol)-grafted-poly(acrylamide)/sodium alginate blend beads, Eur. J. Pharm. Biopharm. 65 (2007) 204–214. doi:10.1016/j.ejpb.2006.08.004.

[144] J. Kodavaty, D.A. P., Mechanical and swelling properties of poly(vinyl alcohol) and hyaluronic acid gels, Def. Sci. J. 64 (2014) 222–229.

[145] S. Ming Kuo, S. Jen Chang, Y. Jiin Wang, Properties of PVA-AA cross-linked HEMA-based hydrogels, J. Polym. Res. 6 (1999) 191–196. doi:10.1007/s10965-006-0087-y.

[146] A.C. Wenceslau, A.F. Rubira, E.C. Muniz, IPN hydrogels based on PNIPAAm and PVA-Ma networks: characterization through measure of LCST, swelling ratio and mechanical properties, Acta Sci. Technol. 34 (2012) 233–241. doi:10.4025/actascitechnol.v34i2.15019.

[147] A.C. Tas, Preparation of Porous Bioceramics by a Simple PVA- Processing Route, Key Eng. Mater. 264–268 (2004) 2079–2082.

[148] A. Szilágyi, M. Zrínyi, Temperature induced phase transition of interpenetrating polymer networks composed of poly(vinyl alcohol) and copolymers of N-isopropylacrylamide with acrylamide or 2-acrylamido-2-methylpropyl-sulfonic acid, Polymer (Guildf). 46 (2005) 10011–10016. doi:10.1016/j.polymer.2005.07.072.

[149] R. Solaro, A. Corti, E. Chiellini, Biodegradation of poly(vinyl alcohol) with different molecular weights and degree of hydrolysis, Polym. Adv. Technol. 11 (2000) 873–878. doi:10.1002/1099-1581(200008/12)11:8/12<873::AID-PAT35>3.0.CO;2-V.

[150] A. Aina, A. Morris, M. Gupta, N. Billa, N. Madhvani, R. Sharma, S. Doughty, V. Shah, Y. Boukari, Dissolution Behavior of Poly Vinyl Alcohol in Water and its Effect on the Physical Morphologies of PLGA Scaffolds, UK J. Pharm. Biosci. 2 (2014) 1. doi:10.20510/ukjpb/2/i1/91124.

[151] E. Chiellini, A. Corti, S. D'Antone, R. Solaro, Biodegradation of poly (vinyl alcohol) based materials, 2003. doi:10.1016/S0079-6700(02)00149-1.

[152] M.T. Silva, G.H. Costa, R. Hage, T.C. B, H. Gracher, A. Benévolo, SYNTHESIS AND CHARACTERIZATION OF HYDROGELS COMPOSED BY DIFFERENT TYPES OF POLY (VINYL ALCOHOL), Network. (2008) 2008.

[153] S. Amiya, S. Tsuchiya, R. Qian, a. Nakajima, The study of microstructyures of poly(vinyl alcohol) by NMR, Pure Appl. Chem. 62 (1990) 2139–2146.

[154] H.S. Mansur, C.M. Sadahira, A.N. Souza, A.A.P. Mansur, FTIR spectroscopy characterization of poly (vinyl alcohol) hydrogel with different hydrolysis degree and chemically crosslinked with glutaraldehyde, Mater. Sci. Eng. C. 28 (2008) 539–548. doi:10.1016/j.msec.2007.10.088.

[155] K. Leja, G. Lewandowicz, Polymer biodegradation and biodegradable polymers - A review, Polish J. Environ. Stud. 19 (2010) 255–266.

[156] N.A. Azahari, N. Othman, H. Ismail, Biodegradation studies of polyvinyl alcohol/corn starch blend films in solid and solution media, J. Phys. Sci. 22 (2011) 15–31.

[157] D. Rong, K. Usui, T. Morohoshi, N. Kato, M. Zhou, T. Ikeda, Symbiotic degradation of polyvinyl alcohol by Novosphingobium sp . and Xanthobacter flavus., J. Environ. Biotechnol. 9 (2009) 131–134.

[158] S.K. Gounder, V. Vediappan, Characterization of Crosslinked Poly (2-Hydroxyethyl Methacrylate-co-N-Vinyl-2-Pyrrolidone) as a Carrier for Controlled Drug Delivery, J. Pharm. Res. 4 (2011) 743–747.

[159] D. Chitkara, A. Shikanov, N. Kumar, A.J. Domb, Biodegradable injectable in situ depot-forming drug delivery systems, Macromol. Biosci. 6 (2006) 977–990. doi:10.1002/mabi.200600129.

[160] L. Yuan, G.Z. Liang, J.Q. Xie, S.B. He, Synthesis and characterization of microencapsulated dicyclopentadiene with melamine-formaldehyde resins, Colloid Polym. Sci. 285 (2007) 781–791. doi:10.1007/s00396-006-1621-5.

[161] Y.Y. Huang, T.W. Chung, Microencapsulation of gentamicin in biodegradable PLA and/or PLA/PEG copolymer, J. Microencapsul. 18 (2001) 457–465. doi:10.1080/02652040010019479.

[162] L.G. Griffith, Polymeric biomaterials, Acta Mater. 48 (2000) 263–277. doi:10.1016/S1359-6454(99)00299-2.

[163] K.A. Blackwood, N. Bock, T.R. Dargaville, M. Ann Woodruff, Scaffolds for growth factor delivery as applied to bone tissue engineering, Int. J. Polym. Sci. 2012 (2012) 1–25. doi:10.1155/2012/174942.

[164] M.J. Shin, Y.J. Shin, S.W. Hwang, J.S. Shin, Microencapsulation of imidazole curing agent by solvent evaporation method using W/O/W emulsion, J. Appl. Polym. Sci. 129 (2013) 1036–1044. doi:10.1002/app.38767.

[165] J. Gamelas, G. Martins, Surface properties of carbonated and non-carbonated hydroxyapatites obtained after bone calcination at different temperatures, Colloids Surfaces A Physicochem. Eng. Asp. 478 (2015) 62–70. doi:10.1016/j.colsurfa.2015.03.044.

[166] M. Figueiredo, A. Fernando, G. Martins, J. Freitas, F. Judas, H. Figueiredo, Effect of the calcination temperature on the composition and microstructure of hydroxyapatite derived from human and animal bone, Ceram. Int. 36 (2010) 2383–2393. doi:10.1016/j.ceramint.2010.07.016.

[167] M. Figueiredo, J. Henriques, G. Martins, F. Guerra, F. Judas, H. Figueiredo, Physicochemical characterization of biomaterials commonly used in dentistry as bone substitutes - Comparison with human bone, J. Biomed. Mater. Res. - Part B Appl. Biomater. 92 (2010) 409–419. doi:10.1002/jbm.b.31529.

[168] G. Martins, J. Freitas, F. Judas, B. Trindade, H. Figueiredo, Evaluating structural differences in cortical bone tissue after demineralization and calcination., Microsc. Microanal. 14 (2008) 162–163. doi:10.1017/S1431927608089769.

[169] M. Figueiredo, S. Cunha, G. Martins, J. Freitas, F. Judas, H. Figueiredo, Influence of hydrochloric acid concentration on the demineralization of cortical bone, Chem. Eng. Res.

Des. 89 (2011) 116–124. doi:10.1016/j.cherd.2010.04.013.

[170] M. Figueiredo, J. Gamelas, G. Martins, Characterization of bone and bone-based graft materials using FTIR spectroscopy, Infrared Spectrosc. - Life Biomed. Sci. (2012) 315–338. doi:10.5772/36379.

[171] S. Joschek, B. Nies, R. Krotz, A. Göpferich, Chemical and physicochemical characterization of porous hydroxyapatite ceramics made of natural bone, Biomaterials. 21 (2000) 1645–1658. doi:10.1016/S0142-9612(00)00036-3.

[172] E.P. Paschalis, F. Betts, E. DiCarlo, R. Mendelsohn, a. L. Boskey, FTIR microspectroscopic analysis of normal human cortical and trabecular bone, Calcif. Tissue Int. 61 (1997) 480–486. doi:10.1007/s002239900371.

[173] E.P. Paschalis, R. Mendelsohn, A.L. Boskey, Infrared assessment of bone quality: A review, Clin. Orthop. Relat. Res. 469 (2011) 2170–2178. doi:10.1007/s11999-010-1751-4.

[174] R.N. Panda, M.F. Hsieh, R.J. Chung, T.S. Chin, FTIR, XRD, SEM and solid state NMR investigations of carbonate-containing hydroxyapatite nano-particles synthesized by hydroxide-gel technique, J. Phys. Chem. Solids. 64 (2003) 193–199. doi:10.1016/S0022-3697(02)00257-3.

[175] C.Y. Ooi, M. Hamdi, S. Ramesh, Properties of hydroxyapatite produced by annealing of bovine bone, Ceram. Int. 33 (2007) 1171–1177. doi:10.1016/j.ceramint.2006.04.001.

[176] B.B. Hole, D.S. Keller, W.M. Burry, J.A. Schwarz, Surface energetics of bone mineral and synthetic hydroxyapatite using inverse gas chromatography, J. Chromatogr. B. 879 (2011) 1847–1850. doi:10.1016/J.JCHROMB.2011.04.035.

[177] S. Mohammadi-Jam, K.E. Waters, Inverse gas chromatography applications: A review, Adv. Colloid Interface Sci. 212 (2014) 21–44. doi:10.1016/J.CIS.2014.07.002.

[178] M.P. Casaletto, S. Kaciulis, G. Mattogno, A. Mezzi, L. Ambrosio, F. Branda, XPS characterization of biocompatible hydroxyapatite-polymer coatings, Surf. Interface Anal. 34 (2002) 45–49. doi:10.1002/sia.1249.

[179] J. a. F. Gamelas, G. V. Duarte, P.J. Ferreira, Inverse gas chromatography and XPS of extracted kraft pulps, Holzforschung. 67 (2013) 273–276. doi:10.1515/hf-2012-0126.

[180] Y. Zhang, P.C. Zhu, D. Edgren, Crosslinking reaction of poly(vinyl alcohol) with glyoxal, J. Polym. Res. 17 (2010) 725–730. doi:10.1007/s10965-009-9362-z.

[181] Y. Huang, J. Fu, X. Huang, X. Tang, Characterization of poly(vinyl alcohol) membranes cross-linked by aldehyde-substituting cyclotriphosphazene, J. Macromol. Sci. Part B Phys. 48 (2009) 941–954. doi:10.1080/00222340903029066.

[182] K.B.R. Devi, K.B. Santhi, R. Mathivanan, P.V. Acetate, Spectra and normal coordinate analysis of poly vinyl acetate, Eng. Sci. Technol. An Int. J. 6 (2012) 205–210.

[183] R.N. Olaru, D.M. Vuluga, F. Georgescu, D. Marinescu, M. Dimonie, Microstructure of partially hydrolyzed polyvinyl alcohols used in PVC-S technology, UPB Sci. Bull. Ser. B Chem. Mater. Sci. 72 (2010) 77–84.

[184] K. Katsuraya, K. Hatanaka, K. Matsuzaki, K. Yamaura, Assignment of finely resolved 13C

NMR spectra of Poly(Vinyl Acetate), Macromol. Rapid Commun. 21 (2000) 697–700. doi:10.1002/1521-3927(20000601)21:10<697::AID-MARC697>3.0.CO;2-2.

[185] T. Terao, S. Maeda, A. Saika, High-Resolution Solid-state 13C NMR of Poly(vinyl alcohol): enhancement of tacticity splitting by intramolecular hydrogen bonds, Macromolecules. 16 (1983) 1535–1538.

[186] M. Kanekiyo, M. Kobayashi, I. Ando, H. Kurosu, T. Ishii, S. Amiya, A structural and dynamic study of poly(vinyl alcohol) in the gel state by solid-state 13C NMR and 1H pulse NMR, J. Mol. Struct. 447 (1998) 49–59. doi:10.1016/S0022-2860(98)00300-7.

[187] J.W. Gilmanl, Thermal Decomposition Chemistry of Poly (vinyl alcohol), Fire Polym. II Mater. Test Hazard Prev. ACS. 599 (1995) 161. http://pubs.acs.org/doi/abs/10.1021/bk-1995-0599.ch011.

[188] O.W. Guirguis, M.T.H. Moselhey, Thermal and structural studies of poly (vinyl alcohol) and hydroxypropyl cellulose blends, Nat. Sci. 04 (2012) 57–67. doi:10.4236/ns.2012.41009.

[189] O.W. Guirguis, M.T.H. Moselhey, Thermal and structural studies of poly (vinyl alcohol) and hydroxypropyl cellulose blends, Nat. Sci. 4 (2012) 57–67. doi:10.4236/ns.2012.41009.

[190] S. Mishra, R. Bajpai, R. Katare, A.K. Bajpai, Radiation induced crosslinking effect on semiinterpenetrating polymer networks of poly(vinyl alcohol), Express Polym. Lett. 1 (2007) 407–415. doi:10.3144/expresspolymlett.2007.58.

[191] R. Shi, J. Bi, Z. Zhang, A. Zhu, D. Chen, X. Zhou, L. Zhang, W. Tian, The effect of citric acid on the structural properties and cytotoxicity of the polyvinyl alcohol/starch films when molding at high temperature, Carbohydr. Polym. 74 (2008) 763–770. doi:10.1016/j.carbpol.2008.04.045.

[192] R. Pauliukaite, M. Ghica, Different Cross-Linking Agents for the Immobilization of Functionalized Carbon Nanotubes Within a Chitosan Film Supported on a Graphite- Epoxy Composite Electrode, Anal. Chem. 81 (2009) 5364–72. doi:10.1021/ac900464z.

[193] H.L. Lin, Y.F. Liu, T.L. Yu, W.H. Liu, S.P. Rwei, Light scattering and viscoelasticity study of poly(vinyl alcohol)-borax aqueous solutions and gels, Polymer (Guildf). 46 (2005) 5541–5549. doi:10.1016/j.polymer.2005.04.074.

[194] P. Coimbra, P. Ferreira, H.C. de Sousa, P. Batista, M.A. Rodrigues, I.J. Correia, M.H. Gil, Preparation and chemical and biological characterization of a pectin/chitosan polyelectrolyte complex scaffold for possible bone tissue engineering applications, Int. J. Biol. Macromol. 48 (2011) 112–118. doi:10.1016/j.ijbiomac.2010.10.006.

[195] V. Crescenzi, G. Paradossi, P. Desideri, M. Dentini, F. Cavalieri, E. Amici, R. Lisi, New hydrogels based on carbohydrate and on carbohydrate-synthetic polymer networks, (1997) 225–239.

[196] S.D. Nogare, A.N. Oemler, Acidimetric Determination of Vicinal Hydroxyl by Means of Sodium Periodate, Anal. Chem. 24 (1952) 902–904. doi:10.1021/ac60065a044.

[197] H. Ochiai, Y. Fujino, Y. Tadokoro, I. Murakami, Binding of borax to poly(vinyl alcohol) in aqueous solution, Polym. Commun. 21 (1980) 485–487.

[198] S.N. Kale, J. Mona, S. Dhobale, T. Thite, S.L. Laware, Intramolecular and intermolecular

crosslinked poly(vinyl alcohol)-borate complexes for the sustained release of fertilizers and enzymes, J. Appl. Polym. Sci. 121 (2011) 2450–2457. doi:10.1002/app.33776.

[199] H. Kurokawa, M. Shibayama, T. Ishimaru, S. Nomura, W. li Wu, Phase behaviour and sol-gel transition of poly(vinyl alcohol)-borate complex in aqueous solution, Polymer (Guildf). 33 (1992) 2182–2188. doi:10.1016/0032-3861(92)90886-2.

[200] M. Shibayama, M. Sato, Y. Kimura, H. Fujiwara, S. Nomura, 11B n.m.r. study on the reaction of poly(vinyl alcohol) with boric acid, Polymer (Guildf). 29 (1988) 336–340. doi:10.1016/0032-3861(88)90343-6.

[201] E. Carretti, I. Natali, C. Matarrese, P. Bracco, R.G. Weiss, P. Baglioni, A. Salvini, L. Dei, A new family of high viscosity polymeric dispersions for cleaning easel paintings, J. Cult. Herit. 11 (2010) 373–380. doi:10.1016/j.culher.2010.04.002.

[202] D. Harpaz, T. Axelrod, L.A. Yitian, E. Eltzov, S.R. Marks, I.Y.A. Tok, Dissolvable Polyvinyl-Alcohol Film, a Time-Barrier to Modulate Sample Flow in a 3D-Printed Holder for Capillary Flow Paper Diagnostics, Materials (Basel). 12 (2019). doi:10.3390/ma12030343.

[203] C.E. Weir, Infrared spectra of the hydrated borates, J. Res. Natl. Bur. Stand. Sect. A Phys. Chem. 70A (1966) 153. doi:10.6028/jres.070a.012.

[204] I. Restrepo, C. Medina, V. Meruane, A. Akbari-Fakhrabadi, P. Flores, S. Rodríguez-Llamazares, The effect of molecular weight and hydrolysis degree of poly(vinyl alcohol)(PVA) on the thermal and mechanical properties of poly(lactic acid)/PVA blends, Polímeros. 28 (2018) 169–177. doi:10.1590/0104-1428.03117.

[205] M. Pluta, M. Murariu, A. Da Silva Ferreira, M. Alexandre, A. Galeski, P. Dubois, Polylactide compositions. II. Correlation between morphology and main properties of PLA/calcium sulfate composites, J. Polym. Sci. Part B Polym. Phys. 45 (2007) 2770–2780. doi:10.1002/polb.21277.

[206] Y. Yang, C. Liu, P.R. Chang, Y. Chen, D.P. Anderson, M. Stumborg, Properties and structural characterization of oxidized starch/PVA/a-Zirconium phosphate composites, J. Appl. Polym. Sci. 115 (2010) 1089–1097. doi:10.1002/app.

[207] J.R. Khurma, D.R. Rohindra, A. V Nand, Synthesis and Properties of Hydrogels Based on Chitosan and Poly(Vinyl Alcohol) Crosslinked by Genipin, J. Macromol. Sci. Part A. 43 (2006) 749–758. doi:10.1080/10601320600602829.

[208] M.J. Moura, M.M. Figueiredo, M.H. Gil, Rheology of chitosan and genipin solutions, Mater. Sci. Forum. 587–588 (2008) 27–31. doi:10.4028/www.scientific.net/MSF.587-588.27.

[209] E.S. Costa-Júnior, E.F. Barbosa-Stancioli, a. a P. Mansur, W.L. Vasconcelos, H.S. Mansur, Preparation and characterization of chitosan/poly(vinyl alcohol) chemically crosslinked blends for biomedical applications, Carbohydr. Polym. 76 (2009) 472–481. doi:10.1016/j.carbpol.2008.11.015.

[210] D. V. Bax, N. Davidenko, D. Gullberg, S.W. Hamaia, R.W. Farndale, S.M. Best, R.E. Cameron, Fundamental insight into the effect of carbodiimide crosslinking on cellular recognition of collagen-based scaffolds., Acta Biomater. 49 (2017) 218–234. doi:10.1016/j.actbio.2016.11.059.

[211] I. Takahashi, S. Suzuki, Y. Imashiro, I. Takahashi, N. Horie, T. Yamane, S. Suzuki, Carbodiimide crosslinking agent, process for preparing the same, and coating material comprising the same. United States Patent US6124398A., US6124398A, 2000. doi:10.1016/0375-6505(85)90011-2.

[212] Y. Li, T.T. Thula, S. Jee, S.L. Perkins, C. Aparicio, E.P. Douglas, L.B. Gower, Biomimetic mineralization of woven bone-like nanocomposites: Role of collagen cross-links, Biomacromolecules. 13 (2012) 49–59. doi:10.1021/bm201070g.

[213] M.D. Shoulders, R.T. Raines, Collagen structure and stability, Annu. Rev. Biochem. 78 (2009) 929–958. doi:10.1146/annurev.biochem.77.032207.120833.

[214] K. Gelse, E. Pöschl, T. Aigner, Collagens - Structure, function, and biosynthesis, Adv. Drug Deliv. Rev. 55 (2003) 1531–1546. doi:10.1016/j.addr.2003.08.002.

[215] J.H. Muyonga, C.G.B. Cole, K.G. Duodu, Fourier transform infrared (FTIR) spectroscopic study of acid soluble collagen and gelatin from skins and bones of young and adult Nile perch (Lates niloticus), Food Chem. 86 (2004) 325–332. doi:10.1016/j.foodchem.2003.09.038.

[216] N. Kottegoda, I. Munaweera, N. Madusanka, V. Karunaratne, A green slow-release fertilizer composition based on urea-modified hydroxyapatite nanoparticles encapsulated wood, Curr. Sci. 101 (2011) 73–78.

[217] F.A. Al-Saif, M.S. Refat, Infrared spectroscopic investigation on the reaction mechanisms of urea with manganese(II), cadmium(II), magnesium(II) and calcium(II) formate at elevated temperature, J. Chem. Pharm. Res. 3 (2011) 616–625.

[218] J.-M. Oh, S.-H. Hwang, J.-H. Choy, The effect of synthetic conditions on tailoring the size of hydrotalcite particles, Solid States Ionics. 151 (2002) 285–291.

[219] J.P. Montheard, M. Chatzopoulos, D. Chappard, 2-Hydroxyethyl methacrylate (HEMA). Chemical properties and applications in biomedical fields, J. Macromol. Sci. - Rev. Macromol. Chem. Phys. C32 (1992) 1–34. doi:10.1080/15321799208018377.

[220] T.S.J. Kashi, M. Erfan, D.C. Watts, Effect of Water on HEMA Conversion by FT-IR Spectroscopy, J. Dent. Tehran Univ. Med. Sci. 4 (2007) 123–129.

[221] D.M. Drăguşin, D.S. Vasilescu, S. Van Vlierberghe, P. Dubruel, I.C. Stancu, Effect of initiator's concentration on properties of gelatin - Hema hydrogels, UPB Sci. Bull. Ser. B Chem. Mater. Sci. 74 (2012) 31–46.

[222] J.M. Seidel, S.M. Malmonge, Synthesis of PolyHEMA Hydrogels for Using as Biomaterials. Bulk and Solution Radical-Initiated Polymerization Techniques, Mater. Res. 3 (2000) 79–83.

[223] J.P. Montheard, M. Chatzopoulos, D. Chappard, 2-Hydroxyethyl methacrylate (hema): Chemical properties and applications in biomedical fields, J. Macromol. Sci. Part C. 32 (1992) 1–33. doi:10.1080/15321799208018377.

[224] A. Guiseppi-Elie, C. Dong, C.Z. Dinu, Crosslink density of a biomimetic poly(HEMA)-based hydrogel influences growth and proliferation of attachment dependent RMS 13 cells, J. Mater. Chem. 22 (2012) 19529–19539. doi:10.1039/c2jm32516k.

[225] S. Kim, B.H. Shin, C. Yang, S. Jeong, J.H. Shim, M.H. Park, Y. Bin Choy, C.Y. Heo, K. Lee, Development of poly(HEMA-Am) polymer hydrogel filler for soft tissue reconstruction by facile polymerization, Polymers (Basel). 10 (2018). doi:10.3390/polym10070772.

[226] M.C. Roberts, New in sity crosslinking chemistries for hydrogelation, The University of Utah, 2008. doi:10.1017/CBO9781107415324.004.

[227] D. Ray, P.K. Sahoo, G.P. Mohanta, Designing of Biodegradable Interpenetrating Polymer Network of Poly (vinyl alcohol-co-acrylic acid)/ sodium chloride hydrogel : An Approach to Drug Delivery, Network. 1 (2008) 144–151.

[228] L.H. Sperling, Interpenetrating Polymer Networks : An Overview, in: A.C. Society (Ed.), Adv. Chem., Washington, DC, 1994: pp. 3–38. doi:10.1021/ba-1994-0239.

[229] M. Sivakumar, K.P. Rao, Synthesis, characterization, and in vitro release of ibuprofen from poly(MMA-HEMA) copolymeric core-shell hydrogel microspheres for biomedical applications, J. Appl. Polym. Sci. 83 (2002) 3045–3054. doi:10.1002/app.10310.

[230] L. Civerchia-Perez, B. Faris, G. Lapointe, J. Beldekas, H. Leibowitzt, C. Franzblau, H.M. Kalckar, Use of collagen-hydroxyethylmethacrylate hydrogels for cell growth (connective tissue/cell surface/cell biology/fibroblasts), Cell Biol. 77 (1980) 2064–2068.

[231] C.J. Hawker, J.L. Hedrick, NMR spectra of diverse polymers (A), Macromolecules. 120 (1996) 2993–2995.

[232] X.L. Yan, W.F. Sun, J. Tang, X. Zhao, 1H NMR Study of Polyvinylalcohol Irradiated by Ultra-violet, Chinese Chem. Lett. 3 (2005) 379–381.

[233] M. Wilhelm, M. Neidho, S. Spiegel, H.W. Spiess, A collection of solid-state 13 C CP / MAS NMR spectra of common polymers, Macromol. Chem. Phys. 200 (1999) 2205–2207. doi:10.1002/(SICI)1521-3935(19991001)200:10<2205::AID-MACP2205>3.0.CO;2-6.

[234] A. Vyalikh, C. Elschner, M. Schulz, R. Mai, U. Scheler, Early Stages of Biomineral Formation—A Solid-State NMR Investigation of the Mandibles of Minipigs, Magnetochemistry. 3 (2017) 39. doi:10.3390/magnetochemistry3040039.

[235] A. Vyalikh, P. Simon, T. Kollmann, U. Scheler, Local Environment in Biomimetic Hydroxyapatite - Gelatin Nanocomposites As Probed by NMR Spectroscopy, J. Phys. Chem. 115 (2011) 1513–1519.

[236] K. Masuda, H. Kaji, F. Horii, CP / MAS 13 C NMR Analyses of Hydrogen Bonding and the Chain Conformation in the Crystalline and Noncrystalline Regions for Poly (vinyl alcohol) Films, J. Polym. Sci. Part B Polym. Phys. 38 (2000) 1–9.

[237] V. Raghunathan, J.M. Gibson, G. Goobes, J.M. Popham, E. a. Louie, P.S. Stayton, G.P. Drobny, Homonuclear and heteronuclear NMR studies of a statherin fragment bound to hydroxyapatite crystals, J. Phys. Chem. B. 110 (2006) 9324–9332. doi:10.1021/jp056644g.

[238] T. Kokubo, H. Takadama, How useful is SBF in predicting in vivo bone bioactivity?, Biomaterials. 27 (2006) 2907–2915. doi:10.1016/j.biomaterials.2006.01.017.

[239] J.-Y. Rho, L. Kuhn-Spearing, Z. P., Mechanical properties and the hierarchical structure of bone, Med. Eng. Phys. 20 (1998) 92–102. doi:10.1007/s10237-008-0128-z.

[240] H.H.K. Xu, C.G. Simon, Fast setting calcium phosphate-chitosan scaffold: Mechanical properties and biocompatibility, Biomaterials. 26 (2005) 1337–1348. doi:10.1016/j.biomaterials.2004.04.043.

[241] A.I. Pearce, R.G. Richards, S. Milz, E. Schneider, S.G. Pearce, Animal models for implant biomaterial research in bone: A review, Eur. Cells Mater. 13 (2007) 1–10. doi:vol013a01 [pii].

[242] C.M. Kang, J. Hwang, J.S. Song, J.H. Lee, H.J. Choi, Y. Shin, Effects of three calcium silicate cements on inflammatory response and mineralization-inducing potentials in a dog pulpotomy model, Materials (Basel). 11 (2018). doi:10.3390/ma11060899.

[243] F. Judas, Contribuição para o estudo de enxertos ósseos granulados alógenos e de biomateriais, Universidade de Coimbra, 2003. http://hdl.handle.net/10316/846.

[244] C.X.F. Lam, D.W. Hutmacher, J. Schantz, M.A. Woodruff, S.H. Teoh, Evaluation of polycaprolactone scaffold degradation for 6 months in vitro and in vivo., J. Biomed. Mater. Res. A. 90 (2009) 906–919. doi:10.1002/jbm.a.32052.

[245] M.R. Hausman, M.B. Schaffler, R.J. Majeska, Prevention of fracture healing in rats by an inhibitor of angiogenesis, Bone. 29 (2001) 560–564. doi:10.1016/S8756-3282(01)00608-1.

[246] W.E. Roberts, B.N. Epker, D.B. Burr, J.K. Hartsfield, J. a. Roberts, Remodeling of Mineralized Tissues, Part II: Control and Pathophysiology, Semin. Orthod. 12 (2006) 238–253. doi:10.1053/j.sodo.2006.08.003.

[247] F.M. Klenke, Y. Liu, H. Yuan, E.B. Hunziker, K.A. Siebenrock, W. Hofstetter, Impact of pore size on the vascularization and osseointegration of ceramic bone substitutesin vivo, J. Biomed. Mater. Res. Part A. 85A (2008) 777–786. doi:10.1002/jbm.a.31559.